

TESIS DOCTORAL

Design and characterization of spatial light modulator optical systems and geometrical phase elements for the generation of structured light

David Marco Castillo

2021

DIRECTORA:
Dra. María del Mar Sánchez López

CODIRECTOR:
Dr. Ignacio Moreno Soriano

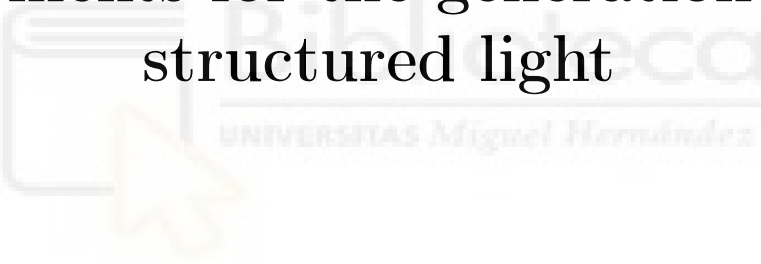


UNIVERSIDAD MIGUEL HERNÁNDEZ DE ELCHE

Programa de Doctorado en
TECNOLOGÍAS INDUSTRIALES Y DE
TELECOMUNICACIÓN



Design and characterization of spatial light modulator optical systems and geometrical phase elements for the generation of structured light



Doctorando: David Marco Castillo
Directora: Dra. María del Mar Sánchez López
Codirector: Dr. Ignacio Moreno Soriano

Programa de Doctorado en Tecnologías Industriales y de Telecomunicación
Universidad Miguel Hernández de Elche
En Elche, julio de 2021

This manuscript contextualizes and presents a work in the field of the experimental generation of optical vortices and vector beams. This thesis is presented under the Doctoral Program in Industrial and Telecommunications Technologies (Programa de Doctorado en Tecnologías Industriales y de Telecomunicación) in the form of a compendium of publications. The five works that comprise this thesis are the following:

- D. Marco, M. M. Sánchez-López, P. García-Martínez, and I. Moreno, "Using birefringence colors to evaluate a tunable liquid-crystal q-plate", *Journal of the Optical Society of America B* **36** (5), D34-D41 (2019).
DOI: <https://doi.org/10.1364/JOSAB.36.000D34>
JCR index: 2.180 (JCR2019 – Optics, 47/97, Q2)
- D. Marco, M. M. Sánchez-López, A. Cofré, A. Vargas, and I. Moreno, "Optimal triplicator design applied to a geometric phase vortex grating", *Optics Express* **27**(10), 14472-14486 (2019).
DOI: <https://doi.org/10.1364/OE.27.014472>
JCR index: 3.669 (JCR2019 – Optics, 19/97, Q1)
- P. García-Martínez, D. Marco, J. L. Martínez-Fuentes, M. M. Sánchez-López, and I. Moreno, "Efficient on-axis SLM engineering of optical vector modes", *Optics & Lasers in Engineering* **125**, 105859 (2020).
DOI: <https://doi.org/10.1016/j.optlaseng.2019.105859>
JCR index: 4.836 (JCR2020 – Optics, 13/99, Q1)
- D. Marco, A. Vargas, M. M. Sánchez-López, and I. Moreno, "Measuring the spatial deformation of a liquid-crystal on silicon display with a self-interference effect", *Optics Letters* **45**(16), 4480-4483 (2020).
DOI: <https://doi.org/10.1364/OL.396105>
JCR index: 3.776 (JCR2020 – Optics, 22/99, Q1).
- D. Marco, G. López-Morales, M. M. Sánchez-López, A. Lizana, I. Moreno, and J. Campos, "Customized depolarization spatial patterns with dynamic retardance functions", *Scientific Reports* **11**, 9415 (2021).
DOI: <https://doi.org/10.1038/s41598-021-88515-x>
JCR index: 4.379 (JCR2020 – Multidisciplinary Sciences, 17/73, Q1).



D^a. María del Mar Sánchez López, Catedrática de Física Aplicada de la Universidad Miguel Hernández de Elche y D. Ignacio Moreno Soriano, Catedrático de Óptica de la Universidad Miguel Hernández de Elche

CERTIFICAN

Que David Marco Castillo, ha realizado bajo su dirección, en el Instituto de Bioingeniería de la Universidad Miguel Hernández de Elche, el trabajo “Design and characterization of spatial light modulator optical systems and geometrical phase elements for the generation of structured light” que se recoge en esta memoria para optar al grado de Doctor.

Y para que conste, de acuerdo con la legislación vigente, firman este certificado para autorizar su presentación en Elche, a 13 de julio de 2021.

Prof. María del Mar Sánchez López
Directora

Prof. Ignacio Moreno Soriano
Codirector

Programa de Doctorado en

TECNologías **I**ndustriales y de **T**elecomunicación

Dr. D. Óscar Reinoso García, Coordinador del Programa de Doctorado en Tecnologías Industriales y de Telecomunicación de la Universidad Miguel Hernández de Elche.

CERTIFICA

Que el trabajo realizado por David Marco Castillo titulado **Design and characterization of spatial light modulator optical systems and geometrical phase elements for the generation of structured light**, ha sido dirigido por la Dra. María Del Mar Sánchez López y codirigido por el Dr. Ignacio Moreno Soriano y se encuentra en condiciones de ser leído y defendido como Tesis Doctoral ante el correspondiente tribunal en la Universidad Miguel Hernández de Elche.

Lo que firmo a los efectos oportunos en Elche, a 13 de julio de 2021

Fdo.: Dr. Óscar Reinoso García
Coordinador del Programa de Doctorado en
Tecnologías Industriales y de Telecomunicación

Agradecimientos

En primer lugar, quiero agradecer a la Dra. María del Mar Sánchez y al Dr. Ignacio Moreno que me dieran la oportunidad de realizar mi tesis doctoral bajo su dirección. Estoy muy agradecido por la cantidad de conocimientos que han compartido conmigo, por la ayuda que me han prestado en todo momento y por su interés genuino por mi presente y futuro.

Me gustaría agradecer a la Dra. Pascuala García su colaboración, su apoyo y que me pusiera en contacto con el Dr. Ignacio Moreno y la Dra. María del Mar Sánchez. Además, agradezco al Dr. Asticio Vargas su colaboración, todo lo que me ha enseñado durante nuestras sesiones en el laboratorio y sus consejos. También agradezco al Dr. Eugenio Roldán y al Dr. Germán de Valcárcel todo lo que me han enseñado durante la carrera y el máster en Valencia.

Quiero agradecer al Dr. Ángel Lizana y al Dr. Juan Campos su colaboración en nuestro último trabajo y quiero destacar la cantidad de cosas que he aprendido en el poco tiempo que hemos tenido la oportunidad de conversar. Además, estoy muy agradecido al Dr. Josep Nicolás, a la Dra. Alba Pereiro y al Dr. Dominique Heinis por darme la oportunidad de pasar un mes en el Sincrotrón ALBA. Fue una experiencia corta, pero enormemente enriquecedora.

Agradezco la ayuda desinteresada del Dr. Aarón Cofré cuando llegué a Elche y su amistad. Quiero dar gracias a Julio César Quiceno y a la Dra. Guadalupe López por ser mucho más que compañeros de investigación. También doy gracias a Abdelghafour Messaadi y a Esther Nabadda por los escasos pero tan buenos ratos que hemos pasado juntos.

No hay palabras en la lengua castellana que expresen el agradecimiento a mi madre Carmen, a mis hermanos Toni y Quique y a mi prima Cristina por todo lo que han hecho por mí y por el amor infinito que me han dado y me siguen dando.

Agradezco enormemente a Zoriana el amor y el apoyo que me da cada día, en los buenos y en los malos ratos, de nuevo, no hay palabras para expresar lo agradecido que estoy de tenerla en mi vida.

Quiero agradecer a mis amigos Los Notarios todo su amor incondicional y que siempre estén ahí. Agradezco también a mis amigos de la carrera su apoyo y todos los buenos ratos que hemos vivido.

También quiero mostrar mi agradecimiento a todas las personas que me han querido y apoyado a lo largo de mi vida y que aquí no he mencionado. Por último, te agradezco a ti que te tomes el tiempo de leer esta tesis.

Summary

This thesis develops optical systems for the generation and control of structured light. These light beams with spatial control of their amplitude, phase and polarization are receiving much attention in the scientific community because of their applications in areas such as microscopy, materials processing, optical communications and polarimetry, among others. Two main kinds of techniques exist to generate these beams. One method is based on geometrical phase (GP) elements, which are advanced diffractive optical components consisting of microstructured retarders, where the spatial distribution of the optical axis allows the encoding of any phase function. The other technique employs spatial light modulators (SLMs), which are pixelated displays that allow the dynamic encoding of arbitrary phase functions.

The thesis is presented as a compendium of five publications where we designed and characterized optical systems based on GP elements and on SLMs to generate light beams with structured polarization (vector beams) and optical vortices. The work is focused on the experimental realization of such vector and vortex beams with these technologies. Thus, it includes an important part devoted to the characterization and evaluation of the components and devices used for this purpose. However, the generation of such structured light requires a deep understanding of the properties of the superposition of light beams with different polarization states. Therefore, the thesis also includes a comprehensive synthesis of the formalism required to describe such control of polarization and on the design of diffractive optical elements used to generate the proper superposition.

The first work consists in a spectral characterization of the retardance and the birefringence colors of a tunable liquid-crystal commercial q -plate operative in the visible and near-IR range. This device enables the realization of vector beams in compact and simple optical setups and, to our knowledge, is the only tunable q -plate model that is commercially available. The retardance tunability makes it very convenient to manipulate vector beams in a wide spectral range from 400 nm to 1600 nm. In addition, we demonstrated that placing the q -plate between crossed linear polarizers and illuminating the system with broadband white light is a simple and fast method to determine the voltage values where it behaves as a first-order retarder. Also, the method allows a rough estimation of the wavelength where the device has π retardance. This tunable device was employed to generate pure and hybrid vector beams with exotic intensity and polarization patterns.

Second, we presented the design of a liquid-crystal geometric-phase diffraction

grating that generates a two-dimensional array of optical vortices with different topological charges. The key aspect of the work is that its design relies on the optimal triplicator phase profile, which ensures the maximum theoretical diffraction efficiency achievable with a pure-phase function. In addition, since it is built as a geometrical phase element, it is a flat and thin element that may be easily incorporated in optical systems where compactness is required. The obtained experimental results have proven that the designed grating can also serve as a topological charge vortex detection system.

The third work presents a technique to efficiently generate vector beams with liquid-crystal on silicon (LCOS) SLMs. SLM-based optical systems are the most versatile way to generate structured light since they are programmable devices. But because of their pixelated structure they present diffraction losses, that make their optical efficiency lower than systems based on geometrical phase elements. In addition, SLMs make the system bulkier, typically requiring the use of beam splitters, and they can present a phase fluctuation effect caused by flicker. All these aspects significantly reduce the efficiency of the system generating vector beams. In this work, we developed an efficient system that uses two LCOS SLMs using a common path geometry. The employed SLMs were free from flicker and, therefore, they could be used to apply a complex amplitude encoding technique that generated the desired beam on axis. As a whole, the optical system represents a very efficient and versatile way to generate vector modes.

The fourth work that constitutes this thesis is a new technique for measuring the backplane deformation of a SLM. This is another major defect that can be present in SLMs and must be taken into account to achieve good results. The technique is based on a self-interference effect that occurs inside the SLM when being illuminated with light of wavelength far from its operation spectral range. In this situation, the anti-reflection coating of the device does not work properly and we can exploit this a priori undesired effect to measure and then correct the backplane deformation. Since the effect is produced by the SLM itself, no external interferometric arrangements are required, thus making this technique robust and stable.

Finally, we used a SLM to generate beams with tailored spatial variation of its degree of polarization across its transverse section. The depolarization spatial variation was generated by imaging a time-varying SLM phase pattern. We generated exotic beams with a spirally-shaped distribution of its degree of polarization, analogous to the spiral phase variation in an optical vortex. The technique might be of interest in testing imaging polarimeters and in the emulation of structured light exhibiting a spatial variation of the degree of polarization as an additional parameter.

These publications represent an advance in the field of the techniques employed to generate vortex and vector light beams, thus making several contributions to the efficient control of polarized light with diffractive elements.

Resumen

Esta tesis doctoral presenta el desarrollo de sistemas ópticos para la generación y el control de luz estructurada. Estos haces de luz con control espacial de su amplitud, fase y polarización están recibiendo mucha atención por parte de la comunidad científica por su potencial en aplicaciones como microscopía, procesamiento de materiales, comunicaciones ópticas y polarimetría, entre otras. Existen dos tipos de técnicas principales para generar estos haces. Una está basada en elementos de fase geométrica (GP), los cuales son componentes ópticos difractivos que consisten en retardadores microestructurados, en los cuales se puede implementar cualquier función de fase en la distribución espacial de sus ejes ópticos. La otra técnica se basa en emplear moduladores espaciales de Luz (SLMs), que consisten en pantallas pixeladas que permiten codificar de forma dinámica funciones de fase arbitrarias.

La tesis se ha presentado como un compendio de artículos formado por cinco publicaciones en los cuales diseñamos y caracterizamos dispositivos ópticos, basados en elementos GP y en SLMs, para generar haces de luz con polarización estructurada (haces vectoriales) y vórtices ópticos. El trabajo está enfocado en la generación experimental de estos haces vectoriales y vórtices ópticos con estas tecnologías. Por lo tanto, incluye una parte importante dedicada a la caracterización y evaluación de los componentes ópticos y dispositivos empleados para dicho propósito. No obstante, la generación de este tipo de luz estructurada requiere una comprensión profunda de las propiedades de la superposición de haces de luz en diferentes estados de polarización. Así pues, la tesis también incluye una síntesis exhaustiva del formalismo requerido para describir dicho control de la polarización, y además, del diseño de elementos ópticos difractivos empleados para producir la superposición adecuada.

El primer trabajo consiste en una caracterización espectral del retardo y de los colores de birrefringencia de una lámina- q comercial retardadora sintonizable de cristal líquido que opera en el rango visible e infrarrojo cercano. Este dispositivo permite generar haces vectoriales en montajes experimentales compactos y sencillos y, que nosotros sepamos, es la única lámina- q sintonizable en el mercado. El hecho de poder sintonizar el retardo hace que la lámina sea adecuada para manipular haces vectoriales en un rango espectral entre los 400 y los 1600 nm. Además, demostramos que situar la lámina entre polarizadores lineales cruzados e iluminarla con luz blanca de amplio espectro es un método sencillo y rápido de determinar los valores de voltaje en los cuales se comporta como un retardador

de primer orden. El método también permite una estimación aproximada de la longitud de onda en la cual la lámina muestra retardo π . Este dispositivo sintonizable fue empleado para generar haces vectoriales puros e híbridos con patrones de intensidad y polarización exóticos.

En segundo lugar, presentamos el diseño de una red de difracción de fase geométrica fabricada en cristal líquido que genera una matriz de vórtices ópticos con diferente carga topológica. El aspecto clave del trabajo es que el diseño está basado en el perfil del triplicador óptimo de fase, el cual asegura la máxima eficiencia de difracción teórica alcanzable con una función pura de fase. Además, puesto que la red está fabricada como un elemento de fase geométrica, es plana y delgada, por lo que puede ser fácilmente incorporada en un sistema óptico donde se requiera compactibilidad. Los resultados experimentales obtenidos han demostrado que la red diseñada puede usarse también como detector de la carga topológica de un vórtice óptico.

El tercer trabajo presenta una técnica para generar haces vectoriales de forma eficiente con SLMs de cristal líquido sobre silicio (LCOS). Los sistemas ópticos basados en SLMs son la forma más versátil de generar luz estructurada, ya que son dispositivos programables. Pero, debido a su estructura pixelada, presentan pérdidas por difracción, lo cual hace que su eficiencia óptica sea más baja que la de los sistemas basados en elementos de fase geométrica. Además, los SLMs hacen que el sistema experimental ocupe más espacio, requiriendo típicamente separadores de haz, y pueden presentar fluctuaciones de fase ocasionadas por el flicker. Todo esto reduce significativamente la eficiencia del sistema generador de haces vectoriales. En este trabajo, desarrollamos un sistema eficiente que usa dos SLMs LCOS en una geometría de camino común. Los SLMs empleados no presentaban flicker, por lo tanto, pudieron ser empleados para aplicar una técnica de codificación de amplitud compleja que generó el haz vectorial deseado en eje. El sistema en su conjunto es una forma muy eficiente y versátil de producir modos vectoriales.

El cuarto trabajo de esta tesis es una técnica nueva para medir la deformación del panel de silicio de un SLM. Esta deformación es otro defecto importante que presentan los SLMs y que hay que tener en cuenta para lograr buenos resultados. La técnica se basa en un efecto interferométrico que ocurre dentro del SLM cuando es iluminado con luz de longitud de onda que está lejos de su rango espectral de operación. Bajo esta circunstancia, la capa antireflejante del dispositivo no funciona correctamente y podemos explotar este efecto, en principio indeseado, para medir y corregir la deformación del panel de silicio. Dado que este efecto lo produce el propio SLM, no se necesitan sistemas interferométricos externos, por lo que la técnica resulta robusta y estable.

Por último, usamos un SLM para generar haces con una variación espacial escogida a voluntad de su grado de polarización en su sección transversal. La variación espacial de la despolarización fue generada haciendo la imagen de un patrón de fase mostrado en el SLM. De este modo, generamos haces exóticos con una distribución espacial en espiral de su grado de polarización, análoga a la variación espiral de la fase en un vórtice óptico. La técnica podría ser interesante

para el calibrado de polarímetros de imagen o para emular luz estructurada con una variación espacial del grado de polarización como un parámetro adicional.

Estas publicaciones representan avances en el campo de las técnicas usadas para generar haces vectoriales y vórtices ópticos, aportando varias contribuciones al control eficiente de la luz polarizada con elementos ópticos difractivos.



Contents

| | | |
|----------|---|-----------|
| 1 | Introduction | 1 |
| 2 | Polarized light | 3 |
| 2.1 | Fully polarized light | 3 |
| 2.1.1 | The polarization ellipse | 3 |
| 2.1.2 | Jones formalism and the polarization ellipse parameters . . . | 4 |
| 2.1.3 | The Poincaré sphere for fully polarized light | 8 |
| 2.2 | Polarization optical components | 13 |
| 2.2.1 | Diattenuators | 13 |
| 2.2.2 | Retarders | 14 |
| 2.2.3 | Experimental realization of linear retarders | 16 |
| 2.2.4 | Spectral characterization of linear retarders | 18 |
| 2.2.5 | Birefringence colors in linear retarders | 22 |
| 2.3 | Partially Polarized Light | 23 |
| 2.3.1 | Stokes parameters for partially polarized light | 25 |
| 2.3.2 | Incoherent superposition of polarized light | 28 |
| 2.3.3 | Experimental generation of partially polarized light | 31 |
| 2.3.4 | Mueller matrices | 33 |
| 2.3.5 | The Lu-Chipman Decomposition | 35 |
| 3 | Diffractive optical elements | 39 |
| 3.1 | Pure phase diffractive optical elements | 39 |
| 3.1.1 | Linear phase gratings and spiral phases | 40 |
| 3.1.2 | Harmonic terms in pure phase gratings. The optimal phase triplicator | 41 |
| 3.2 | Implementation of diffractive optical elements | 45 |
| 3.2.1 | Spatial light modulators | 46 |
| 3.2.2 | Geometrical Phase Elements. The q -plate | 48 |
| 4 | Structured light | 52 |
| 4.1 | High-order Gaussian modes | 52 |
| 4.1.1 | Hermite-Gaussian modes | 53 |
| 4.1.2 | Laguerre-Gaussian modes | 54 |
| 4.1.3 | First-order Gaussian modes superposition | 55 |
| 4.1.4 | Higher-order Laguerre-Gaussian modes superposition | 57 |
| 4.2 | Vector beams | 58 |

| | | |
|----------|--|-----------|
| 4.2.1 | First-order Laguerre-Gaussian modes vector superposition . . | 59 |
| 4.2.2 | First-order Hermite-Gaussian modes vector superposition . . | 64 |
| 4.2.3 | Higher-order and hybrid vector beams | 66 |
| 4.2.4 | Experimental generation of vector beams | 68 |
| 5 | Publications summary | 71 |
| 5.1 | Using birefringence colors to evaluate a tunable liquid-crystal q -plate | 72 |
| 5.2 | Optimal triplicator design applied to a geometric phase vortex grating | 73 |
| 5.3 | Efficient on-axis SLM engineering of optical vector modes | 74 |
| 5.4 | Measuring the spatial deformation of a liquid-crystal on silicon display with a self-interference effect | 75 |
| 5.5 | Customized depolarization spatial patterns with dynamic retardance functions | 76 |
| 6 | Conclusions | 78 |



Chapter 1

Introduction

Optical vortices are beams that present a phase singularity at the center, where the optical field is zero. Orthogonally polarized vortices can be combined to generate vector beams. These are light fields that present a spatial variation of the polarization across its transverse section [1], [2].

The generation of these type of beams has been widely implemented with liquid crystal on silicon (LCOS) spatial light modulators (SLMs). These devices are a very flexible tool, since they are capable of adding an arbitrary phase function to light by means of computer generated holograms (CGHs) [3], [4]. Their main downsides include an introduction of losses due to their pixelated structure, high cost and the fact that they only modulate one polarization component. Since two orthogonal polarization components have to be modulated for generating most types of vector beams, complex experimental arrangements are required to modulate both components.

The advances in the last years in diffractive optical elements led to the fabrication of retarders with a spatial orientation of their fast axis that allowed to modulate the two orthogonal polarization components at the same time [5]. Devices such as q -plates generate two vortices at two orthogonal components, so they can generate vector beams [6]. These retarders are known as geometric phase elements, and they are more efficient and less expensive than SLMs. Nevertheless, the phase functions that they impart are fixed in fabrication.

The properties of vortices and vector beams make them a suitable tool for several applications, such as optical trapping, microscopy, metrology, materials processing and classical and quantum optical communications. These applications require efficient generation systems. Furthermore, simplicity, cost and compactness are essential features for most applications. In addition, the optical components of these systems need to be properly characterized to ensure its ideal performance.

In this thesis, we present the experimental realization of vector and vortex beams with these two different technologies (SLMs and geometric phase elements), so an important part of the thesis is devoted to characterize the employed components and devices. Generating these vector vortex beams requires a deep understanding of the superposition of light beams with different polarization states. Therefore, the thesis also includes a comprehensive synthesis of the formalism re-

quired to describe the engineering of polarization patterns and their interpretation in terms of the corresponding Poincaré sphere.

The objectives of this thesis are the following:

- To characterize the spectral retardance of a tunable liquid-crystal commercial q -plate and relate it to its birefringence colors, thus offering a simple and fast method to determine when the q -plate is acting as a first-order retarder.
- The desing of efficient geometric phase elements capable of parallely generating and detecting optical vortices with different topological charges.
- To develop a robust non-interferometric method for measuring and correcting the backplane deformation of a LCOS SLM to improve the quality of the implemented phase functions.
- To generate beams with a custom spatial distribution of its degree of polarization using a SLM.
- Using the above technique to emulate vector beams where the spatial variation of its degree of polarization is introduced as a new parameter.
- To design an on-axis, flexible and efficient experimental system to generate vector beams by encoding the amplitude and phase of high-order Gaussian modes on LCOS SLMs.
- The implementation of a computing code that allows us to draw the polarization maps of vector beams, where these beams are generated either numerically or experimentally.

The structure of the thesis is organized as follows: After this introduction, the second chapter presents the basic aspects of polarized light, optical components including linear retarders with their spectral characterization, and partially polarized light. Next, the third chapter introduces diffractive optical components and their physical implementation as geometrical phase elements and with spatial light modulators. The fourth chapter describes high-order Gaussian modes, as well as vector beams, and reviews some of the most employed techniques to generate them. Then, the publications that constitute this thesis are summarized in the fifth chapter. Finally, the conclusions that result from this thesis are presented in chapter six. The publications that comprise this thesis can be found in the appendix.

Chapter 2

Polarized light

In this chapter, we review the fundamental aspects of polarized light. First, we introduce fully polarized light and its representation on the Poincaré sphere. Then, we discuss optical retarders, a technique for its spectral characterization, and the birefringence colors they present. These last topics are applied in our work "Using birefringence colors to evaluate a tunable liquid-crystal q -plate" [7]. Finally, we perform a review of partially polarized light and several methods to generate it with quasi-monochromatic sources, which complements our paper "Customized depolarization spatial patterns with dynamic retardance functions" [8].

2.1 Fully polarized light

Classically, light is described as a solution to the electromagnetic (EM) wave equation. A simple solution is the monochromatic plane wave. The electric field of a plane wave is the same along a plane perpendicular to the direction of propagation at a given instant of time. Although such a solution is an idealization, the electric field locally behaves like a plane wave in a wide variety of situations. Therefore, the monochromatic plane wave is suitable for describing many basic and advanced topics in polarization. Furthermore, complex solutions to the EM wave equation can be decomposed as a linear superposition of plane waves.

2.1.1 The polarization ellipse

The electric field of a monochromatic plane wave is described as a vector that harmonically oscillates in time and space on a plane perpendicular to its direction of propagation [9]. For a plane wave propagating along the z axis, the electric field vector can be expressed as a linear superposition of two harmonic waves oscillating on the x and y axes:

$$\vec{\mathbf{E}}(z, t) = (E_{0x}e^{i\delta_x}\hat{\mathbf{x}} + E_{0y}e^{i\delta_y}\hat{\mathbf{y}}) e^{i(\omega t - kz)}, \quad (2.1)$$

where $\hat{\mathbf{x}}$ and $\hat{\mathbf{y}}$ are unitary vectors along the x and y directions, respectively. Equation 2.1 describes the electric field as a complex vector. The real quantities E_{0x} and E_{0y} are the amplitudes for the components along the x and y directions.

The phases for each component are the argument of the complex exponentials. Each component has a constant phase term of δ_x and δ_y . The dependence in time and z inside the time-space propagator ($\omega t - kz$) is the same for both components. The angular frequency $\omega = 2\pi/T$ describes the harmonic evolution in time (t), where T is the time period of the wave. On the other hand, the spatial frequency (wavenumber) $k = 2\pi/\lambda$ describes the harmonic spatial evolution along z , where λ is the wavelength, namely the spatial period. The temporal and spatial harmonic dependence in Eq. 2.1 becomes evident if we take the real part of Eq. 2.1, which is also a solution to the EM wave equation of the form

$$\vec{\mathbf{E}}_{\text{Re}}(z, t) = E_x(z, t)\hat{\mathbf{x}} + E_y(z, t)\hat{\mathbf{y}}, \quad (2.2)$$

$$E_x(z, t) = E_{0x} \text{Re} [e^{i(\omega t - kz + \delta_x)}] = E_{0x} \cos(\omega t - kz + \delta_x), \quad (2.3)$$

$$E_y(z, t) = E_{0y} \text{Re} [e^{i(kz - \omega t + \delta_y)}] = E_{0y} \cos(\omega t - kz + \delta_y), \quad (2.4)$$

where $E_x(z, t)$ and $E_y(z, t)$ are the parametric equations of an ellipse with parameters t and z . The electric field in Eq. 2.2 traces an ellipse in the xy plane as the wave evolves in time and space. Figure 2.1 shows its evolution with z and t for a spatial (2.1(a)) and a temporal (2.1(b)) period. Combining Eqs. 2.3 and 2.4 and eliminating the time-space propagator it is shown that the functions $E_x(z, t)$ and $E_y(z, t)$ are related as [10]

$$\frac{E_x(z, t)^2}{E_{0x}^2} + \frac{E_y(z, t)^2}{E_{0y}^2} - \frac{E_x(z, t)E_y(z, t)}{E_{0x}E_{0y}} \cos \delta = \sin^2 \delta. \quad (2.5)$$

The phase difference between the x and y components is $\delta = \delta_y - \delta_x$. Equation 2.5 is the equation of an ellipse. Note that the ellipse is generally rotated with respect to the x and y axes because of the crossed term modulated by $\cos \delta$. However, when δ is an odd multiple of $\pi/2$, the crossed term vanishes and Eq. 2.5 becomes the well-known equation of a centered ellipse.

2.1.2 Jones formalism and the polarization ellipse parameters

Eq. 2.5 shows that only three parameters are needed to describe the polarization ellipse: the amplitudes for each component E_{0x} , E_{0y} , and the phase difference δ between them. It is convenient to go a step further and impose that the vector $\vec{\mathbf{E}}(z, t)$ in Eq. 2.1 is normalized. This restriction implies that the amplitudes are determined by one parameter α , so the amplitudes are $E_{0x} = \cos \alpha$ and $E_{0y} = \sin \alpha$. Therefore, the angle α is related to both components as

$$\tan \alpha = E_{0y}/E_{0x}, \quad 0 \leq \alpha \leq \pi/2, \quad (2.6)$$

where we have restricted $0 \leq \alpha \leq \pi/2$, thus only changing the weight between the components without adding a negative sign. On the other hand, δ controls the phase difference between the components, and we have restricted $0 \leq \delta \leq 2\pi$.

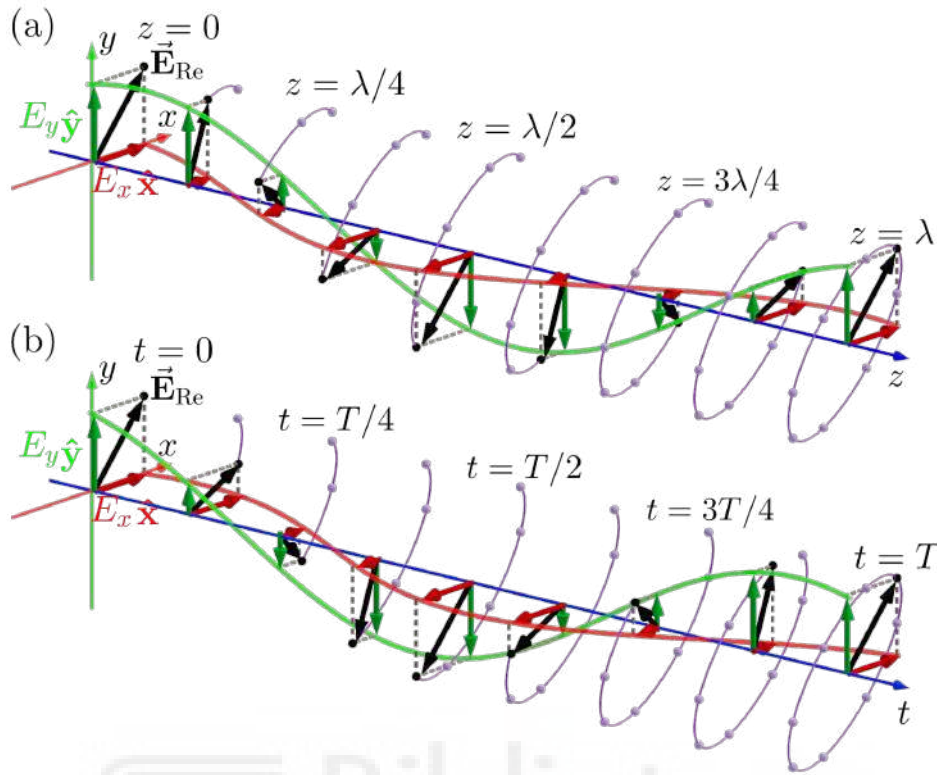


Figure 2.1: Evolution of the electric field vector $\vec{E}_{\text{Re}}(z, t)$ in one (a) spatial (b) temporal period.

Now only α and δ are needed to determine a normalized state of polarization, up to a global phase factor. We express Eq. 2.1 in terms of α as

$$|E(z, t)\rangle = e^{i(kz - \omega t)} |E\rangle, \quad (2.7)$$

$$|E\rangle = \cos \alpha |x\rangle + \sin \alpha e^{i\delta} |y\rangle, \quad (2.8)$$

where $|E\rangle$ is known as the Jones vector. First, note that we have replaced the arrow vector notation by the Dirac notation: $\vec{E}(z, t)$ is $|E(z, t)\rangle$ and \hat{x} and \hat{y} are $|x\rangle$ and $|y\rangle$, respectively. From now on, we will use the Dirac notation for vectors. This will further allow us to express operators describing optical components more compactly. Also note that the Jones vector contains the parameters α and δ , so it fully describes the shape of the polarization ellipse for a normalized electric field vector. Therefore, we will mostly use Jones vectors to describe states of polarization throughout this thesis.

There are several cases where the shape of the ellipse is specially interesting. For instance, when $\delta = 0$ or $\delta = \pi$, Eq. 2.5 turns into the equation of a line with zero intercept and slope $\pm \tan \alpha$. Therefore, for $\delta = 0$ or $\delta = \pi$, the light is said to be linearly polarized i.e., the ellipse has collapsed to a line. The linear polarization is rotated by an angle $\pm \alpha$ with respect to the x axis. The resulting Jones vector for linearly polarized light is

$$|E\rangle = \cos \alpha |x\rangle \pm \sin \alpha |y\rangle. \quad (2.9)$$

When $\alpha = 0$ the light is linearly polarized along the x direction (linear horizontally polarized LHP) described by $|x\rangle$, and when $\alpha = \pi/2$ the light is polarized along the y direction (linear vertically polarized LVP) and it is described by $|y\rangle$. If $\alpha = \pi/4$ the light is linearly polarized along the 45° direction (L45P) for $\delta = 0$, and along the -45° direction (L-45P) for $\delta = \pi$:

$$|45^\circ\rangle = \frac{1}{\sqrt{2}} (|x\rangle + |y\rangle), \quad (2.10)$$

$$|-45^\circ\rangle = \frac{1}{\sqrt{2}} (|x\rangle - |y\rangle). \quad (2.11)$$

Another interesting situation is when $\delta = \pi/2$ or $\delta = 3\pi/2$. The crossed term in Eq. 2.5 vanishes, and it becomes the equation of a centered ellipse. In addition, if the amplitudes for each component are equal ($\alpha = \pi/4$), Eq. 2.5 becomes the equation of a circle. As a result, the polarization vector undergoes a circular motion. Considering that we look at the light as it comes towards us, the electric field vector spins in time in a clockwise direction when $\delta = \pi/2$, and in a counterclockwise direction when $\delta = 3\pi/2$. We call the first case right circular polarization (RCP) and the second left circular polarization (LCP), following the convention in [11]. The Jones vectors describing RCP and LCP are

$$|R\rangle = \frac{1}{\sqrt{2}} (|x\rangle + i |y\rangle), \quad (2.12)$$

$$|L\rangle = \frac{1}{\sqrt{2}} (|x\rangle - i |y\rangle). \quad (2.13)$$

In fact, the electric field vector is generally spinning clockwise or counterclockwise depending on the value of δ , regardless of the ellipse shape. However, there is an exception: the sense of rotation is not defined for linearly polarized light ($\delta = 0, \pi$). Considering consecutive values of t for a constant z in the parametric form of the polarization ellipse (Eqs. 2.3 and 2.4) leads to the conclusion that if $0 < \delta < \pi$ the electric field spins clockwise and if $\pi < \delta < 2\pi$ it does counterclockwise. The evolution of an electric field spinning counterclockwise is depicted in Fig. 2.1(b).

The polarization ellipse for LHP, LVP, L45P, L-45P, RCP, and LCP states can be found in table 2.1. Any Jones vector can be expressed as a linear combination of a pair $\{|x\rangle, |y\rangle\}$, $\{|45^\circ\rangle, |-45^\circ\rangle\}$, and $\{|R\rangle, |L\rangle\}$, since each pair forms a basis. In addition, each basis is orthonormal.

The decomposition of a Jones vector in its circular components $|R\rangle$ and $|L\rangle$ gives rise to a description of the polarization ellipse in terms of two parameters: the orientation angle ψ and the ellipticity angle ε . These parameters provide a better intuition about the shape of the ellipse than α and δ . Figure 2.2 depicts the polarization ellipse and its main parameters. As discussed above, the ellipse is usually rotated. The rotation of the semi-major axis of the ellipse with respect to the x axis is given by the angle ψ . We restrict the rotation ψ to values between

0 and π . Fig. 2.2 also shows a frame of reference $x' y'$ rotated by an angle ψ i.e., the frame of reference where the ellipse is not rotated. We obtain the orthonormal vectors $|x'\rangle$ and $|y'\rangle$ describing linearly polarized light along the x' and y' directions rotating the vectors $|x\rangle$ and $|y\rangle$ by an angle ψ :

$$|x'\rangle = \cos \psi |x\rangle + \sin \psi |y\rangle, \quad (2.14)$$

$$|y'\rangle = -\sin \psi |x\rangle + \cos \psi |y\rangle. \quad (2.15)$$

Consider a Jones vector described by Eq. 2.8 in the $\{|x\rangle, |y\rangle\}$ basis. We express the vector in the $\{|x'\rangle, |y'\rangle\}$ basis as

$$|E\rangle = \cos \alpha' |x'\rangle + \sin \alpha' e^{i\delta'} |y'\rangle. \quad (2.16)$$

The angles α' and δ' control the weight and the phase for each component. These angles differ from the angles α and δ describing the Jones vector $|E\rangle$ in the $\{|x\rangle, |y\rangle\}$ basis. We define α' as $\tan \alpha' = E'_{0y}/E'_{0x}$, where E'_{0x} and E'_{0y} are the amplitudes of the Jones vector along the x' and y' directions, which are the semi-major and semi-minor axes of the ellipse, respectively. Note that the equation of the ellipse 2.5 may be expressed in the new frame of reference by replacing every quantity with a primed quantity. Since the ellipse is centered in the new frame of reference, δ' is an odd multiple of $\pi/2$, so the state is described by the Jones vector

$$|E\rangle = \cos \alpha' |x'\rangle \pm i \sin \alpha' |y'\rangle = \cos \varepsilon |x'\rangle + i \sin \varepsilon |y'\rangle. \quad (2.17)$$

We have expressed the second part of this equation in terms of the ellipticity angle ε by absorbing the \pm sign inside ε . Therefore, $\varepsilon = \pm\alpha'$, where \pm is the sign of the exponential $\exp(i\delta')$. From now on we restrict $-\pi/4 \leq \varepsilon \leq \pi/4$. Note that the parametric equations of the ellipse 2.3 and 2.4 can be obtained for the new frame of reference by replacing $E_x(z, t)$, $E_y(z, t)$, E_{0x} , E_{0y} and δ with $E_{x'}(z, t)$, $E_{y'}(z, t)$, $E_{0x'}$, $E_{0y'}$ and δ' . Therefore, when $\delta' = \pi/2$ the field spins clockwise and when $\delta' = 3\pi/2$ it does counterclockwise. Since $\varepsilon > 0$ when $\delta' = \pi/2$ and $\varepsilon < 0$ when $\delta' = 3\pi/2$, the motion is right-handed for $\varepsilon > 0$ and left-handed for $\varepsilon < 0$. In addition, it is straightforward to see from Eq. 2.17 that when $\varepsilon = 0$ the light is linearly polarized along the $|x'\rangle$ direction.

Using Eqs. 2.14, 2.15 and Eq. 2.17, we obtain the expression for the Jones vector in Eq. 2.8 in terms of the azimuth and ellipticity angles of the ellipse:

$$|E\rangle = (\cos \varepsilon \cos \psi - i \sin \varepsilon \sin \psi) |x\rangle + (\cos \varepsilon \sin \psi + i \sin \varepsilon \cos \psi) |y\rangle. \quad (2.18)$$

As Fig. 2.2 shows, ε controls the relation between the semi-minor $E_{0x'}$ and semi-major $E_{0y'}$ axes of the ellipse, and hence it measures how far is the state from being linear ($\varepsilon = 0$) or circular (RCP for $\varepsilon = \pi/4$ and LCP for $\varepsilon = -\pi/4$).

An interesting expression arises when we express the Jones vector in Eq. 2.18 in the $\{|R\rangle, |L\rangle\}$ basis using Eqs. 2.12 and 2.13:

$$|E\rangle = \cos \chi e^{-i\psi} |R\rangle + \sin \chi e^{i\psi} |L\rangle, \quad (2.19)$$

where $\chi = \pi/4 - \varepsilon$, so $0 \leq \chi \leq \pi/2$. Now the angle ε controls the weight of the circular components and 2ψ is the phase difference between them. When the angle $\chi = 0$ we have RCP light, when $\chi = \pi/2$ we have LCP, and when $\chi = \pi/4$ we have linearly polarized light. Since the orientation of the ellipse is given by ψ , it is evident from Eq. 2.19 that a phase difference of 2ψ between circular components is equivalent to rotating an angle ψ the polarization ellipse.

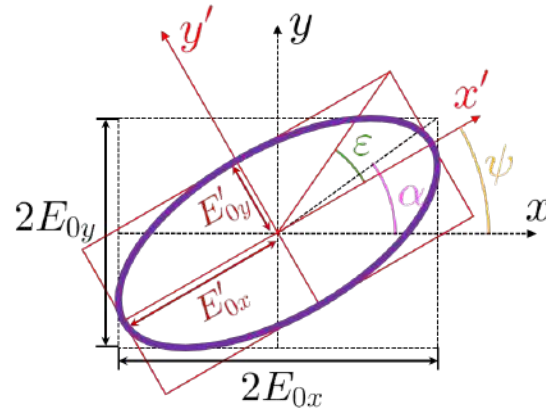


Figure 2.2: The Polarization Ellipse.

2.1.3 The Poincaré sphere for fully polarized light

We have just shown that fully polarized light can be described by means of the angles ψ and χ , where $0 \leq \psi \leq \pi$ and $0 \leq \chi \leq \pi/2$. It is straightforward to deduce that $0 \leq 2\psi \leq 2\pi$ and $0 \leq 2\chi \leq \pi$. These restrictions suggest we can represent a state of polarization as a unique point over a spherical surface of constant radius with an azimuth 2ψ and a polar angle 2χ . Therefore, the angle 2ε is the latitude of the point, and when $\varepsilon = 0$ ($\chi = \pi/4$) i.e., we have linearly polarized light, the point lies on the equator. This spherical representation is known as the Poincaré sphere, and it is depicted in Fig. 2.3. Also note that the Cartesian coordinates of two antipodal points are the same but with opposite signs.

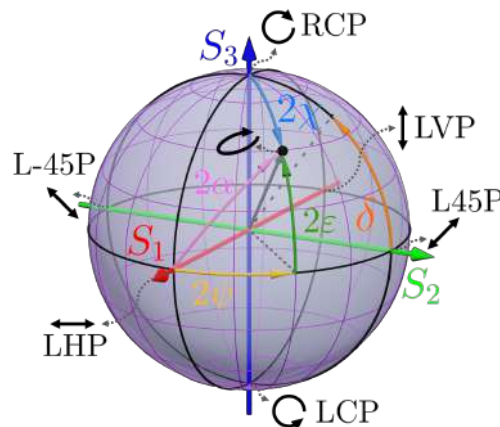


Figure 2.3: The Poincaré sphere.

Using the well-known equations that relate Cartesian to spherical coordinates, we deduce the relations

$$s_1 = \sin 2\chi \cos 2\psi, \quad (2.20)$$

$$s_2 = \sin 2\chi \sin 2\psi, \quad (2.21)$$

$$s_3 = \cos 2\chi, \quad (2.22)$$

where s_1 , s_2 , s_3 are the Cartesian coordinates. These quantities define points lying on the surface of a sphere of radius 1. The position of LHP, LVP, L45P, L-45P, RCP and LCP states on the Poincaré sphere is depicted in Fig. 2.3. The LHP and LVP lie along the s_1 axis, the L45P and L-45P along the s_2 axis, and the RCP and LCP along the s_3 axis, at the poles. Note that every pair of such orthonormal states lie on antipodal points. In fact, this is true for every orthonormal pair of states. We can obtain the coordinates of an antipodal point with the transformations $2\chi \rightarrow \pi - 2\chi$ and $2\psi \rightarrow \pi + 2\psi$. The scalar product of the Jones vectors representing two antipodal points ($|E(\psi, \chi)\rangle$ and $|E(\pi/2 + \psi, \pi/2 - \chi)\rangle$) is $\langle E(\psi, \chi) | E(\pi/2 + \psi, \pi/2 - \chi) \rangle = 0$, so a pair of antipodal points always correspond to orthogonal states¹.

We can choose a sphere with a radius different from 1 in order to represent non-normalized electric fields. If we multiply the Jones vector in Eq. 2.19 by a real positive amplitude $\sqrt{I_0}$, the square of the norm of the electric field is $I_0 = \langle E | E \rangle$. The quantity I_0 is proportional to the beam irradiance [9], and therefore, it is a measurable quantity. The Cartesian coordinates for a non-normalized fully polarized beam are

$$S_1 = I_0 \sin 2\chi \cos 2\psi, \quad (2.23)$$

$$S_2 = I_0 \sin 2\chi \sin 2\psi, \quad (2.24)$$

$$S_3 = I_0 \cos 2\chi. \quad (2.25)$$

These quantities, together with the quantity $S_0 = I_0$, that is proportional to the beam irradiance, are known as the Stokes parameters for a fully polarized beam. The vector (S_1, S_2, S_3) defines a point on the surface of a sphere of radius $S_0 = I_0$, where I_0 is the modulus of the vector. The Stokes parameters and the Jones vector of a fully polarized beam describe its state of polarization. However, the Stokes parameters describing two Jones vectors with the same ψ and χ , but with a different global phase factor, are the same. Therefore, we lose the information of the global phase when we change from Jones vectors to Stokes parameters. As a result, all Jones vectors that are equal but for a global phase factor lie on the same point on the Poincaré sphere. An example is the state L-45P given by Eq. 2.11 in the linear basis. One may calculate the same state in the circular basis with the equation 2.19. Because of the angles restrictions, the equivalent state is linearly polarized at 135° (L135P). States L-45P and L135P have the same Stokes parameters so they are the same point on the Poincaré sphere, although they differ in a global phase of π . The loss of the global phase suggests that Jones vectors

¹ $\langle E | = (|E\rangle)^\dagger$ is the conjugate transpose of $|E\rangle$.

provide a better description for polarized light than Stokes parameters. In fact, they do if we are interested in combining fully polarized beams coherently. However, Jones vectors are not a suitable tool for describing partially polarized light and incoherent superpositions of polarized beams. Conversely, Stokes parameters are suitable indeed, as discussed in section 2.3.

We also depict the angles α and δ in Fig. 2.3. These angles are related to ψ and ε through the equations [10]

$$\tan 2\psi = \tan 2\alpha \cos \delta, \quad 0 \leq \psi \leq \pi, \quad (2.26)$$

$$\sin 2\varepsilon = \sin 2\alpha \sin \delta, \quad -\pi/4 \leq \varepsilon \leq \pi/4. \quad (2.27)$$

The Stokes parameters S_1 , S_2 and S_3 for a normalized fully polarized beam can be expressed in terms of the angles α and δ as

$$S_1 = \cos 2\alpha, \quad (2.28)$$

$$S_2 = \sin 2\alpha \cos \delta, \quad (2.29)$$

$$S_3 = \sin 2\alpha \sin \delta. \quad (2.30)$$

The angles that control the weight for each component and the phase between them in Eqs. 2.8 (linear basis) and 2.19 (circular basis) can be visualized on the Poincaré sphere. First, the angles controlling the weight (α and χ) determine how far is the point representing $|E\rangle$ from each of the two antipodal points that stand for the orthonormal basis vectors. For instance, all the points with the same χ are at the same angular distance 2χ from the point RCP. Similarly, the points with the same α remain at the same angular distance 2α from the point LHP. The points at the same angular distance from RCP (LHP) define a circumference contained in a plane perpendicular to the axis passing through the points RCP (LHP) and LCP (LVP). The angle 2ψ (δ) determines where the state lies on this circumference. These two cases can be displayed in Fig. 2.3.

Let us now provide an intuitive explanation of the geometrical interpretation on the Poincaré sphere of the angles that control the weight and relative phase between two orthogonal elliptical components $|a\rangle$ and $|a^\perp\rangle$. Consider the state

$$|E\rangle = \cos \beta e^{-i\varphi} |a\rangle + \sin \beta e^{i\varphi} |a^\perp\rangle, \quad (2.31)$$

where β controls the weight for each component and 2φ is the phase difference between them. The points with the same β lie at the same spherical angular distance 2β from the point representing $|a\rangle$, and they define a circle on the surface of the sphere contained in a plane perpendicular to the axis passing through the points $|a\rangle$ and $|a^\perp\rangle$. For constant α this is the S_1 axis, and for constant χ it is the S_3 axis. For constant β it is depicted in golden in Fig. 2.4.

In order to visualize the angle 2φ (the phase difference between $|a\rangle$ and $|a^\perp\rangle$) on the Poincaré sphere, we rewrite Eq. 2.31 in terms of two new vectors $|A\rangle$ and

$|B\rangle$:

$$|E\rangle = \cos \varphi |A\rangle + \sin \varphi |B\rangle, \quad (2.32)$$

$$(2.33)$$

$$|A\rangle = \cos \beta |a\rangle + \sin \beta |a^\perp\rangle,$$

$$|B\rangle = -i (\cos \beta |a\rangle - \sin \beta |a^\perp\rangle). \quad (2.34)$$

Note that the components of $|A\rangle$ and $|B\rangle$ have the same magnitude than the components of $|E\rangle$, so they are also at an angular distance 2β from point $|a\rangle$, as Fig. 2.4 shows. The global phase term $-i$ in $|B\rangle$ does not change the position of the point, as discussed above. However, $|B\rangle$ has a minus sign between the components. If we rewrite $|B\rangle$ as $|B\rangle = -i (\cos(-\beta) |a\rangle + \sin(-\beta) |a^\perp\rangle)$, the minus sign can be interpreted as a rotation of -2β , which is the same rotation in magnitude as 2β for $|A\rangle$, but in the opposite direction. Therefore, points $|A\rangle$ and $|B\rangle$ lie at opposite points on a circle on the surface of the sphere defined by the points that are at distance 2β from point $|a\rangle$ (see Fig. 2.4).

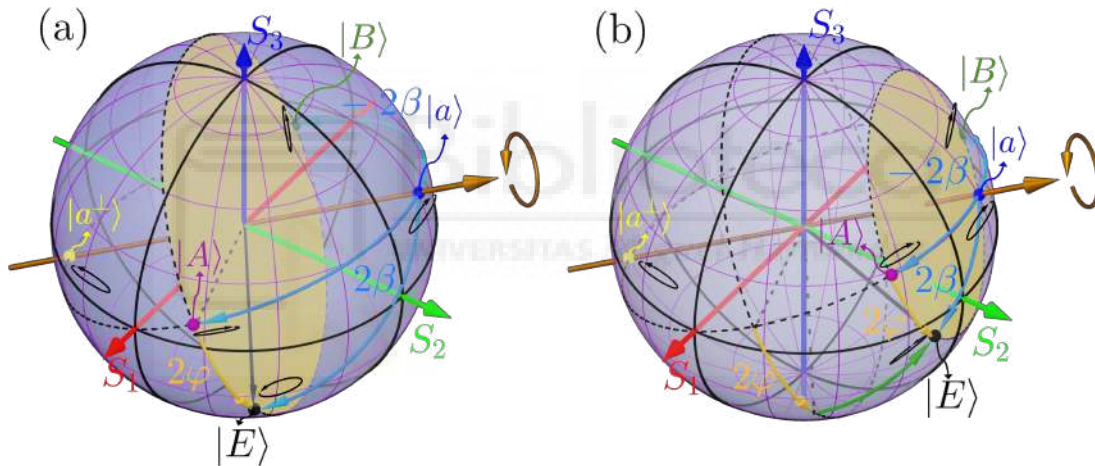


Figure 2.4: Angles β and φ on the Poincaré sphere. (a) Case where $2\beta = \pi/2$. (b) Case where $2\beta = \pi/4$.

The angle φ in Eq. 2.32 plays a similar role as β in Eq. 2.31: it controls the distance from point $|E\rangle$ to $|A\rangle$ and $|B\rangle$. Therefore, the position of point $|E\rangle$ on the circle defined by 2β is given by a rotation of 2φ from $|A\rangle$ to $|E\rangle$. Figure 2.4(a) shows a rotation of 2φ on the circle defined by $2\beta = \pi/2$ and Fig. 2.4(b) for a smaller value of 2β .

We have obtained an interesting result that we will use throughout this thesis: a phase difference 2φ between the two orthogonal components $|a\rangle$ and $|a^\perp\rangle$ defining a state $|E\rangle$, is equivalent to a rotation of 2φ of point $|E\rangle$ around the axis passing through the points $|a\rangle$ and $|a^\perp\rangle$. The sense of rotation is given by the right-hand rule: first, consider that the axis points towards the state with the negative phase in Eq. 2.31 i.e., $|a\rangle$. Let your right hand thumb point in that direction, and the other fingers will curl along the orientation of the rotation on the Poincaré sphere.

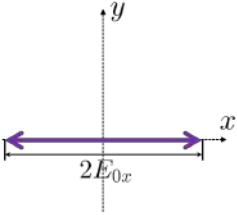
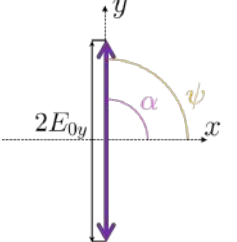
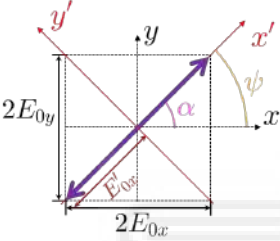
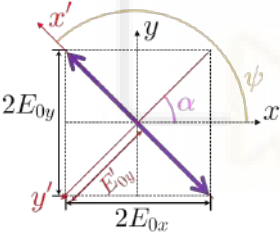
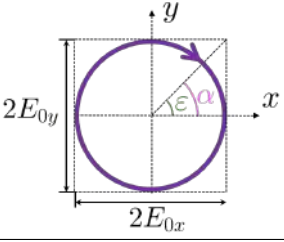
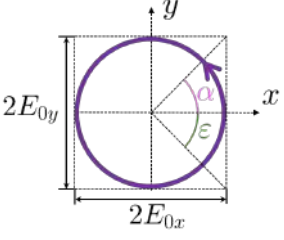
| Polarization ellipse | Jones vector | Stokes parameters |
|---|--|---|
|  | LHP $\alpha = 0$ $\psi = 0$ $\varepsilon = 0$ $\chi = \pi/4$ | $\begin{pmatrix} 1 \\ 1 \\ 0 \\ 0 \end{pmatrix}$ |
|  | LVP $\alpha = \pi/2$ $\psi = \pi/2$ $\varepsilon = 0$ $\chi = \pi/4$ | $\begin{pmatrix} 1 \\ -1 \\ 0 \\ 0 \end{pmatrix}$ |
|  | L45P $\alpha = \pi/4$ $\delta = 0$ $\psi = \pi/4$ $\varepsilon = 0$ $\chi = \pi/4$ | $\frac{1}{\sqrt{2}} \begin{pmatrix} 1 \\ 0 \\ 1 \\ 0 \end{pmatrix}$ |
|  | L-45P/135P $\alpha = \pi/4$ $\delta = \pi$ $\psi = 3\pi/4 \pm \frac{1}{\sqrt{2}}$ $\varepsilon = 0$ $\chi = \pi/4$ | $\begin{pmatrix} 1 \\ 0 \\ -1 \\ 0 \end{pmatrix}$ |
|  | RCP $\alpha = \pi/4$ $\delta = \pi/2$ $\varepsilon = \pi/4$ $\chi = 0$ | $\begin{pmatrix} 1 \\ 0 \\ 0 \\ 1 \end{pmatrix}$ |
|  | LCP $\alpha = \pi/4$ $\delta = 3\pi/2$ $\varepsilon = -\pi/4$ $\chi = \pi/2$ | $\begin{pmatrix} 1 \\ 0 \\ 0 \\ -1 \end{pmatrix}$ |

Table 2.1: Polarization ellipse, Jones vector and Stokes parameters for LHP/LHV/L45P/L-45P: linear horizontally/vertically/45°/-45° polarized light, and RCP/LCP: Right/Left circularly polarized light. The Jones Vectors are expressed in the $\{|x\rangle, |y\rangle\}$ linear basis.

2.2 Polarization optical components

When dealing with fully polarized light, an optical element that changes linearly the state of polarization can be described as a linear operator \mathbf{A} acting over an input Jones vector $|E\rangle_{in}$. As a result, a new state of polarization

$$|E\rangle_{out} = \mathbf{A} |E\rangle_{in} \quad (2.35)$$

is obtained. These operators are usually represented by 2×2 matrices in the linear $\{|x\rangle, |y\rangle\}$ basis known as Jones matrices.

In this thesis we consider optical polarization elements described by normal operators. A normal operator \mathbf{A} satisfies $\mathbf{A}\mathbf{A}^\dagger = \mathbf{A}^\dagger\mathbf{A}$, where \mathbf{A}^\dagger is the adjoint of \mathbf{A} . The spectral theorem ensures normal operators can be decomposed as a sum of its eigenvectors $|a\rangle$ and eigenvalues λ_a :

$$\mathbf{A} = \sum_a \lambda_a |a\rangle \langle a|, \quad (2.36)$$

where its eigenvectors $|a\rangle$ form an orthonormal basis. The product \otimes is known as the outer product, and $|a\rangle \langle a|$ is an operator. For the sake of simplicity, we will omit the symbol \otimes from now on and write the outer product as $|a\rangle \langle a|$. A two-dimensional operator $|a\rangle \langle a|$ can be expressed as a matrix in terms of the components of $|a\rangle$ in a certain basis as

$$|a\rangle \langle a| \rightarrow \begin{pmatrix} a_1 \\ a_2 \end{pmatrix} \otimes (a_1^* \ a_2^*) = \begin{pmatrix} a_1 a_1^* & a_1 a_2^* \\ a_2 a_1^* & a_2 a_2^* \end{pmatrix}. \quad (2.37)$$

Polarization elements described by normal operators are called homogeneous polarization elements [12]. These operators can be expressed as matrices that can be diagonalized in an orthonormal basis. Here we study two types of optical polarization elements given by two types of normal operators: diattenuators and retarders, described by hermitian and unitary operators, respectively.

2.2.1 Diattenuators

When light propagates through an optical element, the fraction of the intensity exiting the component is given by the transmittance T . A diattenuator is an optical element with transmittance T_a for one polarization component $|a\rangle$, and different transmittance T_{a^\perp} for the orthogonal component $|a^\perp\rangle$. Since diattenuators do not produce any change in the phase, they are described by hermitian operators i.e., operators that are equal to its adjoint, and therefore their eigenvalues are real². We express diattenuators as a function of the transmittances:

$$\mathbf{D} = \sqrt{T_a} |a\rangle \langle a| + \sqrt{T_{a^\perp}} |a^\perp\rangle \langle a^\perp|, \quad (2.38)$$

²Consider a hermitian operator \mathbf{A} , so $\mathbf{A} = \mathbf{A}^\dagger$. Since \mathbf{A} is also normal, we apply the spectral theorem: $\mathbf{A} = \lambda_a |a\rangle \langle a| + \lambda_{a^\perp} |a^\perp\rangle \langle a^\perp|$. Its adjoint is $\mathbf{A}^\dagger = \lambda_a^* |a\rangle \langle a| + \lambda_{a^\perp}^* |a^\perp\rangle \langle a^\perp|$. Since $\mathbf{A} = \mathbf{A}^\dagger$, then $\lambda_a = \lambda_a^*$ and $\lambda_{a^\perp} = \lambda_{a^\perp}^*$. Therefore, the eigenvalues of a hermitian operator are real.

where $|a\rangle$ and $|a^\perp\rangle$ are the orthonormal eigenvectors of \mathbf{D} , and $\sqrt{T_a}$ and $\sqrt{T_{a^\perp}}$ its eigenvalues. Since diattenuators do not produce a change in the phase, we restrict the eigenvalues to be positive quantities.

Consider \mathbf{D} acting over a state $|E\rangle = \cos \beta e^{-i\varphi} |a\rangle + \sin \beta e^{i\varphi} |a^\perp\rangle$:

$$\mathbf{D}|E\rangle = \sqrt{T_a} \cos \beta e^{-i\varphi} |a\rangle + \sqrt{T_{a^\perp}} \sin \beta e^{i\varphi} |a^\perp\rangle. \quad (2.39)$$

Since $\sqrt{T_a}$ and $\sqrt{T_{a^\perp}}$ are real positive numbers, the action of a diattenuator only changes the amplitudes of the polarization components.

A particular case of a diattenuator is the perfect polarizer, described by

$$\mathbf{P}_a = |a\rangle \langle a|. \quad (2.40)$$

The perfect polarizer is a diattenuator with one eigenvalue set to zero and the other to one. Therefore, it will only transmit the component in the $|a\rangle$ direction of the initial state $|E\rangle$:

$$\mathbf{P}_a |E\rangle = \langle a|E\rangle |a\rangle. \quad (2.41)$$

The most common type of polarizers are linear polarizers. These devices transmit all the light that is linearly polarized along the direction determined by the orientation θ of its transmission axis, and block the orthogonal component. The state

$$|\theta\rangle = \cos \theta |x\rangle + \sin \theta |y\rangle. \quad (2.42)$$

is fully transmitted. Therefore, a rotated linear polarizer is described as

$$\mathbf{P}_{linear}(\theta) = |\theta\rangle \langle \theta| \rightarrow \begin{pmatrix} \cos^2 \theta & \sin \theta \cos \theta \\ \sin \theta \cos \theta & \sin^2 \theta \end{pmatrix}, \quad (2.43)$$

where the matrix form is expressed in the linear $\{|x\rangle, |y\rangle\}$ basis.

2.2.2 Retarders

A retarder is an element that does not modify the weight of the polarization components of a Jones vector, but adds a relative phase between them. Therefore, unitary operators are a suitable tool for describing retarders. An operator is said to be unitary if its inverse operator is equal to its adjoint: $\mathbf{A}^{-1} = \mathbf{A}^\dagger$. If an operator is unitary it preserves the norm of the vectors when acting on them³.

A retarder that adds a relative phase ϕ between two orthogonal states $|a\rangle$ and $|a^\perp\rangle$ can be expressed as

$$\mathbf{M}_R = e^{-i\phi/2} |a\rangle \langle a| + e^{i\phi/2} |a^\perp\rangle \langle a^\perp|. \quad (2.44)$$

The relative phase ϕ is also known as retardance. If \mathbf{M}_R acts over an input state $|\mathbf{E}\rangle_{in} = \cos \beta e^{-i\varphi} |a\rangle + \sin \beta e^{i\varphi} |a^\perp\rangle$ the resulting state is

³Suppose an operator \mathbf{A} acting over a state $|c\rangle$ resulting in the state $|a\rangle = \mathbf{A}|c\rangle$. The length of the input vector is $\sqrt{\langle c|c\rangle}$ and the length of the resulting vector is $\sqrt{\langle a|a\rangle}$. If $\mathbf{A}^{-1} = \mathbf{A}^\dagger$, and therefore $\mathbf{A}^\dagger \mathbf{A} = \mathbf{I}$, it results that $\langle a|a\rangle = \langle c| \mathbf{A}^\dagger \mathbf{A} |c\rangle = \langle c|c\rangle$, so the length remains unchanged.

$$|\mathbf{E}\rangle_{out} = \mathbf{M}_R |\mathbf{E}\rangle_{in} = \cos \beta e^{-i(\varphi+\phi/2)} |a\rangle + \sin \beta e^{i(\varphi+\phi/2)} |a^\perp\rangle. \quad (2.45)$$

The polarization components of the output state preserve their amplitudes, but the retarder has added an extra phase difference ϕ between them. As explained in subsection 2.1.3, the phase difference ϕ can be viewed as a ϕ radians rotation of the point representing the input state on the surface of the Poincaré sphere. The retarder performs a rotation of the input state around the axis that connects the eigenstates $|a\rangle$ and $|a^\perp\rangle$ of the retarder. Figure 2.5 shows the action of a retarder that adds a phase difference between the $|x\rangle, |y\rangle$ (Fig. 2.5(a)) and $|R\rangle, |L\rangle$ (Fig. 2.5(b)) states. These are linear and circular retarders, respectively.

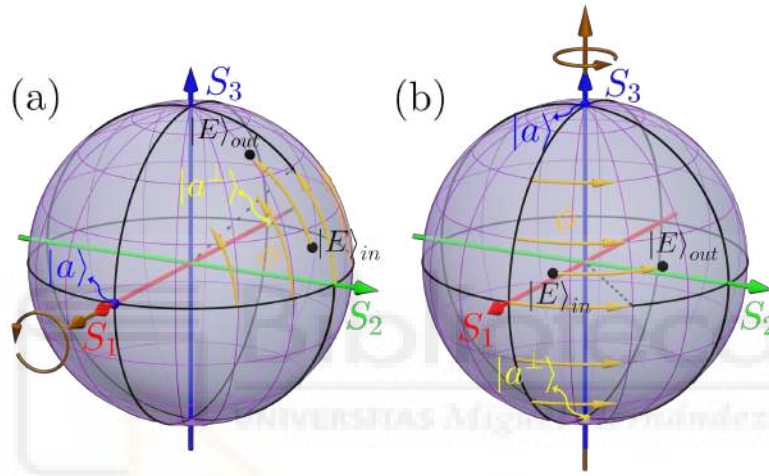


Figure 2.5: Action of a (a) linear and (b) circular retarder over an input state of polarization.

The most common type of retarder is the linear retarder, which adds a phase difference between two orthogonal linear states. We express a linear retarder for states $|x\rangle$ and $|y\rangle$ as

$$\mathbf{M}_{WP} = e^{-i\phi/2} |x\rangle \langle x| + e^{i\phi/2} |y\rangle \langle y| \rightarrow \begin{pmatrix} e^{-i\phi/2} & 0 \\ 0 & e^{i\phi/2} \end{pmatrix}, \quad (2.46)$$

where we have expressed the Jones matrix in the $|x\rangle$ and $|y\rangle$ basis. Linear retarders are the well-known waveplates, where half-wave plates correspond to $\phi = \pi$ and quarter-wave plates to $\phi = \pi/2$. The expression of a linear retarder rotated an angle γ is

$$\mathbf{M}_{WP}(\phi, \gamma) = \cos\left(\frac{\phi}{2}\right) \mathbf{I} + i \sin\left(\frac{\phi}{2}\right) \mathbf{Q}(\gamma), \quad (2.47)$$

where \mathbf{I} is the identity matrix and

$$\mathbf{Q}(\gamma) = e^{-i2\gamma} |R\rangle \langle L| + e^{i2\gamma} |L\rangle \langle R| \rightarrow \begin{pmatrix} \cos 2\gamma & \sin 2\gamma \\ \sin 2\gamma & -\cos 2\gamma \end{pmatrix}. \quad (2.48)$$

The matrix $\mathbf{Q}(\gamma)$ corresponds to a half-wave plate rotated an angle γ . It transforms RCP into LCP and adds a phase 2γ that depends on the orientation of the retarder. Similarly, it transforms LCP into RCP and adds a phase -2γ . This result will be very useful when we introduce geometrical phase elements in the next chapter.

Circular retarders are also an interesting particular case of retarders:

$$\mathbf{M}_{Rot} = e^{-i\phi/2} |R\rangle \langle R| + e^{i\phi/2} |L\rangle \langle L| \rightarrow \begin{pmatrix} \cos(\phi/2) & -\sin(\phi/2) \\ \sin(\phi/2) & \cos(\phi/2) \end{pmatrix}, \quad (2.49)$$

where its Jones matrix is expressed in the $\{|x\rangle, |y\rangle\}$ basis. Note that the Jones matrix of a circular retarder is a rotation matrix. As explained in the previous section, adding a phase difference between the circular components results in a rotation of the polarization ellipse.

2.2.3 Experimental realization of linear retarders

Linear retarders are usually made out of uniaxial birefringent materials, such as quartz, calcite or birefringent polymers [13]. Birefringent materials are composed of asymmetric molecules aligned along a particular direction, so they are anisotropic substances. As a consequence, they display different indices of refraction for linearly polarized light along different directions. A detailed classical description of this phenomenon is given in terms of the Lorentz model in [9]. The direction of anisotropy in an uniaxial birefringent material is determined by a single direction: the so-called optic axis. This means that all directions perpendicular to the optic axis are isotropic, so an oscillating electric field inside the medium experiences the same properties as long as it oscillates perpendicular to the optic axis. Therefore, when light propagates through a birefringent uniaxial material, the linear polarization component perpendicular to the optic axis (ordinary component) always experiences the same refractive index, commonly referred to as the ordinary index n_o . On the other hand, the orthogonal component (extraordinary component) experiences a different refractive index: the extraordinary effective index n_e , which depends on the direction of incidence. A detailed analysis of the light wavefronts [9] of the extraordinary and ordinary components show that they split inside the medium, so generally two displaced orthogonal linearly polarized beams emerge from the material.

Linear retarders are plane-parallel plates where the optic axis is set to be parallel to the incident and output surfaces of the material. In this situation, the beam does not split, and the ordinary and extraordinary components emerge together from the retarder [9]. The result is a single beam where a phase shift is introduced between its polarization component perpendicular (ordinary) and parallel (extraordinary) to the optic axis. The phase shift ϕ , also known as retardance, is given by the relative optical path length difference between the two components multiplied by the wavenumber $k = 2\pi/\lambda$:

$$\phi = \phi_e - \phi_o = \frac{2\pi}{\lambda} \Delta n(\lambda) d, \quad (2.50)$$

where λ is the light wavelength in vacuum, and d is the retarder thickness. The difference between the extraordinary and ordinary indices $\Delta n = n_e - n_o$ is known as the birefringence and depends on λ .

The total retardance ϕ increases as the thickness of the material increases. For most practical purposes, only the effective retardance δ matters, which is given by the modulo 2π of the retardance. Hence, the total retardance can be expressed as

$$\phi = \delta + 2\pi m, \quad (2.51)$$

where m is the order of the retarder [14]. For $m = 0$ we have a zero-order retarder with retardance $\phi = \delta$. For higher m values we have multiple-order retarders.

Linear retarders are also fabricated with liquid-crystal materials. Liquid crystals (LCs) typically consist of long cigar-shaped molecules, as depicted in yellow in Fig. 2.6(a). These anisotropic molecules preserve a large-scale orientation order like crystals do [9]. As a consequence, liquid crystals exhibit birefringence. Furthermore, the molecules have a certain degree of mobility inside the LC, as regular liquids. This fact, together with the polar nature of LC molecules, allows them to rotate when an external electric field is applied. In this situation, the large-scale orientation changes, so the birefringence Δn and consequently the retardance ϕ vary. Therefore, LC retarders are tunable, in the sense that their retardance for a given wavelength can be selected by adjusting the intensity of an external electric field, which is done upon applying a voltage.

There are several types of liquid crystals according to the position and orientation of the molecules. Here, we focus on nematic parallel-aligned liquid crystals. Their molecules are oriented along the same direction inside the medium, although their positions are random. Fig. 2.6(a) shows a scheme of a nematic parallel-aligned liquid-crystal retarder. Note that the molecules (depicted in yellow) have positional order in the picture, but they do not have it in real LCs; we have depicted them ordered for the sake of clarity in the representation of the basic operation principle of the retarder.

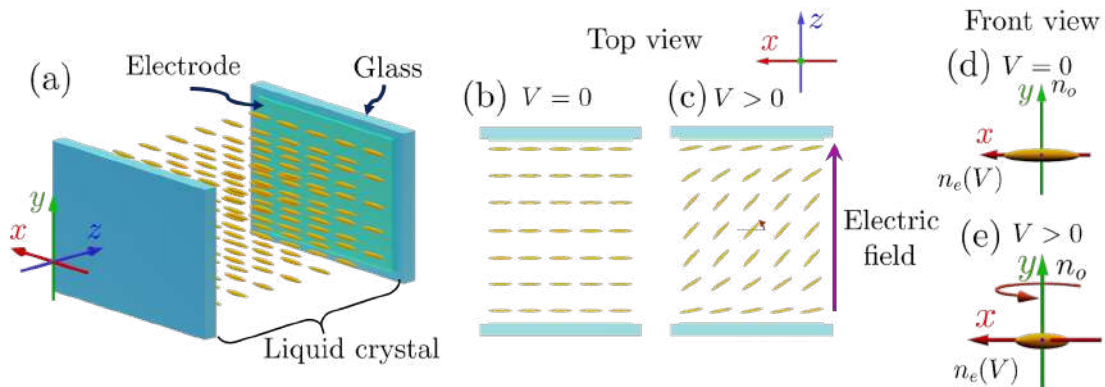


Figure 2.6: (a) Scheme of a nematic parallel-aligned liquid-crystal linear retarder. (b)-(c) Top view when (b) no voltage and when (c) voltage is applied. (d)-(e) Front view of a single LC molecule when (d) no voltage and when (e) voltage is applied.

As shown in Fig. 2.6, the liquid-crystal layer is sandwiched between two electrodes and two glass layers. The direction that governs the crystal anisotropy (the optic axis) is parallel to the input and output surfaces. This direction is known in LCs as the director, and it is the direction of the longest part of the molecules (x direction in Fig. 2.6). Figures 2.6(b) and 2.6(c) are the top view of the retarder when no voltage is applied (2.6(b) for $V = 0$) and when a voltage is applied (2.6(c) for $V > 0$) between the electrodes. A front view perspective of a single LC molecule is given in Figs 2.6(d) ($V = 0$) and 2.6(e) ($V > 0$).

We now describe the mechanism that allows us to change the retardance of the LC device by applying an external electric field. Consider a plane wave propagating along the z direction depicted in 2.6. The polarization component perpendicular to the director (y direction in Fig. 2.6) experiences a refractive index n_o different from the index n_e experienced by the polarization parallel to the director (x direction) (Fig. 2.6(d)). When a voltage is applied between the two electrodes, the molecules rotate around the y axis⁴. The rotation of the molecules involves a change in the orientation of the LC optic axis. Since the rotation is around the y axis, the shape of the molecule along the y direction remains unchanged, so the refractive index for the y component n_o does not change. Conversely, the index $n_e(V)$ along the x component varies with the applied voltage, since the shape of the molecule along the x direction is different. Therefore, the birefringence of the material can be adjusted by applying a voltage, and so the retardance of the device.

As we have pointed out above, if the optic axis is not parallel to the input and output surfaces of the crystal, the light generally splits into two rays. Also, we have just discussed that the optic axis of the LCs is no longer parallel to these faces when a voltage is applied. Therefore, we would expect that two separated beams emerge from the LC retarder. However, LC layers are made so thin that the separation is negligible for most practical purposes. Therefore, we will henceforth consider that there is no beam separation inside the LCs retarders.

2.2.4 Spectral characterization of linear retarders

As Eq. 2.50 shows, the retardance in birefringent materials depends on the wavelength in vacuum of the input light. Linear retarders are usually designed to give a certain retardance at a given wavelength. But they can be used to provide a different retardance for other wavelengths, so it is useful to perform a spectral characterization of their retardance function $\phi(\lambda)$. In addition, for tunable LC retarders, a complete study of the variation of ϕ versus λ and voltage V allows us to set any desired retardance to a given wavelength.

It is worth mentioning that other linear retarders are designed to be achromatic in a wide spectral range. This is the case of Fresnel rhombs [13], since their retardance is based on internal reflections inside the rhomb. As a consequence, they provide a uniform retardance of $\phi = \pi/2$ in a wide wavelength range. A suit-

⁴Note that the molecules close to the electrodes are not able to completely rotate (Fig. 2.6(c)). This causes a residual retardance that can be compensated with additional layers.

able combination of Fresnel rhombs was employed to build an achromatic linear retarder with tunable retardance in [15]. In one of the works of this thesis, we used Fresnel rhombs to generate polychromatic circularly polarized light.

The characterization of a linear retarder is usually performed by illuminating with a broadband spectrum lamp the retarder inserted between two linear polarizers [14]. The polarizers are oriented at $\pm 45^\circ$ with respect to the eigen-axes of the retarder⁵, as shown in Fig. 2.7. Then, the light transmitted by the last polarizer is analyzed with a spectrometer.

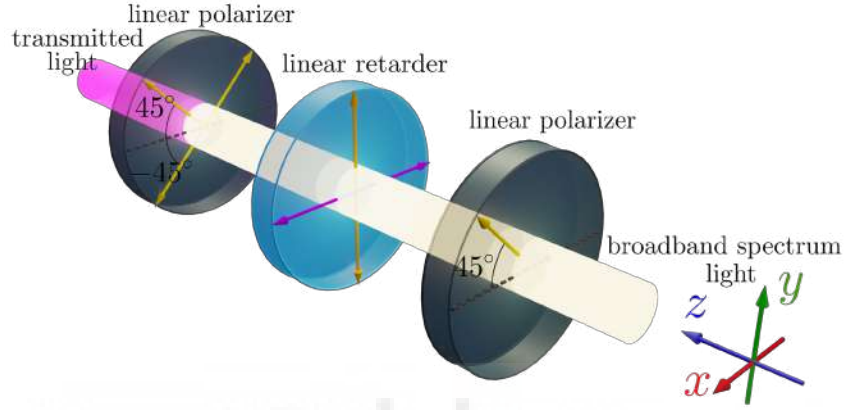


Figure 2.7: Basic set-up for the spectral characterization of a linear retarder.

We describe the light transmitted by the linear retarder before the second polarizer in Fig. 2.7 by making the matrix of a linear retarder in Eq. 2.47 act over a linearly polarized state at 45° :

$$\mathbf{M}_{WP}(\phi(\lambda), \gamma = 0) |45^\circ\rangle = \cos\left(\frac{\phi(\lambda)}{2}\right) |45^\circ\rangle + i \sin\left(\frac{\phi(\lambda)}{2}\right) |-45^\circ\rangle. \quad (2.52)$$

The state is a superposition of the $|45^\circ\rangle$ and $|-45^\circ\rangle$ states weighted by the retardance $\phi(\lambda)$. Since $\phi(\lambda)$ depends on λ , the polarization state is different for each wavelength. Then, the last polarizer transmits the 45° component if its transmission axis is parallel to the input state, and the -45° component if it is perpendicular. The modulus squared of the output state after the last polarizer in the parallel $i_{\parallel}(\lambda)$ and perpendicular $i_{\perp}(\lambda)$ configurations is

$$i_{\parallel}(\lambda) = \cos^2\left(\frac{\phi(\lambda)}{2}\right), \quad (2.53)$$

$$i_{\perp}(\lambda) = \sin^2\left(\frac{\phi(\lambda)}{2}\right). \quad (2.54)$$

The quantities $i_{\parallel}(\lambda)$ and $i_{\perp}(\lambda)$ can be obtained for each λ from the intensity measurements in the crossed $I_{\perp}(\lambda)$ and parallel $I_{\parallel}(\lambda)$ configurations performed by

⁵The eigen-axes of a linear retarder are the directions that its eigenvectors define. Light polarized along one of the eigen-axes gains a global phase inside the retarder, but its state of polarization remains unchanged.

the spectrometer:

$$i_{\parallel}(\lambda) = \frac{I_{\parallel}(\lambda)}{I_{\parallel}(\lambda) + I_{\perp}(\lambda)}, \quad (2.55)$$

$$i_{\perp}(\lambda) = \frac{I_{\perp}(\lambda)}{I_{\parallel}(\lambda) + I_{\perp}(\lambda)}. \quad (2.56)$$

The function $\phi(\lambda)$ is derived from Eqs. 2.53 and 2.54, but is limited by the range of the trigonometric functions. Therefore, to obtain the total retardance, a phase unwrapping correction must be applied [14]. The experimental retardance data are usually fitted to a Cauchy dispersion relation of the form $\phi(\lambda) = A/\lambda + B/\lambda^3$.

As an example, Fig. 2.8 shows the $i_{\parallel}(\lambda)$ and $\phi(\lambda)$ fitted curves as a function of λ for a quartz multiple-order retarder designed to add a retardance of $\pi/2$ for 488 nm. We explain the oscillatory behaviour of $i_{\parallel}(\lambda)$ as follows: since $\phi(\lambda)$ varies with λ , the amplitudes for the $|45^\circ\rangle$ and $|-45^\circ\rangle$ components are different for each wavelength. For wavelengths where $\phi(\lambda)$ is an even multiple of π , the input state $|45^\circ\rangle$ is not modified, so all the light passes when the second polarizer is parallel to $|45^\circ\rangle$. Therefore, there is a maximum in the $i_{\parallel}(\lambda)$ curve. Conversely, when $\phi(\lambda)$ is an odd multiple of π , the state is transformed by the retarder into its orthogonal $|-45^\circ\rangle$. So the final polarizer cancels out the state, and there is a minimum in the function $i_{\parallel}(\lambda)$. For other values of $\phi(\lambda)$ the state after the retarder is a linear combination of $|45^\circ\rangle$ and $|-45^\circ\rangle$ weighted by $\phi(\lambda)$ and we have intermediate situations in the $i_{\parallel}(\lambda)$ curves. Note how the retardance variation in the measured spectral range is more than 25π radians for the quartz retarder; we are witnessing the spectral retardance of a multiple-order retarder. Also note that, since the retardance decreases slower towards longer wavelengths, the function $i_{\parallel}(\lambda)$ oscillates slower as the wavelength increases.

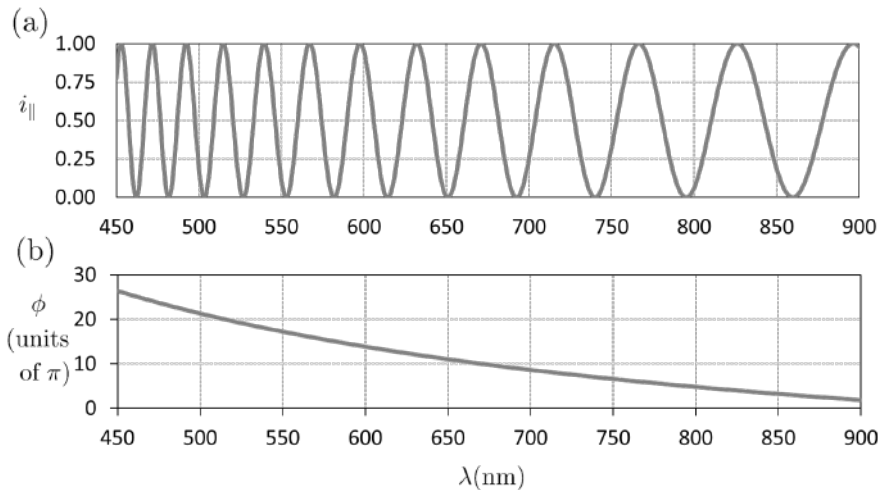


Figure 2.8: (a) $i_{\parallel}(\lambda)$ and (b) $\phi(\lambda)$ fitted functions for a quartz linear retarder. The data has been extracted from [14]. The origin for zero retardance does not correspond to the true zero retardance value; it has been arbitrarily taken in the near-infrared region.

Figure 2.9 shows the curves $i_{\parallel}(\lambda)$ and $\phi(\lambda)$ for a liquid-crystal retarder. The

function $i_{\parallel}(\lambda)$ is depicted for three different applied voltages: (a) 0 V, (b) 1.5 V, and (c) 2.5 V.

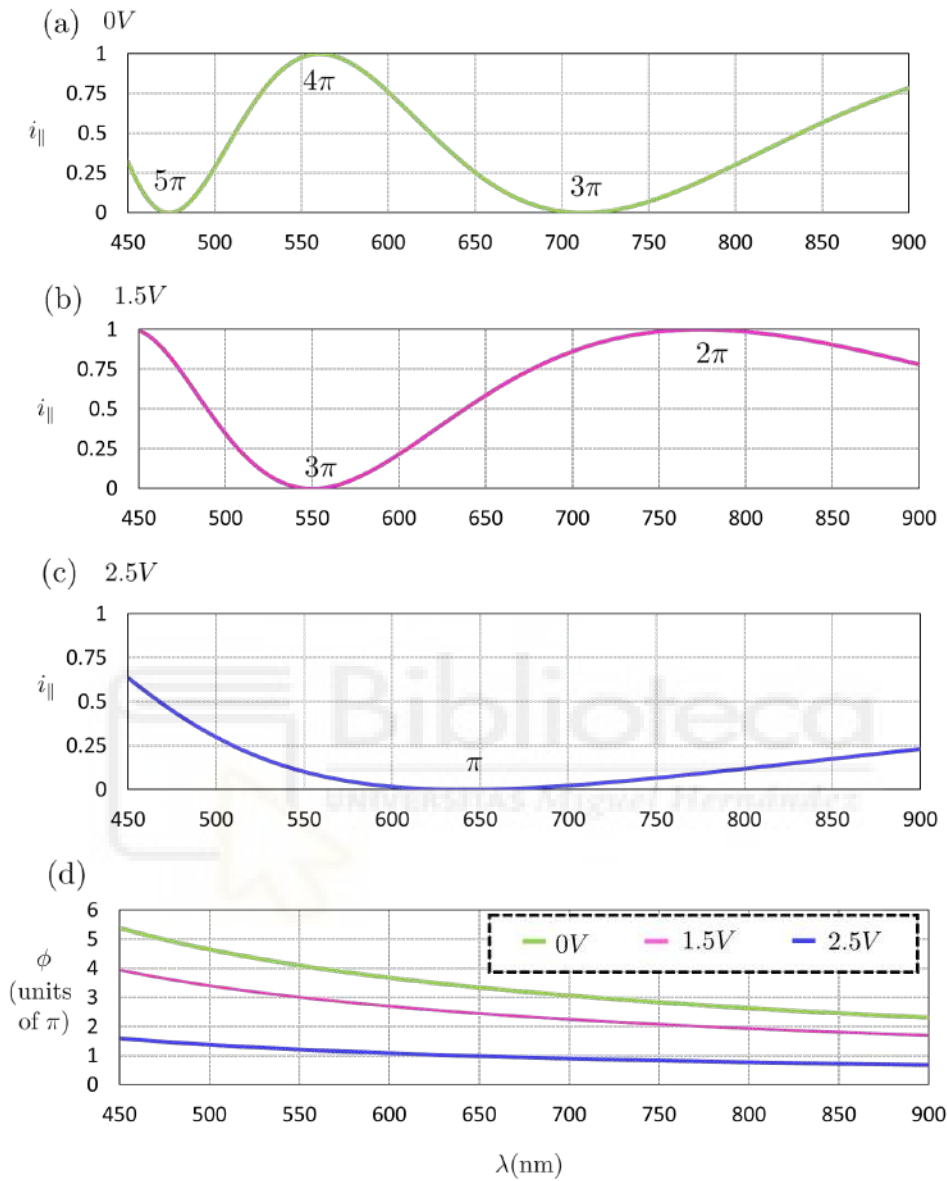


Figure 2.9: (a)-(c) $i_{\parallel}(\lambda)$ and (d) $\phi(\lambda)$ fitted functions for a liquid-crystal linear retarder. The function $i_{\parallel}(\lambda)$ is shown for different voltages applied to the LC retarder: (a) 0 V, (b) 1.5 V, and (c) 2.5 V. The retardance values for the maxima and minima of the $i_{\parallel}(\lambda)$ function are indicated. The data has been extracted from [14].

First, let us consider that no voltage is applied. Under this circumstance, one linear polarization component is along the long direction of the LC molecule, while the orthogonal component is along the short direction (Fig. 2.6(d)). Since the anisotropy for both directions is maximum, the birefringence is maximum too. Therefore, also the total retardance is maximum for zero voltage. As soon as we apply a certain voltage, the molecule starts tilting, so the total retardance decreases. When both polarization components experience the same shape of the

molecule, we would have ideally reached zero retardance. Thus, as we increase voltage, the retardance decreases for each wavelength. This explains why the oscillations in Figs. 2.9(a)-(c) move towards the left side of the spectrum when the voltage is increased. For voltages well above 2.5 V, the function $i_{\parallel}(\lambda)$ would eventually be almost 1 for every visible and near-infrared wavelength, because the function $\phi(\lambda)$ would be almost zero.

2.2.5 Birefringence colors in linear retarders

Liquid crystals act as multiple-order retarders when no voltage is applied (Fig. 2.9(a)), but its retardance is not as high as the retardance for a quartz waveplate (Fig. 2.8(a)). They typically behave as zero-order (from 0 to 2π), first-order (from 0 to 4π) and even slightly higher-order (second-order from 0 to 6π , etc.) retarders in the visible spectrum. So, they are said to be low-order retarders. The order depends on the thickness of the layer and on the birefringence.

Note that the spectra in Figs. 2.9(a)-(c) in the visible region have an associated color. When a retarder is sandwiched between linear polarizers and illuminated with white broadband light, a color is observed after the second polarizer. This color depends on the retardance function $\phi(\lambda)$. The colors that birefringent materials exhibit are commonly known as birefringence colors. In mineralogy, birefringence colors have been widely used to relate the perceived color of samples observed through a polarization microscope with its birefringence. They also have been applied in the study of surface anchoring conditions of liquid-crystal films [16]. In addition, its connection with the modulation properties of twisted nematic liquid-crystal displays has been studied in [17].

It is expected that the spectrum in Fig. 2.9(a) is closer to a green yellowish color than to a blue, provided that the spectra of the input light is flat enough. Conversely, the spectrum in Fig. 2.9(b) is expected to be closer to the blue and violet colors. In both cases, the birefringence colors provide an estimation of where the maxima and minima of $i_{\parallel}(\lambda)$ lie, and therefore, of the spectral retardance. However, the birefringence colors are only clearly visible if first-order retardance values transit the visible spectrum. On the one hand, if the voltage is highly increased, the retarder behaves as a zero-order retarder in the visible region. The spectrum becomes flatter, so the transmitted light is almost white. On the other hand, the spectrum presents rapid oscillations for high order retardances, as in Fig. 2.8(a) for a quartz retarder. If higher-order retardances lie in the visible region, the rapid oscillations in the spectrum will also make the transmitted color almost white. Therefore, placing a retarder between linear polarizers, illuminating with broadband white light, and then looking at the transmitted light with the naked eye, is a simple and fast method to determine if the first-order retardances transit the visible spectrum. In addition, we roughly might know the wavelengths where the retardance is close to an odd or even multiple of π .

In the work "Using birefringence colors to evaluate a tunable liquid-crystal q -plate" [7], we show that a tunable liquid-crystal q -plate exhibits birefringence colors. Q -plates are linear retarders with a spatial distribution of the orientation of their eigen-axes, as we will see in the next chapter. We spectrally characterized

the retardance of the device. In addition, we studied the birefringence colors it exhibits for different applied voltages, and observe that they are related to the spectral retardance. Furthermore, we showed that, as regular LC retarders, q -plates exhibit birefringence colors when the first-order retardance values lie in the visible spectrum.

2.3 Partially Polarized Light

So far, we have described light as a monochromatic electromagnetic wave. The polarization components of the electric field harmonically oscillate in time at the same frequency ω , while their amplitudes and relative phases remain constant in time. These properties cause that the electric field describes an ellipse in one temporal period $2\pi/\omega$ whose shape remains constant over all successive periods. The period $2\pi/\omega$ is of the order of 10^{-15} seconds for visible light.

We can experimentally measure the polarization state of light by means of a linear retarder and a linear polarizer at various configurations, followed by an intensity detector. The integration time of an optical detector, typically about 10^{-3} seconds [18], is several orders of magnitude larger than $2\pi/\omega$. This means that we cannot observe the ellipse being traced by the electric field. Instead, detectors integrate the signal over a huge amount of ω cycles. Since the shape of the ellipse is kept constant for strictly monochromatic light, no matter how large the integration time of our detector is, the averaged state of polarization that it measures within its integration time is the same as the averaged state that we would have measured in a $2\pi/\omega$ cycle (if we could). Regardless of the time we spend doing our measurements, we would detect a definite shape for the ellipse.

However, monochromatic light is an idealization since every light source has a finite-frequency bandwidth $\Delta\omega$ [18]. In fact, sources considered monochromatic, like lasers, actually have a finite bandwidth, which is much smaller than its central frequency $\bar{\omega}$. This type of electromagnetic wave is said to be quasi-monochromatic, and its oscillation at a given point in space $E(t)$ can be expressed as

$$E(t) = E_0(t)e^{i(\phi(t)-\bar{\omega}t)}, \quad (2.57)$$

where its amplitude $E_0(t)$ and phase $\phi(t)$ are functions of time t . These functions are generally fluctuating, in contrast to the equivalent parameters for a perfect monochromatic wave, which are constant. Using Fourier analysis it can be proved that $E_0(t)$ and $\phi(t)$ fluctuate slowly compared to a time interval $\Delta\tau = 2\pi/\Delta\omega$, which is known as the coherence time of light [19]. As a consequence, they remain almost constant within a time interval short compared to $\Delta\tau$. These times typically vary for different sources from 10^{-9} for a broadband spectrum lamp to 10^{-4} seconds for a well-stabilized laser [18], so they are much larger than the period $2\pi/\omega$ of the wave oscillation.

Consider a quasi-monochromatic electromagnetic wave whose polarization components along the x and y directions are described by $E_i(t) = E_{0i}(t)e^{i(\phi_i(t)-\bar{\omega}t)}$, with $i = x, y$. If the phase and amplitude fluctuations in $E_x(t)$ are completely statistically *correlated* with the phase and amplitude fluctuations in $E_y(t)$, regardless

that the light is not perfectly monochromatic, we still will measure a definite shape for the ellipse as we would for perfectly monochromatic light. Under these circumstances, we say that light is *fully polarized*.

Now consider that the mean values of the fluctuating amplitudes $E_{0x}(t)$ and $E_{0y}(t)$ are the same. This implies that if we measure the intensity for each component separately with a detector, we obtain the same averaged intensity for both. In addition, consider that the fluctuations in $E_x(t)$ are completely statistically *uncorrelated* with the fluctuations in $E_y(t)$. Under these two circumstances, there will not be any regular pattern in the ellipses traced over many periods, so we will not measure a preferred shape of the ellipse for long integration times. Nevertheless, since $E_0(t)$ and $\phi(t)$ almost remain constant for both components within a time much shorter than $\Delta\tau$, the ellipse will be almost constant during such a time interval. Therefore, if we could perform measurements of the state of polarization during a short time compared to $\Delta\tau$, we would obtain the shape of the ellipse during that interval. If we were those observers, we would definitely say that the light is fully polarized. But, as we said above, the integration time of the detector is usually much bigger than $\Delta\tau$. As a result, all the random shapes that the ellipse had over such a long time interval are averaged, so we do not measure any preferred shape of the ellipse. Although the light is actually polarized if we measured it in a short enough time interval, we will roughly refer to this phenomenon as *unpolarized light*.

Finally, when the fluctuations in $E_x(t)$ and $E_y(t)$ present some statistical correlations, or they are completely uncorrelated but the mean values of their amplitudes are different, the shape of the ellipse will exhibit some kind of regularity over many periods. Therefore, our detection system will measure some preferential shape of the ellipse, so we say that the light is *partially polarized*.

There are several methods to generate unpolarized light from polarized laser light. For instance, it can be achieved by mixing two independent orthogonal linearly polarized lasers with the same intensity, as R. D. Ramkhalawon et al. did in [20]. Since the fluctuations in the amplitudes and phases of the equi-intense orthogonal polarizations are completely uncorrelated, the light is detected as unpolarized.

Another approach is described in [21] by A. Lizana et al: Consider that we split the $E_x(t)$ and $E_y(t)$ linear polarization components of a laser source with a polarizing beam splitter, and then we recombine them. If the difference between the travelling path of both beams is short compared to $\Delta\ell = c\Delta\tau$ (c is the speed of light in vacuum), which is known as the coherence length of the source, the components will still be strongly correlated, resulting in polarized light for an optical detector. When two strongly correlated beams are superimposed, we say that they have been *coherently added*. Nevertheless, if the path difference is much greater than $\Delta\ell$, the components will no longer be correlated. We then say that the beams have been *incoherently added* in this situation. In addition, if the mean amplitude value of the components $E_x(t)$ and $E_y(t)$ are equal we will measure unpolarized light.

An alternative method is based on the fact that measuring light as polarized

or unpolarized depends on the integration time of our detector. The idea is that, if we sequentially send different states of polarization to our polarization detection system within a time interval shorter than its integration time, the detector will average the states and detect the light as unpolarized. This method was implemented in [22] by A. Peinado et al. using a fast variation of the fast axis of a switchable liquid-crystal ferroelectric retarder. We will go back to this type of technique in this section, since one work in this thesis relies on this method. In addition, we will see that all these methods can also generate partially polarized light through the incoherent addition of polarized states.

2.3.1 Stokes parameters for partially polarized light

Jones vectors are a suitable tool for describing polarized light and the coherent addition of polarized beams. Nevertheless, they can neither describe partially polarized light nor the incoherent addition of polarized beams, but, Stokes parameters can. In this subsection, we introduce the Stokes parameters for describing partially polarized light.

Consider a quasi-monochromatic beam with its $E_x(t)$ and $E_y(t)$ components exhibiting fluctuating amplitude and phase functions as described above. Also, consider that the measured averaged intensities for each component could take any value i.e., they are not necessarily equal. We want to somehow characterize the state of polarization measured by our detection system, even if we do not measure the light to be fully polarized. So, we follow a procedure typically employed for measuring fully polarized light, and hope that we are able to extract some information to characterize partially polarized light from it: we make the beam pass through a system composed of a wave plate with retardance ϕ and its eigen-axes aligned along the x and y directions, and a linear polarizer with its transmission axis rotated an angle θ with respect to the x axis. The resulting electric field after the system is

$$\vec{\mathbf{E}} = (\cos \theta e^{i\phi/2} E_x(t) + \sin \theta e^{-i\phi/2} E_y(t)) \hat{\theta}, \quad (2.58)$$

where $\hat{\theta}$ is the unit vector in the direction of the transmission axis of the polarizer. As explained above, the detector measures the averaged intensity of the electric field over a long temporal period T . Following [10], we define the intensity of an electric field $\vec{\mathbf{E}}(t)$ as the time average of its modulus squared:

$$I = \langle \vec{\mathbf{E}}^*(t) \cdot \vec{\mathbf{E}}(t) \rangle = \lim_{T \rightarrow \infty} \frac{1}{T} \int_0^T \vec{\mathbf{E}}^*(t) \cdot \vec{\mathbf{E}}(t) dt. \quad (2.59)$$

Considering the electric field described in Eq. 2.58 into the last equation, we obtain the averaged intensity that our detector will measure:

$$\begin{aligned} I(\theta, \phi) &= \langle \vec{\mathbf{E}}^* \cdot \vec{\mathbf{E}} \rangle = \cos^2 \theta \langle E_x^*(t) E_x(t) \rangle + \sin^2 \theta \langle E_y^*(t) E_y(t) \rangle \\ &+ \sin \theta \cos \theta (e^{-i\phi} \langle E_x^*(t) E_y(t) \rangle + e^{i\phi} \langle E_y^*(t) E_x(t) \rangle), \end{aligned} \quad (2.60)$$

where

$$\langle E_i^*(t) E_j(t) \rangle = \lim_{T \rightarrow \infty} \frac{1}{T} \int_0^T E_i^*(t) E_j(t) dt. \quad (2.61)$$

With the help of some trigonometric relations the intensity can be rewritten as

$$I(\theta, \phi) = \frac{1}{2} (S_0 + S_1 \cos 2\theta + S_2 \sin 2\theta \cos \phi + S_3 \sin 2\theta \sin \phi), \quad (2.62)$$

where

$$S_0 = \langle E_x^* E_x \rangle + \langle E_y^* E_y \rangle, \quad (2.63)$$

$$S_1 = \langle E_x^* E_x \rangle - \langle E_y^* E_y \rangle, \quad (2.64)$$

$$S_2 = \langle E_x^* E_y \rangle + \langle E_y^* E_x \rangle, \quad (2.65)$$

$$S_3 = i (\langle E_y^* E_x \rangle - \langle E_x^* E_y \rangle), \quad (2.66)$$

and the t dependence in these last equations is explicitly omitted for the sake of simplicity. The quantities S_0 , S_1 , S_2 and S_3 are the Stokes parameters for partially polarized light, and they are a generalization of the Stokes parameters for fully polarized light described in subsection 2.1.3. The intensity of the i component is $\langle E_i^* E_i \rangle$, therefore S_0 is the total intensity of the beam, which we call I_0 . The crossed terms $\langle E_i^* E_j \rangle$ for $i \neq j$ provide the statistical correlation of the complex signals describing the components E_i and E_j [19]. If the signals are completely uncorrelated the crossed terms $\langle E_i^* E_j \rangle$ become zero.

The Stokes parameters can be expressed as a function of the experimentally measured intensities for different configurations of θ and ϕ : $I_x = I(0, 0)$ and $I_y = I(\pi/2, 0)$, which are the intensity of the field components along the x and y directions; $I_{45^\circ} = I(\pi/4, 0)$ and $I_{-45^\circ} = I(-\pi/4, 0)$, which represent the intensities of the components along the 45° and -45° directions; and $I_R = I(\pi/4, \pi/2)$ and $I_L = I(\pi/4, 3\pi/2)$, which are the intensities of the right (I_R) and left (I_L) circular components. Evaluating Eq. 2.62 for these values of θ and ϕ and using basic algebra we get that the Stokes parameters can be expressed as

$$S_0 = I_x + I_y = I_{45^\circ} + I_{135^\circ} = I_R + I_L, \quad (2.67)$$

$$S_1 = I_x - I_y, \quad (2.68)$$

$$S_2 = I_{45^\circ} - I_{135^\circ}, \quad (2.69)$$

$$S_3 = I_R - I_L. \quad (2.70)$$

These equations reveal that Stokes parameters are measurable real quantities. While S_0 gives the total intensity; S_1 , S_2 and S_3 provide how close is the state from being LHP, LVP, L45P, L-45P, RCP and LCP. Since we do not measure a preferred shape of the ellipse for unpolarized light, we expect that it is equally close from being any of these states.

First, let us obtain the Stokes parameters for unpolarized light. As Gabriel Stokes observed in 1852, when unpolarized light is measured with a polarizer, the measured intensity does not depend on the orientation θ of the polarizer transmission axis. If we place a wave plate with retardance ϕ before the analyzer and measure the intensity for any configuration of ϕ and θ it will not depend on ϕ and θ either. In fact, the intensity after the retarder-polarizer system is always half of the incident intensity, independently of ϕ and the orientation θ . The only

way that $I(\theta, \phi)$ in Eq. 2.62 is always half of the intensity and does not depend on ϕ and θ is that $S_1 = S_2 = S_3 = 0$ and $S_0 \neq 0$. As a result, the intensity after the system is half of the incident intensity S_0 : $I(\theta, \phi) = S_0/2$. Therefore, unpolarized light is described by the Stokes parameters $S_0 = I_0$, $S_1 = 0$, $S_2 = 0$, and $S_3 = 0$. This is only possible if the intensities of the x and y components are equal ($\langle E_x^* E_x \rangle = \langle E_y^* E_y \rangle$) and the crossed terms $\langle E_i^* E_j \rangle$ are zero: the polarization components x and y are not statistically correlated and their mean amplitudes are the same.

Now, let us consider the opposite case: fully polarized light. If we calculate the Stokes parameters using Eqs. 2.63-2.66 for the electric field of a strictly monochromatic wave in terms of the azimuth ψ and polar χ parameters (Eq. 2.19) we retrieve the equations 2.23-2.25 for the Stokes parameters of fully polarized light: $S_0 = I_0$, $S_1 = I_0 \sin 2\chi \cos 2\psi$, $S_2 = I_0 \sin 2\chi \sin 2\psi$, and $S_3 = I_0 \cos 2\chi$.

It seems reasonable that these two cases are extreme situations of a more general case: *partially polarized light*. The modulus of the vector (S_1, S_2, S_3) is $I_0 = S_0$ for fully polarized light. On the other hand, when light is unpolarized, the modulus is 0. The intermediate case is described by letting the modulus take intermediate values between 0 and S_0 . The modulus of the vector (S_1, S_2, S_3) can be expressed in terms of a parameter P such that

$$\sqrt{S_1^2 + S_2^2 + S_3^2} = PS_0, \quad (2.71)$$

where P is restricted to be $0 \leq P \leq 1$. Parameter P measures how polarized the beam is, and thus, it is usually called *degree of polarization* (DoP). If $P = 1$ we have fully polarized light and the length of (S_1, S_2, S_3) is I_0 . Conversely, if $P = 0$ we say that light is unpolarized, and the length of (S_1, S_2, S_3) is zero. For partially polarized light the length can take values from 0 to I_0 .

A formal relation between the DoP and the partial polarized nature of light can be found in detail in [19]. Here, instead, we give a rough intuition of why it makes sense that a DoP between 0 and 1 describes partially polarized light. As explained at the beginning of the section, if the E_x and E_y components are somehow statistically correlated, so $\langle E_i^*(t) E_j(t) \rangle \neq 0$, we will detect partially polarized light. Consider now a different situation where light will also be detected as partially polarized: the components are completely uncorrelated, so $\langle E_i^*(t) E_j(t) \rangle = 0$, but the mean values of the amplitude E_x is slightly greater than E_y . We will measure a bigger polarization component along the x direction, and therefore a preferred shape of the ellipse. From Eqs. 2.63-2.66 we get that the S_2 and S_3 Stokes parameters in this case are zero, but S_1 divided by I_0 will be slightly bigger than 0. As a result, the modulus of (S_1, S_2, S_3) divided by $S_0 = I_0$, i.e., the DoP, will be smaller than 1 and bigger than 0 for partially polarized light.

Considering that the modulus of (S_1, S_2, S_3) is $I_0 P$ in the most general case, we can express the Stokes parameters for a general partially polarized beam ($0 \leq P \leq 1$) by multiplying S_1 , S_2 and S_3 with P in the equations of the Stokes

parameters for fully polarized light:

$$S_0 = I_0 \quad (2.72)$$

$$S_1 = I_0 P \sin 2\chi \cos 2\psi \quad (2.73)$$

$$S_2 = I_0 P \sin 2\chi \sin 2\psi \quad (2.74)$$

$$S_3 = I_0 P \cos 2\chi. \quad (2.75)$$

Note that the parameters S_1 , S_2 and S_3 are still the Cartesian coordinates in terms of the spherical coordinates 2χ and 2ψ of a point in a three-dimensional space. For $P = 1$ they define the surface of a sphere of radius I_0 : the Poincaré sphere. As in subsection 2.1.3, the points representing fully polarized states lie on the surface of the sphere ($P = 1$). Nevertheless, points representing partially polarized light are inside the sphere ($0 < P < 1$), and unpolarized light is right at the center of the sphere ($P = 0$). These situations are depicted in Fig. 2.10(a).

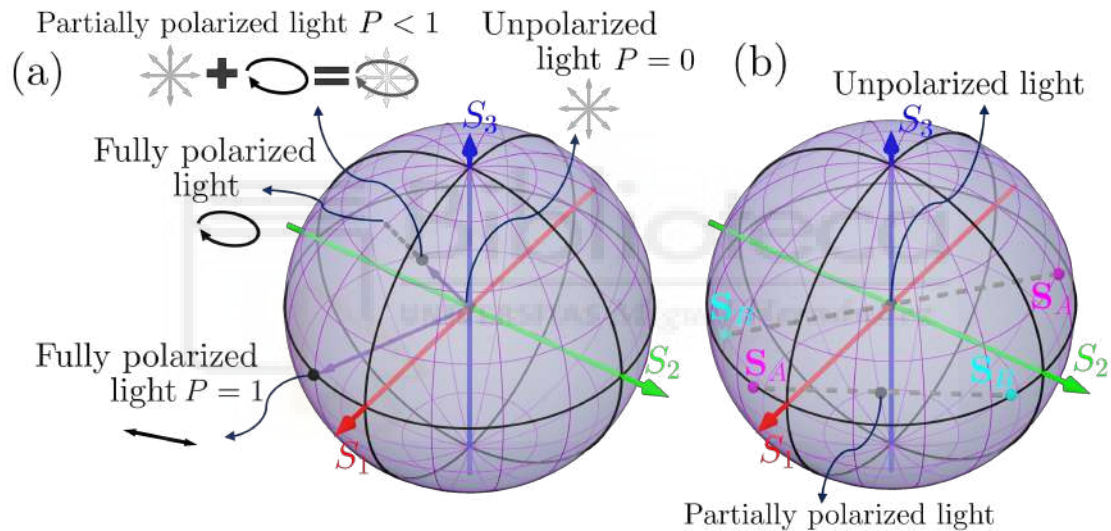


Figure 2.10: Poincaré Sphere for partially polarized light. (a) Representation of Fully polarized light ($P = 1$), partially polarized light ($0 \leq P \leq 1$), and unpolarized light ($P = 0$). (b) Partially polarized light obtained as the sum of two equally-weighted Stokes vectors representing fully polarized light.

2.3.2 Incoherent superposition of polarized light

At the beginning of the section, we presented the concepts of incoherent and coherent superpositions with an illustrative experiment. So far, we know that the *coherent* addition of two polarization states is well described by the sum of their *Jones vectors*: if the states are fully correlated, a good description is obtained by considering the total state as a sum of their Jones vectors, where the ellipses shape remains constant. Here, we will derive that the *incoherent* addition of two polarized beams can be described by the addition of measured intensities along different directions, i.e., by its *Stokes parameters* addition.

Stokes parameters are usually expressed as the components of a vector \mathbf{S} called the Stokes vector:

$$\mathbf{S} = \begin{pmatrix} S_0 \\ S_1 \\ S_2 \\ S_3 \end{pmatrix}.$$

Although the set of Stokes vectors with the addition operation $+$ do not form a group⁶, and therefore they cannot be used to define a vector space with the operation $+$, they are vectors from the computer science point of view: a one-dimensional array data structure. Therefore, we will refer to \mathbf{S} as the Stokes vector throughout this thesis.

Two decompositions can be performed on a Stokes vector that give a glimpse on why the addition of two Stokes vectors describes the incoherent addition of two beams. First, it is straightforward to prove that a Stokes vector with the parameters in Eqs. 2.72-2.75 can be easily decomposed as

$$\mathbf{S} = (1 - P)I_0 \begin{pmatrix} 1 \\ 0 \\ 0 \\ 0 \end{pmatrix} + PI_0 \begin{pmatrix} 1 \\ \sin 2\chi \cos 2\psi \\ \sin 2\chi \sin 2\psi \\ \cos 2\chi \end{pmatrix}, \quad (2.76)$$

where the first Stokes vector describes unpolarized light, and the second describes fully polarized light. This expression shows that partially polarized light can be regarded as a superposition of fully polarized and unpolarized light. Therefore, the decomposition reflects that, when we measure partially polarized light, we are measuring a preferred shape of the ellipse given by the polarized part of the equation above. Partially polarized light is depicted as a point inside the Poincaré sphere in Fig. 2.10(a). The vector (S_1, S_2, S_3) with radius smaller than I_0 ($P < 1$) defining this point is pointing towards a state on the surface of the Poincaré Sphere representing the polarized part of the beam.

An alternative decomposition of the same Stokes vector is:

$$\mathbf{S} = \frac{1 - P}{2P}I_0 \begin{pmatrix} P \\ \sin 2\chi \cos 2\psi \\ \sin 2\chi \sin 2\psi \\ \cos 2\chi \end{pmatrix} + \frac{1 + P}{2P}I_0 \begin{pmatrix} P \\ -\sin 2\chi \cos 2\psi \\ -\sin 2\chi \sin 2\psi \\ -\cos 2\chi \end{pmatrix}. \quad (2.77)$$

Since an antipodal point on a sphere is obtained by adding a minus sign to its Cartesian coordinates, and, as we showed in subsection 2.1.3, antipodal points on the Poincaré sphere represent orthogonal states, this expression shows that

⁶In order to consider the set of the Stokes vectors together with the operation $+$ a group, several axioms must be satisfied. One axiom states that there is an element, called the identity element $\mathbf{S}_\mathbf{I}$, that satisfies $\mathbf{S}_\mathbf{I} + \mathbf{S}_a = \mathbf{S}_a + \mathbf{S}_\mathbf{I} = \mathbf{S}_a$ for every element \mathbf{S}_a in the set. It is easy to find that this element is the vector $\mathbf{S}_\mathbf{I} = (0, 0, 0, 0)$, which represents the absence of light. Another axiom is that for each element \mathbf{S}_a in the set there must be an element \mathbf{S}_a^{-1} (called the inverse of \mathbf{S}_a) such that $\mathbf{S}_a^{-1} + \mathbf{S}_a = \mathbf{S}_a + \mathbf{S}_a^{-1} = \mathbf{S}_\mathbf{I}$. Since S_0 cannot take negative values, the last axiom is not satisfied.

the Stokes vector can be obtained as the sum of two Stokes vectors representing fully polarized orthogonal states. Note that for $P = 0$ we have unpolarized light expressed as a combination of two equally weighted Stokes vectors representing fully polarized orthogonal states.

In fact, a Stokes vector can be expressed as the superposition of other two Stokes vectors, not necessarily fully polarized or orthogonal. For a Stokes vector obtained as a combination of other vectors \mathbf{S}_A and \mathbf{S}_B as $a\mathbf{S}_A + b\mathbf{S}_B$, the output state will be inside a sphere of radius $S_0 = aS_{0A} + bS_{0B}$. Therefore, if we add two Stokes vectors with $S_{0A} = S_{0B} = I_0$ and $a = b = 1/2$, the resulting Stokes vector is at the midpoint on the line connecting the points \mathbf{S}_A and \mathbf{S}_B in a sphere of radius I_0 . This last situation is depicted in Fig. 2.10(b) for the addition of two fully polarized beams lying on antipodal points (thus resulting in unpolarized light) and when they do not (thus resulting in partially polarized light).

We have just seen that a Stokes vector can be expressed as the sum of other two Stokes vectors. One may ask what is the meaning of this sum. On the one hand, adding two fully statistically correlated linearly polarized beams along the x and y axes yields fully polarized light. The fact that the components are completely correlated means we can describe the resulting beam by adding the two Jones vectors describing each beam. In this situation, we say that the beams are *coherently* added. On the other hand, the beams may be fully uncorrelated, in this case we say that we are *incoherently* adding the beams. It turns out, as we will show next, that the beam that results from the incoherent addition of two beams is obtained by the addition of their Stokes vectors.

Consider two Stokes vectors \mathbf{S}_A and \mathbf{S}_B describing the polarization state of two beams A and B . The components $E_{xA}(t)$, and $E_{yA}(t)$ could be perfectly correlated, so \mathbf{S}_A might describe a fully polarized beam. Otherwise, A might be unpolarized or partially polarized. The beam B could also be polarized, partially polarized or unpolarized. Regardless of the DoP of A and B , its superposition is said to be incoherent if the polarization components of A ($E_{xA}(t)$, and $E_{yA}(t)$) are not statistically correlated with the components of B ($E_{xB}(t)$, and $E_{yB}(t)$). As a result, a partially polarized beam can be obtained from the incoherent addition of two uncorrelated fully polarized beams.

This incoherent addition of two Stokes vectors can be obtained from Eqs. 2.63-2.66. Consider that the Stokes parameter in these equations are the Stokes parameters of a beam C obtained from superposition of two beams A and B weighted by the real quantities a and b (representing the amount of each beam): $\vec{E}_C(t) = a\vec{E}_A(t) + b\vec{E}_B(t)$. Therefore, the components $E_x(t)$ and $E_y(t)$ at Eqs. 2.63-2.66 are the components $E_{xC}(t)$ and $E_{yC}(t)$ of the resulting beam. We now express these equations in terms of the components of beams A and B by performing the substitution $E_x \rightarrow E_{xC}(t) = E_{xA}(t) + E_{xB}(t)$ and $E_y(t) \rightarrow E_{yC}(t) = E_{yA}(t) + E_{yB}(t)$. Using the linearity of the time average operation we obtain the parameters ($S_{0C}, S_{1C}, S_{2C}, S_{3C}$) as a linear combination of terms $\langle E_{ik}^*(t)E_{jh}(t) \rangle$, where $i, j = x, y$ and $k, h = A, B$. If beams A and B are uncorrelated, it means that each pair of components for different beams have no statistical similarity. Therefore, every term of the form $\langle E_{ik}^*(t)E_{jh}(t) \rangle$ for $k \neq h$ is zero for an incoherent addition. As

a result, all the crossed terms vanish and we obtain that $\mathbf{S}_C = a^2\mathbf{S}_A + b^2\mathbf{S}_B$. So the resulting beam of two incoherently added beams can be obtained by simply adding its Stokes vectors weighted by the amount of light of each beam.

The resulting Stokes vector of a coherent superposition could be obtained by substituting the plane wave equations of each beam in every term $\langle E_{ik}^*(t)E_{jh}(t) \rangle$. As a consequence, the crossed terms $\langle E_{ik}^*(t)E_{jh}(t) \rangle$ for $k \neq h$ do not vanish, and an interference term arises, so the coherent superposition is not only the addition of Stokes vectors. In fact, it can be described in a simpler and more elegant manner as the superposition of Jones vectors. Alternatively, a situation in between for a partially coherent superposition can be found. However, it is out of the scope of this thesis.

Finally, we compare the coherent and incoherent addition in terms of transformation in the Poincaré sphere. We deduced in the first section of this chapter that the sum of two orthogonal Jones vectors, without any extra phase between them, results in a state lying on the Poincaré sphere surface at an angular distance that depends on the weight of each component (see Fig. 2.4 in subsection 2.1.3). It turns out that the same happens if the states are not orthogonal. When there is a relative phase between them, the resulting state changes, but it moves always on the sphere surface. Therefore, the coherent addition of two polarized beams always yields fully polarized light. Conversely, when we incoherently add two states, we add its Stokes vectors. The resulting state will be somewhere on the straight line that joins the two states. So, it will lie inside the sphere in general, independently of the phase between them. Unlike Jones vector addition, the phase between the states does not matter since the beams are not correlated. Only the phase between the components of each state is relevant since they determine their states of polarization.

2.3.3 Experimental generation of partially polarized light

After this introduction to partially polarized light, we are in a better position to understand the methods for generating partially polarized light, including the ones discussed at the beginning of this section. Several methods have been proposed for generating partially polarized light out of fully polarized light. One of the first methods capable of producing unpolarized light is the Lyot depolarizer [23]. It consists of two quartz linear retarders glued together with a thickness ratio of 1:2. The eigen-axes of the second retarder form an angle of 45° degrees with respect to the eigen-axes of the first. A notable property of Lyot depolarizers is that the input light needs to have a minimum bandwidth to generate complete depolarization. This is because its depolarization mechanisms rely on the response of the different wavelengths to the birefringence of the material. As a consequence, different polarization states for different wavelengths are generated, so an effective depolarization effect is measured. Therefore, this kind of depolarizers does not work for quasi-monochromatic beams. In addition, the degree of polarization of the output beam cannot be controlled for the same input light.

To generate unpolarized light with a quasi-monochromatic source other approaches must be employed. A common technique is based on using patterned

micro-retarder arrays that generate a pseudo-random spatial distribution of the polarization [24]. All these different polarization states will lie at distinct points on the detector area. Provided that the detector integration area is large enough, these states will be averaged, so the light will be detected as unpolarized. However, none of these devices allow us to dynamically control the degree of polarization. Not at least without replacing the device by another with a different distribution of the retarder axes such that one preferred shape of the polarization ellipse is generated, which will result in a partial polarization effect.

One approach for controlling the degree of polarization at will that relies on the spatial integration of two fully polarized beams lying at different areas of the detector is performed by Lizana et al. in [21]. The distance between the two beams inside the detector was large enough so they do not interfere. This type of spatial effective depolarization effect can be understood as follows. First, we know that the Stokes parameters are computed by subtracting intensities measured for different configurations of the polarization state analyzer system as Eqs. 2.67-2.70 show ($I_x, I_y, I_R...$). We also know that each of these intensities results from averaging the intensities at every point of the detector. Therefore, the intensities I_x, I_y , etc. of the measured state are the intensities resulting from adding the measured intensities for each beam weighted by the area that each beam takes up on the detector surface. This means that the Stokes vector describing the resulting beam can be obtained by spatially averaging the Stokes vectors of the two beams at different areas. The result is equivalent to an incoherent addition of two polarized beams. Therefore, as Eq. 2.76 reveals, the detector will measure light as unpolarized when these beams are orthogonal and equally weighted. The degree of polarization of the resulting beam can be changed by controlling the weight of each beam. Furthermore, a set of linear retarders allows Lizana et al. in [21] to transform the polarization of the resulting partially polarized state. As a result, any point in the Poincaré sphere can be reached.

In the same work, they use a different approach for generating partially polarized light. As explained at the beginning of this section, they split a laser beam into its two orthogonal horizontal and vertical linear polarization components. Then, they recombine the beams after one of them has traveled a distance greater than the coherence length of the source. The result is an incoherent superposition of two orthogonal fully polarized beams with the same intensity, yielding unpolarized light. In the last section, we learned that the state resulting from an incoherent addition can be obtained by adding the Stokes vectors of the beams. If now we decrease the intensity of one beam with respect to the other, the incoherent addition of them will result in partially polarized light, instead of unpolarized. After the recombination, a system of linear retarders can change the state of polarization, again being able to produce any state in the Poincaré sphere.

At the beginning of the section, we also mentioned the work of D. Ramkhalwon et al. [20], where they combine two equally-weighted uncorrelated linearly polarized orthogonal laser sources. This results in an equi-intense incoherent superposition of orthogonal beams, so light is detected as unpolarized. Analogously to the experiment previously described, they generate partially polarized light

by changing the intensity ratio between the two orthogonal polarizations. After that, they could move the state to any point in the Poincaré sphere with a linear retarder.

Finally, effective depolarization with quasi-monochromatic sources can be achieved by sending a state of polarization that changes in time faster than the integration time of the detector. We have briefly introduced how A. Peinado et al. achieve this situation by rapidly switching the fast axis of a liquid-crystal ferroelectric retarder [22], reaching switching rates of kHz. As explained at the beginning of this section, the detector adds and averages the instantaneous intensity of the beam over a long temporal period. If within this period we are capable of sending to the detector different polarization states, each measurement of the intensity ($I_x, I_y, I_R...$) for different times in the Stokes parameters of Eqs. 2.67-2.70 will be averaged. This means that the intensities will be added weighted by the time interval in which each state is sent to the detector. Consider we send two polarization states in a time T , the first state described by \mathbf{S}_A during a time t_A , and the second \mathbf{S}_B during $t_B = T - t_A$. The resulting effective state $\langle \mathbf{S}_e \rangle$ will be described by temporary averaging their Stokes parameters:

$$\langle \mathbf{S}_e \rangle = \frac{1}{T} [t_A \mathbf{S}_A + (T - t_A) \mathbf{S}_B]. \quad (2.78)$$

The degree of polarization of light can be controlled by changing the time that each state is sent to the detector. After, the state can be changed with a linear retarder. Alternatively, we could have mixed different fully polarized states at different time intervals t_A and t_B , so we could cover all the Poincaré sphere with no need for a retarder after state $\langle \mathbf{S}_e \rangle$.

In the work "Customized depolarization spatial patterns with dynamic retardance functions" [8], we used the above-described technique with a tunable multi-pixel liquid-crystal on silicon spatial light modulator, instead of a single-pixel retarder. As a result, we generated beams with a tailored spatially varying degree of polarization along their section.

2.3.4 Mueller matrices

In section 2.2 we showed that the action of an optical component over a polarized beam can be described by a Jones matrix acting over a Jones vector. Analogously, the action of an optical component over a fully or partially polarized beam can be described as the action of a 4×4 matrix

$$\mathbf{M} = \begin{pmatrix} m_{00} & m_{01} & m_{02} & m_{03} \\ m_{10} & m_{11} & m_{12} & m_{13} \\ m_{20} & m_{21} & m_{22} & m_{23} \\ m_{30} & m_{31} & m_{32} & m_{33} \end{pmatrix}, \quad (2.79)$$

commonly referred to as a Mueller matrix, over a Stokes vector \mathbf{S} , so the resulting state is

$$\mathbf{S}' = \mathbf{M}\mathbf{S}. \quad (2.80)$$

The elements of the Mueller matrix, as the Stokes parameters, are real numbers. A Jones matrix has four complex elements. Therefore, it contains a maximum of eight degrees of freedom. Each possible Jones Matrix can be expressed as a Mueller matrix [10]. However, when converting a Jones matrix to a Mueller matrix, the information of the global phase is lost, as in the conversion from a Jones vector to a Stokes vector. So, the resulting Mueller matrix will have a maximum of seven degrees of freedom. But, a remarkable property of Mueller matrices is that they can describe elements that may reduce the degree of polarization, namely *depolarizers*, while Jones matrices cannot. In the most general case a Mueller matrix will contain $4 \times 4 = 16$ independent elements. The elements of the Mueller matrix can be obtained by measuring the output Stokes parameters for different input polarizations [10].

A Matrix that will be used in this thesis is the Mueller matrix of a linear retarder (waveplate) with its eigen-axes along the x and y directions and retardance ϕ :

$$\mathbf{M}_{WP} = \begin{pmatrix} 1 & 0 & 0 & 0 \\ 0 & 1 & 0 & 0 \\ 0 & 0 & \cos \phi & -\sin \phi \\ 0 & 0 & \sin \phi & \cos \phi \end{pmatrix}. \quad (2.81)$$

This matrix will leave the parameter S_0 constant, so it will not change the intensity of the incoming light, as expected from a retarder. The 3×3 sub-matrix (defined by leaving out the elements of the form m_{i0} and m_{0i}) is a rotation matrix in 3D space around the S_1 axis. So, as explained in subsection 2.2.2, it rotates a point in the Poincaré sphere around the S_1 axis. As retarders, diattenuators can also be expressed as Mueller matrices. However, we will not be using Mueller matrices for diattenuators in this thesis.

Another matrix that will be used is the Mueller matrix of a pure nonuniform depolarizer:

$$\mathbf{M}_{\Delta \text{pure}} = \begin{pmatrix} 1 & 0 & 0 & 0 \\ 0 & a_1 & 0 & 0 \\ 0 & 0 & a_2 & 0 \\ 0 & 0 & 0 & a_3 \end{pmatrix}, \quad (2.82)$$

where $|a_1|$, $|a_2|$, and $|a_3|$ are less or equal to 1. The action of this matrix over an input Stokes vector $(S_{in0}, S_{in1}, S_{in2}, S_{in3})$ gives as a result an output vector $(S_{in0}, a_1 S_{in1}, a_2 S_{in2}, a_3 S_{in3})$. The effect of the matrix is to independently reduce the amount of S_1 , S_2 and S_3 , yielding to a general reduction of the DoP. The principal depolarization factors are defined as $\Delta_i = 1 - |a_i|$, for $i = 1, 2, 3$. These factors measure the depolarization power of the matrix for horizontal/vertical linearly polarized light (Δ_1); for linearly polarized light along the 45° and -45° directions (Δ_2); and for right/circular polarized light (Δ_3).

As we mentioned in the previous section, an effective partially polarized beam can be achieved by temporally averaging a time-varying polarization state. For instance, this state could be generated by a fast switching of the eigen-axes of a ferroelectric liquid-crystal retarder. Equation 2.78 shows the resulting effective state $\langle \mathbf{S}_e \rangle$ of temporally averaging two states \mathbf{S}_A and \mathbf{S}_B . We consider these states

are generated by a linear retarder at different configurations (of the phase or of its eigen-axes) described by the Mueller matrices \mathbf{M}_A and \mathbf{M}_B . The states \mathbf{S}_A and \mathbf{S}_B are then: $\mathbf{S}_A = \mathbf{M}_A \mathbf{S}_{in}$ and $\mathbf{S}_B = \mathbf{M}_B \mathbf{S}_{in}$. We assume that the depolarization effect of the retarder can be described as an effective Mueller matrix $\langle \mathbf{M}_e \rangle$ acting over an input state \mathbf{S}_{in} to give $\langle \mathbf{S}_e \rangle$ as $\langle \mathbf{S}_e \rangle = \langle \mathbf{M}_e \rangle \mathbf{S}_{in}$. Therefore, if the action of the retarder during the times t_A and $t_B = T - t_A$ are given by \mathbf{M}_A and \mathbf{M}_B , respectively, the effective Mueller matrix is:

$$\langle \mathbf{M}_e \rangle = \frac{1}{T} [t_A \mathbf{M}_A + (T - t_A) \mathbf{M}_B]. \quad (2.83)$$

We will use this result later to study the effective Mueller matrix obtained by temporal averaging of the phase pattern encoded on a liquid-crystal on silicon spatial light modulator.

2.3.5 The Lu-Chipman Decomposition

S. Y. Lu and R. A. Chipman proved in 1996 [12] that any Mueller matrix can be decomposed as the product of a diattenuator \mathbf{M}_D , a retarder \mathbf{M}_R , and a depolarizer \mathbf{M}_Δ as

$$\mathbf{M} = \mathbf{M}_\Delta \mathbf{M}_R \mathbf{M}_D. \quad (2.84)$$

In this thesis, we use this method to derive the retardance and depolarizance of an effective Mueller matrix obtained by a temporal average, as Eq. 2.83 shows, for a spatial light modulator [8].

A general Mueller matrix (Eq. 2.79) can be expressed as follows:

$$\mathbf{M} = m_{00} \begin{pmatrix} 1 & \vec{D}^T \\ \vec{P} & \mathbf{m} \end{pmatrix}, \quad (2.85)$$

where

$$\vec{D}^T = \frac{1}{m_{00}} (m_{01} \quad m_{02} \quad m_{03}) \quad (2.86)$$

is the transposed diattenuation vector,

$$\vec{P} = \frac{1}{m_{00}} \begin{pmatrix} m_{10} \\ m_{20} \\ m_{30} \end{pmatrix} \quad (2.87)$$

is the polarizance vector, and

$$\mathbf{m} = \frac{1}{m_{00}} \begin{pmatrix} m_{11} & m_{12} & m_{13} \\ m_{21} & m_{22} & m_{23} \\ m_{31} & m_{32} & m_{33} \end{pmatrix} \quad (2.88)$$

is the normalized 3×3 Mueller matrix built by discarding all the elements with a 0 in its indices.

When a Mueller matrix acts over a Stokes vector, the parameter S_{0out} of the output vector is only determined by the first row of the Mueller Matrix, namely

by the diattenuation vector \vec{D} . Since $S_{0\text{out}}$ is the output intensity, the elements of \vec{D} control the contribution that each Stokes parameter of the input vector ($S_{1\text{in}}$, $S_{2\text{in}}$ and $S_{3\text{in}}$) has on the output intensity. Basically, the diattenuation vector tells us how the transmittance of the system depends on the input polarization state.

Now consider a Mueller matrix acting over an input Stokes vector describing unpolarized light, so its Stokes vector is $(1, 0, 0, 0)$. The resulting vector will be $(m_{00}, m_{10}, m_{20}, m_{30})$, so the state is determined by the first column of the Mueller matrix. Therefore, the polarizance vector \vec{P} determines the amount that an input unpolarized beam has been polarized along the S_1 , S_2 , and S_3 axes. The modulus of the polarizance vector is called the polarizance:

$$P = |\vec{P}| = \frac{1}{m_{00}} \sqrt{m_{10}^2 + m_{20}^2 + m_{30}^2}, \quad (2.89)$$

and it gives the DoP of the resulting output state when the input state is unpolarized.

The matrix of a diattenuator can be expressed as [12]

$$\mathbf{M}_D = m_{00} \begin{pmatrix} 1 & \vec{D}^T \\ \vec{D} & \mathbf{m}_D \end{pmatrix},$$

where $\mathbf{m}_D = \sqrt{1 - D^2} \mathbf{I} + [\hat{D} \hat{D}^T (1 - \sqrt{1 - D^2})]$. The matrix \mathbf{I} is the 3×3 identity matrix. The vector $\hat{D} = \vec{D}/D$ is the unitary vector of \vec{D} , so D is its modulus.

The matrix \mathbf{M}_D is straightforwardly calculated from the \vec{D} vector obtained from the Mueller matrix first row elements. Once we have the matrix \mathbf{M}_D , the procedure to obtain the matrices \mathbf{M}_R and \mathbf{M}_Δ is different depending on the singularity of \mathbf{M}_D . If \mathbf{M}_D is singular, as in the case of a polarizer, the procedure described in the appendix at [12] must be followed. In this thesis, we did not deal with singular matrices, so we calculate the inverse of \mathbf{M}_D and use it to obtain the other two matrices in the decomposition in Eq. 2.84. If \mathbf{M}_D is not singular we can get its inverse as

$$\mathbf{M}_D^{-1} = \frac{1}{m_{00}(1 - D^2)} \left[\begin{pmatrix} 1 & -\vec{D}^T \\ -\vec{D} & \mathbf{I} \end{pmatrix} + \frac{1}{\sqrt{1 - D^2} + 1} \begin{pmatrix} 0 & \vec{0}^T \\ \vec{0} & \vec{D} \vec{D}^T \end{pmatrix} \right].$$

The most general matrix for a depolarizer that also can polarize is given by

$$\mathbf{M}_\Delta = \begin{pmatrix} 1 & \vec{0}^T \\ \vec{P}_\Delta & \mathbf{m}_\Delta \end{pmatrix}, \quad (2.90)$$

where \vec{P}_Δ is the polarizance vector of the depolarizer and it determines its polarizing properties, and \mathbf{m}_Δ is a 3×3 symmetric matrix and determines its depolarizing properties. If \mathbf{m}_Δ is diagonal, its eigenvalues λ_i are related to the principal depolarizing factors Δ_i along the S_1 , S_2 and S_3 axes, which are the principal axes of the depolarizer, as $\Delta_i = 1 - \lambda_i$, for $i = 1, 2, 3$. These depolarizing factors are the same factors that we introduced in the previous subsection. But the three principal axes can be along any three orthogonal axes, so, in the most general case, \mathbf{m}_Δ is

a symmetric matrix with its eigen-axes being the principal axes of the depolarizer and its eigenvalues λ_i related to the depolarizing factors Δ_i as $\Delta_i = 1 - \lambda_i$, where i indicates each of the three principal axes.

The matrix of a retarder \mathbf{M}_R is

$$\mathbf{M}_R = \begin{pmatrix} 1 & \vec{0}^T \\ \vec{0} & \mathbf{m}_R \end{pmatrix}, \quad (2.91)$$

where \mathbf{m}_R is a 3×3 sub-matrix that describes a rotation in the 3D space S_1, S_2, S_3 . The axis that defines the rotation in the Poincaré sphere is given by the 3D vector that points from the center of the sphere towards the state with the negative phase in the Jones matrix of a general retarder in Eq. 2.44 in section 2.2.2. The axis is depicted in golden in Fig. 2.5 for a (a) linear retarder with its eigen-axes along the horizontal/vertical polarizations and (b) a circular retarder.

To obtain \mathbf{M}_Δ and \mathbf{M}_R we multiply Eq. 2.84 by \mathbf{M}_D^{-1} and define \mathbf{M}' as

$$\mathbf{M}' = \mathbf{M}\mathbf{M}_D^{-1} = \mathbf{M}_\Delta\mathbf{M}_R. \quad (2.92)$$

The matrix \mathbf{M}' is calculated as the product $\mathbf{M}\mathbf{M}_D^{-1}$. Using Eqs. 2.90 and 2.91, the product $\mathbf{M}_\Delta\mathbf{M}_R$ is

$$\mathbf{M}' = \mathbf{M}_\Delta\mathbf{M}_R = \begin{pmatrix} 1 & \vec{0}^T \\ \vec{P}_\Delta & \mathbf{m}' \end{pmatrix}, \quad (2.93)$$

where $\mathbf{m}' = \mathbf{m}_\Delta\mathbf{m}_R$. The matrix \mathbf{m}' is directly obtained as the 3×3 sub-matrix of $\mathbf{M}\mathbf{M}_D^{-1}$. From the two previous equations it follows that \vec{P}_Δ is directly obtained as

$$\vec{P}_\Delta = (\vec{P} - \mathbf{m} \cdot \vec{D}) / (1 - D^2). \quad (2.94)$$

Once we have \mathbf{m}' we calculate \mathbf{m}_Δ by multiplying \mathbf{m}' by its transpose matrix $(\mathbf{m}')^T$. Using that the transpose of a rotation matrix is its inverse and that \mathbf{m}_Δ is symmetric we obtain that

$$\mathbf{m}'(\mathbf{m}')^T = \mathbf{m}_\Delta^2. \quad (2.95)$$

We know $\mathbf{m}'(\mathbf{m}')^T$, so we calculate its eigenvalues: λ_1, λ_2 and λ_3 . From the previous equation we know that the eigenvalues of \mathbf{m}_Δ are $\sqrt{\lambda_1}, \sqrt{\lambda_2}$ and $\sqrt{\lambda_3}$. The matrix \mathbf{m}_Δ can be obtained as [10]

$$\mathbf{m}_\Delta = \pm [\mathbf{m}'(\mathbf{m}')^T + \kappa_1\mathbf{I}]^{-1} [\kappa_2\mathbf{m}'(\mathbf{m}')^T + \kappa_3\mathbf{I}], \quad (2.96)$$

$$\kappa_1 = \sqrt{\lambda_1\lambda_2} + \sqrt{\lambda_2\lambda_3} + \sqrt{\lambda_3\lambda_1}, \quad (2.97)$$

$$\kappa_2 = \sqrt{\lambda_1} + \sqrt{\lambda_2} + \sqrt{\lambda_3}, \quad (2.98)$$

$$\kappa_3 = \sqrt{\lambda_1\lambda_2\lambda_3}. \quad (2.99)$$

If the determinant of \mathbf{m}' is positive, we take the plus sign, and, if it is negative, the minus sign. Since the matrix \mathbf{m}_R is a rotation matrix it has a positive determinant, so the sign of the determinant of \mathbf{m}' determines the sign of \mathbf{m}_Δ . The eigenvalues of \mathbf{m}_Δ are assumed to have the same sign, although actually there is also an ambiguity in their signs [10].

The depolarizance factors are obtained from \mathbf{m}_Δ as explained above. The matrix \mathbf{M}_Δ is obtained from \vec{P}_Δ and \mathbf{m}_Δ . Then, \mathbf{M}' is derived from \mathbf{m}' and \vec{P}_Δ . Finally, the retarder matrix \mathbf{M}_R is just

$$\mathbf{M}_\Delta^{-1}\mathbf{M}' = \mathbf{M}_R. \quad (2.100)$$

The total retardance R of \mathbf{M}_R is

$$R = \arccos\left(\frac{\text{Tr}(\mathbf{M}_R)}{2} - 1\right), \quad (2.101)$$

where R goes from 0 to π .

This procedure will be used in one of the works of this thesis, when analyzing the customized depolarization spatial patterns generated encoding dynamic retardance functions on a spatial light modulator [8].



Chapter 3

Diffractive optical elements

This chapter introduces the diffractive optical elements (DOEs) that have been used in this thesis. We consider phase-only DOEs, since they ideally do not introduce losses. Here, we use two techniques to implement DOEs: liquid-crystal *spatial light modulators* (SLMs) and liquid-crystal *geometrical phase elements*.

3.1 Pure phase diffractive optical elements

Diffraction is a characteristic phenomenon of all kind of waves. Historically, it was considered as a limiting factor in optical systems, where it imposes a limit of resolution power of imaging systems. However, the technological advances at the end of the 20th century allowed using diffraction to accomplish optical functions.

The term diffractive optics refers to the area of optics that exploits diffraction to generate such optical functions. Some basic functions are diffractive gratings, diffractive lenses, axicons or spiral phases. In general, DOEs can be calculated as computer generated holograms (CGHs). Two major aspects must be considered when dealing with DOEs: the design of the optical function to produce the desired effect, and the implementation of this function as a real physical element.

Diffractive optical elements are described by a complex transmittance function $\tau(x, y)$. Although this function in general can have an amplitude, here we only consider pure phase functions. Then, the transmittance is given by

$$\tau(x, y) = e^{i\varphi(x, y)}, \quad (3.1)$$

where the phase function $\varphi(x, y)$ takes values from 0 to 2π in standard diffractive elements. The term $\varphi(x, y)$ is proportional to the x or y coordinate for a linear blazed grating, proportional to the radial coordinate $r = \sqrt{x^2 + y^2}$ for a diffractive axicon, proportional to r^2 for a diffractive lens, or proportional to the azimuthal coordinate $\theta = \arctan2(y, x)$ for a spiral phase. In this thesis, we mostly consider three phase-only functions: The spiral phase, the linear blazed grating, and the optimal triplicator grating. The rest of the phase profiles we used are mostly combinations of these three.

3.1.1 Linear phase gratings and spiral phases

The transmission profile of a *linear grating* periodic along the x coordinate is given by

$$\tau_{linear}(x) = e^{i2\pi x/p}, \quad (3.2)$$

where p is the period of the grating. Figure 3.1(a) shows the phase function of a linear grating $\varphi(x, y) = 2\pi x/p$ as an 8-bit gray level image that ranges from 0 ($\varphi(x, y) = 0$) to 255 ($\varphi(x, y) = 2\pi$). The grating has a phase variation of 2π in one period. The linear grating ideally deviates all the input light to the first ($n = +1$) diffraction order. At the bottom part of Fig. 3.1(a), the intensity of a Gaussian beam at the Fourier plane after passing through a linear diffraction grating is depicted.

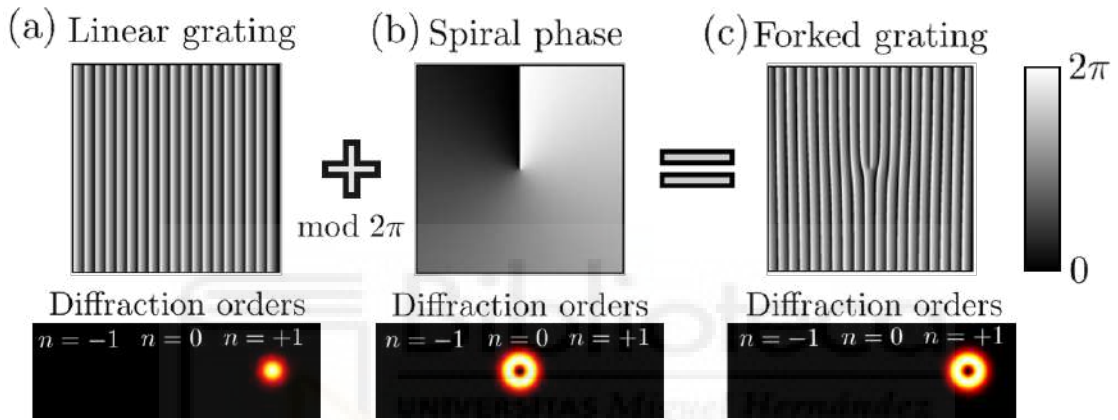


Figure 3.1: (a) Linear grating, (b) Spiral phase with $\ell = +1$, and (c) Forked grating phase profiles as 8-bit grayscale images. The n diffraction orders they generate at the Fourier plane when they are illuminated with a Gaussian beam are depicted at the bottom. The forked grating is obtained by adding modulo 2π the linear phase grating and the spiral phase.

A central phase function for this thesis is the *spiral phase* function, which adds a phase that varies continuously along the azimuthal coordinate θ . The phase varies from 0 to 2π a number of times ℓ along θ : $\varphi_{spiral}(\theta) = \ell\theta$. The quantity ℓ is known as the topological charge and its sign determines the sense of increasing phase. The transmission profile of a spiral phase is:

$$\tau_{spiral}(\theta) = e^{i\ell\theta}. \quad (3.3)$$

When a spiral phase function is added to a beam, the phase that the beam acquires twists its wavefronts around the axis of propagation. As a result, the wavefronts of the resulting beam form a helicoid, as shown in Fig. 3.2. For $\ell = \pm 1$, the wavefronts have the shape of a single helicoid. As the topological charge increases, they form double helicoids (for $\ell = \pm 2$), triple helicoids (for $\ell = \pm 3$) and so on. The sign of ℓ determines the sense of twisting of the wavefronts. So, beams with the same absolute value of the topological charge will have the same wavefront shape, but they will twist in opposite circular directions (clockwise and counterclockwise)

as shown in Fig. 3.2. The twisting of the phase causes a phase singularity at the center of the beam. The electric field of the light cancels out right at the center and this causes a zero in the intensity, which gives rise to a ring-shaped intensity pattern. As shown in Fig. 3.2, the size of the ring increases as the topological charge absolute value does. Note that the intensity profile is the same for beams with the same absolute value of the topological charge. These beams are known as *optical vortices* or *vortex beams* [25].

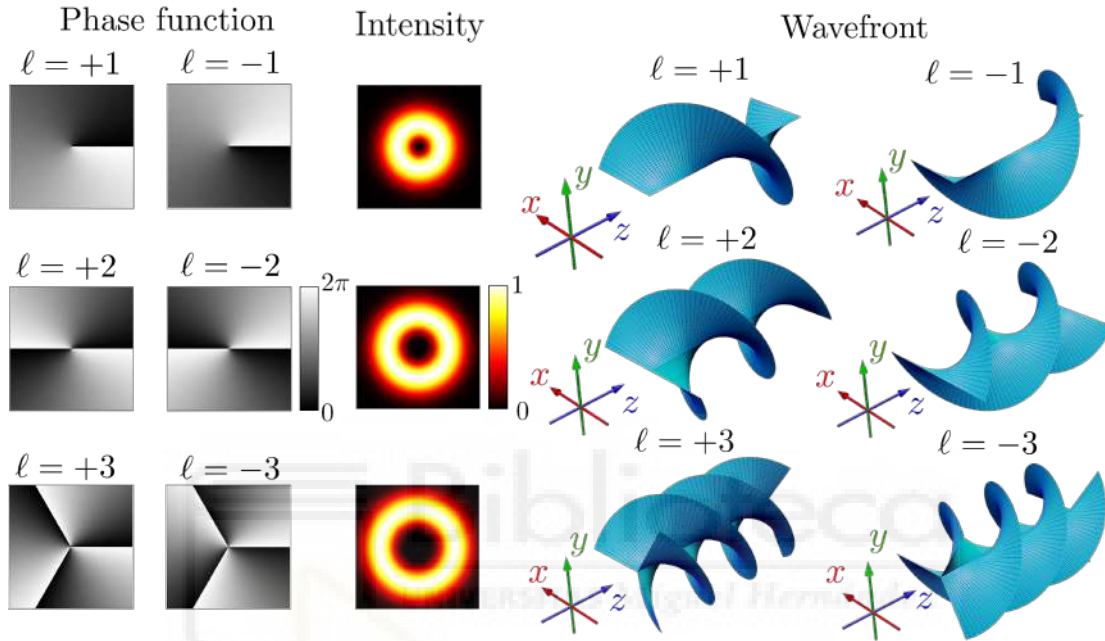


Figure 3.2: Optical vortices with topological charges $\ell = \pm 1$, $\ell = \pm 2$, and $\ell = \pm 3$. The spiral phase functions that generate the beams are shown at the left, and the resulting wavefront that each function generates for an incident plane wave at the right. The ring-shaped intensity profiles in a transverse plane increase with the absolute value of ℓ .

Phase functions can be added modulo 2π to obtain a new phase function that inherits the properties from both phase functions. An example that we will use in this thesis is the *forked grating*. This grating results from the modulo 2π addition of a linear grating and a spiral phase, as Fig. 3.1(c) depicts. Its transmission profile is then:

$$\tau_{fork}(x, \theta) = e^{i(\ell\theta + 2\pi x/p)}. \quad (3.4)$$

The forked grating deviates all the light to the first diffraction order and it adds a spiral phase. As a result, we obtain a deviated optical vortex of charge ℓ , as shown at the bottom of Fig. 3.1(c).

3.1.2 Harmonic terms in pure phase gratings. The optimal phase triplicator

In this thesis, we consider the standard situation in Fourier Optics, where we evaluate the diffractive element in a Fourier transform (FT) related plane, obtained

within the paraxial approximation, either by looking at the far field diffraction pattern (Fraunhofer diffraction) or by using a converging lens to obtain the FT in its back focal plane. We also consider DOEs with features larger enough than the wavelength, so the scalar approximation of diffraction can be considered [26]. Under these approximations, the transmission profile of a diffraction grating can be decomposed as an infinite sum of plane waves by means of a Fourier series [27]:

$$\tau(x) = e^{i\varphi(x)} = \sum_{-\infty}^{+\infty} \tau_n e^{in2\pi x/p}, \quad (3.5)$$

where we considered the grating as a one-dimensional phase-only function periodic in x . The quantity p is the period of the grating. Each exponential in this sum is a plane wave generating a diffraction order given by the integer number n . The Fourier coefficients τ_n are given by

$$\tau_n = \frac{1}{p} \int_0^p \tau(x) e^{-in2\pi x/p} dx. \quad (3.6)$$

The diffraction orders in the far field are given by the Fourier transform $T(\nu)$ of the transmission profile $\tau(x)$:

$$T(\nu) = \sum_{-\infty}^{+\infty} \tau_n \delta\left(\nu - \frac{n}{p}\right), \quad (3.7)$$

where ν is the spatial frequency and δ is the Dirac delta function. Each $\delta(\nu - n/p)$ is a displaced delta function that corresponds to a diffraction order n . The amplitude of each term is the n -th coefficient τ_n in the sum at Eq. 3.5. The intensity of each order is the square of the modulus of these amplitudes:

$$I_n = |\tau_n|^2.$$

Since the transmission profile of the linear phase grating (Eq. 3.2) contains a single complex exponential, it is evident from Eq. 3.7 that it will generate a single diffraction order, as depicted in Fig. 3.1(a).

Phase gratings that generate a desired number of diffraction orders with the same intensity have been widely studied in literature [28]. For instance, binary phase gratings where the zones of the two phase values are equal have proven to provide two or three equi-energetic orders. When there is a phase difference of π between the two values, they generate two equally intense orders with ideally 40.5% of the intensity of the input light for each order. This results in a diffraction efficiency (ratio between the intensity of the input light and the intensity of the desired orders) η of $\eta = 81\%$. On the other hand, when the phase difference is 0.630π they are able to generate a triplicator, i.e., three diffraction orders with the same intensity. The diffraction efficiency of this triplicator is $\eta = 86\%$ [27]. A different approach are Dammann gratings [29]. These are binary phase gratings with a phase difference of π where the transition points are selected to generate different equi-intense orders. Although they are able to generate more than three

diffraction orders with the same intensity, their efficiency as a triplicator is only of $\eta = 66.42\%$. Other different profiles can be calculated to generate a grating with arbitrary content of diffraction orders [30], [31].

In 1998, F. Gori et al. derived the phase profile of the optimal phase triplicator [32]. This profile is continuous, thus it is much more difficult to implement than binary profiles. Nevertheless, it provides the maximum diffraction efficiency that can be achieved when generating three equi-energetic orders with a scalar phase function. The phase function of the optimal triplicator is

$$\varphi_{trip}(x) = \arctan \left[a \cos \left(\frac{2\pi x}{p} \right) \right], \quad (3.8)$$

where $a = 2.65718\dots$. This function is depicted in Fig. 3.3(b) together with the phase function of a linear grating of the same period (3.3(a)). The energy contained in the three main orders $n = 0, +1, -1$ is the 92.56% of the incoming energy. Therefore, using Eq. 3.5, the transmission can be approximated as the three main orders of its Fourier expansion:

$$\tau_{trip}(x) = e^{i\varphi_{trip}(x)} \approx \tau_0 + \tau_{+1}e^{i2\pi x/p} + \tau_{-1}e^{-i2\pi x/p}, \quad (3.9)$$

where τ_0 , τ_{+1} and τ_{-1} are the Fourier expansion coefficients for the 0, +1 and -1 orders, respectively. These coefficients are given by Eq. 3.6. The square of their modulus gives the intensity of each order: $|\tau_0|^2 = |\tau_{+1}|^2 = |\tau_{-1}|^2 = 30.85\%$.

In general, the coefficients τ_n are complex numbers. While their modulus gives the intensity of the order, the argument gives the phase. Using Eqs. 3.9 and 3.6 it can be shown that there is a $\pi/2$ phase difference between the 0 and the ± 1 orders:

$$\tau_{+1} = \tau_{-1} = i\tau_0. \quad (3.10)$$

In most of the cases, only the intensity is of interest. However, as we demonstrated in the work "Optimal triplicator design applied to a geometrical phase vortex grating" [33], this phase difference is essential to understand the polarization transformations that the optimal triplicator performs when it is implemented as a geometrical phase element (see subsection 3.2.2 for geometrical phase elements).

Figure 3.3 illustrates how a modification of the phase profile can be used to engineer the diffraction orders of the grating. The transformation of the linear phase profile, with phase values from 0 to 2π , to the optimal triplicator profile, can be viewed as a phase look-up table (LUT), i.e., a new phase function $\varphi'(\varphi(x, y))$, where its value at the (x, y) coordinates depends only on the value that the original phase function $\varphi(x, y)$ takes at that point.

In the same manner as the triplicator profile converts the single diffraction order of the linear grating into three equally-intense orders, the same phase LUT transformation can be applied to other phase-only functions to engineer the harmonic content of diffractive elements, provided that the phase values of the original function $\varphi(x, y)$ are evenly distributed [34]. Therefore, if $\tau'(x, y) = e^{i\varphi'(\varphi(x, y))}$ represents the phase DOE with a modified phase profile, it can be expanded as:

$$\tau'(\varphi(x, y)) = \sum_{-\infty}^{+\infty} \tau'_n e^{in\varphi(x, y)}, \quad (3.11)$$

where

$$\tau'_n = \frac{1}{2\pi} \int_0^{2\pi} \tau'(\varphi(x, y)) e^{-in\varphi} d\varphi. \quad (3.12)$$

Given the periodicity 2π of the phase modulation, the coefficients τ'_n in the last equation take the same form as those in Eq. 3.6 for a grating with the phase profile associated to the $\varphi'(\varphi(x, y))$ LUT function.

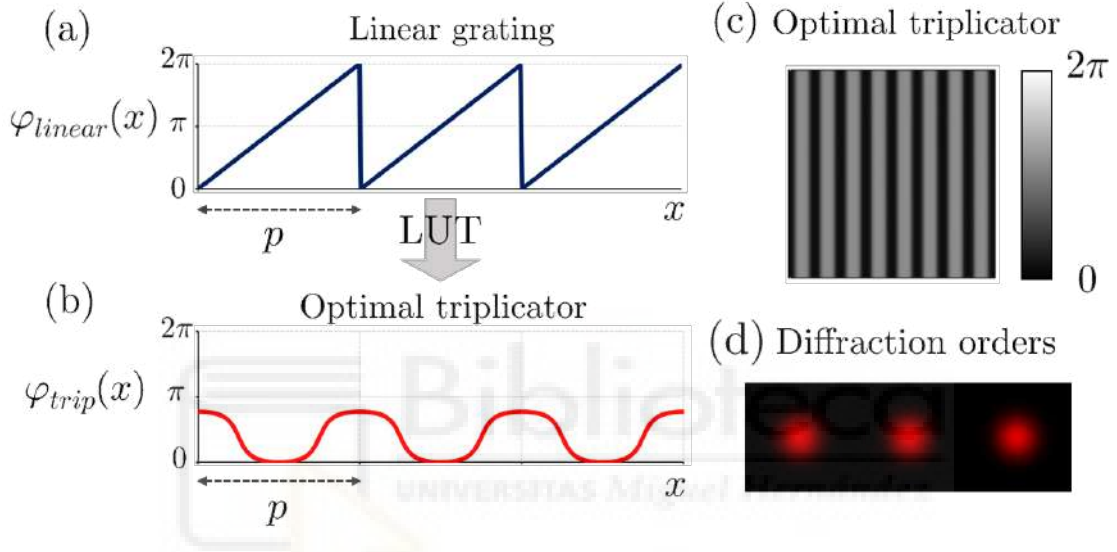


Figure 3.3: Phase profile from 0 to 2π of (a) the linear grating and (b) the optimal triplicator. (c) Optimal triplicator phase function as a gray-level image. (d) Diffraction pattern generated by the optimal triplicator.

An illustrative example is depicted in Fig. 3.4 for a forked grating and the triplicator profile. The original forked grating is given by the phase function $\varphi(x, y) = \ell\theta + 2\pi x/p$, as shown in Fig. 3.4(a). This grating generates a single $n = +1$ order with a vortex beam with topological charge ℓ . Figure 3.4(b) shows the modified forked grating with a new phase obtained after the phase LUT is applied to the phase function $\varphi(x, y)$. Note how the forked phase pattern in Fig. 3.4(b) resembles the triplicator profile in Fig. 3.3(c), but with the fork shape at the center of the pattern. Using Eq. 3.11, the transmittance pattern of the forked optimal triplicator grating is obtained from the phase $\varphi(x, y) = \ell\theta + 2\pi x/p$ of the forked grating as

$$\tau_{trip-fork}(x, \theta) = \text{LUT} [\tau_{fork}(x, \theta)] = \sum_{-\infty}^{+\infty} \tau_n e^{in(\ell\theta + 2\pi x/p)}. \quad (3.13)$$

Since the triplicator profile has been applied, most of the energy (92.56%) is concentrated on the $n = 0, \pm 1$ terms, so the transmission profile of the forked optimal triplicator grating can be approximated as

$$\tau_{trip-fork}(x, \theta) \approx \tau_0 [1 + ie^{i(\ell\theta+2\pi x/p)} + ie^{-i(\ell\theta+2\pi x/p)}], \quad (3.14)$$

where we used the relation $\tau_{+1} = \tau_{-1} = i\tau_0$. Each term in the above sum corresponds to a diffraction order. So, the diffraction pattern contains three diffraction orders $n = 0, \pm 1$, but they have different topological charges. While the order $n = +1$ maintains the original charge ℓ , the orders $n = 0$ and $n = -1$ have topological charges 0 and $-\ell$, respectively. Therefore, the central order does not show a vortex, while the lateral orders show vortices with opposite topological charge.

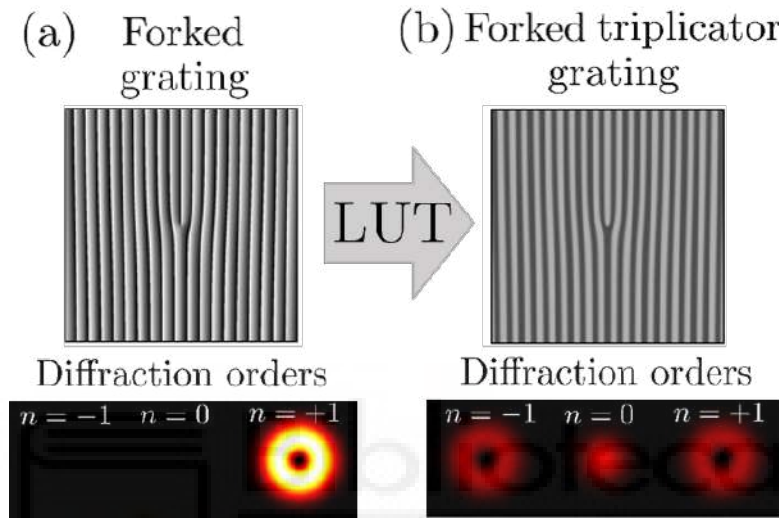


Figure 3.4: (a) Forked grating with topological charge $\ell = +1$. (b) Forked optimal triplicator grating obtained through a look-up table (LUT).

3.2 Implementation of diffractive optical elements

Once the phase DOE is designed, the next step is its correct implementation on a physical substrate. A recent work [35] suggests four technological generations for this implementation, depending on the optical property of the material that is modified. The first generation employed a physical variation of the thickness of a plate to produce the phase variations. The second generation is based on a modification of the refractive index. In this thesis, we used the third and fourth generations described in [35]. The third one is based on anisotropic liquid-crystal (LC) *spatial light modulators* (SLMs), where the effective extraordinary index can be modified at different pixels in a voltage controlled way [36]. Finally, the fourth generation for DOE implementation is based on micro-retarder elements, where the orientation of the fast axis of each microretarder can be controlled [37], and, in some cases, the retardance too [38]. These elements are named as *geometrical phase DOEs* or *Pancharatnam-Berry DOEs*. The optical response of these last two methods depends on the polarization of the input light. Therefore, they introduce new degrees of freedom compared to the two first generations of DOE fabrication methods, which are pure scalar diffractive elements.

3.2.1 Spatial light modulators

Spatial light modulators are optoelectronic microdisplays, where the size and number of pixels allow the implementation of DOEs [39]. Two main SLM technologies compete nowadays: Liquid-crystal SLMs, and digital micromirror devices (DMDs). Liquid-crystal technology is very useful since it is capable to directly provide phase modulation. However, it typically presents very limited refresh rates, and threshold intensity limit. On the other hand, DMDs are very fast devices, and are able to resist high power. Nevertheless, they are typically limited to binary amplitude modulation, and some kind of encoding technique is required to encode phase modulation. This dramatically reduces their efficiency to display DOEs.

In this thesis, we have used parallel-aligned liquid crystal on silicon (LCOS) SLMs. Fig. 3.5 shows a simplified scheme of this type of SLM. These are pixelated liquid-crystal linear retarders with homogeneous alignment and its optic axis along the same direction at every point, as the ones we described in subsection 2.2.3. The liquid-crystal layer is embeded between a transparent electrode and a pixelated electrode layer. As a consequence, the effective birefringence, and therefore, the retardance, can be adjusted independently at each pixel by applying a voltage between the electrodes.

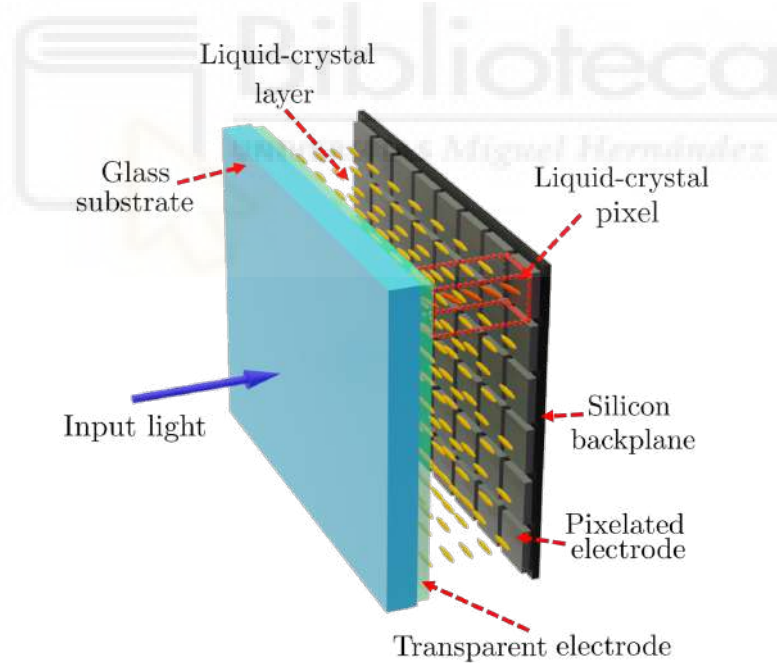


Figure 3.5: Simplified scheme of a liquid crystal on silicon (LCOS) spatial light modulator (SLM).

A SLM with its optic axis aligned along the x direction can be described as a linear retarder where its retardance $\varphi(x, y)$ is a function that changes with the spatial coordinates x and y :

$$\mathbf{M}_{SLM} = e^{i\varphi_0} \left(e^{i\varphi(x,y)} |x\rangle \langle x| + |y\rangle \langle y| \right), \quad (3.15)$$

where φ_o is the ordinary phase, and the retardance is $\varphi(x, y) = \varphi_e(x, y) - \varphi_o$, where $\varphi_e(x, y)$ is the extraordinary phase. As in tunable liquid-crystal retarders, the effective phase $\varphi_e(x, y)$ of the linear polarization component parallel to the liquid crystal (LC) director (extraordinary axis) can be varied by applying a voltage, while the phase for the orthogonal component φ_o (ordinary axis) remains unchanged. Therefore, we can change the retardance $\varphi(x, y)$ through a variation in the extraordinary phase $\varphi_e(x, y)$ (which we chose to be along the x axis in Eq. 3.15). Since we can select the retardance between two polarization components at each pixel, we can use SLMs for generating patterns where the polarization changes at each point. In addition, if we illuminate the SLM with a state of polarization $|x\rangle$, the light will gain a global phase function $\varphi(x, y)$. So, SLMs can be employed to implement pure phase diffractive optical elements for an input state $|x\rangle$.

Contrary to the liquid-crystal retarders described in subsection 2.2.3, LCOS SLMs are reflective devices. The light enters the SLM, passes through the LC layer and is reflected at a highly reflective mirror placed before the pixelated electrode layer, which we did not show in Fig. 3.5 for the sake of simplicity. After being reflected, the light passes again through the liquid-crystal layer and exits the device. Therefore, the retardance $\varphi(x, y)$ in Eq. 3.15 is twice the value provided by the liquid-crystal layer.

This ideal behavior of LCOS SLMs as pixelated pure retarder mirrors is actually affected by several secondary effects that degrade their response as DOE. The main aspects to consider are the phase fluctuation originated by flicker, the cross-talk between pixels (known as the fringing effect), and the backplane deformation that can introduce severe aberrations. Figure 3.6 depicts the deformation of the silicon backplane of an SLM. This last effect has been studied in the one of the work of this thesis: "Measuring the spatial deformation of a liquid-crystal on silicon display with a self-interference effect" [40].

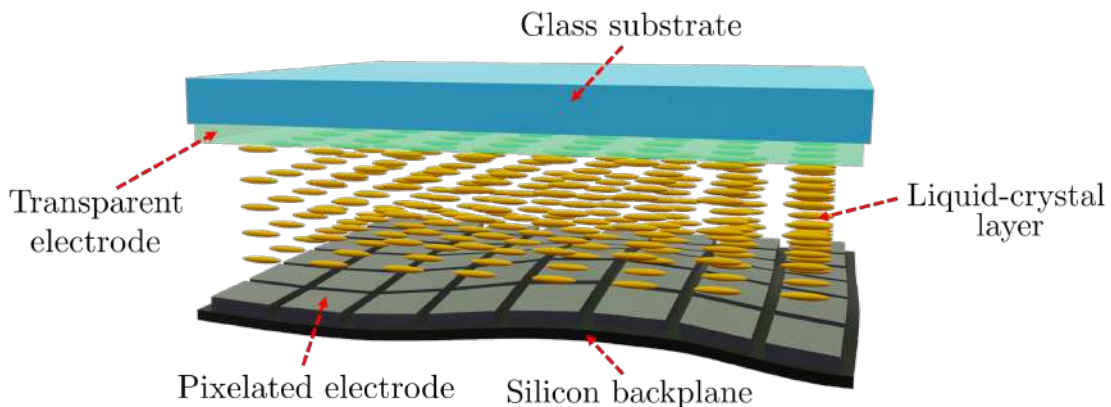


Figure 3.6: Liquid crystal on silicon (LCOS) spatial light modulator (SLM) simplified scheme with a silicon backplane deformation.

3.2.2 Geometrical Phase Elements. The q -plate

As we mentioned in subsection 2.2.2, the equation of a linear retarder with ϕ retardance and γ orientation with respect to the x axis is

$$\mathbf{M}_{WP}(\phi, \gamma) = \cos\left(\frac{\phi}{2}\right) \mathbf{I} + i \sin\left(\frac{\phi}{2}\right) \mathbf{Q}(\gamma), \quad (3.16)$$

where \mathbf{I} is the identity matrix and

$$\mathbf{Q}(\gamma) = e^{-i2\gamma} |R\rangle \langle L| + e^{i2\gamma} |L\rangle \langle R| \rightarrow \begin{pmatrix} \cos 2\gamma & \sin 2\gamma \\ \sin 2\gamma & -\cos 2\gamma \end{pmatrix}, \quad (3.17)$$

where the last matrix is expressed in the $\{|x\rangle, |y\rangle\}$ basis. When the retarder is a half-wave plate, i.e., $\phi = \pi$, the matrix of the retarder $\mathbf{M}_{WP}(\phi, \gamma)$ is directly given by $\mathbf{Q}(\gamma)$ (up to a global i phase factor). Now, consider the matrix $\mathbf{Q}(\gamma)$ acting over two different states describing right-circularly polarized light (RCP) $|R\rangle$ and left-circularly polarized light (LCP) $|L\rangle$. The resulting states are

$$\mathbf{Q}(\gamma) |R\rangle = e^{i2\gamma} |L\rangle, \quad (3.18)$$

$$\mathbf{Q}(\gamma) |L\rangle = e^{-i2\gamma} |R\rangle. \quad (3.19)$$

From these equations, we deduce that when RCP passes through a half-wave plate it turns into LCP and gains a global phase 2γ , which is twice the orientation of the principal retarder axis. Alternatively, RCP gains a global phase of -2γ and turns into LCP.

This effect has been exploited to impart global spatially variant phase functions to circularly polarized light by means of the so-called *geometrical phase (GP) elements*, also named *Pancharatnam-Berry elements*. These elements are linear retarders that present a spatial variation of the principal axis orientation γ across its transverse plane [35], [37]. Since the function that circularly polarized light gains when passes through a half-wave retarder is twice the orientation of γ , the GP element axes distribution can be designed according to the desired phase function $\varphi(x, y)$ that we want to impart to a beam. Concretely, the distribution of γ is designed to be $\gamma(x, y) = \varphi(x, y)/2$. Therefore, the operator describing a geometrical phase element can be obtained by regarding the orientation angle γ of the linear retarder as a spatial function $\gamma(x, y)$ that implements a phase function $\varphi(x, y)/2$:

$$\mathbf{M}_{GP}(\phi, \varphi(x, y)) = \cos\left(\frac{\phi}{2}\right) \mathbf{I} + i \sin\left(\frac{\phi}{2}\right) \mathbf{Q}(\varphi(x, y)), \quad (3.20)$$

where

$$\begin{aligned} \mathbf{Q}_{GP}(\varphi(x, y)) &= e^{-i\varphi(x, y)} |R\rangle \langle L| + e^{i\varphi(x, y)} |L\rangle \langle R| \\ &\rightarrow \begin{pmatrix} \cos \varphi(x, y) & \sin \varphi(x, y) \\ \sin \varphi(x, y) & -\cos \varphi(x, y) \end{pmatrix}. \end{aligned} \quad (3.21)$$

From now on we consider that the retardance of the device is always set to π , so it is described by the matrix $\mathbf{Q}_{GP}(\varphi(x, y))$. When this matrix acts over circularly polarized light, the resulting states are:

$$\mathbf{Q}(\varphi(x, y)) |R\rangle = e^{i\varphi(x, y)} |L\rangle, \quad (3.22)$$

$$\mathbf{Q}(\varphi(x, y)) |L\rangle = e^{-i\varphi(x, y)} |R\rangle. \quad (3.23)$$

As a consequence, each circular component is turned into its orthogonal and both gain a global phase function $\varphi(x, y)$ with opposite sign.

Following this procedure, any of the above mentioned phase profiles can be implemented as a geometrical phase element. For instance, Fig. 3.7 shows a linear grating implemented as a liquid-crystal geometrical phase element. Since the phase that RCP and LCP polarization gain are equal but opposite in sign, the circular components of an input linearly polarized beam are diffracted in opposite angles. The LCP component of the beam is transformed into RCP and gains a phase $-\varphi_{linear}(x)$, so it is sent to the -1 order, while the RCP component is transformed into LCP and gains a phase $\varphi_{linear}(x)$, so is sent to the $+1$ order.

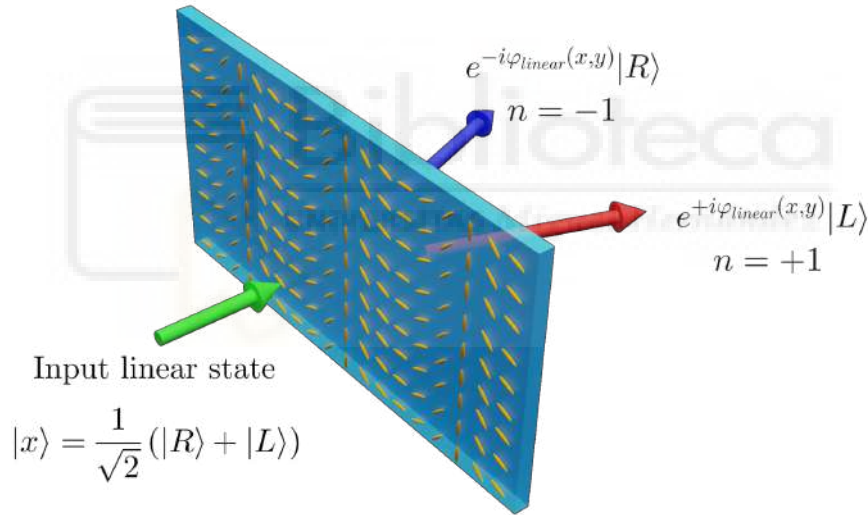
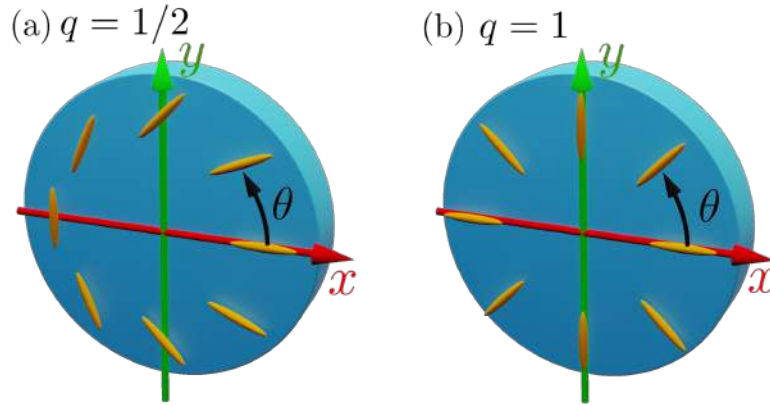


Figure 3.7: Geometric-phase linear grating scheme.

A geometrical phase element that we have studied in this thesis is the q -plate [41], [42]. These are plates where the optic axis orientation γ continuously follows q times the azimuthal coordinate θ . Therefore, they have a spiral phase function of topological charge $\ell = 2q$ implemented. Figure 3.8 depicts two examples of liquid-crystal q -plates with $q = 1/2$ (a), and $q = 1$ (b), so they generate vortices with charge $\ell = \pm 1$ and $\ell = \pm 2$, respectively. From Eqs. 3.22 and 3.23 it is straightforward that the LCP component of an input beams is turned into RCP and gains a spiral phase of $-2q\theta$ when passing through a q -plate. Conversely, RCP light is converted into LCP and gains a spiral phase of $2q\theta$.

If the input state is a linear combination of RCP and LCP, the q -plate generates a beam with a spatially variant polarization pattern along the θ coordinate. Beams that have a polarization pattern that spatially changes are called *vector*


 Figure 3.8: Q -plate with (a) $q = 1/2$ and (b) $q = 1$.

beams. Let us consider an elliptical state in the circular basis whose polarization ellipse has an orientation ψ and ellipticity angle $\pi/4 - \chi$:

$$|E\rangle = \cos \chi e^{-i\psi} |R\rangle + \sin \chi e^{+i\psi} |L\rangle \quad (3.24)$$

passing through a q -plate with $\phi = \pi$. The resulting state is obtained by making Eq. 3.21, for the function $\varphi(x, y) = 2q\theta$, act over the above state:

$$|E\rangle = \cos \chi' e^{-i\psi'(\theta)} |R\rangle + \sin \chi' e^{+i\psi'(\theta)} |L\rangle. \quad (3.25)$$

The output state is written in terms of the ellipticity angle $\pi/4 - \chi'$, where $\chi' = \pi/2 - \chi$, and the orientation $\psi'(\theta) = 2q\theta - \psi$ of its polarization ellipse. We deduce from the above equation that, for a given input state, the output state will have the same ellipticity χ' at every point. Nevertheless, its orientation $\psi'(\theta)$ is a linear function of the azimuthal coordinate θ . The orientation follows $2q$ times the polar coordinate, and it starts to sweep the coordinate ($\theta = 0$) with an initial orientation of $-\psi$. Figure 3.9 depicts several vector beams in the far field generated by a q -plate with $\phi = \pi$. Notice that, since both circular components carry opposite spiral phases but with the same absolute value, we obtain in all cases the ring-shaped intensity profile characteristic of the optical vortices with topological charge $\ell = \pm 2q$.

Figures 3.9(a)-(c) show vector beams generated with a q -plate with $q = 1/2$, so the orientation of their polarization ellipses directly follows the azimuthal coordinate. Figures 3.9(a),(b) correspond to a linearly polarized input state $\chi = \pi/4$. In this situation, the polarization map of the resulting vector beam only presents linear states. If, in addition, we consider that the orientation of the input state is $\psi = 0$, i.e., an input $|x\rangle$ state, then the orientation of the ellipse at $\theta = 0$ is $\psi' = 0$, and the resulting linear states follow a radial pattern, as shown in Fig. 3.9(a). Conversely, if $\psi = \pi/2$, the orientation at $\theta = 0$ is $\psi' = -\pi/2$, so every ellipse in this pattern (Fig. 3.9(b)) is $-\pi/2$ radians rotated with respect to the radial pattern. Figure 3.9(c) shows the vector beam generated when the input state is elliptical. As expected, the ellipses have the same ellipticity at every point, but its orientation changes with the polar coordinate. A last example is shown in Fig.

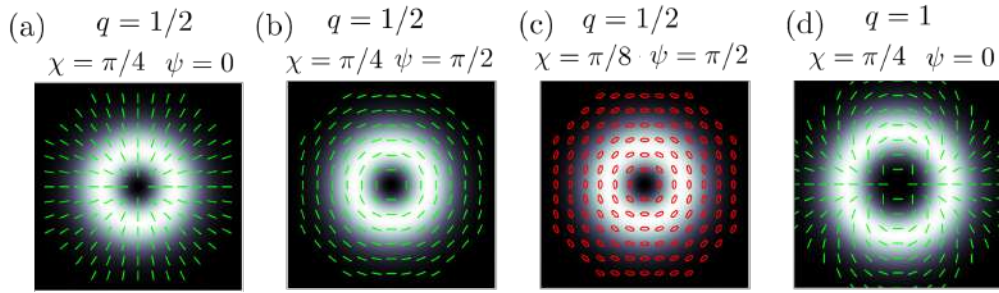


Figure 3.9: Vector beams at the Fourier plane generated by a q -plate with (a)-(c) $q = 1/2$ and (d) $q = 1$. Linear states are depicted in green, while left-handed allipses are plotted in red.

3.9(d) for a q -plate with $q = 1$. In this case, the polarization ellipse sweeps twice the polar coordinate, and the intensity profile is a larger ring, since the vortices generated have a topological charge $\ell = \pm 2$.

It is worth mentioning that a liquid-crystal q -plate can be sandwiched between electrodes, so its retardance can be tuned out of π . In this situation, the identity term in Eq. 3.20 causes that part of the vector describing the incident light does not gain a spiral phase. As a consequence, the superposition of the transformed and non-transformed parts of the state generates more exotic polarization patterns, including *hybrid vector beams*, as we demonstrated in [43]. Hybrid vector beams are described in subsection 4.2.3 in the next chapter. In the work "Using birefringence colors to evaluate a tunable liquid-crystal q -plate" [7], we spectrally characterize a tunable liquid-crystal q -plate and relate its spectral retardance with the classical birefringence colors visible in linear retarders.

Chapter 4

Structured light

Light beams that exhibit a custom spatial distribution of intensity, phase, and polarization are commonly referred to as structured light beams [2], [44]. High-order Gaussian spatial modes with different polarizations can be combined to generate vector beams. These beams have a spatially varying polarization pattern across their transverse section. In this thesis, we generate high-order Gaussian modes and vector beams in the work "Efficient on-axis SLM engineering of optical vector modes" [45]. Therefore, we introduce in this chapter the mathematical description for this type of structured light beams, and we review several techniques to experimentally generate these spatial modes and vector beams.

4.1 High-order Gaussian modes

High-order Gaussian modes are solutions to the paraxial wave equation. Hermite-Gaussian and Laguerre-Gaussian modes are solutions in Cartesian and cylindrical coordinates, respectively. Laguerre-Gaussian beams have, in general, a spiral phase term, so they present helical wavefronts. In 1992, L. Allen et al. demonstrated that beams with helical wavefronts carry orbital angular momentum (OAM) [46]. These beams have been used in optical tweezers to make a particle spin through an orbital angular momentum transference [47].

In addition, beams with OAM have been proposed to increase the bandwidth of optical communications [48],[49]. This application is based on the idea that, since there is an infinite number of beams with different values of OAM, this infinite space can be exploited to encode information.

A noticeable property of Laguerre-Gaussian beams is that they have a ring-shaped transverse intensity profile with zero intensity at the center. This property has been used in STED (Stimulated Emission Depletion) microscopy [50]. The technique employs two lasers of a different wavelength. A first laser stimulates the fluorescence while a second laser inhibits it. Since the second laser has a doughnut-shaped intensity profile, it inhibits the fluorescence everywhere but in its central dark region. This effect has been proven to overcome the classical diffraction limit of resolution. A complete review of the applications of beams with OAM can be found in [51] and [52].

4.1.1 Hermite-Gaussian modes

Hermite-Gaussian modes are solutions to the paraxial wave equation in Cartesian coordinates. Their mathematical expression is given by the following equation [53]:

$$HG_{mn}(x, y, z) = \frac{A_{mn}}{\omega(z)} H_m\left(\frac{\sqrt{2}x}{\omega(z)}\right) H_n\left(\frac{\sqrt{2}y}{\omega(z)}\right) e^{-r^2/\omega(z)^2} e^{i[kr^2/2R(z) - \varphi_G^{mn}(z)]}, \quad (4.1)$$

where

$$A_{mn} = \sqrt{\frac{2^{1-m-n}}{\pi m! n!}} \quad (4.2)$$

is a normalization constant, and H_m and H_n are the m -th and n -th Hermite polynomials, respectively. These polynomials are obtained as a function of the spatial Cartesian coordinates x and y , and as a function of the beam's width $\omega(z)$:

$$\omega(z) = \omega_0 \sqrt{1 + \left(\frac{z}{z_R}\right)^2}, \quad (4.3)$$

The width $\omega(z)$ depends on the z coordinate. It also depends on ω_0 , which is the beam's width at the plane where it is focused ($z = 0$), namely its minimum width. The quantity ω_0 is known as the waist. The width $\omega(z)$ is also a function of the Rayleigh length $z_R = \pi\omega_0^2/\lambda$. The term

$$G = e^{-r^2/\omega(z)^2} \quad (4.4)$$

depends on the radial coordinate $r = \sqrt{x^2 + y^2}$, and it is the Gaussian envelope of the beam. The complex exponential

$$W_{mn} = e^{i[kr^2/2R(z) - \varphi_G^{mn}(z)]} \quad (4.5)$$

is a phase term. The first term in the sum inside the exponential is related with the curvature of the beam wavefront. The quantity

$$R(z) = z + \frac{z_R^2}{z} \quad (4.6)$$

is the radius of curvature. It turns out that the wavefront is plane at the waist ($z = 0$), so $R(z) = \infty$. Conversely, far from z_R , the radius of curvature becomes almost z , so the wavefront is spherical. The last term in the sum inside the complex exponential in Eq. 4.5 is:

$$\varphi_G^{mn}(z) = (m + n + 1)\varphi_G(z). \quad (4.7)$$

This phase depends on a quantity known as the Gouy phase:

$$\varphi_G(z) = \arctan(z/z_R), \quad (4.8)$$

which drives a π shift on the whole beam as it propagates from $-\infty$ to ∞ . It changes slowly far from the waist, but it does rapidly near the Rayleigh length. Figure 4.1 shows the transverse intensity and phase profiles at the waist ($z = 0$) for several Hermite-Gaussian modes with different indices m and n .

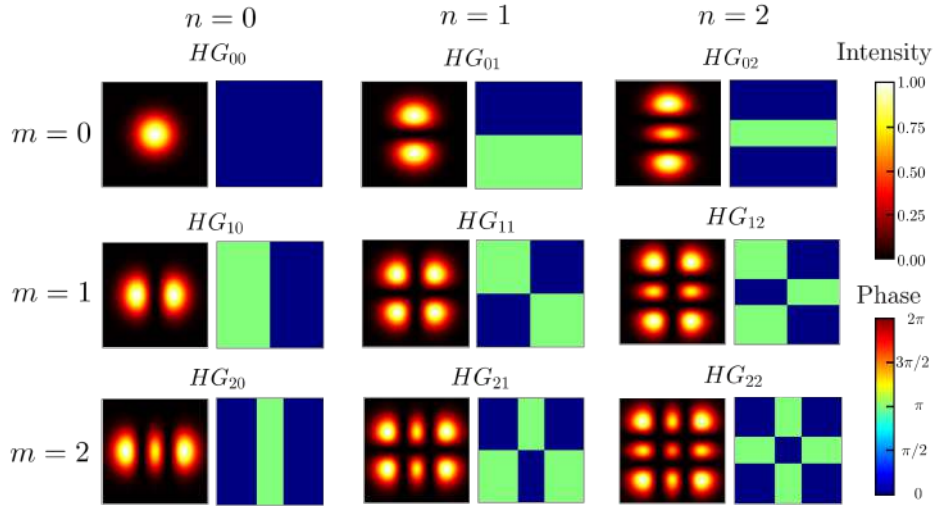


Figure 4.1: Transverse intensity and phase for the first Hermite-Gaussian modes at the waist ($z = 0$) with indices m (rows) and n (columns).

4.1.2 Laguerre-Gaussian modes

Laguerre-Gaussian modes are solutions to the paraxial Helmholtz equation in cylindrical coordinates. The Laguerre-Gaussian mode with radial index p and azimuthal index ℓ can be expressed as [53]

$$LG_p^\ell(r, \theta, z) = \frac{A_p^{|\ell|}}{\omega(z)} \left(\frac{\sqrt{2}r}{\omega(z)} \right)^{|\ell|} L_p^{|\ell|} \left(\frac{2r^2}{\omega^2(z)} \right) e^{-r^2/\omega(z)^2} e^{i[kr^2/2R(z) - \varphi_G^{p|\ell|}(z) + \ell\theta]}, \quad (4.9)$$

where $L_p^{|\ell|}(2r^2/\omega^2)$ are the generalized Laguerre polynomials evaluated at $2r^2/\omega^2$, and

$$A_p^{|\ell|} = p! \sqrt{\frac{2}{\pi p! (|\ell| + p)!}}$$

is a normalization constant. Analogously to the Hermite-Gaussian beams, the phase term contains information about the curvature and the Gouy phase:

$$W_{p|\ell|} = e^{i[kr^2/2R(z) - \varphi_G^{p|\ell|}(z)]}, \quad (4.10)$$

where

$$\varphi_G^{p|\ell|}(z) = (2p + |\ell| + 1)\varphi_G(z) \quad (4.11)$$

depends on the Gouy phase in Eq. 4.8. Furthermore, Laguerre-Gaussian beams contain a spiral phase term $\ell\theta$ that depends on the azimuthal coordinate θ . Now, let us consider that the radius of curvature is set to ∞ , i.e., the wavefront is plane. Therefore, as described in subsection 3.1.1 in the previous chapter, the wavefronts form a helicoid for $\ell = 1$, and several helicoids for greater values of ℓ . The term $\ell\theta$ causes a phase singularity at the center of the Laguerre-Gaussian beams for $|\ell| > 0$, as we show in Fig. 4.2. These beams are optical vortices with topological charge ℓ .

In this thesis, we mostly consider Laguerre-Gaussian beams with $p = 0$. In this situation, the Laguerre polynomials are 1, so the amplitude of the mode is proportional to $r^{|\ell|}$ (Eq. 4.9). If we also consider that $|\ell| > 0$, the intensity will decay towards the center of the beam until it reaches zero at $r = 0$, resulting in a doughnut-shaped intensity profile, as shown in Fig. 4.2. For $p > 0$, the Laguerre polynomials modulate the amplitude. As a consequence, the intensity profile present a set of concentric rings. Note that the intensity does not depend on the sign of ℓ .

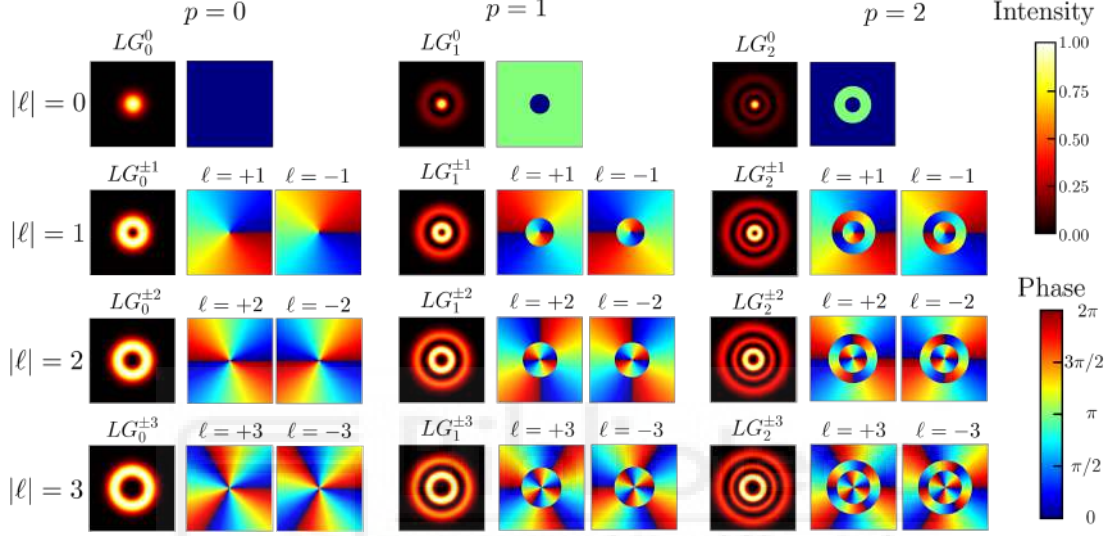


Figure 4.2: Transverse intensity and phase profile for several Laguerre-Gaussian modes at the waist ($z = 0$). The rows represent beams with the same modulus of the azimuthal number ℓ . The columns depict beams with constant radial number p .

4.1.3 First-order Gaussian modes superposition

There are infinite Hermite-Gaussian and Laguerre-Gaussian modes. Since, in addition, each set of modes form a complete basis, each family of modes can be expanded as a linear combination of the other [2]. In this thesis, we mainly focus on the first-order beams HG_{10} , HG_{01} , LG_0^{+1} and LG_0^{-1} . The HG_{10} and HG_{01} modes can be expressed as linear combinations of the LG_0^{+1} and LG_0^{-1} modes and vice versa following the derivation of E. Galvez in [53]. First, the HG_{10} and HG_{01} Hermite-Gaussian modes can be expressed as a function of the x and y coordinates using Eq. 4.1:

$$HG_{10} = CGWx, \quad (4.12)$$

$$HG_{01} = CGWy, \quad (4.13)$$

where C is

$$C = \frac{2\sqrt{2}}{\sqrt{\pi}\omega^2(z)}, \quad (4.14)$$

and the term G is given by Eq. 4.4. The quantity W is given by Eq. 4.5, and it is common for both modes since $W_{m=1n=0} = W_{m=0n=1} = W$.

On the other hand, the Laguerre-Gaussian modes LG_0^{+1} and LG_0^{-1} can be expressed in terms of the coordinates r and θ using Eq. 4.9:

$$LG_0^{\pm 1} = \frac{C}{\sqrt{2}} GW r e^{\pm i\theta}. \quad (4.15)$$

It is straightforward to deduce from Eq. 4.10 that the term W is the same as in the first-order Hermite-Gaussian modes above.

Using Eq. 4.12, 4.13 and 4.15 together with the fact that $x = r \cos \theta$, $y = r \sin \theta$ and Euler's identity, the modes $LG_0^{\pm 1}$ can be expressed as a linear combination of HG_{10} and HG_{01} :

$$LG_0^{\pm 1} = \frac{1}{\sqrt{2}} (HG_{10} \pm iHG_{01}). \quad (4.16)$$

In addition, the HG_{10} and HG_{01} beams can be expressed as

$$HG_{10} = \frac{1}{\sqrt{2}} (LG_0^{+1} + LG_0^{-1}), \quad (4.17)$$

$$HG_{01} = \frac{-i}{\sqrt{2}} (LG_0^{+1} - LG_0^{-1}). \quad (4.18)$$

These equations make clear the analogy between these modes and the linear $|x\rangle$, $|y\rangle$ and the circular $|R\rangle$, $|L\rangle$ polarization states. In fact, if we perform the substitutions $HG_{10} \rightarrow |x\rangle$, $HG_{01} \rightarrow |y\rangle$, $LG_0^{+1} \rightarrow |R\rangle$ and $LG_0^{-1} \rightarrow |L\rangle$ in the last three equations, we notice that modes HG_{10} and HG_{01} are related to the modes LG_0^{+1} and LG_0^{-1} in the same manner as the states $|x\rangle$ and $|y\rangle$ are related to $|R\rangle$ and $|L\rangle$ (Eqs. 2.12 and 2.13 in subsection 2.1.2).

Now consider a HG_{10} mode rotated by an angle ψ . Using $x = r \cos \theta$, $y = r \sin \theta$ and Euler's identity it can be shown that

$$HG_{10}(\psi) = \cos \psi HG_{10} + \sin \psi HG_{01} = \frac{1}{\sqrt{2}} (e^{-i\psi} LG_0^{+1} + e^{i\psi} LG_0^{-1}). \quad (4.19)$$

Therefore, a HG_{10} mode rotated by an angle ψ can be obtained as the linear superposition of the LG_0^{+1} and LG_0^{-1} modes with a phase difference of 2ψ between them. Again, the connection with polarization is evident: as we showed at the end of subsection 2.1.2, a phase difference of 2ψ between two equally-weighted circular components yields linear polarization rotated an angle ψ .

All these properties suggest we can make an analogy between the sum of these modes and the sum of polarization states following the expression of a Jones vector in the circular basis given by Eq. 2.19. As a result, the expression of a more general mode obtained as the superposition of LG_0^{+1} and LG_0^{-1} modes weighted by an angle χ and with 2ψ phase shift between them can be written as:

$$f(r, \theta, z) = \cos \chi e^{-i\psi} LG_0^{+1} + \sin \chi e^{i\psi} LG_0^{-1}, \quad (4.20)$$

Following the analogy with polarization states, analogous Stokes parameters that define a new Poincaré sphere have been derived for beams described by the above equation. This sphere is commonly referred to as the *Orbital Angular Momentum (OAM) Poincaré sphere*, which was proposed in 1998 by M. J. Padgett and J. Courtial [54]. The OAM sphere is depicted in Fig. 4.3. The HG_{10} and HG_{01} modes lie at antipodal points on the S_1 axis as the $|x\rangle$ and $|y\rangle$ states do in the standard Poincaré sphere. As expected, the HG_{01} mode rotated $\psi = \pi/4$ and $\psi = -\pi/4$ lies on the S_2 axis. All the rotated Hermite-Gaussian modes lie on the equator, as linear polarization states do in the regular Poincaré sphere. The two states LG_0^{+1} and LG_0^{-1} play the role of the circular polarizations, so they are on the S_3 axis at the poles. Finally, we show a state obtained as a non equally-weighted combination of the LG_0^{+1} and LG_0^{-1} modes. Note how its shape is between the shape of a Laguerre and a Hermite beam.

Infinite Poincaré spheres can be defined for the superposition of higher-order modes. As shown in [55] and [2], it is possible to define a sphere with two arbitrary $LG_p^{+\ell}$ and $LG_p^{-\ell}$ modes at the poles.

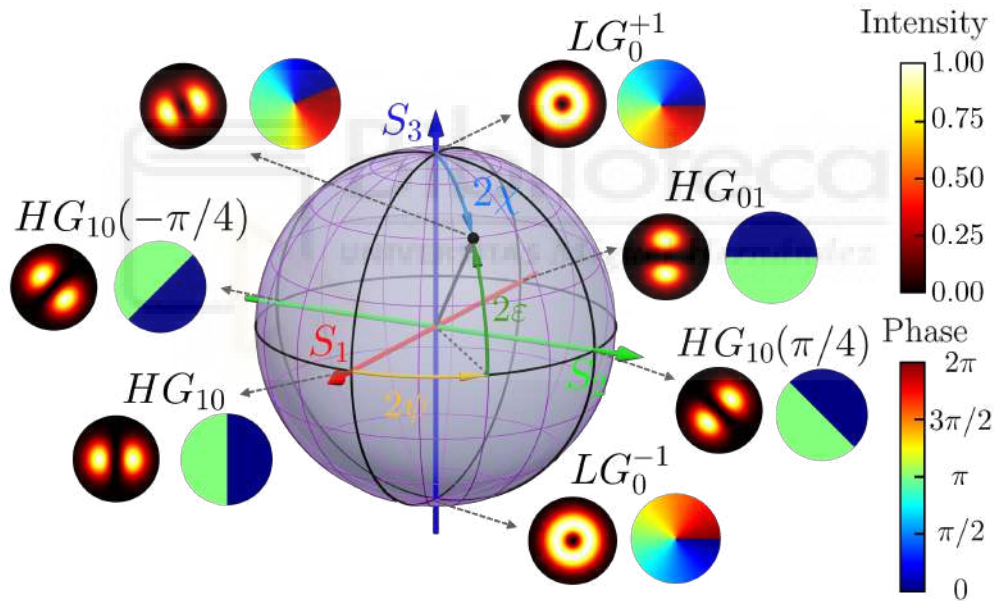


Figure 4.3: OAM Poincaré sphere. Each scalar mode is a point on the surface of the sphere. The intensity and phase for each mode are depicted.

4.1.4 Higher-order Laguerre-Gaussian modes superposition

In this subsection, we provide examples of combining higher-order order Laguerre-Gaussian modes, since we experimentally generate this type of beams in the work "Efficient on-axis SLM engineering of optical vector modes". We consider equally-weighted combinations of Laguerre-Gaussian beams described as

$$f = \frac{1}{\sqrt{2}} [LG_{p1}^{\ell_1} + e^{i\phi} LG_{p2}^{\ell_2}], \quad (4.21)$$

where ϕ is a relative phase between the components. Figure 4.4 shows the intensity profile at $z = 0$ for different combinations. For $p = 0$, the intensity profile of these beams consists of several lobes whose position can be derived by performing an approximation on the above equation. We consider that we are at the waist ($z = 0$), and we neglect the differences in the radial dependence of the two beams. Therefore, we only regard the interference of the spiral phases of each beam and their relative phase, which is enough to calculate the number of lobes and their positions for beams with $p = 0$. Then, a new beam f' can be defined, where we neglect the mentioned properties:

$$f' = e^{i\ell_1\theta} + e^{i\phi} e^{i\ell_2\theta} = e^{i(\ell_1+\ell_2/2)\theta} e^{i\phi/2} (e^{i(\ell_1-\ell_2/2)\theta} e^{-i\phi/2} + e^{-i(\ell_1-\ell_2/2)\theta} e^{i\phi/2}). \quad (4.22)$$

The square of the real amplitude of f' is proportional to the following quantity:

$$i_{f'} \propto \frac{1}{2} \{1 + \cos[(\ell_1 - \ell_2)\theta - \phi]\}. \quad (4.23)$$

The number of lobes is $n = |\ell_1 - \ell_2|$, since this quantity indicates the number of times that the cosine function reaches a maximum along the θ coordinate. For $\phi = 0$, the intensity is maximum for $\theta = 0$, so there is a lobe. Conversely, if $\phi = \pi$, the intensity is zero for $\theta = 0$. Therefore, ϕ rotates the lobe pattern. Figures 4.4(a) and 4.4(b) show the intensity profile of two LG_0^{-3} and LG_0^{-3} beams combined. The number of lobes is $n = |-3 - 3| = 6$. In Fig. 4.4(b), there is a phase difference of $\phi = \pi$ between the beams, which causes a rotation in the pattern. Figures 4.4(b) and 4.4(c) show the combinations $LG_1^{-3} + LG_0^{+8}$ and $LG_1^{-3} + LG_2^{+8}$, respectively. Note that these two last patterns present lobes with different shapes along the radial coordinate. Nevertheless, the number of lobes along the θ coordinate for a constant value of the radial coordinate is still $n = |\ell_1 - \ell_2|$, since it is determined by the relative azimuthal phase variation of the beams.

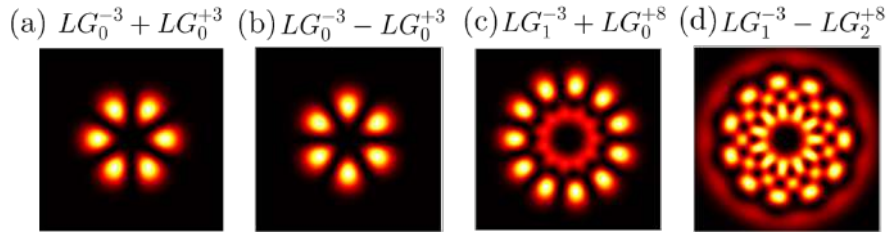


Figure 4.4: Intensity profiles for different combinations of Laguerre-Gaussian modes.

4.2 Vector beams

Beams with a spatial variation of the polarization state across their transverse section are known as vector beams. They have applications in several fields [1]. For instance, in laser material processing, vector beams with a radial linear polarization distribution have proven to provide a laser cutting efficiency larger than homogeneous polarized beams [56]. This is related to the fact that a strong longitudinal component of the field is generated when they are focused on a tiny area.

These beams also have been used for optical trapping, where they increased the axial trapping efficiency with respect to homogeneous polarized light [57]. In addition, they produce extremely narrow spots under tight focusing conditions [58]. Vector beams have also been suggested for optical communications, where the polarization patterns are regarded as information channels [59]. All these applications employ vector beams in the VIS or IR range. Recently extreme ultraviolet (EUV) vector beams in the form of ultrafast pulses have been proven by high-order harmonic generation in an infrared vector beam [60], thus opening potential applications in EUV lithography and ultrafast diffraction imaging.

Vector beams can be generated by adding two spatial modes with different polarizations so that the state cannot be expressed as the product of a mode and a polarization state. These types of states are said to be non-separable. A general form of a vector beam formed by the sum of two Laguerre-Gaussian modes with orthogonal polarizations $|a\rangle$ and $|a^\perp\rangle$ is

$$|V\rangle = \cos \beta e^{-i\varphi} LG_{p_1}^{\ell_1} |a\rangle + \sin \beta e^{i\varphi} LG_{p_2}^{\ell_2} |a^\perp\rangle, \quad (4.24)$$

where β controls the weight of each term in the sum and 2φ is their relative phase.

4.2.1 First-order Laguerre-Gaussian modes vector superposition

In this thesis, we restrict ourselves to a subset of vector beams built as the superposition of two modes LG_0^{-1} and LG_0^{+1} in two orthogonal polarizations. This type of beams are given by the following relation:

$$|V\rangle = \cos \beta e^{-i\varphi} LG_0^{-1} |a\rangle + \sin \beta e^{i\varphi} LG_0^{+1} |a^\perp\rangle. \quad (4.25)$$

This beam can be rewritten using Eq. 4.15 as a function of the radial r and azimuthal beam coordinates θ :

$$|V\rangle = \frac{CGWr}{\sqrt{2}} (\cos \beta e^{-i(\varphi+\theta)} |a\rangle + \sin \beta e^{i(\varphi+\theta)} |a^\perp\rangle). \quad (4.26)$$

Note that there is a global r term. As a result, vector beams expressed in this manner exhibit the characteristic doughnut shape of $LG_0^{\pm 1}$ modes. In addition, note that the polarization properties are contained in the term inside the parentheses. Therefore, for a given β and φ , the polarization at each point does not depend on the radial coordinate r , but only on the azimuthal coordinate θ . This means that points with the same θ coordinate have the same polarization state.

The most common type of vector beam is built using the circular basis:

$$|V\rangle = \cos \chi e^{-i\psi} LG_0^{-1} |R\rangle + \sin \chi e^{i\psi} LG_0^{+1} |L\rangle, \quad (4.27)$$

where we changed the symbol β by χ and φ by ψ . Let us recall that the angles represent the same thing, we only changed their symbols. We did this because, when using the circular basis, the orientation and ellipticity of the ellipses in the polarization patterns are determined by ψ and χ in Eq. 4.27, respectively, and

these are the greek letters we used in subsection 2.1.3 for the orientation (ψ) and ellipticity angle ($\pi/4 - \chi$) parameters of the ellipse. We will next explain the polarization patterns that these beams exhibit across its transverse section. For this purpose, it is convenient to rewrite the latter equation using Eq. 4.15:

$$|V\rangle = \frac{CGWr}{\sqrt{2}} (\cos \chi e^{-i(\psi+\theta)} |R\rangle + \sin \chi e^{i(\psi+\theta)} |L\rangle). \quad (4.28)$$

For $\theta = 0$, the term inside the parentheses is the equation of a polarization state expressed in the circular basis with orientation ψ and ellipticity angle $\pi/4 - \chi$ (Eq. 2.19 in subsection 2.1.2). So, the state will lie on the surface of the Poincaré sphere with azimuth 2ψ and a polar angle 2χ . Now, consider that we slightly move along the beam coordinate θ . The coordinate θ is added to the phase ψ inside the complex exponentials in Eq. 4.28. Therefore, a change in θ is equivalent to a change in ψ . This means that, as we move along θ in the transverse section of the beam, we are moving on the Poincaré sphere along the circumference defined by a plane perpendicular to the axis that passes through the points $|R\rangle$ and $|L\rangle$. As explained in subsection 2.1.3, this plane is defined by χ . Note that the polarization ellipses for all points with the same χ have the same ellipticity. Figure 4.5 shows different paths for several values of χ that correspond to distinct vector beams. The quantity χ defines a parallel on the sphere that sets the polarization pattern of the vector beam. As we move along the coordinate θ of the beam, we move along this parallel on the Poincaré sphere.

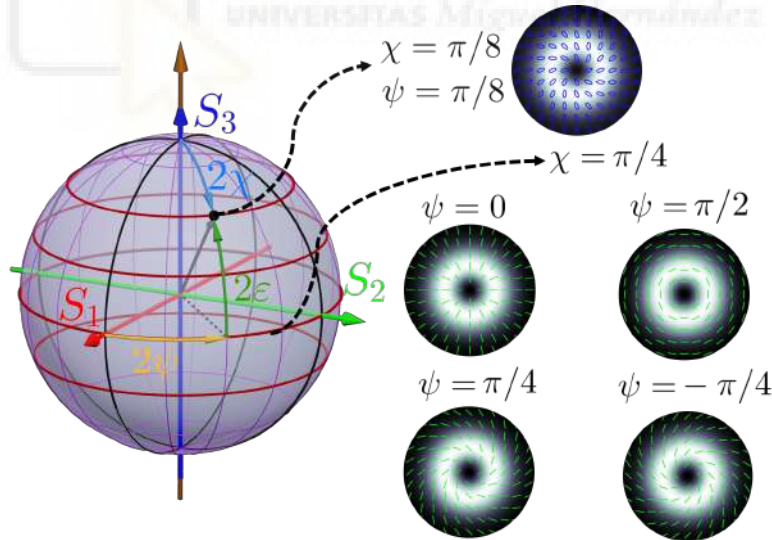


Figure 4.5: Depiction of the polarization patterns along the azimuthal coordinate θ of the vector beams in Eq. 4.27 as paths on the Poincaré sphere. The paths for different values of χ are depicted in reddish brown. Linear polarization is depicted in green. Right-handed ellipses are shown in blue.

In addition, an infinite set of vector beams can be obtained for each value of χ , i.e., for each parallel. This is because the point on the sphere where we start to sweep the parallel when increasing θ is given by ψ : the angle ψ is the orientation

of the polarization ellipse at $\theta = 0$. As we increase θ , the orientation of the ellipse is $\psi + \theta$. Figure 4.5 also shows different vector beams obtained for several values of ψ for each parallel. For $\chi = \pi/4$, we are sweeping the equator of the sphere, therefore, all the polarization states have zero ellipticity, i.e., they are linear states. The point where we start to sweep the parallel is given by the angular coordinate 2ψ , and defines the polarization at $\theta = 0$. For $\psi = 0$, we start at the $|x\rangle$ state at $\theta = 0$, so the orientation of the ellipse for a θ azimuthal coordinate is just θ . This vector beam presents a *radial* distribution of the polarization. For $\psi = \pi/2$ we start at $|y\rangle$, and the orientation of the ellipse is given by $\pi/2 + \theta$. This beam is known as *azimuthal*. Alternatively, for $\psi = \pm\pi/4$, the polarization at $\theta = 0$ is $|45^\circ\rangle$ and $|-45^\circ\rangle$, respectively, so we obtain the so called *slanted* and *anti-slanted* vector beams.

Equation 4.27 shows that each vector beam of this form is defined by two angles: χ and ψ . It was shown above that, to define a vector beam of this family, we only need to locate a parallel on the Poincaré sphere given by the angular coordinate 2χ , and identify the point given by the angular coordinate 2ψ where we start to sweep the parallel for $\theta = 0$. This suggests that it is possible to define a new Poincaré sphere where each point with coordinates 2χ and 2ψ corresponds to a vector beam. This sphere is known as the *higher-order Poincaré sphere* [61], and it is depicted in Fig. 4.6.

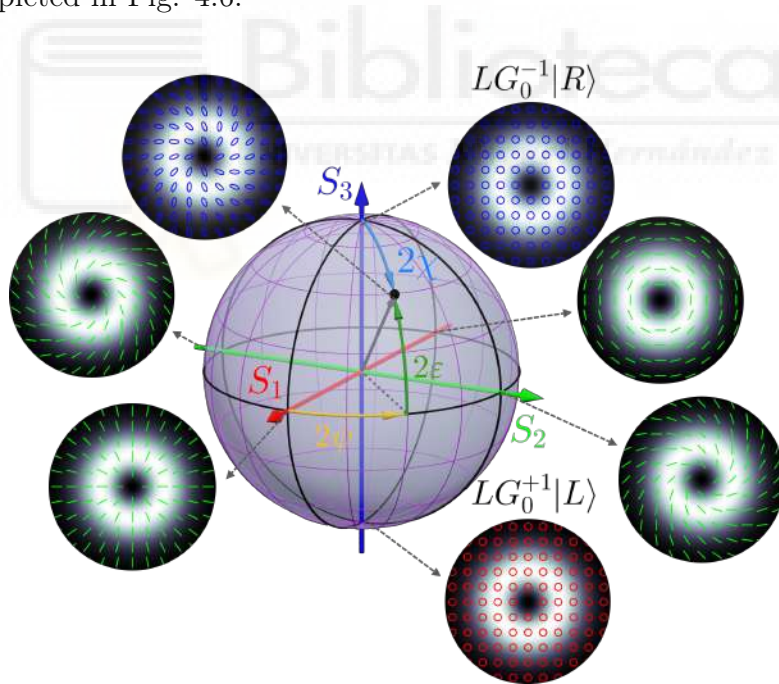


Figure 4.6: Higher-order Poincaré sphere for the vector beam in Eq. 4.27 obtained from the superposition of Laguerre-Gaussian modes in the states $|R\rangle$ and $|L\rangle$. Linear polarization is depicted in green. Right-handed and Left-handed ellipses are blue and red, respectively.

The circularly polarized modes LG_0^{-1} and LG_0^{+1} lie at the poles. Therefore, as expected from Eq. 4.27, we have a single right-circularly polarized mode LG_0^{-1} for $\chi = 0$ and a left-circularly polarized mode LG_0^{+1} for $\chi = \pi/2$. The equally-

weighted superposition of these modes ($\chi = \pi/4$) results in linear vector beams lying on the sphere equator. The radial and azimuthal vector beams are on the S_1 axis playing the role of the $|x\rangle$ and $|y\rangle$ states in the regular Poincaré sphere, respectively. On the other hand, the slanted and anti-slanted beams lie on the S_2 axis, analogously to $|-45^\circ\rangle$ and $|45^\circ\rangle$. As in the regular Poincaré sphere, antipodal points on the higher-order sphere represent orthogonal states. In addition, any state on the sphere can be obtained as a linear superposition of two orthogonal states that also belong to the sphere.

It is worth mentioning that, if the Laguerre-Gaussian modes in Eq. 4.27 are exchanged ($LG_0^{+1} \rightarrow LG_0^{-1}$ and $LG_0^{-1} \rightarrow LG_0^{+1}$), now the sign of θ in Eq. 4.28 is flipped. As a result, the orientation of the ellipse in the polarization patterns rotates in the opposite azimuthal direction. These new vector beams also define a different Poincaré sphere, as shown in [61].

Consider that we choose a different basis in Eq. 4.25. For instance, the $|x\rangle$ and $|y\rangle$ basis, thus obtaining vector beams of the form

$$|V\rangle = \cos \alpha e^{-i\delta/2} LG_0^{-1} |x\rangle + \sin \alpha e^{i\delta/2} LG_0^{+1} |y\rangle. \quad (4.29)$$

As we did for the circular basis, we have changed the symbols β and φ by the symbols α and $\delta/2$ that we chose in subsection 2.1.2 in Eq. 2.8 to express a polarization state in the $\{|x\rangle, |y\rangle\}$ basis. In subsection 2.1.2, the angle α described the relative amplitude between the $|x\rangle$ and $|y\rangle$ components, while δ is the phase difference between them. Following the procedure for the circular basis, we next show the paths that these beams describe on the Poincaré sphere. We rewrite the above equation using Eq. 4.15:

$$|V\rangle = \frac{CGWr}{\sqrt{2}} (\cos \alpha e^{-i(\theta+\delta/2)} |x\rangle + \sin \alpha e^{i(\theta+\delta/2)} |y\rangle). \quad (4.30)$$

Again, the term inside the parentheses contains all the information about the polarization map. If we set $\theta = 0$, we see that the polarization state will lie on a circumference defined by a plane perpendicular to the axis passing through the $|x\rangle$ and $|y\rangle$ points on the Poincaré sphere. The plane is determined by 2α . Analogously to the circular case, now the angle δ determines the point where we start to sweep the circumference. So, for $\alpha = \pi/4$, the circumference is on the $S_1 = 0$ plane, as shown in Fig. 4.7.

A higher-order Poincaré sphere has also been defined for this type of vector beams. Figure 4.8 shows this sphere, where the linearly polarized Laguerre-Gaussian modes are at the poles. At the equator, we have an equally-weighted superposition of $LG_0^{-1} |x\rangle$ and $LG_0^{+1} |x\rangle$ states. Note that the angles 2α and δ play the role of the spherical coordinates on the higher-order sphere in Fig. 4.8. However, in the regular Poincaré sphere (Fig. 4.7), 2α and δ are a rotated version of the spherical coordinates 2χ and 2ψ .

We have just shown that, depending on the $|a\rangle$ and $|a^\perp\rangle$ base vectors that we choose in Eq. 4.25, different families of vector beams are obtained, which can be represented on a higher-order Poincaré sphere. We can extend the reasoning that we followed for the linear and circular basis to any elliptical basis. Equation

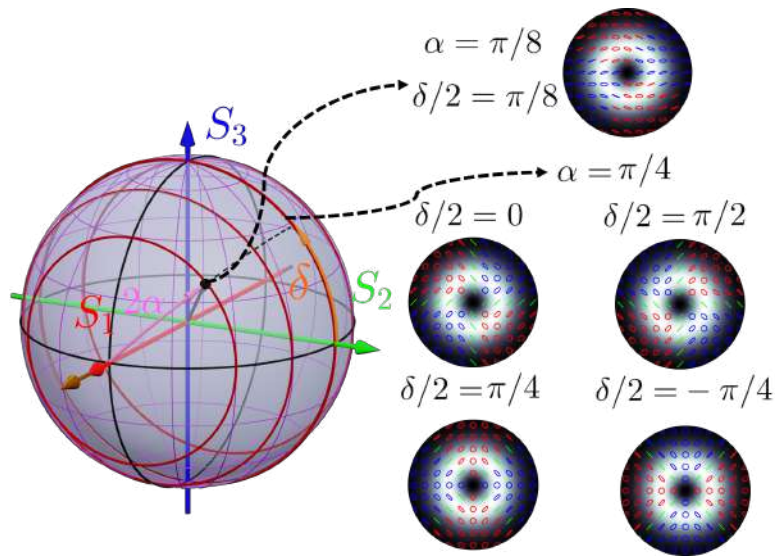


Figure 4.7: Depiction of the polarization patterns along the azimuthal coordinate θ of the vector beams in Eq. 4.29 as paths on the Poincaré sphere. The paths for different values of α are depicted in reddish brown. Linear polarization is depicted in green. Right-handed and Left-handed ellipses are blue and red, respectively.

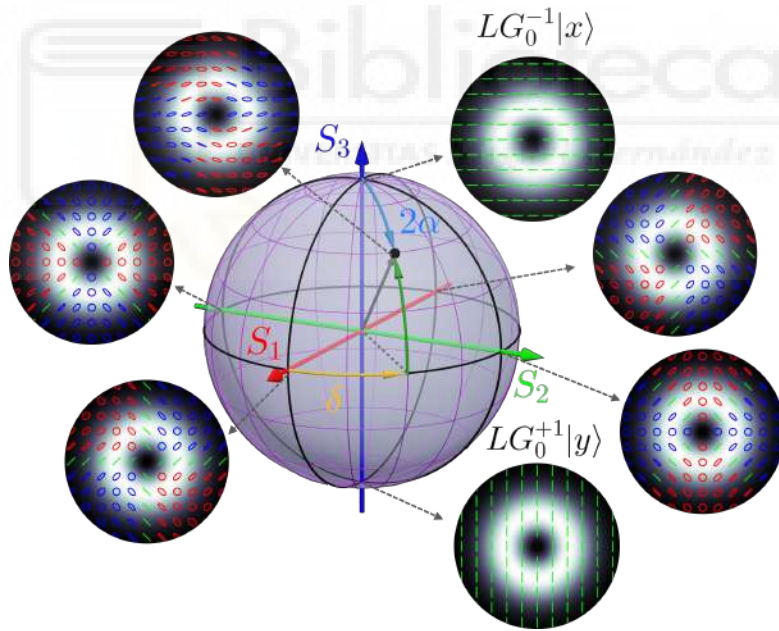


Figure 4.8: Higher-order Poincaré sphere for the vector beam in Eq. 4.29 obtained from the superposition of Laguerre-Gaussian modes in the states $|x\rangle$ and $|y\rangle$. Linear polarization is depicted in green. Right-handed and Left-handed ellipses are blue and red, respectively.

4.26 shows that 2β determines the circular trajectory on the Poincaré sphere that the vector beam sweeps along its azimuthal coordinate θ . This trajectory lies on a plane perpendicular to the axis passing through the $|a\rangle$ and $|a^\perp\rangle$ points. On the other hand, 2φ sets the starting point ($\theta = 0$) on the trajectory. Figure

4.9 shows several trajectories for different values of β and φ . The higher-order Poincaré sphere that these beams define is depicted in Fig. 4.10. In this sphere, the spherical coordinates are 2β and 2φ , and the elliptically polarized Laguerre-Gaussian states are at the poles.

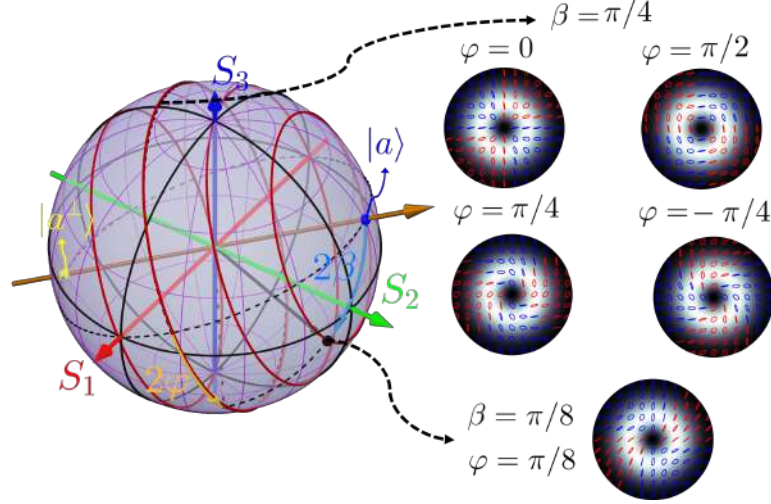


Figure 4.9: Depiction of the polarization patterns along the azimuthal coordinate θ of the vector beams in Eq. 4.25 as paths on the Poincaré sphere. The paths for different values of β are depicted in reddish brown. Linear polarization is depicted in green. Right-handed and Left-handed ellipses are blue and red, respectively.

4.2.2 First-order Hermite-Gaussian modes vector superposition

In this thesis, we also generate vector beams by adding two orthogonally polarized first-order Hermite-Gaussian beams HG_{10} and HG_{01} . We focus here on a small subset of these vector beams: the ones that can be obtained as an equally-weighted superposition of Laguerre-Gaussian beams in any polarization basis. So, we set $\beta = \pi/4$ in Eq. 4.25:

$$|V\rangle = \frac{1}{\sqrt{2}} (e^{-i\varphi} LG_0^{-1} |a\rangle + e^{i\varphi} LG_0^{+1} |a^\perp\rangle). \quad (4.31)$$

Using Eqs. 4.12, 4.13 and 4.15 we can rewrite these beams as a combination of Hermite-Gaussian beams in two elliptical polarization states $|a'\rangle$ and $|a'^\perp\rangle$:

$$|V\rangle = \frac{1}{\sqrt{2}} (HG_{10} |a'\rangle + HG_{01} |a'^\perp\rangle), \quad (4.32)$$

where

$$|a'\rangle = \frac{1}{\sqrt{2}} (e^{-i\varphi} |a\rangle + e^{i\varphi} |a^\perp\rangle) \quad (4.33)$$

$$|a'^\perp\rangle = \frac{-i}{\sqrt{2}} (e^{-i\varphi} |a\rangle - e^{i\varphi} |a^\perp\rangle). \quad (4.34)$$

For $\varphi = 0$, we obtain the radial state, as depicted in Fig. 4.11(a). Vectors $|a'\rangle$ and $|a'^{\perp}\rangle$ are then $|x\rangle$ and $|y\rangle$, respectively. So a radial beam can be obtained as the superposition of two Hermite-Gaussian beams in the $|x\rangle$ and $|y\rangle$ basis:

$$|V\rangle = \frac{1}{\sqrt{2}} (HG_{10} |x\rangle + HG_{01} |y\rangle). \quad (4.37)$$

Let us consider a linear basis for the components in Eq. 4.31: $|a\rangle = |y\rangle$ and $|a^{\perp}\rangle = |x\rangle$. Now, for $\varphi = 0$, the same vector beam can be expressed as:

$$|V\rangle = \frac{1}{\sqrt{2}} (HG_{10} |45^{\circ}\rangle + iHG_{01} |-45^{\circ}\rangle). \quad (4.38)$$

The resulting beam is shown in Fig. 4.11(b). Its polarization pattern is similar to the state lying on the S_1 axis positive direction on the higher-order Poincaré sphere in Fig. 4.8. However, the ellipticity of the ellipses is flipped because the position of the linear states has been exchanged ($|x\rangle \rightarrow |y\rangle$ and $|y\rangle \rightarrow |x\rangle$).

Finally, we set $|a\rangle = |-45^{\circ}\rangle$ and $|a^{\perp}\rangle = |45^{\circ}\rangle$. For $\varphi = 0$, the equivalent Hermite-Gauss superposition is

$$|V\rangle = \frac{1}{\sqrt{2}} (HG_{10} |x\rangle + iHG_{01} |y\rangle). \quad (4.39)$$

This state can be achieved by mixing two Hermite-Gaussian beams with $|x\rangle$ and $|y\rangle$ polarizations with a $\pi/2$ phase shift between them. The resulting pattern is depicted in Fig. 4.11(c).

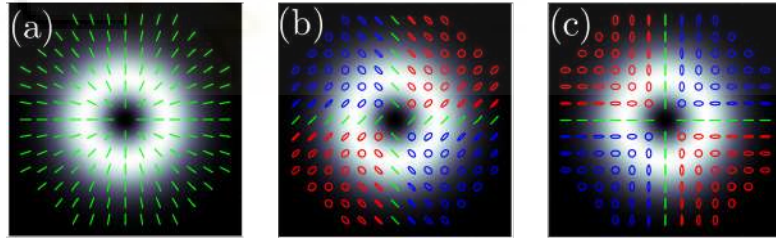


Figure 4.11: Polarization maps and intensity profile of the vector beams described by Eqs. (a) 4.37, (b) 4.38, and (c) 4.39.

4.2.3 Higher-order and hybrid vector beams

So far, we have described a small subset of vector beams. The linear combination of two Laguerre-Gaussian modes with $p = 0$, and $\ell_1 = \ell$ and $\ell_2 = -\ell$ forms a subset of vector beams described by the formula

$$|V\rangle = \cos \beta e^{-i\varphi} LG_0^{\ell} |a\rangle + \sin \beta e^{i\varphi} LG_0^{-\ell} |a^{\perp}\rangle. \quad (4.40)$$

These beams are commonly referred to as pure vector beams, and the beams that we studied in the previous subsection belong to this family. For instance, for $|a\rangle = |R\rangle$, $|a^{\perp}\rangle = |L\rangle$, $\beta = \pi/4$, $\varphi = 0$ and $\ell = 1$ we obtain a beam with a linear polarization whose orientation follows the azimuthal coordinate: the radial beam.

Conversely, if we set $\ell = 2$, the orientation of the polarization ellipse continuously varies from 0 to 2π two times along azimuthal coordinate, as shown in Fig. 4.12(a).

Now we focus on the most general vector superposition of two Laguerre-Gaussian beams given by Eq. 4.24, but we consider that $p = 0$. The Gouy phase in Eq. 4.11 for each mode depends on the modulus of ℓ . Therefore, provided that $|\ell|$ is different for each Laguerre-Gaussian beam, it causes a relative phase between the polarization components $|a\rangle$ and $|a^\perp\rangle$ that changes as the beam propagates, i.e., it depends on z). Since it depends on the modulus of ℓ , this phase is common for both LG_0^ℓ and $LG_0^{-\ell}$ beams in Eq. 4.40, so they preserve their polarization pattern as they propagate. Instead, the polarization pattern of the beams obtained as a vector superposition of two Laguerre-Gaussian beams with different $|\ell|$ will change with the z coordinate. The beams that belong to this last family are known as hybrid vector beams. The simplest case can be obtained by adding a right-circularly polarized LG_0^0 mode with a left-circularly polarized LG_0^{+1} mode:

$$|V\rangle = \frac{1}{\sqrt{2}} (LG_0^0 |R\rangle + LG_0^{+1} |L\rangle). \quad (4.41)$$

Its polarization map is depicted in Fig. 4.12(b). This beam belongs to a subset of beams that contain all the polarization states on the Poincaré sphere surface in their polarization pattern. They are known as Full Poincaré Beams, and were proposed by A. M. Beckley, T. G. Brown, and M. A. Alonso in 2010 [62]. The ellipticity of the polarization ellipses in the map changes along the radial coordinate r and remains constant along the azimuthal coordinate θ . Right at the center of the beam, where there is no contribution of $LG_0^{+1} |L\rangle$ component, the light is right-circularly polarized. As we move from the center, there is a circular region where the amplitudes of the $LG_0^0 |R\rangle$ and $LG_0^{+1} |L\rangle$ components are equal, so the light is linearly polarized. After that region, the ellipse becomes left handed. Ideally, when there is only contribution from the term $LG_0^{+1} |L\rangle$ we have left-circularly polarized light. On the other hand, the orientation of the ellipses varies along θ and is constant along r . Poincaré beams have been proposed for Mueller polarimetry of homogeneous samples [63]. Since these beams simultaneously provide all the states on the Poincaré sphere, only one input vector state is needed to determine the Mueller matrix of a homogeneous sample.

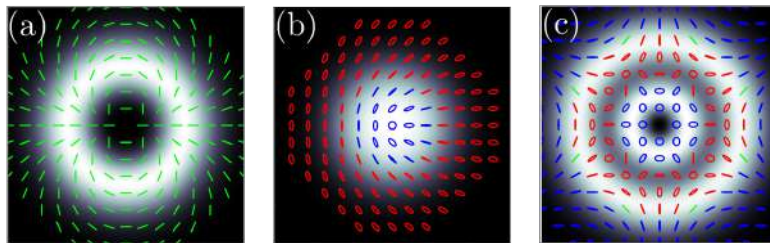


Figure 4.12: (a) Higher-order pure vector beam. (b) Full Poincaré beam. (c) Hybrid vector beam.

There are infinite spatial modes, so we could imagine any combination of polarized modes to produce all kinds of exotic polarization patterns. During the realization

of my PhD, I developed a MATLAB script where several Laguerre-Gaussian and Hermite-Gaussian modes can be added with different polarization components. The amplitude and phase of the components can also be controlled. The program plots the intensity and the phase of the modes combination. In addition, it plots the intensity and the polarization map of the resulting vector beam. Fig. 4.12(c) shows the polarization map and the intensity that the code provides for the combination

$$|V\rangle = \frac{1}{\sqrt{2}} (LG_1^{+1} |R\rangle + LG_0^{-3} |L\rangle). \quad (4.42)$$

Furthermore, customized combinations of modes can be added at each polarization component, and an elliptical retarder can be placed after the simulated vector beam. The MATLAB code can be downloaded from [64].

4.2.4 Experimental generation of vector beams

As we have studied in this chapter, vector beams can be obtained as the superposition of two different orthogonally polarized structured beams. This superposition can be achieved by several methods [2], [65]. One of the most popular and versatile methods relies on SLMs. We showed in the previous chapter that LCOS SLMs can be used to display arbitrary phase functions. So, for instance, different spiral phases can be encoded into orthogonal polarization components and generate vector beams. Nevertheless, only one linear polarization component is modulated when passing through a standard parallel-aligned LCOS SLM (the one parallel to the LC director), so different arrangements have been proposed to overcome this limitation.

One technique [66] employs an SLM in a $4f$ optical system to display a spiral phase and a diffraction grating. In the Fourier plane, the ± 1 diffraction orders are filtered and its state of polarization is modified so their recombination at the output produces the vector beam. The technique is useful but introduces large losses due to the filtering.

Another approach consists in dividing the SLM screen into two adjacent holograms. In [3], the orthogonal components of a beam are splitted by a Wollaston prism and each component is sent to a different half of the screen. The polarization of one of the components is modified before the SLM with a retarder so it matches the modulation axis of the SLM. After the SLM, they are recombined again in the prism. A conceptually similar approach was used in [67].

A different method used a transmissive SLM where the display was divided into two holograms [68]. This technique does not require the splitting of the beam. Instead, the experimental arrangement makes the light pass twice through the SLM [69]. An alternative technique is based on using two SLMs so that each component is modulated by a different SLM [70]. First, a SLM modulates the linear component along its director axis. Then, since the LC director of the two SLMs is along the same direction, a half-wave retarder is placed in between. The retarder rotates $\pi/2$ the orientation of the linear polarization state so it matches the director of the second SLM. Finally, the second SLM modulates the other

polarization component. All these different SLM based arrangements have been proven very useful to generate vector beams. However, many of them require the use of beam splitters for splitting and recombining the constituent beams, thus significantly reducing the output power compared to the input. This is why some works focused on systems, either in line [70] or using polarizing beam splitters [71], designed to improve this power budget. In the work "Efficient on-axis SLM engineering of optical vector modes" [45], we obtain vector beams from a superposition of Hermite-Gaussian and Laguerre-Gaussian modes generated in the SLMs using an in-line architecture that avoids using beam splitters. Some works used the flexibility offered by SLMs to simultaneously encode multiple functions that generate in parallel multiple vector beams [72], [73].

The rigorous generation of these modes also requires a complex amplitude modulation. There are several methods useful to encode amplitude information with phase-only SLMs [74]. They are mostly based on adding an additional phase term to the desired phase so that this added phase diffracts light out of the main beam [75]. In our case, we used a technique [76] that consists in randomly selecting between the phase of the desired pattern and the phase of a diverging optical element, with a probability that depends on the desired amplitude. This technique was demonstrated to be useful to encode amplitude since it diffracts light out of the propagation axis when low amplitude is desired, and keeps the original phase when high values of amplitude are needed [76]. The advantage of this technique is that it generates the desired beam along the propagation axis, thus being very useful in an in-line system.

Despite the great flexibility that SLMs offer, they are expensive devices that require bulky and complex experimental setups to generate vector beams. A more compact way to generate them is based on geometrical phase elements, like q -plates [41], [77]. In the previous chapter, we showed that q -plates can generate scalar vortices when they are illuminated with circularly polarized light, and they provide vector beams when the input light is elliptically or linearly polarized. In this situation, a vector beam described as the sum of two circularly polarized orthogonal spiral phases of opposite sign is produced. When the q -plate is illuminated with a Gaussian mode LG_0^0 , this vector sum can be approximated in the far field [78] as the sum of two orthogonal circularly polarized Laguerre-Gaussian modes $LG_0^{+\ell}$ and $LG_0^{-\ell}$, where ℓ is twice the q parameter of the q -plate. Therefore, they exhibit polarization patterns as the ones shown in Fig. 4.6 (radial, azimuthal...).

In some works, q -plates are combined with SLMs to apply different topological charges in the orthogonal polarization components, thus generating hybrid vector beams [79]. In addition, hybrid vector beams with a LG_0^0 in one polarization component and a vortex in the orthogonal (as the Poincaré beam in Fig. 4.12(b)) have been generated using a single SLM [80], since only one of the two orthogonal polarization components needs to be modulated.

Liquid-crystal tunable q -plates can also generate hybrid vector beams when their retardance is not $\phi = \pi$ [78]. We obtained hybrid vector beams with a commercial tunable liquid-crystal q -plate [81] tuned at $\phi = \pi/2$ in [43], and we studied how the polarization pattern of the beams changed as they propagated. For in-

stance, we generated Poincaré beams similar to the one in Eq. 4.41 by illuminating a $q = 1/2$ q -plate with a right-circularly polarized LG_0^0 mode. This result can be understood from the general equation of a geometrical phase element (Eq. 3.20) in subsection 3.2.2. The identity matrix keeps the initial mode unchanged, while the action of the $\mathbf{Q}_{GP}(\varphi(x, y))$ matrix can be approximated in the far field to do the transformation $LG_0^0 |R\rangle \rightarrow LG_0^{+1} |L\rangle$. Therefore, the beam is similar to the one in Eq. 4.41, but with a $\pi/2$ phase between the components because of the imaginary i term in Eq. 3.20.

Since the retardance ϕ in liquid crystal q -plates depends on the wavelength of the incident beam, meta-material q -plates have been proposed to generate broadband vector beams, since they generate the same vector beam in a wide wavelength range [82].

Another limitation of LC q -plates is that they impart global phase functions only to the circular components and, in addition, the phase functions are constrained to be opposite for orthogonal polarizations. Alternative meta-material based q -plates [83] and other optical elements have also been proposed to overcome these limitations [84], [38].



Chapter 5

Publications summary

In this chapter we summarize the publications that comprise this thesis. They are the following five articles, all published in international journals with impact index:

- D. Marco, M. M. Sánchez-López, P. García-Martínez, and I. Moreno, "Using birefringence colors to evaluate a tunable liquid-crystal q-plate", *Journal of the Optical Society of America B* **36** (5), D34-D41 (2019).
DOI: <https://doi.org/10.1364/JOSAB.36.000D34>
JCR index: 2.180 (JCR2019 – Optics, 47/97, Q2)
- D. Marco, M. M. Sánchez-López, A. Cofré, A. Vargas, and I. Moreno, "Optimal triplicator design applied to a geometric phase vortex grating", *Optics Express* **27**(10), 14472-14486 (2019).
DOI: <https://doi.org/10.1364/OE.27.014472>
JCR index: 3.669 (JCR2019 – Optics, 19/97, Q1)
- P. García-Martínez, D. Marco, J. L. Martínez-Fuentes, M. M. Sánchez-López, and I. Moreno, "Efficient on-axis SLM engineering of optical vector modes", *Optics & Lasers in Engineering* **125**, 105859 (2020).
DOI: <https://doi.org/10.1016/j.optlaseng.2019.105859>
JCR index: 4.836 (JCR2020 – Optics, 13/99, Q1)
- D. Marco, A. Vargas, M. M. Sánchez-López, and I. Moreno, "Measuring the spatial deformation of a liquid-crystal on silicon display with a self-interference effect", *Optics Letters* **45**(16), 4480-4483 (2020).
DOI: <https://doi.org/10.1364/OL.396105>
JCR index: 3.776 (JCR2020 – Optics, 22/99, Q1).
- D. Marco, G. López-Morales, M. M. Sánchez-López, A. Lizana, I. Moreno, and J. Campos, "Customized depolarization spatial patterns with dynamic retardance functions", *Scientific Reports* **11**, 9415 (2021).

DOI: <https://doi.org/10.1038/s41598-021-88515-x>

JCR index: 4.379 (JCR2020 – Multidisciplinary Sciences, 17/73, Q1).

These publications share the common research line centered in the methods for the generation of vortex and vector beams with liquid-crystal on silicon (LCOS) spatial light modulators (SLMs) and geometrical phase diffractive optical elements (DOEs). Next, we present a summary and highlights of each paper. The articles can be found in the appendix after the list of references.

5.1 Using birefringence colors to evaluate a tunable liquid-crystal q -plate

This is the first work of this thesis that led to a publication. Here, we measured the spectral retardance of a commercial tunable liquid-crystal q -plate. We used a device from the company Arcoptix which is, to our knowledge, the only commercially available tunable q -plate. Since the device retardance can be tuned by applying a voltage, we performed a complete study of the retardance dependence with wavelength and voltage. In addition, since q -plates are retarders, they present birefringence colors, so we related these colors to its spectral birefringence.

The spectral characterization was performed following the typical technique for measuring the spectral retardance of linear retarders described in subsection 2.2.4. The q -plate was placed between polarizers and illuminated with broadband white light. Then, the spectral retardance was retrieved from the measured spectra after the last polarizer. Nevertheless, we used circular polarizers instead of linear polarizers. However, since q -plates are linear retarders where the principal is rotating azimuthally, we had to adapt the technique and use circular polarizers instead of linear polarizers. But these circular polarizers must be broadband, so they produce and detect circularly polarized light for all wavelengths in the considered spectral range. In order to obtain circularly polarized light for every wavelength we used Fresnel rhombs, since they provide a constant retardance in a wide wavelength range.

At first, we performed the spectral characterization of the q -plate with the purpose of using it later with lasers of different wavelengths. Afterwards, we noticed the birefringence colors that the device presented under broadband white illumination. In addition, the color could be varied by applying a voltage, since the voltage changes the birefringence. As we explained in subsection 2.2.5, these colors are expected in low-order linear retarders. For the q -plate, we saw that the color was white for most voltages. However, for voltages where the first-order retardance values were transiting the visible part of the spectrum, the birefringence colors were appreciable. In addition, birefringence colors also were noticeable when the q -plate was placed between crossed linear polarizers. Therefore, we showed a simple and fast method to determine when a q -plate was acting as a first-order retarder in the visible part of the spectrum consisting in illuminating it with broadband white light between linear polarizers. In addition, the birefringence colors provided a rough estimation of the wavelength where the q -plate presented a retardance π .

We also studied the birefringence color properties as a function of the voltage applied, and presented their trajectory as points in the CIE_{xy} chromaticity diagram.

This work was presented at the Spanish National Meeting on Color (Reunión Nacional del Color, Linares, 2019), where it was awarded with the prize to the best communication of the session. It was also presented at the Spanish National Meeting of Optics (Reunión Nacional de Óptica, Castellón, 2018) and at the Workshop on Biophotonics and Optical Angular Momentum (Palaiseau, Paris, 2018).

5.2 Optimal triplicator design applied to a geometric phase vortex grating

This second work demonstrates the design, analysis and characterization of a geometric-phase liquid-crystal diffraction grating generating an array of 3×3 optical vortices with topological charges ranging from -4 to $+4$, and optimal diffraction efficiency. The design is based on the application of the optimal triplicator phase profile derived by Gori and coworkers [32] to two forked linear phase gratings horizontally and vertically oriented. The application of the optimal triplicator profile to a forked linear grating is shown in subsection 3.1.2.

We explained the different polarization behavior observed on two sets of diffraction orders, which stems from the $\pi/2$ relative phase between the zero and the ± 1 diffraction orders of the optimal triplicator. We should note here that, while in the triplicator design proposed by Gori et al. only the magnitude of the Fourier coefficients for the 0 and ± 1 orders was discussed, our theoretical analysis demonstrates an imaginary i factor between the ± 1 orders and the 0 order. This is crucial when implementing the design with geometrical phase, since it determines the polarization transformations that the diffraction orders experience.

Such two-dimensional vortex diffraction grating was fabricated by the company Thorlabs, which offers a facility to produce custom masks composed of an array of microretarders, each of which has a fast axis aligned to a different angle than its neighbor. In our case, it is a patterned half-wave retarder for 633 nm, with 853×853 microretarders, where the liquid crystal director of each microretarder is aligned to an angle given by the phase mask we designed as the two-dimensional vortex grating. The grating was characterized and the experimental results agree well with the theoretical analysis. The possibility of producing these diffractive microretarder masks is a very interesting option for small laboratories that do not have facilities to fabricate such elements.

It is worth mentioning that, although the theoretical efficiency of the two-dimensional grating was 86%, we experimentally obtained an efficiency of about 76%. This was mostly caused by the limited spatial resolution of the fabricated grating. Since the optimal triplicator profile is continuous, infinite resolution would be required to obtain the maximum diffraction efficiency. Nevertheless, we believe that higher resolution microretarders might lead to efficiency values close to the

theoretical.

Finally, we consider that our proposal of applying the optimal triplicator design to a geometric-phase vortex grating might be relevant in applications of vortex generation/detection with low light intensity levels, where the optimal diffraction efficiency is key.

This work was presented as an oral talk in the International Optical Society of America Network of Students (Castelldefels, Barcelona, 2019), in the Scientific Conference of Structured Light, Polarimetry and Imaging (Jornada científica en Luz estructurada, Polarimetría e Imagen, Elche, 2019), and in the virtual forum SPIE Photonics Europe (2020). It has also been presented as a poster in the Biennial Meeting of the Spanish Royal Society of Physics (Reunión Bienal de la Real Sociedad Española de Física, Zaragoza, 2019).

5.3 Efficient on-axis SLM engineering of optical vector modes

In this third work, we designed and demonstrated experimentally an efficient optical setup to generate any arbitrary polarized vector beam which combines recent advances in spatial light modulators. The technique was based on employing two LCOS SLMS, free from flicker, working in phase-only modulation and operating on axis in a robust Z configuration.

The experimental implementation of the proposed technique relies on the versatility of LCOS devices, which provide on demand, real-time dynamic holographic means to create optical fields. This makes necessary the accurate characterization of these devices and the development of reverse engineering techniques to derive physical models able to predict their optical modulation. Therefore, we characterized two LCOS SLMs from the company Hamamatsu. These devices exhibit high diffraction efficiency (96% for zero-order) and are free from flicker, thus they do not present phase fluctuations that cause and unwanted zero order. Note that LCOS-systems with flicker must be operated off-axis due to the zero-order (DC) component caused by this flicker effect. Noteworthy, the optical system demonstrated in this work can be operated on-axis. This fact has the advantage of employing the complete space-bandwidth product of the device, and of making unnecessary the use of beam splitters in the optical setup, thus presenting high diffraction efficiency compared with other methods in the literature, as those described in subsection 4.2.4.

The efficiency of the proposed optical system was tested by obtaining arbitrary vector beams from linear combinations of Hermite-Gaussian and Laguerre-Gaussian modes addressed to the LCOS devices. Each of the two LCOS panels separately modulates an orthogonal linear polarization in an inline Z-configuration. This type of configuration is very robust and efficient since it has a common path for both polarization components and no beam splitters are required. As mentioned in section 4.2, higher-order Gaussian spatial modes with different polarizations can be combined to generate beams with custom spatially varying polariza-

tion patterns across their transverse section.

In this work, specific examples of the modes described in section 4.1 were realized with the proposed optical setup. Since LCOS SLMs operate in phase-only modulation regime, we applied the method reported in [76] to encode complex valued computer-generated holograms onto phase-only displays. This method is very efficient in terms of light budget since it does not require adding a carrier phase function and does not reduce the available space-bandwidth product. It also reconstructs the desired field on axis. We obtained a good agreement between the experimental results and the theoretical analysis within the Jones matrix formalism. The polarization spatial patterns were obtained using the MATLAB code developed in this thesis [64]. This tool has been used in another work where we used the tunable q -plate to generate exotic hybrid vector beams [43].

Since tailored light beams with controllable polarization and phase are becoming ubiquitous in a wide variety of research fields, we believe this method can be of interest for the applications of vector beams in areas like optical communications, advanced microscopy, optical trapping, and laser microfabrication.

5.4 Measuring the spatial deformation of a liquid-crystal on silicon display with a self-interference effect

In this fourth article, we presented a technique to characterize the deformation of the backplane panel of a LCOS SLM from an interference effect generated in the SLM when it is illuminated with a wavelength far from the operation range. Since the antireflection coating does not work properly for wavelengths out of the operation range, a significant part of the light is reflected at the outer surface. We verified the good flatness of the outer surface of the SLM, so the light reflected at this plane can be considered as the reference beam. The maximum measured deformation was less than 0.1λ , which is comparable to a flat mirror. On the other hand, a fraction of the input light enters the SLM, it is modulated by the liquid-crystal layer, gets reflected at the backplane panel and emerges again from the display. Therefore, an interference pattern is directly visible at the beam reflected by the SLM.

The novelty of this work was to exploit this in principle undesired effect to derive the spatial deformation of the backplane panel of a LCOS SLM. Since it is a self-interference effect in the SLM, no external interferometric system is required, which makes the setup extremely robust and stable under external conditions. We showed that this interference is affected by the spatial deformation of the LCOS backplane. Therefore, the backplane deformation can be measured from this interference.

Because the light that enters the SLM can be modulated, different interference patterns are obtained by addressing different uniform gray levels to the display. Since they are not the regular two-beam interferograms, but instead they are Gires-Tournois type interferograms, the interference shows very narrow

dark fringes, so standard heterodyne techniques cannot be applied. Therefore, I developed some image processing tools that we applied to these interferograms, captured for different addressed gray levels, to derive the deformation of the LCOS backplane.

We demonstrated the effect with a LCOS SLM designed to operate in the infrared range but illuminated with visible green light from a He-Ne laser. We characterized the spatial non-uniformity of the SLM and obtained a correction mask from the position of the fringes of minimum intensity for different interferograms. Experimental results show a good correction in the near and far field. By correcting the phase values applying the dispersion relation measured for the liquid-crystal layer, the correction mask is demonstrated also to be useful in the infrared wavelengths for which the SLM is designed. Since the experimental setup is extremely simple, it makes the technique affordable and fast to implement.

This work was selected as an Editor's Pick by the editor of the journal *Optics Letters*, and it was presented as an online oral talk in the virtual forum *Frontiers in Optics* of the Optical Society of America (2020).

5.5 Customized depolarization spatial patterns with dynamic retardance functions

Finally, in this fifth paper, we presented a method to generate tailored effective depolarization spatial patterns. Here, we exploit the possibility to change in real time the pattern displayed on a spatial light modulator SLM. The technique was based on displaying a time-varying pixelated retardance pattern on a LCOS SLM. Therefore, a spatially-varying polarization pattern that also varies in time was sent to the polarization detection system. Then, since the detector integration time was set to be greater than the rate of change of the polarization patterns, beams with a spatial variation of their effective degree of polarization across its transverse section were generated. As we mentioned in section 2.3, the emulation of depolarization by means of sending several polarization states in a time shorter than the detector integration time has already been performed with liquid-crystal ferroelectric retarders by Peinado et al. in [22]. The novelty of this work was to use a multi-pixel SLM, thus depolarization spatial patterns were achieved.

We sequentially displayed two retardance patterns within one integration time of the detector. As a result, the resulting Mueller matrix describing the SLM was obtained from the averaged sum of the two spatially-varying Mueller matrices that describe the SLM for each spatial retardance configuration. The matrix was decomposed as the action of a linear retarder followed by a depolarizer. We provided an intuitive geometrical explanation of the transformations that these matrices perform over the input state on the Poincaré sphere.

A good concordance between the theoretical and experimental results of retardance and depolarization for different depolarization patterns was found. The depolarization patterns were measured with an imaging polarization state analyzer composed of a polarization camera and a quarter-wave plate. Despite LCOS SLMs

can display up to 60 patterns in one second, the integration time of the camera was set to 1 second, so each retardance pattern was displayed during 0.5 seconds. Such a long integration time was chosen because when the frame rate of the SLM was increased the transition times of the liquid crystal molecules started to be noticeable, as time-resolved measurements with an oscilloscope showed. As a consequence, the resulting Mueller matrix started to deviate from the ideal behaviour we supposed in our simplified model. Therefore, this work is presented as a proof-of-concept that proves that effective depolarization patterns can be achieved, and that provides a simplified model that captures the essence of the idea. Higher kHz rates could be achieved with faster ferroelectric SLMs.

We generated several depolarization patterns, including a beam with an azimuthal variation of its degree of polarization (DoP) in its transverse section. This pattern is equivalent to a spiral phase pattern, but, instead of a spatial phase variation, we obtained a spatial variation of the DoP. Therefore, we think that this technique might be used to emulate structured light with the degree of polarization as an additional parameter.

This method might also be of interest where a locally-controlled DoP is required, like in emulating spatially variant depolarization samples or in the calibration of Mueller imaging polarimeters.

This work has been presented as an online poster at the Spanish Optoelectronics Meeting (Reunión Española de Optoelectrónica, 2021).



Chapter 6

Conclusions

In this manuscript, we have described some of the basic theoretical aspects of polarization and structured light beams. In addition, we have reviewed several actual methods employed to generate vector beams. The purpose of this introduction was to contextualize our published works, where we have characterized and designed experimental setups based on spatial light modulators and geometric phase elements for the generation of optical vortices and vector beams.

The first work performed in the three years that comprise this thesis was the spectral calibration of a liquid-crystal tunable commercial q -plate. Although our first intention was to characterize the device for operating with several laser sources, we soon noticed that it exhibits birefringence colors. This fact led to the design of a simple and fast method to determine when the q -plate is operating as a first-order retarder, and roughly estimate the wavelength where the retardance was π . The method consists in illuminating the q -plate with broadband white light between crossed linear polarizers and observe the birefringence colors. As a result, the previously mentioned properties can be roughly obtained even with the naked eye. On the other hand, based on the accurate characterization of the device retardance in the range of 400-1600 nm and as a function of the applied voltage, this commercial q -plate can be used to generate pure and hybrid vector beams at any desired wavelength. This was applied in work [43], which is not part of this thesis.

In the next work, we designed a two-dimensional liquid-crystal geometric-phase diffraction grating that allows the parallel generation of an array of 3×3 optical vortices with different topological charges ranging from -4 to $+4$. In addition, the grating was used to detect the topological charge of an input vortex. The advantage of our design is that the encoded phase profile relies on the optimal phase triplicator profile, which renders three diffraction orders with the maximum possible efficiency that can be achieved with a phase-only function. The implementation of such phase profiles as geometric phase elements combines the efficiency of the phase design with the compactness that geometric phase elements offer. In addition, we proved that there is a $\pi/2$ factor between the 0 and ± 1 diffraction orders that the triplicator profile generates. Furthermore, we demonstrated the effect of this phase shift on the polarization of the diffraction orders when the triplicator is encoded as a geometric phase element.

We then presented a fourth work where we designed an experimental setup to generate vector beams by combining two orthogonally polarized high-order Gaussian modes generated with two LCOS SLMs. Each orthogonal polarization was modulated by a SLM free from flicker in an in-line Z configuration. Therefore, the system operates on-axis, thus avoiding the need of beam splitters, so it provides high efficiency. In order to properly generate the Gaussian modes, we employed a technique to encode complex amplitude on the LCOS SLMs which does not require a carrier phase and does not reduce the space-bandwidth product.

The fourth work in this thesis emerged from an in principle undesired effect. With the purpose of achieving large phase modulation, we used SLMs designed for the infrared region with visible light. Since their anti-reflection coating is not properly designed for visible light, a significant amount of the light was reflected at the outer part of the SLM. We used this effect to deduce the backplane deformation of a LCOS SLM from the interference patterns generated between this light and the fraction that reaches the backplane. Since the interference effect is produced inside the SLM, there is no need for an external interferometric system, thus being a stable and experimentally easy to implement method.

In the last work, we generated spatially variant depolarization patterns by temporary averaging two retardance patterns displayed on a SLM. This technique might be useful to emulate depolarizing samples. We also demonstrated the generation of a beam with a spirally-shaped degree of polarization spatial pattern. Therefore, the method could be used to emulate different new types of structured light when the spatial variation of the degree of polarization is considered as an additional parameter.

During my PhD, I developed a MATLAB code that represents the polarization map and the intensity pattern of two polarized states with an arbitrary content of high-order Gaussian modes. These maps were used in the work "Efficient on-axis SLM engineering of optical vector modes" [45] and in the work [43], which is not part of this thesis. The software can be downloaded and modified from [64].

I also would like to mention that I had the pleasure of spending one month at ALBA Synchrotron this last year. My work there consisted in the calibration of a spatial light modulator to perform super resolution three-dimensional structured illumination cryogenic fluorescence microscopy. All the knowledge in SLMs calibration attained through these years was key during that month, and it was an tremendously fruitful experience.

Conclusiones

En esta memoria hemos descrito algunos de los aspectos teóricos básicos de polarización y haces de luz estructurada. Además, hemos resumido algunos de los métodos que existen actualmente para generar haces vectoriales. El propósito de esta introducción ha sido el contextualizar los trabajos publicados de esta tesis, en los que hemos caracterizado y diseñado montajes experimentales basados en moduladores espaciales de luz y en elementos de fase geométrica para la generación de vórtices ópticos y haces vectoriales.

El primer trabajo realizado en estos tres años de tesis fue la calibración experimental de una lámina- q (q -plate) comercial, de cristal líquido sintonizable. Si bien nuestra primera intención fue caracterizar el dispositivo para hacerlo operar con varias fuentes láser, pronto nos percatamos de que muestra colores de birrefringencia. Este hecho condujo al diseño de un método rápido y sencillo para determinar cuándo la q -plate está actuando como un retardador de primer orden, y a estimar de forma aproximada la longitud de onda para la cual el retardo es π . El método consiste en iluminar la q -plate con luz blanca de amplio espectro, situarla entre polarizadores cruzados y observar los colores de birrefringencia. Como resultado, las propiedades antes mencionadas pueden obtenerse de forma aproximada incluso a simple vista. Por otro lado, basándonos en la precisa caracterización del retardo en el rango de 400-1600 nm y en función del voltaje aplicado, esta lámina- q comercial puede ser utilizada para generar haces vectoriales puros e híbridos en cualquier longitud de onda que se desee. Así se hizo en el trabajo [43], el cual no forma parte del compendio de publicaciones de esta tesis.

En el siguiente trabajo, diseñamos una red de difracción bidimensional de fase geométrica basada en cristal líquido, que permite la generación en paralelo de una red de 3×3 vórtices ópticos con diferentes cargas topológicas comprendidas entre -4 y $+4$. Además, esta red fue empleada para detectar la carga topológica de un vórtice incidente. La ventaja de nuestro diseño es que el perfil de fase codificado tiene su base en el perfil de fase del triplicador óptimo, el cual produce tres órdenes de difracción con la máxima eficiencia posible de obtener con una función sólo de fase. La implementación de estos perfiles de fase como elementos de fase geométrica combina la eficiencia en el diseño de la fase con la ventaja de ser elementos extremadamente compactos. Así mismo, demostramos que el perfil del triplicador genera un factor $\pi/2$ entre el orden de difracción 0 y los órdenes ± 1 . Es más, demostramos el efecto que este desfase tiene sobre la polarización de los órdenes de difracción cuando el triplicador se codifica como elemento de fase geométrica.

Seguidamente se presentó un cuarto trabajo en el que diseñamos un montaje experimental con el que generar haces vectoriales combinando dos modos Gaussianos de alto orden de polarizaciones ortogonales, los cuales son generados mediante dos moduladores LCOS. Cada polarización ortogonal era modulada con un SLM libre de fluctuaciones (flicker) en una configuración en Z. Por lo tanto, el sistema opera en eje, evitándonos así el uso de divisores de haz y por consiguiente, aumentando la eficiencia. Con el fin de generar adecuadamente los modos Gaussianos, empleamos una técnica que permite codificar la amplitud compleja en el modulador LCOS sin necesidad de añadir una fase portadora y por lo tanto sin reducir la anchura de banda espacial del dispositivo.

El cuarto trabajo de esta tesis surgió de un efecto en principio no deseado. Con el propósito de conseguir una alta modulación de fase, iluminamos con luz en el rango visible un modulador SLM diseñado para la región infrarroja. Como su recubrimiento antirreflejante no está diseñado para la luz visible, una parte significativa de la luz se refleja en la cara externa del SLM. Empleamos este efecto para deducir la deformación de la cara trasera de un LCOS SLM a partir del patrón de interferencias generado entre esta luz y la fracción que alcanza la cara trasera. Dado que la interferencia se produce dentro del SLM, no hay necesidad de añadir un sistema interferométrico externo, por lo que este método es estable y fácil de implementar experimentalmente.

En el último trabajo generamos patrones de despolarización variables espacialmente mediante el promedio temporal de dos patrones de retardo mostrados en el SLM. Esta técnica puede ser útil para emular muestras despolarizantes. También demostramos la generación de un haz cuyo grado de polarización muestra un patrón espiral. Por lo tanto, este método podría ser empleado para emular nuevos tipos de luz estructurada en los que la variación espacial del grado de polarización es considerado como un parámetro adicional.

Durante mi doctorado he desarrollado un código MATLAB que representa el mapa de polarización y el patrón de intensidad de dos estados de polarización con un contenido arbitrario de modos Gaussianos de alto orden. Estos mapas fueron usados en el trabajo "Efficient on-axis SLM engineering of optical vector modes" [45] y en el trabajo [43], el cual no forma parte de esta tesis. El software puede descargarse y modificarse en [64].

También querría mencionar que tuve el placer de realizar una estancia de un mes en el sincrotrón ALBA este último año de tesis. Mi trabajo allí consistió en la calibración de un modulador espacial de luz para realizar microscopía criogénica de fluorescencia, de superresolución con iluminación estructurada tridimensional. Todo el conocimiento en SLMs adquirido en estos años fue clave durante ese mes en ALBA, y fue una experiencia tremendamente fructífera.

Bibliography

- [1] Q. Zhan, "Cylindrical vector beams: from mathematical concepts to applications", *Adv. Opt. Photonics* **1**(1), 1-57 (2009).
- [2] C. Rosales-Guzmán, B. Ndagano, and A. Forbes, "A review of complex vector light fields and their applications", *J. Opt.* **20**(12), 123001 (2018).
- [3] C. Maurer, A. Jesacher, S. Fürhapter, S. Bernet, and M. Ritsch-Marte, "Tailoring of arbitrary optical vector beams", *New J. Phys.* **9**(3), 78 (2007).
- [4] C. Rosales-Guzmán and A. Forbes, *How to Shape Light with Spatial light Modulators*, SPIE Press: Bellingham, WA (2017).
- [5] N. A. Rubin, A. Zaidi, M. Juhl, R. P. Li, J. P. B. Mueller, R. C. Devlin, K. Léosson, and F. Capasso, "Polarization state generation and measurement with a single metasurface", *Opt. Express* **26**(17), 21455 (2018).
- [6] A. Rubano, F. Cardano, B. Piccirillo, and L. Marrucci, "Q-plate technology: a progress review", *J. Opt. Soc. Am. B* **36**, D70-D87 (2019).
- [7] D. Marco, M. M. Sánchez-López, P. García-Martínez, and I. Moreno, "Using birefringence colors to evaluate a tunable liquid-crystal q-plate", *JOSA B* **36**(5), D34-D41 (2019).
- [8] D. Marco, G. López-Morales, M. M. Sánchez-López, A. Lizana, I. Moreno, and J. Campos, "Customized depolarization spatial patterns with dynamic retardance functions", *Sci. Rep.* **11**(1), 1-13 (2021).
- [9] E. Hecht, *Optics*, Pearson Education (2017).
- [10] D. H. Goldstein, *Polarized Light*, CRC press (2017).
- [11] B. E. A. Saleh and M. C. Teich, *Fundamentals of photonics*, John Wiley & Sons (1991).
- [12] S. Y. Lu and R. A. Chipman, "Interpretation of Mueller matrices based on polar decomposition", *JOSA A* **13**(5), 1106-1113 (1996).
- [13] A. Messaadi, "Retardadores ópticos en un rango espectral extendido: caracterización y filtros birrefringentes", PhD Thesis, Universidad Miguel Hernández de Elche, Spain (2021).

-
- [14] A. Messaadi, M. M. Sánchez-López, P. García-Martínez, A. Vargas, and I. Moreno, "Optical system for measuring the spectral retardance function in an extended range", *J. Eur. Opt. Soc. – Rapid Pub.* **12**(1), 21 (2016).
- [15] A. Messaadi, M. M. Sánchez-López, A. Vargas, P. García-Martínez, and I. Moreno, "Achromatic linear retarder with tunable retardance", *Opt. Lett.* **43**(14), 3277-3280 (2018).
- [16] Y. Zou, J. Namkung, Y. Lin, D. Ke, and R. Lindquist, "Interference colors of nematic liquid crystal films at different applied voltages and surface anchoring conditions," *Opt. Express* **19**(4), 3297–3303 (2011).
- [17] J. L. Martínez, P. García-Martínez, M. M. Sánchez-López, and I. Moreno, "Accurate color predictability based on a spectral retardance model of a twisted-nematic liquid-crystal display", *Opt. Commun.* **284**(10-11), 2441-2447 (2011).
- [18] C. Brosseau, *Fundamentals of Polarized Light: a Statistical Optics Approach*, Wiley-Interscience (1998).
- [19] E. Wolf, *Introduction to the Theory of Coherence and Polarization of Light*, Cambridge University Press (2007).
- [20] R. D. Ramkhalawon, T. G. Brown, and M. A. Alonso, "Imaging the polarization of a light field", *Opt. Express* **21**(4), 4106-4115 (2013).
- [21] A. Lizana, I. Estévez, F. A. Torres-Ruiz, A. Peinado, C. Ramirez, and J. Campos, "Arbitrary state of polarization with customized degree of polarization generator", *Opt. Lett.* **40**(16), 3790–3793 (2015).
- [22] A. Peinado, A. Lizana, and J. Campos, "Use of ferroelectric liquid crystal panels to control state and degree of polarization in light beams", *Opt. Lett.* **39**(3), 659-662 (2014).
- [23] W. Burns, "Degree of polarization in the Lyot depolarizer", *J. Light. Technol.* **1**(3), 475–479 (1983).
- [24] https://www.thorlabs.com/newgrouppage9.cfm?objectgroup_id=8043
- [25] S. Franke-Arnold, and N. Radwell, "Light served with a twist", *Opt. Photonics News* **28**(6), 28-35 (2017).
- [26] J. W. Goodman, *Introduction to Fourier Optics*, Roberts & Co. Publishers (2005).
- [27] F. Aroca, and I. Moreno, "Comparison and experimental realization of different phase only grating designs and optimal triplicators", *Opt. Pura Apl.* **49**(3), 155-166 (2016).

-
- [28] D. Prongué, H. P. Herzig, R. Dändliker, and M. T. Gale, "Optimized kinoform structures for highly efficient fan-out elements", *Appl. Opt.* **31**(26), 5706-5711 (1992).
- [29] H. Dammann, and E. Klotz, "Coherent optical generation and inspection of two-dimensional periodic structures", *Opt. Acta (Lond.)* **24**(4), 505-515 (1977).
- [30] J. Albero, I. Moreno, J. A. Davis, D. M. Cottrell, and D. Sand, "Generalized phase diffraction gratings with tailored intensity", *Opt. Lett.* **37**(20), 4227-4229 (2012).
- [31] J. Albero, J. A. Davis, D. M. Cottrell, C. E. Granger, K. R. McCormick, and I. Moreno, "Generalized diffractive optical elements with asymmetric harmonic response and phase control", *Appl. Opt.* **52**(15), 3637-3644 (2013).
- [32] F. Gori, M. Santarsiero, S. Vicalvi, R. Borghi, G. Cincotti, E. Di Fabrizio, and M. Gentili, "Analytical derivation of the optimum triplicator", *Opt. Commun.* **157**(1-6), 13-16 (1998).
- [33] D. Marco, M. M. Sánchez-López, A. Cofré, A. Vargas, and I. Moreno, "Optimal triplicator design applied to a geometric phase vortex grating", *Opt. Express* **27**(10), 14472-14486 (2019).
- [34] I. Moreno, C. Iemmi, A. Márquez, J. Campos, and M. J. Yzuel, "Modulation light efficiency of diffractive lenses displayed in a restricted phase-modulated display", *Appl. Opt.* **43**(34), 6278-6284 (2004).
- [35] L. De Sio, D. E. Roberts, Z. Liao, S. Nersisyan, O. Uskova, L. Wickboldt, N. Tabiryan, D. M. Steeves, and B. R. Kimball, "Digital polarization holography advancing geometrical phase optics", *Opt. Express* **24**(16), 18297-18306 (2016).
- [36] Z. Zhang, Z. You, and D. Chu, "Fundamentals of phase-only liquid crystal on silicon (LCOS) devices", *Light Sci. Appl.* **3**(10), e213-e213 (2014).
- [37] J. Kim, Y. Li, M. N. Miskiewicz, C. Oh, M. W. Kudenov, and M. J. Escuti, "Fabrication of ideal geometric-phase holograms with arbitrary wavefronts", *Optica*, **2**(11), 958-964 (2015).
- [38] J. B. Mueller, N. A. Rubin, R. C. Devlin, B. Groever, and F. Capasso, "Metasurface polarization optics: independent phase control of arbitrary orthogonal states of polarization", *Phys. Rev. Lett.* **118**(11), 113901 (2017).
- [39] T. Haist and W. Osten, "Holography using pixelated spatial light modulators—part 1: theory and basic considerations", *Journal of Micro/Nanolithography, MEMS, and MOEMS*, **14**(4), 041310 (2015).

-
- [40] D. Marco, A. Vargas, M. M. Sánchez-López, and I. Moreno, "Measuring the spatial deformation of a liquid-crystal on silicon display with a self-interference effect", *Opt. Lett.* **45**(16), 4480-4483 (2020).
- [41] L. Marrucci, C. Manzo, and D. Paparo, "Optical spin-to-orbital angular momentum conversion in inhomogeneous anisotropic media", *Phys. Rev. Lett.* **96**(16), 163905 (2006).
- [42] L. Marrucci, "Liquid crystal q-plates: classical and quantum photonic applications", *Proc. of SPIE* **8475** 84750P (2012).
- [43] J. C. Quiceno-Moreno, D. Marco, M. M. Sánchez-López, E. Solarte, and I. Moreno, "Analysis of hybrid vector beams generated with a detuned q-plate", *Appl. Sci.* **10**(10), 3427 (2020).
- [44] A. Forbes, "Structured light: tailored for purpose", *Opt. Photonics News* **31**(6), 24-31 (2020).
- [45] P. García-Martínez, D. Marco, J. L. Martínez-Fuentes, M. M. Sánchez-López, and I. Moreno, "Efficient on-axis SLM engineering of optical vector modes", *Opt. Lasers Eng.* **125**, 105859 (2020).
- [46] L. Allen, M. W. Beijersbergen, R. J. C. Spreeuw, and J. P. Woerdman, "Orbital angular momentum of light and the transformation of Laguerre-Gaussian laser modes", *Phys. Rev. A* **45**(11), 8185–8189 (1992).
- [47] N. B. Simpson, K. Dholakia, L. Allen, and M. J. Padgett, "Mechanical equivalence of spin and orbital angular momentum of light: an optical spanner", *Opt. Lett.* **22**(1), 52–54 (1997).
- [48] G. Gibson, J. Courtial, M. Padgett, M. Vasnetsov, V. Pas'ko, S. Barnett, and S. Franke-Arnold, "Free-space information transfer using light beams carrying orbital angular momentum", *Opt. Express* **12**(22), 5448–5456 (2004).
- [49] J. Wang, J.-Y. Yang, I. M. Fazal, N. Ahmed, Y. Yan, H. Huang, Y. Ren, Y. Yue, S. Dolinar, M. Tur, and A. E. Willner, "Terabit free-space data transmission employing orbital angular momentum multiplexing", *Nat. Photonics* **6**(7), 488–496 (2012).
- [50] S. W. Hell and J. Wichmann, "Breaking the diffraction resolution limit by stimulated emission: stimulated-emission-depletion fluorescence microscopy", *Opt. Lett.* **19**(11), 780–782 (1994).
- [51] A. M. Yao and M. J. Padgett, "Orbital angular momentum: origins, behavior and applications", *Adv. Opt. Photonics* **3**(2), 161–204 (2011).
- [52] M. J. Padgett, "Orbital angular momentum 25 years on", *Opt. Express* **25**(10), 11265-11274 (2017).

-
- [53] E. J. Galvez, "Vector beams in free space". Chapter 3 in *The Angular Momentum of Light*. D. L. Andrews and M. Babiker, editors. Cambridge University Press (2012).
- [54] M. J. Padgett and J. Courtial, "Poincaré-sphere equivalent for light beams containing orbital angular momentum", *Opt. Lett.* **24**(7), 430-432 (1999).
- [55] M. R. Dennis, and M. A. Alonso, "Swings and roundabouts: optical Poincaré spheres for polarization and Gaussian beams", *Philos. Trans. A Math. Phys. Eng. Sci.* **375**(2087), 20150441 (2017).
- [56] V. G. Niziev and A. V. Nesterov, "Influence of beam polarization on laser cutting efficiency", *J. Phys. D Appl. Phys.* **32**(13), 1455 (1999).
- [57] M. Michihata, T. Hayashi, and Y. Takaya, "Measurement of axial and transverse trapping stiffness of optical tweezers in air using a radially polarized beam", *Appl. Opt.* **48**(32), 6143-6151 (2009).
- [58] G. M. Lerman, and U. Levy, "Effect of radial polarization and apodization on spot size under tight focusing conditions", *Opt. Express* **16**(7), 4567-4581 (2008).
- [59] G. Milione, M. P. J. Lavery, H. Huang, Y. Ren, G. Xie, T. A. Nguyen, E. Karimi, L. Marrucci, D. A. Nolan, R. R. Alfano, and A. E. Willner, "4x20 Gbit/s mode division multiplexing over free space using vector modes and a q-plate mode (de)multiplexer", *Opt. Lett.* **40**, 1980-1983 (2015).
- [60] C. Hernández-García, A. Turpin, J. San Román, A. Picón, R. Drevinskas, A. Cerkauskaitė, P. G. Kazansky, C. G. Durfee, and I. J. Sola, "Extreme ultraviolet vector beams driven by infrared lasers", *Optica* **4**(5), 520-526 (2017).
- [61] G. Milione, H. I. Sztul, D. A. Nolan, and R. R. Alfano, "Higher-order Poincaré sphere, Stokes parameters, and the angular momentum of light", *Phys. Rev. Lett* **107**(5), 053601 (2011).
- [62] A. M. Beckley, T. G. Brown, and M. A. Alonso. "Full Poincaré beams". *Opt. Express* **18**(10), 10777-10785 (2010).
- [63] J. C. Suárez-Bermejo, J. C. G. de Sande, M. Santarsiero, and G. Piquero, "Mueller matrix polarimetry using full Poincaré beams", *Opt. Lasers Eng.* **122**, 134-141 (2019).
- [64] <https://github.com/DavidMarcoCastillo>
- [65] J. Chen, C. Wan, and Q. Zhan, "Vectorial optical fields: recent advances and future prospects", *Sci. Bull.* **63**(1), 54-74 (2018).
- [66] X. L. Wang, J. Ding, W. J. Ni, C. S. Guo, and H. T. Wang, "Generation of arbitrary vector beams with a spatial light modulator and a common path interferometric arrangement", *Opt. Lett.* **32**(24), 3549-3551 (2007).

- [67] S. Liu, S. Qi, Y. Zhang, P. Li, D. Wu, L. Han, and J. Zhao, "Highly efficient generation of arbitrary vector beams with tunable polarization, phase, and amplitude", *Photonics Res.* **6**(4), 228-233 (2018).
- [68] I. Moreno, J. A. Davis, T. M. Hernandez, D. M. Cottrell, and D. Sand, "Complete polarization control of light from a liquid crystal spatial light modulator", *Opt. Express* **20**(1), 364-376 (2012).
- [69] I. Moreno, J. A. Davis, D. M. Cottrell, and R. Donoso, "Encoding high-order cylindrically polarized light beams", *Appl. Opt.* **53**(24), 5493-5501 (2014).
- [70] E. J. Galvez, S. Khadka, W. H. Schubert, and S. Nomoto, "Poincaré-beam patterns produced by nonseparable superpositions of Laguerre–Gauss and polarization modes of light", *Appl. Opt.* **51**(15), 2925-2934 (2012).
- [71] S. Chen, X. Zhou, Y. Liu, X. Ling, H. Luo, and S. Wen, "Generation of arbitrary cylindrical vector beams on the higher order Poincaré sphere", *Opt. Lett.* **39**(18), 5274-5276 (2014).
- [72] I. Moreno, J. A. Davis, K. Badham, M. M. Sánchez-López, J. E. Holland, and D. M. Cottrell, "Vector beam polarization state spectrum analyzer", *Sci. Rep.* **7**(1), 1-10 (2017).
- [73] C. Rosales-Guzmán, N. Bhebhe, and A. Forbes, "Simultaneous generation of multiple vector beams on a single SLM", *Opt. Express* **25**(21), 25697-25706 (2017).
- [74] T. W. Clark, R. F. Offer, S. Franke-Arnold, A. S. Arnold, and N. Radwell, "Comparison of beam generation techniques using a phase only spatial light modulator", *Opt. Express* **24**(6), 6249-6264 (2016).
- [75] J. A. Davis, D. M. Cottrell, J. Campos, M. J. Yzuel, and I. Moreno, "Encoding amplitude information onto phase-only filters", *Appl. Opt.* **38**(23), 5004-5013 (1999).
- [76] J. L. Martínez-Fuentes, and I. Moreno, "Random technique to encode complex valued holograms with on axis reconstruction onto phase-only displays", *Opt. Express* **26**(5), 5875-5893 (2018).
- [77] F. Cardano, E. Karimi, S. Slussarenko, L. Marrucci, C. de Lisio, and E. Santamato, "Polarization pattern of vector vortex beams generated by q-plates with different topological charges", *Appl. Opt.* **51**(10), C1-C6 (2012).
- [78] F. Cardano, E. Karimi, L. Marrucci, C. de Lisio, and E. Santamato, "Generation and dynamics of optical beams with polarization singularities", *Opt. Express* **21**(7), 8815-8820 (2013).
- [79] M. M. Sánchez-López, J. A. Davis, I. Moreno, A. Cofré, and D. M. Cottrell, "Gouy phase effects on propagation of pure and hybrid vector beams", *Opt. Express* **27**(3), 2374-2386 (2019).

-
- [80] M. Q. Cai, Z. X. Wang, J. Liang, Y. K. Wang, X. Z. Gao, Y. Li, C. Tu, and H. T. Wang, "High-efficiency and flexible generation of vector vortex optical fields by a reflective phase-only spatial light modulator", *Appl. Opt.* **56**(22), 6175-6180 (2017).
- [81] http://www.arcoptix.com/Q_Plate.htm.
- [82] Z. Zhao, J. Wang, S. Li, and A. E. Willner, "Metamaterials-based broadband generation of orbital angular momentum carrying vector beams", *Opt. Lett.* **38**(6), 932-934 (2013).
- [83] M. Beresna, M. Gecevičius, P. G. Kazansky, and T. Gertus, "Radially polarized optical vortex converter created by femtosecond laser nanostructuring of glass", *Appl. Phys. Lett.* **98**(20), 201101 (2011).
- [84] R. C. Devlin, A. Ambrosio, N. A. Rubin, J. B. Mueller, and F. Capasso, "Arbitrary spin-to-orbital angular momentum conversion of light", *Science* **358**(6365), 896-901 (2017).



Appendix

List of publications



Using birefringence colors to evaluate a tunable liquid-crystal q -plate

DAVID MARCO¹, MARÍA DEL MAR SÁNCHEZ-LÓPEZ^{1,*}, PASCUALA GARCÍA-MARTÍNEZ², AND IGNACIO MORENO³

¹Instituto de Bioingeniería, Universidad Miguel Hernández, 03202 Elche, Spain.

²Departamento de Óptica, Universidad de Valencia, 46100 Burjassot, Spain.

³Departamento de Ciencia de Materiales, Óptica y Tecnología Electrónica, Universidad Miguel Hernández, 03202 Elche, Spain.

*mar.sanchez@umh.es

Received XX Month XXXX; revised XX Month, XXXX; accepted XX Month XXXX; posted XX Month XXXX (Doc. ID XXXXX); published XX Month XXXX

Q-plates are geometrical phase elements that enable the realization of vector beams in simple and compact optical setups. In this work, we consider a tunable liquid-crystal commercial q -plate operative in the visible and near IR range and study its spectral and color birefringence properties under broadband illumination. We first characterize the spectral retardance function of the device in a wide range from 400-1600 nm and determine how it changes upon applied voltage. Then we evaluate the color transmission characteristics when inserting the q -plate between crossed and parallel linear polarizers. These color properties agree with the trajectory in the CIExy chromaticity diagram as the applied voltage changes. Finally, we demonstrate that a simple visual inspection of the transmitted birefringence color perceived when placing the q -plate between crossed polarizers can be used to obtain a rapid estimation of the q -plate retardance at given wavelength ranges. © 2018 Optical Society of America

<http://dx.doi.org/10.1364/AO.99.099999>

1. Introduction

Spatially-variant birefringent elements are becoming very popular to conceive new optical components, such as lenses, gratings, spiral phase plates, etc, in what has been named flat optical metasurfaces [1], geometric-phase elements [2,3], or fourth generation (4G) diffractive optical elements [4]. They are in essence diffractive waveplates where the orientation of the optical axis is spatially modulated in the plane of the waveplate. Among these elements, q -plates are specially interesting since they are employed to generate vector beams [5,6]. When fabricated with liquid-crystals (LC), they can be made tunable via a small voltage applied through coated electrodes [7,8]. While some research prototypes have been reported, to our knowledge, the only existing commercial tunable q -plate device is offered by the company ARCOptix [9]. Here we use this device in combination with a broadband light source to analyze the spectral content of the transmitted light as a function of voltage and the color patterns that are visible when it is placed in between polarizers.

While most of the work developed with q -plates involves monochromatic light, there is an increasing interest in the last years in their application with polychromatic light. For instance, axially symmetric Fresnel rhomb wave-plates have been used to generate achromatic vector beams [10,11] or achromatic angular momentum [12]. These devices use the achromatic retardance induced by Fresnel reflections. Alternatively, circular Bragg reflection from chiral uniaxial media can be exploited to generate reflective broadband q -plates [13].

Other approaches to achieve broadband vector beams require the use of complex optical systems based on spatial light modulators [14].

On the contrary, q -plates based on the material's retardance, as those made of liquid-crystals, exhibit an important retardance dispersion that affects the polarization efficiency conversion [15]. Tunable liquid-crystal q -plates have been demonstrated to operate at different wavelengths, including not only visible [7,8] but also near infrared (NIR) wavelengths [16]. It is also of interest when multiple wavelengths illuminate the q -plate simultaneously, as it is the case when generating a supercontinuum vector beam [17], or for their application in stimulated emission depletion (STED) microscopy, where maximum and zero polarization efficiency conversions are required simultaneously for two selected wavelengths [18]. In some cases, the q -plate can be operated at $\pi/2$ or at $3\pi/2$ retardance, thus generating hybrid vector beams [15,19].

Therefore, it is of great importance to accurately measure the device spectral retardance function $\phi(\lambda)$ in order to evaluate the polarization efficiency conversion for different wavelengths. The measurement of $\phi(\lambda)$ in regular linear retarders is typically done by placing the retarder between crossed and parallel linear polarizers, oriented at 45° with respect to the neutral axes, and illuminating the system with a light source of continuous broadband spectrum [20]. The transmitted light spectrum presents a typical oscillatory behavior with wavelength and can be measured by means of a spectrometer. Then, the spectral retardance function $\phi(\lambda)$ is calculated to give the best fit to the experimental data [21]. We have recently developed a system that combines two spectrometers, one for the visible (VIS) and another for

the near infrared (NIR) ranges, that allows us to measure $\phi(\lambda)$ in a wide spectral range from 400 to more than 1600 nm [22]. However, this technique cannot be directly applied to q -plates, since their optical axis rotates azimuthally in the waveplate plane. Instead, it is more convenient to calibrate the q -plate retardance by inserting the device between circular polarizers [8,15].

The spectral variation of the light transmitted by anisotropic samples placed between crossed polarizers has been used for decades in mineralogy and microscopy. Illuminated under white light, low order anisotropic samples exhibit chromatic effects, known as birefringence colors or interference colors, that can be used to identify materials or minerals according to birefringence. This effect has been applied in liquid-crystal devices for instance to evaluate surface anchoring conditions [23], or to evaluate the modulation properties of twisted-nematic displays [24].

As it will be shown, liquid-crystal q -plate devices also exhibit such birefringence colors. In this work we analyze the birefringence color properties of a tunable liquid-crystal commercial q -plate, and how they can be used to estimate the voltage ranges where the device is tuned for maximum polarization conversion efficiency.

The paper is organized as follows: after this introduction, Section 2 briefly summarizes the q -plate theory. Then, in Section 3 we describe the optical system employed to measure the q -plate spectral retardance. We provide experimental results of the spectrum transmitted by the q -plate inserted between circular polarizers, and this information is used to retrieve the spectral retardance of the device. In Section 4, these spectra are related with the perceived color of the intensity pattern behind the analyzer. We discuss that, when placing the device in between crossed linear polarizers, the intensity pattern is equivalent to that provided by a tuned q -plate illuminated with monochromatic light, but the bright areas show a birefringence color that changes under the applied voltage. This color can be employed to estimate the retardance function of the device. Finally, Section 6 presents the conclusions of our work.

2. Q-plate theory

Q -plates are spatially-variable retarders whose optical axis rotate a fraction q of the azimuthal angle θ , i.e. $\theta = \arctan(y/x)$, thus acting as polarization converters [6]. This q value is always an integer or a semi-integer, so that the principal axis does not exhibit discontinuity lines on the plate, but only a defect in the center that sets the order ($\ell = 2q$) of the output vector beam. Therefore, these retarders can be described by the following Jones matrix [8]:

$$\mathbf{M}_q(\phi) = \mathbf{R}(-q\theta) \cdot \mathbf{W}(\phi) \cdot \mathbf{R}(+q\theta), \quad (1)$$

where the rotation matrix and the Jones matrix of a linear retarder with ϕ retardance and aligned along the $x - y$ coordinates are given, respectively, by:

$$\mathbf{R}(\theta) = \begin{pmatrix} \cos(\theta) & \sin(\theta) \\ -\sin(\theta) & \cos(\theta) \end{pmatrix}, \quad (2a)$$

and

$$\mathbf{W}(\phi) = \begin{pmatrix} \exp(+i\phi/2) & 0 \\ 0 & \exp(-i\phi/2) \end{pmatrix}. \quad (2b)$$

The q -plate Jones matrix obtained in Eq. (1) can then be written as:

$$\mathbf{M}_q(\phi) = \cos\left(\frac{\phi}{2}\right) \mathbf{I} + i \sin\left(\frac{\phi}{2}\right) \mathbf{Q}_q \quad (3)$$

where \mathbf{I} represents the identity matrix, and

$$\mathbf{Q}_q = \begin{pmatrix} \cos(2q\theta) & \sin(2q\theta) \\ \sin(2q\theta) & -\cos(2q\theta) \end{pmatrix} \quad (4)$$

is the Jones matrix of a tuned q -plate ($\phi = \pi$) [6]. Equation (3) shows that the q -plate maximum conversion efficiency is achieved whenever the retardance is an odd multiple of π radians, i.e., the retarder layer is a half-wave retarder. In this situation, the device transforms an input linear polarization onto an ℓ -order linearly polarized vector beam, and converts input circular polarization onto the opposite circular polarization adding an optical vortex of topological charge $\ell = \pm 2q$, where the sign depends on the helicity of the input circular polarization [6].

Equation (3) reveals that the action of a q -plate device with arbitrary retardance on an input polarization state is the superposition of the input state with the state resulting from the action of a regular tuned q -plate. The weight of each term, $\cos(\phi/2)$ and $\sin(\phi/2)$ respectively, depends on the actual retardance of the device. Interesting combinations for the generation of pure and hybrid vector beams were recently discussed [15].

Typically, liquid-crystal q -plates include a single low-order retarder layer, thus their spectral retardance decreases monotonically with wavelength according to the usual expression:

$$\phi = \frac{2\pi}{\lambda} \Delta n \cdot d, \quad (5)$$

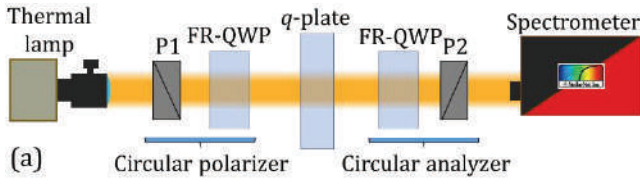
where d is the LC layer thickness and $\Delta n = n_e - n_o$ is the birefringence of the LC material. If in addition the q -plate is electrically tunable, then the effective extraordinary index $n_e(V)$ is voltage dependent, and so it is the retardance $\phi(V)$. As reported in previous works, maximum retardance is achieved without applied voltage, while the retardance decreases for higher voltages [7,8].

Given the above considerations, the precise accurate determination of the spectral function retardance as a function of both the wavelength and the applied voltage $\phi(\lambda, V)$ is of great interest to determine the voltages where the q -plate provides the maximum polarization conversion efficiency for a given operating wavelength. Also, one may be interested in generating hybrid vector beams by operating the device at quarter-wave retardance.

3. Spectral characterization of the q -plate

The retardance characterization of a regular waveplate usually involves placing the retarder in between two crossed linear polarizers oriented at 45° with respect to the neutral axes [20-22]. However, in a q -plate the axes rotate azimuthally, and therefore this method cannot be applied directly. Instead, the q -plate retardance can be measured by placing the device in between crossed circular polarizers [6,12].

Following the procedure in [15] we have spectrally characterized a commercial LC q -plate from ARCOptix [9] (also called variable spiral plate) of $q=0.5$ and nominal operational wavelength range 400-1700 nm. The device retardation is controlled by an AC bias between 0V and 8V. The q -plate is inserted in between two broadband crossed or parallel circular polarizers and it is illuminated with light of a continuous spectrum, as shown in Fig. 1. As derived from Eq. (3), when the q -plate is illuminated with circular polarized light, the output state is a linear combination of right-circularly polarized (RCP) and left-circularly polarized (LCP) light. If we place a circular analyzer, which is crossed/parallel with respect to the input circular polarizer, the normalized transmission at the end of the system is given by:



(a) Schematic of the optical setup for the spectral characterization of the q -plate. (b) Picture of the experimental setup. P1 and P2 are linear polarizers, and FR-QWP are Fresnel rhombs quarter-wave retarders.

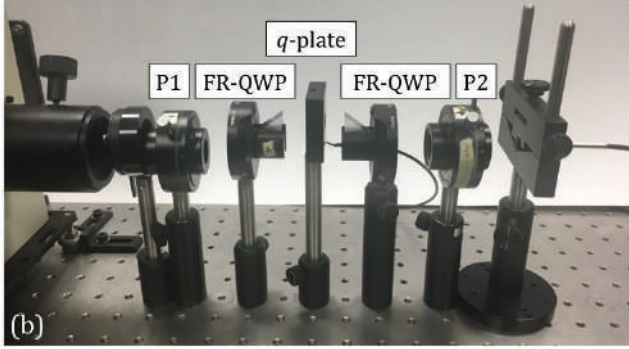


Fig. 1. (a). Scheme of the optical setup for the spectral characterization of the q -plate. (b) Picture of the experimental setup. P1 and P2 are linear polarizers, and FR-QWP are Fresnel rhombs quarter-wave retarders.

$$i_{cros}^{cir} = \sin^2\left(\frac{\phi(\lambda)}{2}\right), \quad (6a)$$

$$i_{par}^{cir} = \cos^2\left(\frac{\phi(\lambda)}{2}\right). \quad (6b)$$

We illuminate the system with a quartz tungsten halogen (QTH) lamp from Oriel (model 66882), with adjustable power from 10 to 250 watts. It provides light of continuous broadband spectrum from 400 nm to more than 1600 nm. We build the broadband circular polarizers by orienting two calcite Glan-Taylor cube polarizers (Edmund Optics, with an operation range from 350 to 2200 nm) at 45° with respect to the neutral axes of two achromatic quarter-wave Fresnel rhombs. The Fresnel rhombs (Thorlabs, model FR600QM) exhibit a maximum retardance deviation of less than 3° [25] in the 400 to 1550 nm range. The spectral transmission of the whole system is measured by two different spectrometers. For the visible range, we capture the beam with a STN-F600_UVVIS-SR optical fiber that sends the light to a VIS spectrometer (Stellar-Net, model STN-BLK-C-SR), which measures light from 200 nm to 1080 nm. To measure in the near infrared, we send the beam directly to a NIR spectrometer (Stellar-Net, model STE-RED-WAVE-NIR-512-25), which operates in the 900 nm to 1700 nm range. We measured the NIR data with the lamp set at a power of 20 watts, while the VIS data required a power of 40 watts in order to have more light in the violet region.

Figure 2 shows the spectrum $I_S(\lambda)$ of the maximum possible transmission of the optical system (q -plate between circular polarizers), measured in the visible range with the QTH lamp power set at 40 W. It was obtained by adding for each wavelength the output irradiance values for crossed and parallel circular polarizers. It follows the typical spectrum of a QTH lamp, where the irradiance diminishes gradually as the wavelength decreases. The spectrum $I(\lambda)$ of the light transmitted by the q -plate system between polarizers is then given by:

$$I(\lambda) = i(\lambda)I_S(\lambda), \quad (7)$$

where $i(\lambda)$ is the normalized spectral transmission, which depends on the selected polarization configuration. For crossed/parallel circular polarizers, $i(\lambda)$ is given by Eqs. (6). We consider $I(\lambda)$ in the next section for the color evaluation of the q -plate device.

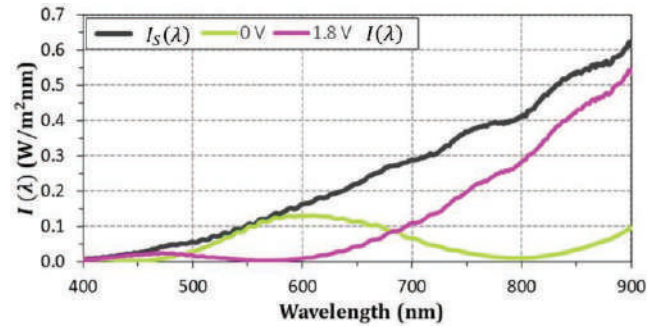


Fig. 2. Spectrum $I_S(\lambda)$ of the maximum transmission of the optical system with the QTH lamp power set at 40 W (black line). This spectrum was obtained by adding the two irradiances measured for the q -plate between crossed and parallel circular polarizers with no bias voltage. Transmitted spectrum $I(\lambda)$ of the q -plate between crossed circular polarizers at 0V (green line) and 1.8V (pink line).

However, as mentioned before, we extend the spectral characterization range by adding in NIR measurements. Figure 3 shows the normalized spectral transmission when the q -plate is illuminated between crossed circular polarizers, for different applied voltages. Blue points correspond to data measured with the VIS spectrometer, while red points correspond to data captured with the NIR spectrometer. These data were obtained by measuring the spectrum for crossed circular polarizers and for parallel circular polarizers. Then the spectrum for crossed polarizers was divided by the addition of the spectra for crossed and parallel polarizers. These calculations were made for every wavelength measured by the spectrometers, and the resulting normalized curve is directly comparable to Eq. (6a).

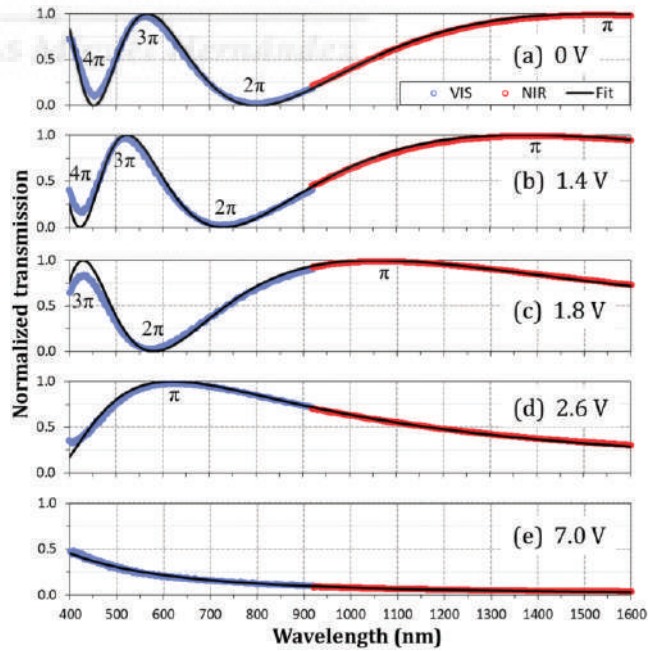


Fig. 3. (a)–(e) Normalized spectral transmission of the q -plate between crossed circular polarizers for bias voltages: 0 V, 1.4 V, 1.8 V, 2.6 V and 7.0 V. Measured data are shown in blue and red for the VIS and NIR spectrometers, respectively. Black curves denote the calculated transmission that best fit the experimental data.

The curves in Fig. 3 show the expected behavior. The transmitted spectrum shows oscillations originated by the wavelength dependence

of the retardance (Eq. (5)) and the sinusoidal transmission (Eq. (6a)). The maxima in the curves in Fig. 3 denote the wavelengths where the retardance is an odd multiple of π . At these wavelengths there is a full conversion from a homogeneous polarized beam to the corresponding vector beam. On the contrary, the minima of the curves denote the wavelengths for which the retardance is an even number of π . For these wavelengths, the q -plate shows a null polarization conversion, according to Eq. (3). Note that the experimental data do not reach the values 0 or 1 in the violet region. We attribute this effect to the high noise contribution, due to the weak intensity of the light provided by the lamp in this region. Nevertheless, the data in Fig. 3 can be used to fit the spectral retardance function.

The retardance for each wavelength and for each measured voltage is retrieved from:

$$\phi(\lambda) = 2\arcsin\left(\sqrt{i_{cross}^{cir}(\lambda)}\right), \quad (8)$$

which is derived from Eq. (6a). Since this equation only provides phase values between 0 and π radians, we impose the condition that the retardance must be a continuous and monotonically decreasing function of wavelength [22], in agreement with Eq. (5). Together with the knowledge that the retardance decreases as the voltage increases, it is thus possible to easily identify the order of the retarder. Starting from the maximum applied voltage (Fig. 3(e)), where only minimal residual retardance is observed, the retardance increases for lower voltages. This allows identifying the retardance of π radians as the maximum located around 600 nm for $V=2.6V$ (Fig. 3(d)). This maximum shifts to wavelengths around 1050 nm, 1400 nm and 1600 nm when the voltage decreases to 1.8V (Fig. 3(c)), 1.4V (Fig. 3(b)), and to zero (Fig. 3(a)). Following this procedure it is possible to easily identify other wavelengths where the retardance is $\phi(\lambda) = m\pi$, as indicated in Fig. 3.

Note that this analysis is relevant for the application of q -plates in STED microscopy [18]. In that case, the sample must be illuminated with a Gaussian beam of wavelength that excites the fluorescence, and a vortex beam of a second wavelength that inhibits fluorescence—except within the optical singularity—. Different pairs of wavelengths can be used. Different pairs of wavelengths appropriate to be applied with different dyes common in STED microscopy were reported by Yan *et al* [18]. Among all the possible pairs indicated in that reference, we find that the ARCoOptix q -plate would only be useful for STED microscopy with the 532-440 nm pair and setting the bias voltage at about 1.3V. Namely, we find maximum polarization conversion efficiency at 537 nm (fluorescence inhibition wavelength) and minimum efficiency at 438 nm (fluorescence activating wavelength). Note that a q -plate made of the same liquid-crystal, but with a thicker layer, would provide more oscillations in the spectrum, and therefore could be used for STED microscopy at a wider number of wavelength pairs [18,26].

Figure 4(a) shows the spectral retardance fitted from the spectra in Fig. 3. We assume that the refractive indices of the retarder can be described by a Cauchy dispersion relation [27]. Therefore, we fit the experimental spectral retardance function given in Eq. (8) to $\phi_{fit}(\lambda) = A/\lambda + B/\lambda^3$, and find the constants A and B that best recover the experimental retardance. The values of the fitted retardance are then used into Eq. (6) in order to calculate the normalized transmission, which is plotted as a black continuous line in Fig. 3 together with the experimental data.

The curves in Fig. 4(a) show the expected behavior, where the retardance progressively decreases with wavelength and with the applied voltage. We select four wavelengths and show their retardance dependence with voltage in Fig. 4(b). These wavelengths correspond to the violet diode laser (405 nm), the He-Ne laser (633 nm), a near IR laser (980 nm) and the optical communications band (1550 nm). Of course, any other wavelength in the measured range could be evaluated. Slight

discontinuities in the retardance curve for 405 nm are observed, that we attribute to the low signal-to-noise ratio at this wavelength, due to the low intensity provided by the thermal lamp at short wavelengths.

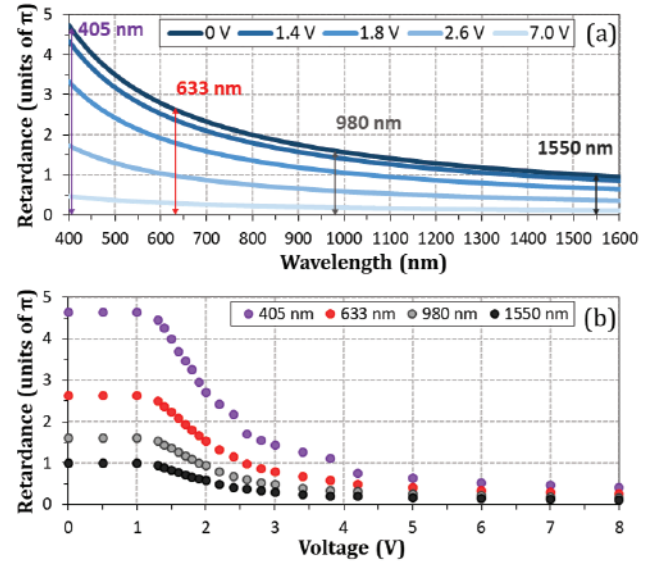


Fig. 4. (a) Spectral retardance of the q -plate for various voltages; (b) Q -plate retardance versus voltage for four selected wavelengths.

The previous results demonstrate a systematic and accurate experimental procedure to derive the spectral retardance function of the q -plate. The variations with voltage of the spectral transmission have implications in the color that is perceived when the device is placed between linear polarizers. In the next section we analyze these effects.

4. Study of the birefringence colors

Birefringence colors have been known for decades to give information about the spectral retardance of materials. In this section we relate the color properties of the light transmitted by the q -plate placed in between polarizers with the spectral transmission results discussed in the previous section. Note that the only relevant information for this purpose is the illuminant spectrum (Fig. 2) and the transmission in the visible spectral region, so we can at this point ignore the NIR measurements.

Birefringence colors are observed when placing the sample between crossed linear polarizers. Note that in this situation the identity matrix term in Eq. (3) does not play any role. Since this term does not transform the input polarization, its corresponding output will be blocked by the output analyzer. It is a simple Jones matrix calculation to derive that the intensity pattern transmitted by the system composed by the q -plate inserted in between crossed linear polarizers is now given by

$$i_{cross}^{lin} = \sin^2\left(\frac{\phi(\lambda)}{2}\right) \sin^2(2q\theta). \quad (9)$$

The term $\sin^2(2q\theta)$ in this equation yields an azimuthal distribution of the transmitted intensity, with the typical two-lobe dark pattern generated by linearly polarized first-order vector beams illuminating a linear analyzer. The above relation indicates that the q -plate inserted between crossed linear polarizers shows the same intensity pattern with two dark lobes for all wavelengths, and only the intensity of the bright lobes changes with wavelength according to the factor $\sin^2(\phi(\lambda)/2)$. Note that this factor is exactly the one in Eq. (6a) which is shown in Fig. 3. But when the q -plate is located between crossed

circular polarizers, the transmission is spatially uniform as provided by Eq. (6a), which is devoid of the azimuthal term.

A q -plate inserted between linear polarizers generates a characteristic spatial pattern in the form of azimuthal lobes when illuminated with monochromatic light. Eq. (9) reveals that exactly the same pattern will be generated for all wavelengths if the q -plate is between crossed linear polarizers. Therefore, in this situation, if the system is illuminated with polychromatic light, it will present a uniform color in the bright lobes, fixed by the spectral transmission curves shown in Fig. 3. Note that this is the case only when the linear polarizers are crossed. In other configurations, where the polarizers would not be crossed, the identity term in Eq. (3) will contribute also to the transmitted light, providing thus a color variation along the azimuthal pattern.

As shown in the previous section, the ARCOptix q -plate retardance can be tuned via an applied voltage, and so does the normalized transmission. Therefore, the color of these bright areas can be varied with voltage, and it can be used to achieve a fast evaluation of the operation conditions of the device.

This is shown in Fig. 5. Figure 5(a) shows pictures of the q -plate placed between two crossed linear polarizers, that were taken with a Nikon D3300 photographic camera. All images display the same intensity pattern with two bright lobes and two dark lobes, as expected for a q -plate with $q=0.5$. Note how the color of the bright areas changes as different voltages are applied to the device. However, the color is always uniform. The two dark lobes indicate the spatial regions where the output polarization is crossed with respect to the transmission axis of the analyzer.

This is not the case of Fig. 5(b), where the q -plate is now placed between parallel linear polarizers. The intensity pattern obtained for the parallel linear polarizers configuration is:

$$i_{par}^{lin} = \cos^2\left(\frac{\phi(\lambda)}{2}\right) + \sin^2\left(\frac{\phi(\lambda)}{2}\right) \cos^2(2q\theta). \quad (10)$$

Note that this expression contains two terms: the first term is spatially uniform, and thus provides a uniform background; the second term, varies with the azimuthal angle with a spatial distribution that is complementary to the one in Eq. (9). As a consequence, now white lobes appear where dark areas were present with crossed polarizers. Therefore, the azimuthal color variation now changes from white to a color complementary to that observed with crossed polarizers. This is similar to the birefringent colors observed with linear retarders [28], but the q -plate generates them along the azimuthal coordinate.

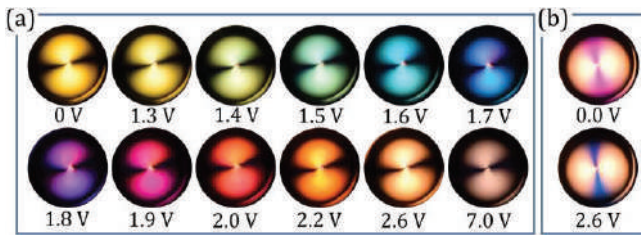


Fig. 5. Photographs of the q -plate with various applied voltages and placed between (a) crossed and (b) parallel linear polarizers.

In order to evaluate the color properties shown in Fig. 5(a), first we calculate the tristimulus values of the light transmitted at the end of the system with crossed polarizers by projecting the measured spectral irradiance $I(\lambda, V)$ onto the basis of the color matching functions. According to the CIE 1931-XYZ standard observer, the tristimulus values can be obtained as [29]:

$$X(V) = \int_0^\infty I(\lambda, V) \bar{x}(\lambda) d\lambda, \quad (11a)$$

$$Y(V) = \int_0^\infty I(\lambda, V) \bar{y}(\lambda) d\lambda, \quad (11b)$$

$$Z(V) = \int_0^\infty I(\lambda, V) \bar{z}(\lambda) d\lambda, \quad (11c)$$

where $\bar{x}(\lambda)$, $\bar{y}(\lambda)$ and $\bar{z}(\lambda)$ are the color matching functions, that represent the response of the human eye to an arbitrary electromagnetic spectrum. The curve $I(\lambda, V)$ is given by Eq. (7), considering, for every voltage value, the corresponding normalized transmission obtained for crossed circular polarizers (Eq. (6a)). The chromaticity coordinates are calculated as

$$x(V) = \frac{X(V)}{X(V)+Y(V)+Z(V)}, \quad (12a)$$

$$y(V) = \frac{Y(V)}{X(V)+Y(V)+Z(V)}, \quad (12b)$$

$$z(V) = \frac{Z(V)}{X(V)+Y(V)+Z(V)}. \quad (12c)$$

Then, the perceived color as the applied voltage changes is described by the coordinates $x(V)$ and $y(V)$ of the corresponding point in the CIExy chromaticity diagram. Figure 6(a) shows this diagram and the trajectory of the corresponding chromaticity coordinates as the applied voltage increases.

It is interesting to remark that these birefringence colors are visible when the q -plate retarder exhibits a first-order retardance. The spectral normalized transmission in Fig. 3 shows that a 2π retardance (identified as the minimum transmission) transmits the visible wavelengths for voltages between 1.5V and 2.0V. For smaller retardances, the spectrum varies so slowly that the transmitted light would appear white. For higher-order retardances, the transmitted spectrum oscillates so rapidly that there is enough energy in all regions of the visible light, and again it would look white. However, for the first-order retardance, the birefringence colors are clearly visible. This is therefore an extremely simple method to determine when the retardance is approximately 2π .

Finally, in order to fully characterize the color perception of the output transmittance, the information about the brightness is also required and that is determined by the illuminance function $I_V(V)$, calculated as:

$$I_V(V) = K_n Y(V), \quad (13)$$

where $K_n = 683 \text{ lm/W}$ denotes the maximum photopic luminous efficiency of the human eye. Figure 6(b) shows the illuminance function versus the applied voltage. The higher value for illuminance corresponds to 1.4V. At this value, as can be appreciated in Fig. 3(b), most of the transmitted light is in the green region of the visible spectrum, where the maximum visual response of the human eye lays. The illuminance lowest value is obtained for a voltage of 1.8V where, as Fig. 3(c) shows, the spectral transmittance reaches its lowest value around 560 nm. In this case, the higher contribution of the transmitted light is in the blue and red regions of the visible spectrum, which contribute less to the illuminance. Note that this transition around the minimum illuminance corresponds to a detour of the $y(x)$ trajectory in Fig. 6(a) around the cyan-blue-magenta region. Thus, the minimum illuminance is again a sign that the 2π retardance transmits the center of the visible spectrum.

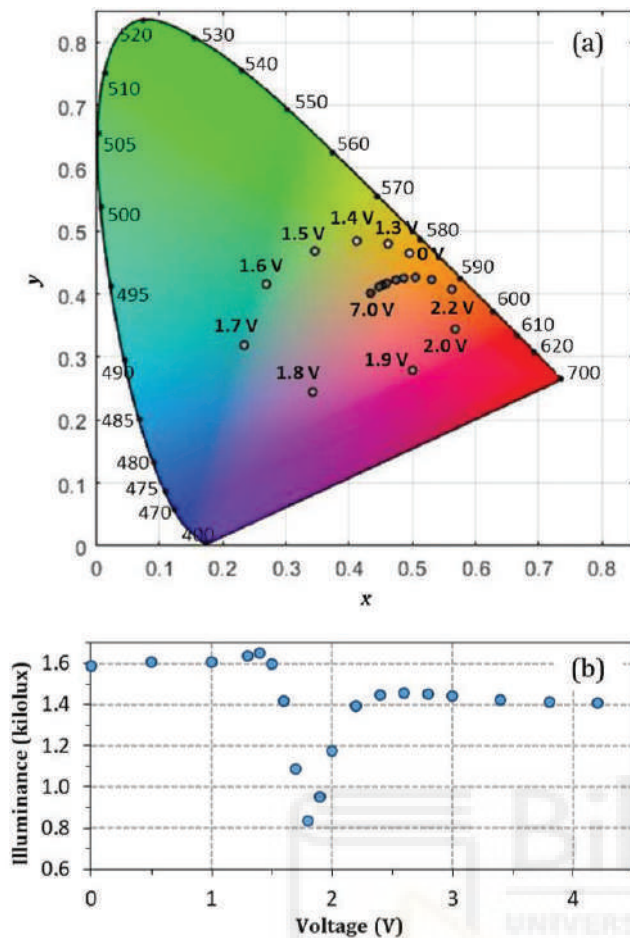


Fig. 6 (a) Chromaticity CIExy diagram for different voltages. The voltage values not indicated for some points are: 2.4 V, 2.6 V, 2.8 V, 3 V, 3.4 V, 3.8 V and 4.2 V. (b) Illuminance for different applied voltages.

5. Conclusions

In summary, a study of the spectral and color properties of a tunable liquid-crystal commercial q -plate operating in the VIS and NIR range has been presented. First, we apply a previously reported experimental system to characterize the q -plate retardance as a function of wavelength and voltage in the range from 400 to 1600 nm. For that purpose, the q -plate was placed between crossed and parallel circular polarizers built with quarter-wave Fresnel rhombs and Glan-Taylor linear polarizers. The spectral transmission curves obtained in such a wide spectral range allows easily identifying the order of the retardance by simply regarding the evolution of the transmission minima and maxima as the voltage changes. A pair of wavelengths and the required bias voltage is identified for a possible application of this commercial q -plate in STED microscopy.

In the second part of the paper, we provided a comprehensive description of the color properties perceived upon changing the bias voltage when placing the q -plate between linear polarizers. This is a common situation for a q -plate under monochromatic light. Here instead, the device is illuminated with broadband light. We demonstrated that the typical intensity pattern consisting of azimuthal dark lobes (displayed by a q -plate tuned at π retardance) is obtained for all wavelengths, provided the input and output linear polarizers are crossed. In this situation, the bright lobes exhibit a uniform color, with the birefringence color being determined by the spectral transmission.

These color properties are accounted for by the trajectory in the CIExy chromaticity diagram as the applied voltage changes.

Finally, we have shown a strong variation of the birefringence color when the first-order retardance transits the visible region of the spectrum. Thus, this can be considered as an extremely simple method to determine when the q -plate is reaching a retardance of about 2π radians, a technique capable to be used even with the naked eye. Alternatively, low cost spectrometers [30] could also be applied to make the kind of measurements here presented.

Funding Information. This research has been funded by Generalitat Valenciana, Conselleria d'Educació, Investigació, Cultura i Esport (PROMETEO-2017-154) and Ministerio de Economía, Industria y Competitividad of Spain and European Union (MIMECO/FEDER funds, grant FIS2015-66328-C3-3-R).

References

1. N. Yu and F. Capasso, "Flat optics with designer metasurfaces", *Nat. Materials* **13**, 139–150 (2014).
2. J. Kim, Y. Li, M.N. Miskiewicz, C. Oh, M.W. Kudenov, and M.J. Escuti, "Fabrication of ideal geometric-phase holograms with arbitrary wavefronts", *Optica* **2**(11), 958-964 (2015).
3. R. Drevinskas and P.G. Kazansky, "High-performance geometric phase elements in silica glass"; *APL Photonics* **2**, 066104 (2017).
4. L. De Sio, D. E. Roberts, Z. Liao, S. Nersisyan, O. Uskova, L. Wickboldt, N. Tabiryan, D.M. Steeves, and B. R. Kimball, "Digital polarization holography advancing geometrical phase optics", *Opt. Express* **24**(16), 18297-18306 (2016).
5. M. Stalder and M. Schadt, "Linearly polarized light with axial symmetry generated by liquid-crystal polarization converters," *Opt. Lett.* **21**, 1948-1950 (1996).
6. L. Marrucci, C. Manzo, and D. Paparo, "Optical spin-to-orbital angular momentum conversion in inhomogeneous anisotropic media," *Phys. Rev. Lett.* **96**, 163905 (2006).
7. S. Slussarenko, A. Murauski, T. Du, V. Chigrinov, L. Marrucci, and E. Santamato, "Tunable liquid crystal q -plates with arbitrary topological charge," *Opt. Express* **19**, 4085-4090 (2011).
8. J. A. Davis, N. Hashimoto, M. Kurihara, E. Hurtado, M. Pierce, M. M. Sánchez-López, K. Badham, and I. Moreno, "Analysis of a segmented q -plate tunable retarder for the generation of first-order vector beams," *Appl. Opt.* **54**, 9583-9590 (2015).
9. http://www.arcoptix.com/Q_Plate.htm
10. T. Wakayama, K. Komaki, Y. Otani, and T. Yoshizawa, "Achromatic axially symmetric wave plate", *Opt. Express* **20**(28), 29260-29265 (2012).
11. T. Wakayama, O. G. Rodríguez-Herrera, J. Scott Tyo, Y. Otani, M. Yonemura, and T. Yoshizawa, "Generation of achromatic, uniform-phase, radially polarized beams", *Opt. Express* **22**(3), 3306-3315 (2014).
12. F. Bouchard, H. Mand, M. Mirhosseini, E. Karimi, and R. W. Boyd, "Achromatic orbital angular momentum generator", *New J. Phys.* **16**, 123006 (2014).
13. M. Rafayelyan and E. Brasselet, "Bragg-Berry mirrors: reflective broadband q -plates", *Opt. Lett.* **41**(17), 3972-3975 (2016).
14. K. J. Mitchell, N. Radwell, S. Franke-Arnold, M. J. Padgett, and D. B. Phillips, "Polarisation structuring of broadband light", *Opt. Express* **25**(21), 25079-25089 (2017).
15. M. M. Sánchez-López, I. Abella, D. Puerto-García, J. A. Davis, I. Moreno, "Spectral performance of a zero-order liquid-crystal polymer commercial q -plate for the generation of vector beams at different wavelengths," *Opt. Laser Technol.* **106**, 168–176 (2018).
16. K. Badham, S. Delaney, N. Hashimoto, M. M. Sánchez-López, M. Kurihara, A. Tanabe, I. Moreno, and J. A. Davis, "Generation of vector beams at 1550 nm telecommunications wavelength using a segmented q -plate," *Opt. Eng.* **55**, 030502 (2016).

17. Y. S. Rumala, G. Milione, T. A. Nguyen, S. Pratavieira, Z. Hossain, D. Nolan, S. Slussarenko, E. Karimi, L. Marrucci, and R. R. Alfano, "Tunable super-continuum light vector vortex beam generator using a q -plate," *Opt. Lett.* **38**, 5083-5086 (2013).
18. L. Yan, P. Gregg, E. Karimi, A. Rubano, L. Marrucci, R. Boyd, and S. Ramachandran, "Q-plate enabled spectrally diversified orbital-angular-momentum conversion for stimulated emission depletion microscopy," *Optica* **2**, 900-903 (2015).
19. M. Beresna, M. Gecevičius, P. G. Kazansky, and T. Gertus, "Radially polarized optical vortex converter created by femtosecond laser nanostructuring of glass", *Appl. Phys. Lett.* **98**, 211101 (2011).
20. M. Emam-Ismael, "Spectral variation of the birefringence, group birefringence and retardance of a gypsum plate measured using the interference of polarized light," *Opt. Laser Technol.* **41**, 615-621 (2009).
21. A. Vargas, R. Donoso, M. Ramírez, J. Carrión, M. M. Sánchez-López and I. Moreno, "Liquid crystal retarder spectral retardance characterization based on a Cauchy dispersion relation and a voltage transfer function", *Opt. Review*, **20**(5), 378-384 (2013).
22. A. Messaadi, M. M. Sánchez-López, P. García-Martínez, A. Vargas, and I. Moreno, "Optical system for measuring the spectral retardance function in an extended range," *J. Eur. Opt. Soc. – Rapid Pub.* **12**, 21 (2016).
23. Y. Zou, J. Namkung, Y. Lin, D. Ke, and R. Lindquist, "Interference colors of nematic liquid crystal films at different applied voltages and surface anchoring conditions", *Opt. Express* **19**(4), 3297-3303 (2011).
24. J. L. Martínez, P. García-Martínez, M. M. Sánchez-López, I. Moreno, "Accurate color predictability based on a spectral retardance model of a twisted-nematic liquid-crystal display", *Opt. Commun.* **284**, 2441–2447 (2011).
25. https://www.thorlabs.com/newgrouppage9.cfm?objectgroup_id=154 (visited 2018/11/25).
26. <https://nanobiophotonics.mpibpc.mpg.de/dyes/> (visited 2018/11/25).
27. J. Li, C.H. Wen, S. Gauza, R. Lu, and S.T. Wu, "Refractive indices of liquid crystals for display applications", *J. Displ. Technol.* **1**, 51–61 (2005).
28. P. Velásquez, M. M. Sánchez-López, I. Moreno, D. Puerto, and F. Mateos, "Interference birefringent filters fabricated with low cost commercial polymers", *Am. J. Phys.* **73**(4), 357-361 (2005).
29. D. Malacara, *Color Vision and Colorimetry*, SPIE Press, Bellingham (2002).
30. T. C. Muñoz Hernández, E. González-Valencia, P. Torres, D. L. Aristizábal Ramírez, "Low-cost spectrometer for educational applications using mobile devices"; *Opt. Pura Apl.* **50**(3), 221-228 (2017).





Optimal triplicator design applied to a geometric phase vortex grating

DAVID MARCO,¹ MARÍA M. SÁNCHEZ-LÓPEZ,¹ AARÓN COFRÉ,^{2,3} ASTICIO VARGAS,² AND IGNACIO MORENO^{3,*}

¹*Instituto de Bioingeniería, Departamento de Física Aplicada, Universidad Miguel Hernández de Elche, 03202 Elche, Spain*

²*Departamento de Ciencias Físicas, Universidad de La Frontera, Temuco, Chile*

³*Departamento de Ciencia de Materiales, Óptica y Tecnología Electrónica, Universidad Miguel Hernández de Elche, 03202 Elche, Spain*

**i.moreno@umh.es*

Abstract: In this work, a geometric phase liquid-crystal diffraction grating based on the optimal triplicator design is realized, i.e., a phase-only profile that generates three diffraction orders with equal intensity and maximum diffraction efficiency. We analyze the polarization properties of this special diffraction grating and then use embedded spiral phases to design geometric phase vortex diffraction gratings. Finally, the fabrication of a two-dimensional version of such a design using a micro-patterned half-wave retarder is demonstrated, where the phase distribution is encoded as the orientation of the fast axis of the retarder. This proof-of-concept element is made of liquid crystal on BK7 substrate where the orientation of the LC is controlled via photoalignment, using a commercially available fabrication facility. Experimental results demonstrate the parallel generation of vortex beams with different topological charge and different states of polarization.

© 2019 Optical Society of America under the terms of the [OSA Open Access Publishing Agreement](#)

1. Introduction

The design and realization of diffraction gratings of evenly distributed intensity among a number of diffraction orders has been extensively studied. One initial approach that became very popular are Damman gratings [1], which consist on gratings with a binary profile, where the transition points must be conveniently selected to provide the desired number of equally intense orders. Since then, this field continued to receive attention and applications such as diffractive elements for beam splitting and optical array illuminators were developed [2]. In 1998, Franco Gori and his associates introduced the analytical derivation of the optimal phase triplicator [3], a diffraction grating with a continuous phase-only profile that generates three diffraction orders (zero order and plus and minus first orders) with equal intensity and maximum diffraction efficiency. Although fabricating a grating with a continuous profile is more complicated than making binary profiles, the efficiency of Gori's design (about $\eta = 93\%$) is very attractive, and the simplicity and beauty of its analytical expression makes it very easy to program and implement in a phase-only spatial light modulator (SLM) [4,5]. Some years after Gori's design, Romero and Dickey developed a generalized theory for designing continuous phase-only gratings that generate an arbitrary number of diffraction orders [6].

The interest of such grating profiles is not only limited to standard diffraction gratings. If combined with other phase functions (like those representing a lens or a helical plate), they can yield vortex gratings generating diffraction orders of different topological charges [7–9], or creating a three-dimensional array [10]. These vortex gratings have been extended to more complicated diffraction gratings in order to obtain vector beams. This is usually done by employing SLMs in different arrangements [11–13] to create the superposition of two beams with orthogonal polarizations and opposite vortex charge [14].

Despite the great flexibility that SLM offer, their use implies the realization of bulky systems. An alternative for making such elements more compact is based on encoding them as geometric phase (GP) elements, also known as Pancharatnam-Berry phase elements [15,16]. These are spatially variant half-wave retarders, where the orientation of the principal axis changes in-plane according to a given function. When illuminated with circularly polarized light, GP diffractive elements change the helicity of the circular polarization, but also imparts to the beam a phase function equal to twice the angular orientation of the retarder's principal axis. This way it is possible to create planar diffractive optical elements.

GP diffractive elements can be fabricated by photo-aligning liquid-crystals (LC) [15,17]. LC based GP elements can be reconfigurable upon applying a voltage [18] and consequently the operating wavelength can be tuned. Instead, they can operate in a wide spectral range when based on cholesteric LC structures [19]. More complex designs involve not only controlling the orientation of the spatial retarder, but also the spatial variation of an additional phase, thus encoding two independent phase functions onto the two circular polarizations [20]. In this case, these elements are typically fabricated by nanostructuring metasurfaces [21]. While metamaterial-based GP elements are advantageous in terms of much higher energy damage threshold which renders them especially appropriate for operation with high-power lasers, LC based GP elements are easier to fabricate and represent a lower-cost method of fabrication. In fact, commercially available GP elements, such as vortex retarders and polarization sensitive lenses, can be exploited to design new optical systems [22]. In addition, some manufacturers offer the possibility to fabricate GP elements on demand, designed by the user.

This is the case in this work. Here we present the design and characterization of a special liquid-crystal GP diffraction grating. It creates a bidimensional array of 3×3 diffraction orders, obtained by combining two phase-only Gori's triplicators, one along the horizontal direction and another along the vertical direction. In addition, spiral phases of charges $\ell = 1$ and $\ell = 3$ are embedded in each direction. As a result, the grating generates in these nine diffraction orders vortex beams with topological charges that change from $\ell = -4$ to $\ell = +4$.

This diffraction grating is then fabricated as a GP diffractive element. For that purpose, we benefit from the facility provided by Thorlabs Inc. to fabricate customized liquid-crystal patterned retarders. These are composed of an array of microretarders with different orientation of the fast axis [23]. In our case, we ordered a custom half-wave retarder for the wavelength of 632.8 nm, where the axis alignment of the microretarders follow the above-mentioned diffraction grating profile. As a result, the designed grating is encoded as a GP diffraction grating. We demonstrate the expected array of vortex beams with different charges when the grating is illuminated with circular polarization. The polarization conversion is achieved when the grating is illuminated with circularly polarized light. When it is illuminated with linearly polarized light, however, the central order shows a different polarization conversion with respect to the lateral orders. We show that this is a consequence of Gori's triplicator design, that includes a $\pi/2$ phase shift between the central order and the two lateral orders, which was not reported before. We note that a closely related design was presented recently in [24], where a 2D triplicator grating was combined with a spiral phase and fabricated as a GP metasurface. Our design differs, since it yields different charges onto different orders (opposed to the design in [24] where the same charge is obtained in the 3×3 diffraction orders).

The paper is organized as follows: after this Introduction, section 2 describes the grating's design, where a first part reviews Gori's triplicator. This scalar analysis is extended to a GP grating in Section 3, thus requiring a vector analysis that is based on the Jones matrix formalism. Section 4 describes the experimental system and discusses the experimental results, which demonstrate an excellent agreement with the expected results. Finally, Section 5 summarizes the conclusions of the work. The Appendix included at the end contains the required mathematical derivations for the sake of clarity.

2. The scalar grating design

In this section we describe the design of the phase vortex grating. First, we review Gori's design in a pure scalar treatment. Then we extend it to its application to a fork grating, i.e. a blaze grating with an embedded spiral phase. Finally, we describe the polarization effects when this grating profile is implemented as a geometric-phase diffractive element.

2.1. Gori's triplicator phase-only profile

As mentioned, in [3] Gori and his associates developed an analytical solution for the scalar phase-only triplicator, i.e., a diffraction grating exhibiting a continuous phase-only profile that generates three diffraction orders (zero and ± 1) of the same intensity and reaching the maximum diffraction. The phase profile they derived is given by

$$\phi(x) = \arctan \left[a \cos \left(\frac{2\pi x}{p} \right) \right], \quad (1)$$

where x denotes the transversal coordinate, p is the grating's period and $a = 2.65718$ is a numerical constant derived in [3]. We note here that in Gori's paper, the cosine function in Eq. (1) is instead a sine function, but this only implies a half period lateral displacement of the grating. We selected the cosine function in Eq. (1) because we found it simpler to analyze the Fourier spectrum, calculation that is presented in the Appendix of this manuscript.

The transmittance of the triplicator grating is given by

$$\tau_{rip}(x) = \exp[i\phi(x)] = \sum_{n=-\infty}^{+\infty} \tau_n \exp\left(in \frac{2\pi x}{p}\right), \quad (2)$$

where τ_n indicate the Fourier transform coefficients:

$$\tau_n = \frac{1}{p} \int_{-p/2}^{p/2} \exp[i\phi(x)] \exp\left(-in \frac{2\pi x}{p}\right) dx. \quad (3)$$

According to [3], the square magnitude of the three main diffraction orders is $|\tau_0|^2 = |\tau_{+1}|^2 = |\tau_{-1}|^2 = 30.85\%$, rendering a total diffraction efficiency $\eta = |\tau_0|^2 + |\tau_{+1}|^2 + |\tau_{-1}|^2 = 92.56\%$. We note that this triplicator optimal efficiency is notably higher than that provided by the Dammann grating producing three diffraction orders, which is only of 66.42% [4,25].

Figure 1(a) shows three periods of the phase profile $\phi(x)$ given by Eq. (1) (black curve), which is compared with a linear blazed phase grating of the same period (blue curve). One interesting characteristic to note about Gori's triplicator profile is that the phase modulation changes from a minimum value of -0.39π to a maximum value of $+0.39\pi$, thus only requiring a total phase modulation of 0.78π to be perfectly displayed. Therefore, it is possible to implement it using SLM devices of very low phase levels [5]. Figure 1(b) illustrates the gray-level image that must be displayed onto a phase-only SLM to generate this triplicator.

Given the very reduced intensity of the diffraction orders different than order 0 and ± 1 , we can consider that the triplicator merely generates these three diffraction orders (Fig. 1(c)) and Eq. (2) can be approximated as

$$\tau_{rip}(x) = \exp[i\phi(x)] \cong \tau_0 + \tau_{+1} \exp\left(i \frac{2\pi x}{p}\right) + \tau_{-1} \exp\left(-i \frac{2\pi x}{p}\right). \quad (4)$$

An important point that was not analyzed by Gori et al. in [3] is the relative phase shift between these three diffraction orders. In the Appendix, it is shown that there is a $\pi/2$ phase shift between the $+1$ and -1 orders with respect to the zero order, hence, they hold the following relation

$$\tau_{+1} = \tau_{-1} = i\tau_0. \quad (5)$$

As we show later, this i factor has crucial impact when this design is implemented with geometric phase.

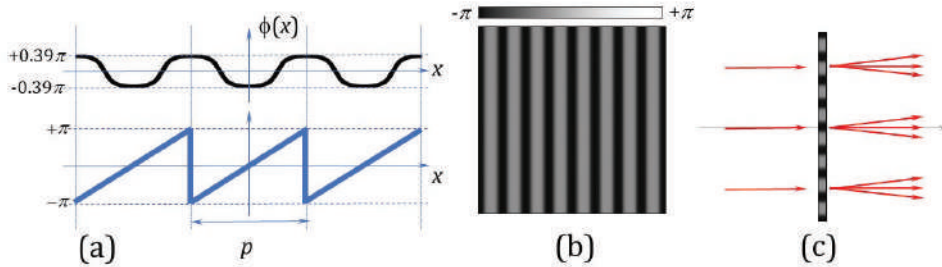


Fig. 1. (a) Gori's triplicator phase profile compared to the linear blaze grating profile. (b) Gray level image to generate a triplicator in a phase-only SLM. (c) Schematics of the triplication grating action.

2.2. The vortex triplicator grating

Figure 1(a) can be viewed as a phase look-up table (LUT) that assigns the phase of the triplicator profile to the corresponding phase value of the blazed (linear) profile, i.e.

$$\tau_{trip}(x) = \text{LUT}[\tau_{linear}(x)], \quad (6)$$

where $\tau_{linear}(x) = \exp(i2\pi x/p)$. In this way, the phase LUT applies to all the phase values ranging from $-\pi$ to $+\pi$, and the triplicator design can be extended to more complex optical functions, different than a simple diffraction grating. An equivalent approach was applied for instance in [8] to binary phase Dammann grating profiles.

This is the case of the fork blazed phase grating. This grating is obtained by adding a spiral phase pattern to a linear blazed grating, whose transmittance is given by:

$$\tau_{fork}(x, \theta) = \exp\left[i\left(\frac{2\pi x}{p} + \ell \theta\right)\right]. \quad (7)$$

This phase-only function can be regarded as a blazed diffraction grating which generates a single first-order diffraction order that carries a vortex of charge ℓ . If this phase profile is modified, the other diffraction orders appear, with different topological charges. Different types of modifications of this blazed vortex grating have been demonstrated, including binary phase or Dammann grating type profiles [26–29].

By applying the LUT in Fig. 1(a) to this fork blazed grating, the optimum triplicator version of the fork grating is obtained. This is shown in Fig. 2. The addition modulo 2π of a linear phase grating and a spiral phase of charge $\ell = 1$, see Fig. 2(a), results in the classical fork phase-only grating as shown in Fig. 2(b). This grating, when illuminated with a plane wave, generates a single first order diffracted vortex beam that carries a topological charge $\ell = 1$. When the triplicator LUT is applied to this blazed vortex grating the resulting grating (Fig. 2(c)) shows the fork grating shape, but its profile adopts the form of the triplicator, as in Fig. 1(a).

Mathematically, the application of the triplicator LUT results in the same Fourier series expansion as in Eq. (2), i.e.:

$$\tau_{trip-fork}(x, \theta) = \text{LUT}[\tau_{fork}(x, \theta)] = \sum_{n=-\infty}^{+\infty} \tau_n \exp\left[in\left(\frac{2\pi x}{p} + \ell \theta\right)\right]. \quad (8)$$

To simplify the analysis, we consider only the diffracted orders $n_x = 0$, and $n_x = \pm 1$, all of them having the same magnitude $|\tau_{0, \pm 1}| = 0.555$ (equal intensities $|\tau_{0, \pm 1}|^2 = 0.3085$), but with a relative phase shift given by Eq. (5). Thus, within this approximation Eq. (8) can be written as

$$\tau_{trip-fork}(x, \theta) = \tau_0 \left\{ 1 + i \exp \left[i \left(\frac{2\pi x}{p} + \ell \theta \right) \right] + i \exp \left[-i \left(\frac{2\pi x}{p} + \ell \theta \right) \right] \right\}. \quad (9)$$

The first term in the right side of Eq. (9) corresponds to the zero order, with no topological charge. The other terms are two linear phases corresponding to the first and to the minus first diffraction orders, which carry charges ℓ and $-\ell$ respectively. Note that this grating diffracts in the horizontal direction. The above equation can be rewritten in a more compact way as

$$\tau_{trip-fork}(x, \theta) = \tau_0 \left[1 + 2i \cos \left(\frac{2\pi x}{p} + \ell \theta \right) \right], \quad (10)$$

where the cosine term includes the $n_x = +1$ and $n_x = -1$ orders of charge ℓ and $-\ell$, respectively.

Next, another equivalent triplicator grating is designed, but now oriented to diffract in the vertical direction. For that purpose, we use another fork grating from a blazed grating of the same period and a spiral phase pattern with $\ell = 3$, as shown in Fig. 2(d). Its combination, shown in Fig. 2(e), is again modified according to the triplicator profile, resulting in the pattern in Fig. 2(f). This grating generates three diffraction orders in the vertical direction. Once again, the zero diffraction order does not have vorticity, but the vertically diffracted beams, $n_y = +1$ and $n_y = -1$, carry vortices of charges $\ell = 3$ and $\ell = -3$ respectively.

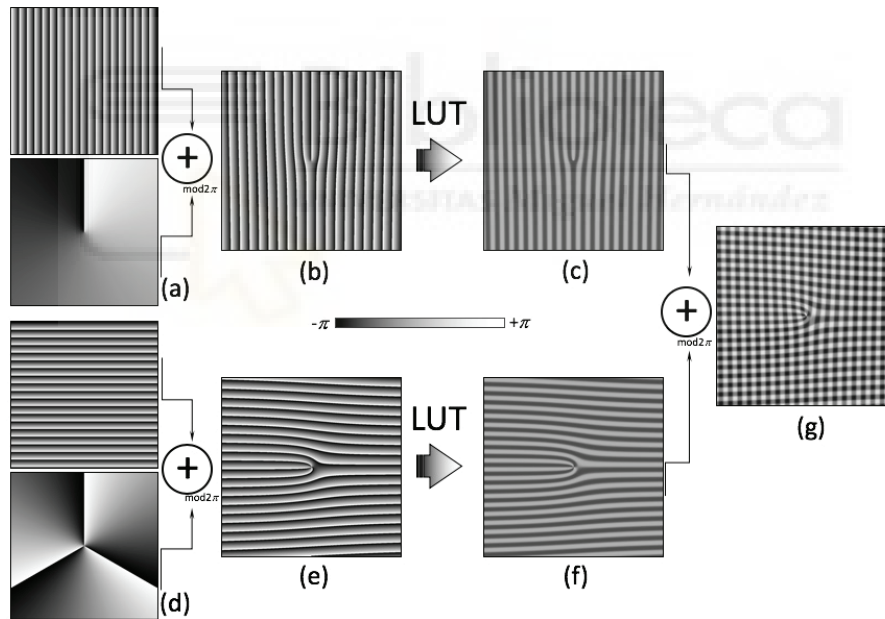


Fig. 2. Scheme showing the design procedure to achieve the 3×3 vortex grating design with optimal efficiency.

Finally, we combine both triplicator vortex gratings by making their product, i.e., by adding modulo 2π the two phase-only functions. The resulting phase pattern is a 2D diffraction grating as shown in Fig. 2(g), that creates an array of 3×3 diffraction orders, as shown in Fig. 3. The transmittance of this 2D grating is obtained from the multiplication of two terms like in Eq. (10) for the x and y directions:

$$\tau_{2D \text{ trip-fork}}(x, y, \theta) = \tau_0^2 \left[1 + 2i \cos \left(\frac{2\pi x}{p} + \theta \right) \right] \left[1 + 2i \cos \left(\frac{2\pi y}{p} + 3\theta \right) \right], \quad (11)$$

where we made explicit the topological charges of 1 and 3 for the x and y directions respectively.

This product can be expanded to read as:

$$\frac{\tau_{2D \text{ trip-fork}}(x, y, \theta)}{\tau_0^2} = 1 + 2i \cos\left(\frac{2\pi x}{p} + \theta\right) - 2 \cos\left(\frac{2\pi(y-x)}{p} + 2\theta\right) + 2i \cos\left(\frac{2\pi y}{p} + 3\theta\right) - 2 \cos\left(\frac{2\pi(y+x)}{p} + 4\theta\right) \quad (12)$$

The first unit term is the zero order, while each cosine term represents a pair of ± 1 diffraction orders. Note that the first and third cosine terms, which correspond to the orders diffracted along the horizontal ($n_x = \pm 1, n_y = 0$) and vertical direction ($n_x = 0, n_y = \pm 1$) respectively, are pure imaginary and therefore have a $\pi/2$ phase shift with respect to the zero order. On the contrary, the second and fourth cosine terms in Eq. (12), which correspond to the orders diffracted along the diagonal directions, are real. The second cosine term corresponds to the anti-diagonal diffraction orders ($n_x = -1, n_y = +1$) and ($n_x = +1, n_y = -1$), while the fourth cosine term corresponds to the diagonal orders, ($n_x = n_y = +1$) and ($n_x = n_y = -1$).

Equation (12) also reveals that the topological charge changes on each diffraction order as

$$\ell(n_x, n_y) = n_x + 3n_y, \quad (13)$$

where (n_x, n_y) are the pair of indices indicating the diffraction order ($n_x, n_y = +1, 0, -1$). Therefore the topological charges take values $+4, +3, \dots, 0, \dots, -3, -4$, at the nine diffraction orders. Figure 3 illustrates the array of 3×3 orders yielded by the grating design in Eq. (12), with indication of the topological charge at each diffraction order defined by the pair of indices (n_x, n_y) .

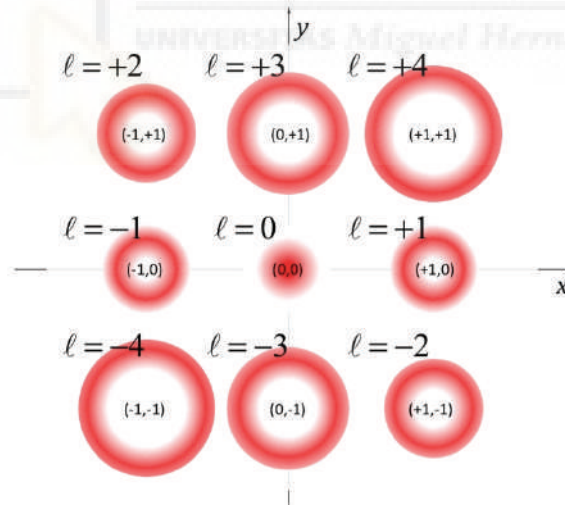


Fig. 3. Scheme of the expected array of diffraction orders and the corresponding topological charges. The pair of numbers on each diffraction order denote the order (n_x, n_y) .

3. The geometric phase 2D vortex grating

In this work, we build the transmission profile of Eq. (12) as a geometric phase element, where the phase function $\phi(x, y)$ is encoded as the rotation angle α of the principal axis of a half-wave retarder. Figure 4(a) illustrates this method. The Jones matrix for a half-wave retarder with orientation α is given by:

$$\mathbf{M} = \begin{pmatrix} \cos 2\alpha & \sin 2\alpha \\ \sin 2\alpha & -\cos 2\alpha \end{pmatrix} \quad (14)$$

In a geometric phase element, α is a spatially-variant function given by $\alpha(x,y) = \phi(x,y)/2$ where ϕ is the phase to be encoded. Q-plates are a particular case where a spiral phase is encoded as geometric phase [30].

The above matrix can be expressed as:

$$\mathbf{M} = \frac{1}{2}(\mathbf{A}e^{i\phi} + \mathbf{A}^\dagger e^{-i\phi}), \quad (15)$$

with

$$\mathbf{A} = \begin{pmatrix} 1 & -i \\ -i & -1 \end{pmatrix}. \quad (16)$$

If we consider a phase-only function corresponding to a diffraction grating as those described above, $\tau(x,y) = \exp[i\phi(x,y)]$, it is convenient to write Eq. (15) in the following form:

$$\mathbf{M}(\tau) = \begin{pmatrix} 1 & 0 \\ 0 & -1 \end{pmatrix} \text{Re}(\tau) + \begin{pmatrix} 0 & 1 \\ 1 & 0 \end{pmatrix} \text{Im}(\tau). \quad (17)$$

Note that the Jones matrix acting on the real part of τ corresponds to a half-wave retarder (HWR) with its axis oriented along the coordinate system. On the contrary, the Jones matrix acting on the imaginary part of τ corresponds to an aligned HWR plus a rotation of 90° .

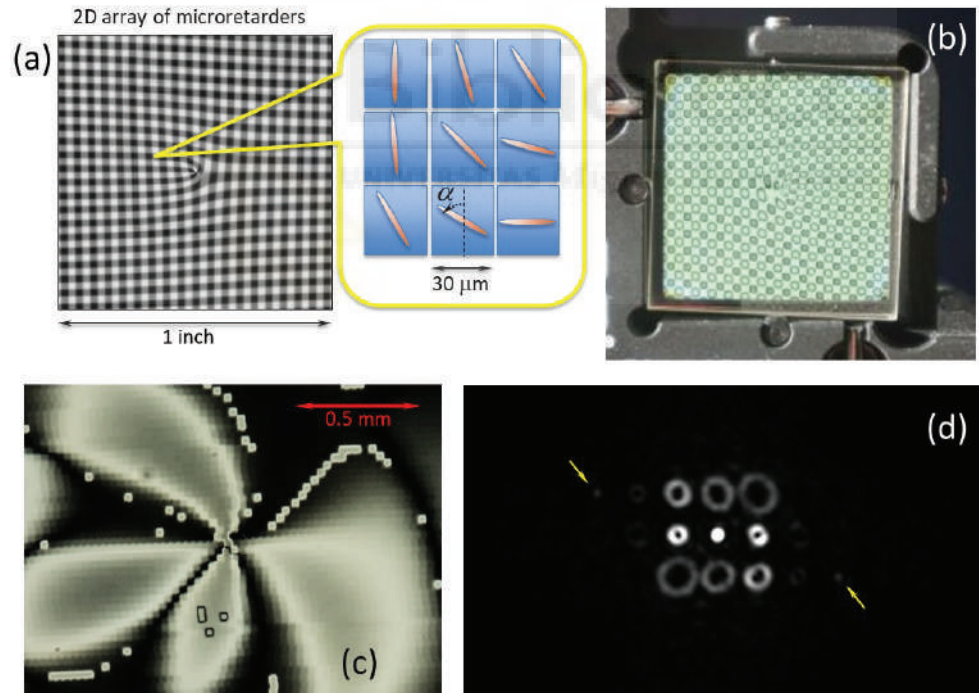


Fig. 4. (a) Illustration of the phase grating encoding as a geometric phase element. (b) Picture of the grating between crossed polarizers. (c) Detail of the center of the grating viewed through a polarizing microscope between crossed polarizers. (d) Fourier transform pattern, saturated on purpose in order to visualize how the energy is basically confined to the 3×3 target orders.

Thus, if we apply the geometric phase to the phase profile in Eq. (12), Eq. (17) is given by:

$$\mathbf{M} = \begin{pmatrix} 1 & 0 \\ 0 & -1 \end{pmatrix} \times \left[1 - 2 \cos \left(\frac{2\pi(y-x)}{p} + 2\theta \right) - 2 \cos \left(\frac{2\pi(y+x)}{p} + 4\theta \right) \right] + \begin{pmatrix} 0 & 1 \\ 1 & 0 \end{pmatrix} \times \left[2 \cos \left(\frac{2\pi x}{p} + \theta \right) + 2 \cos \left(\frac{2\pi y}{p} + 3\theta \right) \right] \quad (18)$$

Equation (18) reveals a different polarization behavior in two sets of diffraction orders. For those in the first row in Eq. (18) i.e., orders $(+1, +1)$, $(-1, +1)$, $(0,0)$, $(+1,-1)$ and $(-1,-1)$, the polarization transformation induced by the grating is equivalent to an aligned HWR. On the contrary, for those orders described in the second row in Eq. (18), i.e., orders $(1,0)$, $(0,1)$, $(-1,0)$ and $(0,-1)$, the polarization transformation induced by the grating is equivalent to that of an aligned HWR plus a 90° polarization rotation.

4. Experimental system and results

We next show a proof-of-concept experiment where we use a geometric phase grating made using the capability offered by Thorlabs Inc. to provide customized patterned retarders [23]. The 2D vortex triplicator grating was fabricated as a patterned retarder with half-wave retardance for the wavelength of 632.8 nm. The complete element is composed of an array of 853×853 micro-retarders, each one of $30 \times 30 \mu\text{m}^2$, thus the grating size is about $1'' \times 1''$. The encoded grating was designed with a period p of 19 pixels. This large value was selected as a trade-off between having enough number of pixels per period to accurately reproduce the triplicator phase profile, and reaching a diffraction angle that, although small, is enough to separate the diffracted lowest vortex beams. Each micro-retarder has its fast axis aligned to a different angle, given by the designed phase mask. These patterned retarders are made of liquid crystals and liquid-crystal polymers and, using photo alignment technology, the fast axis of each micro-retarder can be oriented to any angle within a resolution of $<1^\circ$. The grating was fabricated onto a BK7 substrate and with antireflection coating type A (for 350 - 700 nm), and it was mounted onto a square kinematic mount from Edmund Optics (model #58-860). Figure 4(b) shows a picture of the mounted grating, viewed between crossed polarizers, while Fig. 4(c) shows a detail of the central part viewed through a polarizing microscope (Nikon Eclipse). The picture shows the center of the grating where the singularity is created.

Let us now evaluate the diffraction pattern rendered by this grating. Figure 5 shows a scheme of the optical system. We use a 632.8 nm wavelength He-Ne laser beam that is spatially filtered and collimated. A quarter-wave retarder (Q) is used to generate circularly polarized light impinging on a polarization state generator (PSG) composed by a linear polarizer (P) and a quarter-wave retarder (Q). The PSG is applied in order to generate an arbitrary input state of polarization illuminating the geometric phase grating. Setting up the PSG requires changing the orientation of the polarizers; therefore, using circularly polarized light as input to the PSG ensures that the input intensity does not change when the PSG is reconfigured.

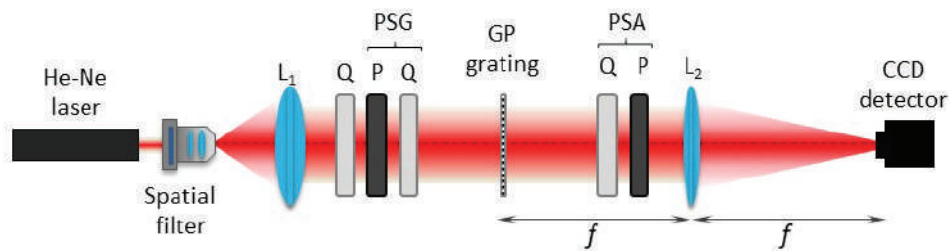


Fig. 5. Scheme of the experimental setup. PSG: polarization state generator; PSA: polarization state analyzer; Q: quarter-wave retarder; L: linear polarizer; L_1 , L_2 converging lenses.

Behind the grating, a polarization state analyzer (PSA) composed by another quarter-wave plate and another linear polarizer is used to analyze the generated beams. A converging lens of $f = 100$ cm focal length focuses the beam onto a CCD detector that captures the Fourier transform pattern. Figure 4(d) shows a capture of the Fourier transform plane. This result was obtained with input linear polarization and no PSA. The 3×3 vortex beam array is successfully obtained, in agreement with the expected result in Fig. 3. The focused beams exhibit the typical doughnut shapes, with increasing diameter according to the topological charges in each diffraction order. Note, however, that we are operating at the limit, since the beams that focus with largest diameters (those with charges $\ell = \pm 3$ and $\ell = \pm 4$) are not completely separated and their interference causes some distortion. Nevertheless, this result represents a successful proof-of-concept of the vortex triplicator grating.

Figure 4(d) shows a big area of the Fourier transform pattern, which is saturated on purpose. This is done to clearly visualize that the energy is basically concentrated in the central array of 3×3 central orders. Other higher diffraction orders, although weak, are visible, especially those located at diffraction orders $(+3, -1)$ and $(-3, +1)$, where the total topological charge is cancelled and therefore the focused beam appears as a bright spot (they are marked with a yellow arrow). We experimentally measured the intensity of the 3×3 central orders compared to the total intensity at the Fourier transform plane and obtained a ratio of about $\eta \approx 0.74$. This value is lower, but not far, from the theoretical efficiency of a 2D triplicator grating, $\eta = \eta_x \eta_y = (0.926)^2 = 0.857$, due to the limited spatial resolution in the fabrication of the grating.

In order to exhaustively analyze the polarization properties of the grating, Fig. 6 shows additional experimental results, where now only the central orders are shown. The PSG is configured to the six typical states used in polarimetry: linear states with orientations $0, \pm 45^\circ$ and 90° , and the two circular states right, and left. These polarization states are drawn as symbols on the left column in Fig. 6. For each PSG configuration, the PSA is first set without analyzer and is then set to transmit the six typical polarization states. These are indicated with the same symbols on the top of the figure.

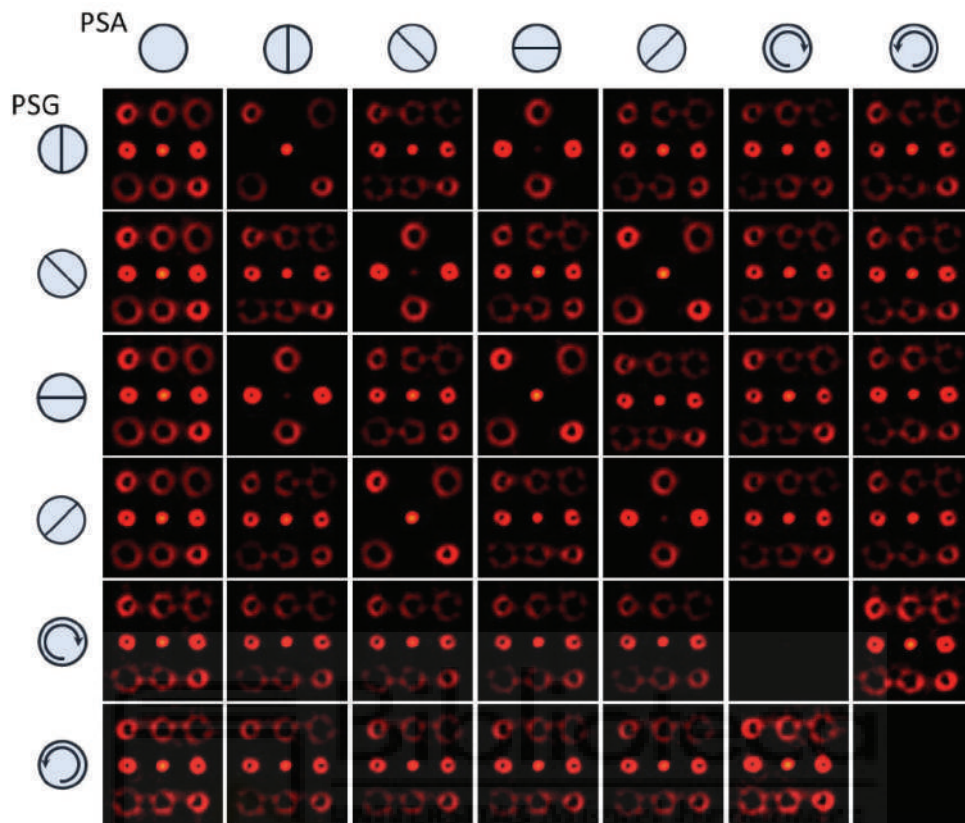


Fig. 6. Experimental results of the Fourier plane for six different configurations of the PSG without analyzer (left column), and with six different configurations of the PSA.

The left column of CCD captures in Fig. 6 shows the diffracted pattern when no analyzer is included. In all cases, the 3×3 vortex beam array is successfully obtained. However, the polarization of each order changes, and this is noticeable when the PSA is included and configured to detect different states. When the grating is illuminated with linearly polarized light (results in the first four rows in Fig. 6), we can identify two sets of diffraction orders with different polarization, as expected from the discussion in Section 3. According to Eq. (18), the zero order and the diagonal orders experience a polarization transformation with respect to the input polarization equivalent to that caused by a half-wave retarder oriented along the x - y axes. On the contrary, those orders diffracted in the x and y directions ($(1,0)$, $(0,1)$, $(-1,0)$ and $(0,-1)$) transform the input polarization states as if they traversed a polarization rotator of 90° followed by an aligned half-wave retarder.

These polarization changes can be clearly noticed in the first row of results. Since the input light is vertical linearly polarized, the first set of five orders exit the grating with the same vertical polarization, while the other four orders exit with horizontal linear polarization. This is shown by the extinction of the two set of orders when the PSA is configured vertical and horizontal respectively. On the contrary, when the PSA is linear at $\pm 45^\circ$ or circular all nine orders are visible. The other cases when the grating is illuminated with a linear state confirm these results. Note that these polarization changes arise from the relative $\pi/2$ phase shift between the zero order and the ± 1 orders in Gori's triplicator design. Note that the different polarization behavior in these two sets of diffraction orders was also observed in a recently reported 2D grating design [24]. Although the design in that work is different to ours,

it also includes the product of two triplicators in the x - y directions, and therefore the relative $\pi/2$ phase shift is expected to play also a role.

The situation is different when circularly polarized light illuminates the grating, as shown in the two bottom rows in Fig. 6. Here the grating acts as a pure geometric phase grating, imparting the encoded spatial phase, but the change in polarization in both cases is uniform to all orders and consists in a change of helicity of the circular polarization (input right circular polarization is transformed into left, and viceversa). This is shown by the fact that all diffraction orders are visible when the PSA is set to detect linear states. When it is configured to detect the circular states, the state equal to the input one is completely cancelled, while the opposite is fully transmitted.

As a final result, we examine the use of the GP vortex grating as a vortex beam detector. For that purpose, we include a q -plate behind the PSG. When the PSG is set to generate a circular polarization state, the q -plate output is a vortex beam with topological charge $\pm 2q$ and the opposite circular polarization. Figure 7 shows the results captured at the Fourier plane when we illuminate the vortex grating with the output from a q -plate with $q = 1/2$ for two cases.

In Fig. 7(a) the q -plate is illuminated with R circular polarization, so its output is a vortex beam with L circular polarization and topological charge $\ell_{in} = +1$. This input charge is compensated on the diffraction order having charge $\ell = -1$ and therefore a bright spot on the $(-1, 0)$ order appears. In the second case in Fig. 7(b), the q -plate is illuminated with L circular polarization, and now the beam impinging on the grating is a vortex beam with R circular polarization and topological charge $\ell_{in} = -1$. Now the bright spot appears on the $(+1, 0)$ diffraction order where the grating generates the vortex beam with charge $\ell = +1$. These results show that the grating could be used also as a vortex beam detector, although now the resolution limits are clearly visible in the distortion of the orders having higher topological charges.

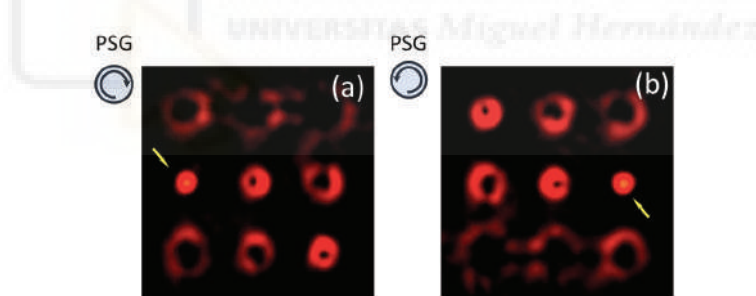


Fig. 7. Experimental results at the Fourier plane for the 2D vortex grating illuminated with two circularly polarized vortex beams of charges (a) $+1$ (b) -1 . No PSA is included. The yellow arrow indicates the position of the bright spot, revealing the input charge.

5. Conclusions

In summary, we have proposed, analyzed and demonstrated the application of the triplicator phase profile to a 2D vortex grating. We completed Gori's et al analysis in [3] by showing the $\pi/2$ relative phase between the zero and the ± 1 diffraction orders, which is key to render different polarization at two sets of diffraction orders. We designed the 2D vortex triplicator grating and ordered its fabrication as a geometric-phase liquid-crystal grating by using a commercially available capability offered to fabricate customized retarders. The fabricated grating has been evaluated experimentally and confirms the theoretical predictions.

This grating is an interesting diffractive element since, when being illuminated with a plane wave, it creates a bidimensional array of 3×3 vortex beams of integer topological charges ranging from $+4$ to -4 , and with the optimal diffraction efficiency. The same grating

could be used also as a detector of vortex beams, where the charge is detected by seeking the diffraction order where the singularity is cancelled [26]. The advantage of the triplicator design relies on its optimal diffraction efficiency, which might be of great importance in applications with low light intensity levels.

Finally, we have shown an experimental proof-of concept using a commercial capability to fabricate customized non-standard geometric-phase diffraction gratings. Despite the limited spatial resolution, this opens interesting possibilities to researchers in the field who do not have facilities to fabricate such geometric-phase elements.

Appendix

In this Appendix we review the derivation of Gori's triplicator and derive the condition in Eq. (5), which we have shown to be the cause of the different polarization behavior at different diffraction orders. The coefficients for the Fourier expansion of the optimum triplicator are calculated for the 0, +1 and -1 terms.

The zero order in the Fourier expansion of the optimal triplicator in Eq. (1) takes the form:

$$\tau_0 = \frac{1}{p} \int_{-p/2}^{p/2} \exp[i\phi(x)] dx = \frac{1}{p} \int_{-p/2}^{p/2} \exp\left[\arctan\left(a \cos\left(\frac{2\pi x}{p}\right)\right)\right] dx. \quad (19)$$

If the change of variable $\delta = 2\pi x/p$ is applied, Eq. (19) is reduced to

$$\tau_0 = \frac{1}{2\pi} \int_{-\pi}^{\pi} \exp[\arctan(a \cos \delta)] d\delta, \quad (20)$$

which is expanded in two integrals by applying Euler's formula

$$\tau_0 = \frac{1}{2\pi} \int_{-\pi}^{\pi} \cos[\arctan(a \cos \delta)] d\delta + \frac{i}{2\pi} \int_{-\pi}^{\pi} \sin[\arctan(a \cos \delta)] d\delta. \quad (21)$$

These two integrals can be calculated using the trigonometric relations

$$\cos(\arctan \varphi) = \frac{1}{\sqrt{1+\varphi^2}}, \quad (22)$$

$$\sin(\arctan \varphi) = \frac{\varphi}{\sqrt{1+\varphi^2}}, \quad (23)$$

so Eq. (21) can be rewritten as

$$\tau_0 = \frac{1}{2\pi} \int_{-\pi}^{\pi} \frac{1}{\sqrt{1+a^2 \cos^2 \delta}} d\delta + \frac{i}{2\pi} \int_{-\pi}^{\pi} \frac{a \cos \delta}{\sqrt{1+a^2 \cos^2 \delta}} d\delta, \quad (24)$$

Since both integrals are even functions they can be written as

$$\tau_0 = \frac{1}{\pi} \int_0^{\pi} \frac{1}{\sqrt{1+a^2 \cos^2 \delta}} d\delta + \frac{i}{\pi} \int_0^{\pi} \frac{a \cos \delta}{\sqrt{1+a^2 \cos^2 \delta}} d\delta, \quad (25)$$

But note that the second integral in Eq. (25) is antisymmetric around the value $\delta = \pi/2$, and therefore it vanishes. Consequently, τ_0 is a pure real and positive value given by

$$\tau_0 = \frac{1}{\pi} \int_0^{\pi} \frac{1}{\sqrt{1+a^2 \cos^2 \delta}} d\delta = \frac{2}{\pi} K(-a^2), \quad (26)$$

where K is the complete elliptic integral of the first kind. For the numerical constant $a = 2.65718$ derived in the triplicator design [3], the zero order coefficient τ_0 is 0.555.

Next, let us calculate the coefficients for the +1 and -1 orders. In this case

$$\tau_{\pm 1} = \frac{1}{p} \int_{-p/2}^{p/2} \exp \left[\arctan \left(a \cos \left(\frac{2\pi x}{p} \right) \right) \right] \exp \left(\pm i \frac{2\pi x}{p} \right) dx, \quad (27)$$

If the change of variable $\delta = 2\pi x/p$ is again applied, Eq. (2) reduces to

$$\tau_{\pm 1} = \frac{1}{2\pi} \int_{-\pi}^{\pi} \exp \left[\arctan (a \cos \delta) \right] \exp (\pm i \delta) d\delta. \quad (28)$$

Applying Euler formula to each exponential function in Eq. (28), four different terms are obtained

$$\begin{aligned} \tau_{\pm 1} = & \frac{1}{2\pi} \int_{-\pi}^{\pi} \cos (\arctan (a \cos \delta)) \cos \delta d\delta + \\ & \mp \frac{1}{2\pi} \int_{-\pi}^{\pi} \sin (\arctan (a \cos \delta)) \sin \delta d\delta + \\ & \pm \frac{i}{2\pi} \int_{-\pi}^{\pi} \cos (\arctan (a \cos \delta)) \sin \delta d\delta + \\ & + \frac{i}{2\pi} \int_{-\pi}^{\pi} \sin (\arctan (a \cos \delta)) \cos \delta d\delta, \end{aligned} \quad (29)$$

and considering Eqs. (22) and (23), the following decomposition is obtained

$$\begin{aligned} \tau_{\pm 1} = & \frac{1}{2\pi} \int_{-\pi}^{\pi} \frac{\cos \delta}{\sqrt{1+a^2 \cos^2 \delta}} d\delta \mp \frac{1}{2\pi} \int_{-\pi}^{\pi} \frac{a \cos \delta \sin \delta}{\sqrt{1+a^2 \cos^2 \delta}} d\delta + \\ & \pm \frac{i}{2\pi} \int_{-\pi}^{\pi} \frac{\sin \delta}{\sqrt{1+a^2 \cos^2 \delta}} d\delta + \frac{i}{2\pi} \int_{-\pi}^{\pi} \frac{a \cos^2 \delta}{\sqrt{1+a^2 \cos^2 \delta}} d\delta. \end{aligned} \quad (30)$$

Now, the same kind of symmetry considerations can be applied to these four terms. The second and third terms are odd functions about zero, so their definite integrals are zero. And the first and fourth terms in the sum are both even functions about zero, so its definite integral can be expressed as twice the integral from 0 to π , i.e.

$$\tau_{\pm 1} = \frac{1}{\pi} \int_0^{\pi} \frac{\cos \delta}{\sqrt{1+a^2 \cos^2 \delta}} d\delta + \frac{i}{\pi} \int_0^{\pi} \frac{a \cos^2 \delta}{\sqrt{1+a^2 \cos^2 \delta}} d\delta. \quad (31)$$

Then, by noticing that the first term is an odd function about $\pi/2$, this first integral turns to be also zero, and the only remaining term is the fourth term, which is given by

$$\tau_{\pm 1} = \frac{ia}{\pi} \int_0^{\pi} \frac{\cos^2 \delta}{\sqrt{1+a^2 \cos^2 \delta}} d\delta = i \frac{2}{\pi a} \left[E(-a^2) - K(-a^2) \right], \quad (32)$$

where E denotes the complete elliptic integral of the second kind. Note that both orders get the same pure positive imaginary value. For $a = 2.65718$, this value is $\tau_{\pm 1} = 0.555i$.

Funding

Conselleria d'Educació, Investigació, Cultura i Esport (PROMETEO-2017-154); Ministerio de Economía y Competitividad (FIS2015-66328-C3-3-R); Fondo Nacional de Desarrollo Científico y Tecnológico, Chile (FONDECYT) (1151290).

References

1. H. Dammann and E. Klotz, "Coherent optical generation and inspection of two-dimensional periodic structures," *Opt. Acta (Lond.)* **24**(4), 505–515 (1977).
2. J. N. Mait, "Design of binary-phase and multiphase Fourier gratings for array generation," *J. Opt. Soc. Am. A* **7**(8), 1514–1518 (1990).
3. F. Gori, M. Santarsiero, S. Vicalvi, R. Borghi, G. Cincotti, E. di Fabrizio, and M. Gentili, "Analytical derivation of the optimum triplicator," *Opt. Commun.* **157**(1-6), 13–16 (1998).
4. F. Aroca and I. Moreno, "Comparison and experimental realization of different phase-only grating designs and optimal triplicators," *Opt. Pura Apl.* **49**(3), 155–166 (2016).
5. A. Cofré, P. García-Martínez, A. Vargas, and I. Moreno, "Vortex beam generation and other advanced optics experiments reproduced with a twisted-nematic liquid-crystal display with limited phase modulation," *Eur. J. Phys.* **38**(1), 014005 (2017).
6. L. A. Romero and F. M. Dickey, "The mathematical theory of laser beam-splitting gratings," *Prog. Opt.* **54**, 319–386 (2010).
7. A. V. Carpentier, H. Michinel, J. R. Salgueiro, and D. Olivieri, "Making optical vortices with computer-generated holograms," *Am. J. Phys.* **76**(10), 916–921 (2008).
8. I. Moreno, J. A. Davis, D. M. Cottrell, N. Zhang, and X.-C. Yuan, "Encoding generalized phase functions on Dammann gratings," *Opt. Lett.* **35**(10), 1536–1538 (2010).
9. T. Lei, M. Zhang, Y. Li, P. Jia, G. N. Liu, X. Xu, Z. Li, C. Min, J. Lin, C. Yu, H. Niu, and X. Yuan, "Massive individual orbital angular momentum channels for multiplexing enabled by Dammann gratings," *Light Sci. Appl.* **4**(3), e257 (2015).
10. J. A. Davis, D. M. Cottrell, K. R. McCormick, J. Albero, and I. Moreno, "Arithmetic of focused vortex beams in three-dimensional optical lattice arrays," *Appl. Opt.* **53**(10), 2040–2050 (2014).
11. C. Maurer, A. Jesacher, S. Fühapter, S. Bernet, and M. Ritsch-Marte, "Tailoring of arbitrary optical vector beams," *New J. Phys.* **9**(3), 78 (2007).
12. I. Moreno, J. A. Davis, K. Badham, M. M. Sánchez-López, J. E. Holland, and D. M. Cottrell, "Vector beam polarization state spectrum analyzer," *Sci. Rep.* **7**(1), 2216 (2017).
13. C. Rosales-Guzmán, N. Bhebhe, and A. Forbes, "Simultaneous generation of multiple vector beams on a single SLM," *Opt. Express* **25**(21), 25697–25706 (2017).
14. F. Yue, D. Wen, C. Zhang, B. D. Gerardot, W. Wang, S. Zhang, and X. Chen, "Multichannel polarization-controllable superpositions of orbital angular momentum states," *Adv. Mater.* **29**(15), 1603838 (2017).
15. J. Kim, Y. Li, M. N. Miskiewicz, C. Oh, M. W. Kudenov, and M. J. Escuti, "Fabrication of ideal geometric-phase holograms with arbitrary wavefronts," *Optica* **2**(11), 958–964 (2015).
16. L. De Sio, D. E. Roberts, Z. Liao, S. Nersisyan, O. Uskova, L. Wickboldt, N. Tabiryan, D. M. Steeves, and B. R. Kimball, "Digital polarization holography advancing geometrical phase optics," *Opt. Express* **24**(16), 18297–18306 (2016).
17. P. Chen, Y.-Q. Lu, and W. Hu, "Beam shaping via photopatterned liquid crystals," *Liq. Cryst.* **43**(13–15), 2051–2061 (2016).
18. P. Chen, B.-Y. Wei, W. Ji, S.-J. Ge, W. Hu, F. Xu, V. Chigrinov, and Y.-Q. Lu, "Arbitrary and reconfigurable optical vortex generation: A high-efficiency technique using director-varying liquid crystal fork gratings," *Photon. Res.* **3**(4), 133–139 (2015).
19. P. Chen, L.-L. Ma, W. Duan, J. Chen, S.-J. Ge, Z.-H. Zhu, M.-J. Tang, R. Xu, W. Gao, T. Li, W. Hu, and Y.-Q. Lu, "Digitalizing self-assembled chiral superstructures for optical vortex processing," *Adv. Mater.* **30**(10), 1705865 (2018).
20. J. P. Balthasar Mueller, N. A. Rubin, R. C. Devlin, B. Groever, and F. Capasso, "Metasurface polarization optics: independent phase control of arbitrary orthogonal states of polarization," *Phys. Rev. Lett.* **118**(11), 113901 (2017).
21. M. Beresna, M. Gecevičius, P. G. Kazansky, and T. Gertus, "Radially polarized optical vortex converter created by femtosecond laser nanostructuring of glass," *Appl. Phys. Lett.* **98**(20), 201101 (2011).
22. A. Cofré, A. Vargas, F. A. Torres-Ruiz, M. M. Sánchez-López, and I. Moreno, "Geometrical-phase lens based optical system for the spin-splitting of vector beams," *Opt. Lasers Eng.* **110**, 401–409 (2018).
23. https://www.thorlabs.com/newgrouppage9.cfm?objectgroup_id=9098
24. M. Yannai, E. Maguid, A. Faerman, Q. Li, J.-H. Song, V. Kleiner, M. L. Brongersma, and E. Hasman, "Spectrally interleaved topologies using geometric phase metasurfaces," *Opt. Express* **26**(23), 31031–31038 (2018).
25. C. Zhou and L. Liu, "Numerical study of Dammann array illuminators," *Appl. Opt.* **34**(26), 5961–5969 (1995).
26. I. Moreno, J. A. Davis, B. M. L. Pascoguin, M. J. Mitry, and D. M. Cottrell, "Vortex sensing diffraction gratings," *Opt. Lett.* **34**(19), 2927–2929 (2009).

27. P. Chen, S.-J. Ge, L.-L. Ma, W. Hu, V. Chigrinov, and Y.-Q. Lu, "Generation of equal-energy orbital angular momentum beams via photopatterned liquid crystals," *Phys. Rev. Appl.* **5**(4), 044009 (2016).
28. Z. Xie, T. Lei, X. Weng, L. Du, S. Gao, Y. Yuan, S. Feng, Y. Zhang, and X. Yuan, "A miniaturized polymer grating for topological order detection of cylindrical vector beams," *IEEE Photonics Technol. Lett.* **28**(24), 2799–2802 (2016).
29. P. Chen, S.-J. Ge, W. Duan, B.-Y. Wei, G.-X. Cui, W. Hu, and Y.-Q. Lu, "Digitalized geometric phases for parallel optical spin and orbital angular momentum encoding," *ACS Photonics* **4**(6), 1333–1338 (2017).
30. L. Marrucci, C. Manzo, and D. Paparo, "Optical spin-to-orbital angular momentum conversion in inhomogeneous anisotropic media," *Phys. Rev. Lett.* **96**(16), 163905 (2006).



Efficient on-axis SLM engineering of optical vector modes

Pascuala García-Martínez¹, David Marco², José Luis Martínez-Fuentes³,
María del Mar Sánchez-López^{2,4} and Ignacio Moreno³

1. Departamento de Óptica, Universitat de València, 46100 Burjassot, Valencia Spain
2. Instituto de Bioingeniería, Universidad Miguel Hernández de Elche, 03202 Elche, Spain
3. Departamento de Ciencia de Materiales, Óptica y Tecnología Electrónica, Universidad Miguel Hernández de Elche, 03202 Elche, Spain
4. Departamento de Física Aplicada, Universidad Miguel Hernández de Elche, 03202 Elche, Spain

Abstract

This work presents a method for the efficient experimental generation of arbitrary polarized vector beam modes. The optical system employs two liquid-crystal on silicon (LCOS) spatial light modulators (SLM) in a common path architecture, avoiding the use of beam-splitters. Each SLM displays a different phase-only mask, each one encoding a different pattern onto two orthogonal linear polarization components of the input beam. These phase-only masks are designed using a recently proposed random technique to encode complex amplitude values. This encoding technique reconstructs the complex function on-axis, thus avoiding incorporating carrier phases. By addressing such properly designed phase-only holograms we demonstrate arbitrary scalar modes on each polarization component, whose superposition results in a vector beam mode. Different superpositions of Laguerre-Gaussian and Hermite-Gaussian modes are obtained and the generated vector beam modes are analyzed. Moreover, the addition of a phase-bias proves itself useful to perform a phase-shifting technique in order to evaluate the correct phase of the generated vector beam.

1. INTRODUCTION

Vector beams (VBs), as light beams with defined spatially-variant intensity, phase and polarization features, are important for many applications including tight focusing [1], optical tweezing [2], materials processing [3], or super-resolution microscopy [4]. Cylindrically polarized optical beams with the radial or azimuthal polarization as paradigmatic cases, have attracted the most attention from researchers because of their special properties [5].

VBs can also be defined as pure laser modes with an additional spatial polarization modulation [6]. There have been several methods to generate such beams, based on the fact that they can be generated as the superposition of scalar modes having orthogonal polarization [7]. Initial techniques included the manipulation of a laser resonator in order to directly emit a desired vector beam [8], or the use of interferometric arrangements [9]. More recently, they have been generated with spatially variant uniaxial flat elements, which can be fabricated with subwavelength gratings [10], or with liquid-crystal materials [11]. These elements, often referred to as q -plates, are in general designed to generate low-order VBs [12,13]. However, higher-order Laguerre-Gaussian q -plates have also been developed [14].

An alternative method to generate vector beams is based on spatial light modulators (SLM). While these methods require bulky optical systems, their programmability offer a great flexibility, and several different optical arrangements have been proposed. The commonly used parallel-aligned liquid-crystal SLM can modulate only one polarization component, parallel to the liquid-crystal director. Therefore, in order to control two polarization components, they usually require either dividing the device screen in two halves [15,16], using two SLMs [17], or

passing the beam twice through the SLM after a proper polarization transformation [18]. In other schemes, the parallel generation (or detection) of VBs is accomplished by adding linear phase carriers [19,20]. Achromatic VBs have been obtained by using reflective digital micro-mirror SLMs, which are free from chromatic aberration, but require additional elements for polarization control [21]. In all these cases, the SLM operates externally to the laser cavity. However, laser modes have also been generated by inserting a reflective phase-only SLM in the laser cavity [22], thus achieving the controllable generation of Hermite-Gauss (*HG*) and Laguerre-Gauss (*LG*) scalar beams. A similar scheme was extended to generate VBs [23].

In all cases, the use of SLMs introduces an important efficiency loss. This loss primarily arises from the pixelated structure of the devices, which generates additional diffraction orders. Furthermore, the optical arrangements usually employ beam-splitters that reduce the power budget. For this reason, recent works report on highly efficient optical arrangements to generate vector beams [24,25]. In addition, the generation of higher-order beams requires some kind of amplitude modulation encoding. There have been many different proposals to achieve such amplitude encoding [26,27], which have been successfully applied to the encoding of different scalar beams [28-30]. In many cases, the amplitude encoding technique involves the use of a linear phase carrier and a consequent Fourier-filtering, which is mostly carried out off-axis, thus additionally contributing to a relevant reduction of the light budget and additional difficulties of stability and optical implementation. This operation, though, is sometimes mandatory when using SLMs that generate a strong DC component (usually due to flickering effects in the device) which prevents operating the system on axis [31].

In this work we combine recent advances to achieve an efficient way of generating VBs using SLMs. First, we use an optical setup based on two LCoS (liquid-crystal on silicon) SLMs arranged in a Z configuration. This type of configuration, already used in [32], is very robust, stable, and efficient since it has a common path for both polarization components and no beam splitters are required. We previously used this architecture for implementing a polarization diffraction grating based polarimeter [33] and customized structured polarized dual polarization split lenses [34]. In the new system here presented, though, we use two Hamamatsu LCoS-SLMs, devices that are free of flicker thus allowing operating the system on-axis, as opposed to the previous systems that were operated off-axis due to the zero-order (DC) component caused by this flicker effect. In addition, we use a recently developed method to encode complex valued computer-generated holograms (CGH) onto phase-only displays [35]. This method is based on a random spatial multiplexing of two phase-only diffractive patterns (the phase information of the desired signal pattern and a diverging optical element that controls the amplitude) and creates the desired hologram reconstruction on axis. Therefore, it is very efficient in terms of light budget since it does not require adding a carrier phase function and does not reduce the available space bandwidth product. This encoding technique was successfully applied to demonstrate a simultaneous aberration and aperture control in a visual simulator system [36], and here we experimentally apply it to generate VBs. By addressing different combinations of scalar modes belonging to the Orbital Angular Momentum (OAM) Poincaré sphere [37,38] encoded onto orthogonal polarization states, we build different VBs [39]. Finally, we demonstrate that our two SLM-based optical system enables to easily apply a phase-shifting technique that proves itself very useful to obtain the exact phase distribution of the superpositions of different generated modes.

The paper is organized as follows: after this introduction, Section 2 describes the optical system for the independent control of polarization components. Then, in Section 3 we explain the design of phase-only holograms for displaying complex-valued functions. Experimental results are shown in Section 4. In Section 5 we use phase-shifting techniques to estimate the phase of the optical beams finally obtained. Conclusions are given in section 6.

2. OPTICAL SYSTEM FOR THE INDEPENDENT CONTROL OF POLARIZATION COMPONENTS

Figure 1 shows the scheme of the optical setup. We use an input He-Ne laser ($\lambda=633$ nm) that is spatially filtered and collimated. Two LCoS-SLMs are arranged in a Z configuration. The angle between the incident ray and the reflected ray on each modulator is about 11° . LCoS1 and LCoS2 devices are on conjugated planes by means of a $4f$ -system obtained by two lenses of the same focal length, thus obtaining a minus one magnification. Both devices are parallel-aligned LCoS displays from Hamamatsu (model X10468-01). We measured a reflectivity of more than $R = 78\%$ for both devices. And they have 800×600 pixels, with $20 \mu\text{m}$ pixel pitch, an effective area of $15.8 \times 12 \text{ mm}^2$ and 98% fill factor, thus providing more than 96% efficiency to the main reflected beam (zero order). Therefore, the total device efficiency at the zero order is about $\eta \sim 75\%$. As mentioned earlier, an important characteristic of these devices is that they are free of flicker. Therefore, the reflected beam does not present zero order (DC) component and the displayed holograms can be designed to generate reconstruction on-axis, and therefore make full use of this 75% zero-order efficiency.

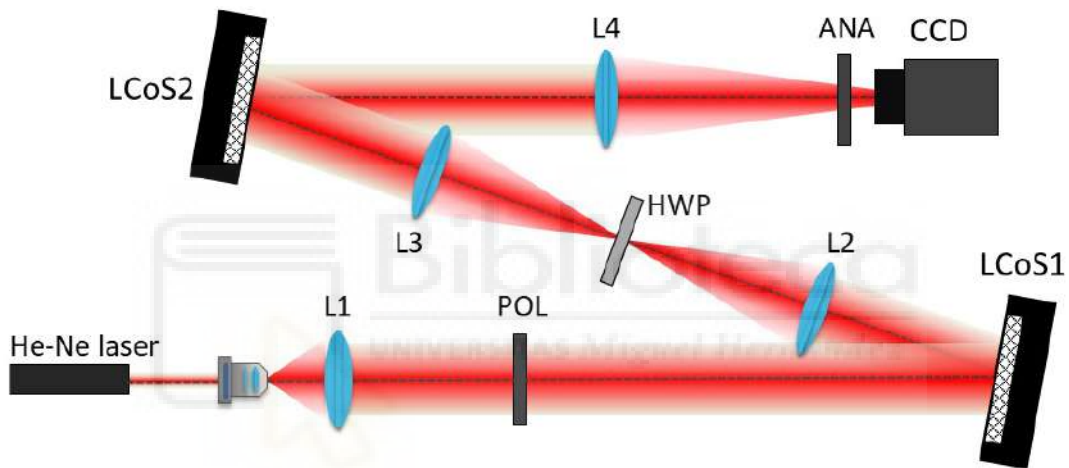


Fig. 1. Scheme of the optical setup. LCoS1 and LCoS2 are two liquid-crystal on silicon SLMs, with the liquid-crystal director oriented horizontally. A $4f$ -system (lenses L2 and L3) images LCoS1 onto LCoS2. POL: input linear polarizer. ANA: output polarization analyzer. HWP: half-wave plate. CCD: charge couple device detector.

The input polarizer (POL) is oriented at 45° to ensure equal magnitude on both horizontal and vertical polarization components. Parallel-aligned LCoS displays only modulate the linear polarization component parallel to the LC director. In our devices, this corresponds to the laboratory horizontal direction. Therefore, a phase pattern addressed to LCoS1 modulates the horizontal component of the input beam, while the vertical polarization component is unaffected. A half-wave plate (HWP) oriented at 45° is added after LCoS1 in order to transform the horizontal linear polarization component into the vertical component of the input beam (and viceversa). In this way, LCoS2-SLM modulates the polarization component that was not modulated by LCoS1-SLM, while leaving unaffected the polarization component that was already modulated by the first SLM. Thus, the output beam has two orthogonal horizontal and vertical polarization components that are independently modulated through the phase-only mask implemented by the two LCoS-SLMs.

The output beam emerging from the system is phase-only modulated in its vertical and horizontal components, and therefore the output Jones vector can be written as:

$$\vec{J}(x, y) = \begin{pmatrix} J_x(x, y) \\ J_y(x, y) \end{pmatrix} = \begin{pmatrix} e^{i\psi_1(x,y)} \\ e^{i\psi_2(x,y)} \end{pmatrix}, \quad (1)$$

where $J_x(x, y)$ and $J_y(x, y)$ denote the spatial pattern encoded onto the vertical and horizontal linear polarization components respectively, and $e^{i\psi_k(x,y)}$, $k = 1, 2$, denotes the phase-only masks displayed onto LCoS1 and LCoS2 SLMs respectively. A lens focuses the beam, which is captured by a CCD camera. This final lens could be a physical converging lens or, as we use in this work, can be encoded onto the phase-only holograms $\psi_k(x, y)$ displayed on the LCoS SLMs. Finally, a polarizer analyzer (ANA) verifies the polarization output.

3. TECHNIQUE FOR ENCODING A COMPLEX FUNCTION ONTO A PHASE-ONLY SLM

Since LCoS devices work in phase-only modulation regime, a method to encode complex values onto phase-only displays is required. Here we used the codification method described in [35], which is based on a random spatial multiplexing of two phase-only functions: the phase information of the desired pattern and a diverging optical diffractive element to redirect undesired light out of the optical axis. This codification method presents interesting features: 1) it does not require any iterative algorithms, thus it is not computationally costly; 2) the desired complex optical field is reconstructed on-axis; and 3) no phase carriers are required. Next, we briefly review this method.

Let $F(x, y) = M(x, y)e^{i\varphi(x,y)}$ be the complex function to be encoded, where $M(x, y)$ and $\varphi(x, y)$ represent its magnitude and phase. A new multiplexed phase-only function $e^{i\psi(x,y)}$ is designed as:

$$e^{i\psi(x,y)} = R(x, y)e^{i\varphi(x,y)} + \bar{R}(x, y)e^{i\xi(x,y)}, \quad (2)$$

where $R(x, y)$ is a binary-amplitude (0-1) pattern, $\bar{R}(x, y) = 1 - R(x, y)$ is its complementary pattern, and $e^{i\xi(x,y)}$ is the phase function of a diverging element, in our case a high-frequency negative diffractive axicon, $\xi(x, y) = -2\pi r/p$, $r = \sqrt{x^2 + y^2}$ denoting the radial coordinate, and p denoting the axicon's period. The role of $R(x, y)$ is to select, at each pixel, between the phase function $\varphi(x, y)$ and the diverging axicon phase function $\xi(r)$.

The negative diffractive axicon acts as a circular blazed diffraction grating that diverges the light away from the optical axis. This light can be very easily filtered by a circular aperture. This way, the magnitude information $M(x, y)$ is encoded onto the new multiplexed phase-only function $\psi(x, y)$ via the function $R(x, y)$ which is defined as

$$R(x, y) = \begin{cases} 1 & \text{if } M(x, y) > rnd(x, y), \\ 0 & \text{if } M(x, y) \leq rnd(x, y), \end{cases} \quad (3)$$

where $rnd(x, y)$ is a distribution of random numbers in the interval $[0, 1]$.

This phase-only encoding technique of the complex function $M(x, y)e^{i\varphi(x,y)}$ can be easily understood as follows. If the required amplitude $M(x, y)$ is close to 1, it is better represented

by the phase-only function $e^{i\varphi(x,y)}$ and $R(x,y) = 1$ is the good choice. On the contrary, for pixels where $M(x,y)$ is close to 0, light should be removed. The diverging axicon performs this operation directing light out of the optical axis. Therefore, $R(x,y) = 0$ is the right choice for these pixels. For intermediate values of $M(x,y)$, Eqs. (2)-(3) provide an adequate random choice between the two phase-only functions.

Note that the light directed out of the optical axis by the encoded axicon involves the arising of a ring of light at the Fourier transform planes, while the hologram reconstruction appears on axis [35]. Therefore, this ring of light must be filtered in order to achieve good results. Since the diffractive axicon has a high spatial frequency, the filtering can be easily done by means of a circular aperture located in the Fourier transform planes. For the mask displayed in LCoS1-SLM, a circular aperture can be placed at the back focal plane of the lens after the SLM. In our case, the HWP circular mount acted as the circular aperture, thus blocking the ring generated by the first axicon. For the second mask displayed on the LCoS2-SLM, the ring of light appears in the plane where the CCD camera detector is placed, but outside the detector area which is centered on the final reconstruction. Therefore, it has no impact on the final image.

The accuracy of this encoding technique for the implementation of digital complex holograms was analyzed in detail in Ref. [35]. The signal-to-noise ratio and efficiency of the hologram reconstruction depends on the required amplitude modulation, as well as on the characteristics of the random function applied in the algorithm. The authors were able to achieve a hologram efficiency around 35%. In that work, the technique was applied to the generation of higher-order scalar Laguerre-Gauss (LG) and Hermite-Gauss (HG) laser modes. Here, we apply it for the generation of VBs in the optical system described in Section 2.

4. VECTOR BEAMS, ORBITAL ANGULAR MOMENTUM AND HIGHER-ORDER POINCARÉ SPHERES

Although VBs are natural solutions to the vectorial Helmholtz equation they are very often generated as coaxial superpositions of orthogonal scalar fields with orthogonal polarizations [7]. The system in Fig. 1 directly allows the superposition of different *HG* or *LG* modes encoded on the vertical and horizontal polarization states. The use of SLMs also enables us to add an extra constant relative phase (β) between the vertical and horizontal polarization components. This is equivalent to adding a linear retarder with retardance β and neutral axes oriented along vertical/horizontal directions. It is well-known that this is also very useful to provide different realizations of VBs. The output Jones vector in Eq. (1) can be approximated by

$$\vec{J}(x,y) = \begin{pmatrix} J_x(x,y) \\ J_y(x,y) \end{pmatrix} \simeq \begin{pmatrix} M_1(x,y)e^{i\varphi_1(x,y)} \\ M_2(x,y)e^{i\varphi_2(x,y)}e^{i\beta} \end{pmatrix}. \quad (4)$$

where the complex functions $M_k(x,y)e^{i\varphi_k(x,y)}$, $k = 1,2$, denote the magnitude and phase encoded on each polarization component. As mentioned earlier, in order to generate VBs we will encode the complex functions that correspond to *HG* or *LG* modes. We designed the functions $\varphi_k(x,y)$ to include the quadratic phase corresponding to a lens that replaces the final physical lens (L4) in the system in Fig. 1.

At this point, it is interesting to remind the relations between different generalized Poincaré spheres represented in Fig. 2. Figure 2(a) shows the standard Poincaré sphere, where each polarization state corresponds to a point on the sphere. The equator defines the linear states, while the circular right- and left-handed states:

$$\hat{\mathbf{e}}_{\mathbf{R}} = \frac{1}{\sqrt{2}} \begin{pmatrix} 1 \\ +i \end{pmatrix}, \quad \hat{\mathbf{e}}_{\mathbf{L}} = \frac{1}{\sqrt{2}} \begin{pmatrix} 1 \\ -i \end{pmatrix}, \quad (5)$$

lie on the north and south pole respectively. In general, an elliptic state given by

$$\hat{\mathbf{e}}_{\alpha, \varepsilon} = \sin\left(\varepsilon + \frac{\pi}{4}\right) e^{-i\alpha} \hat{\mathbf{e}}_{\mathbf{R}} + \cos\left(\varepsilon + \frac{\pi}{4}\right) e^{i\alpha} \hat{\mathbf{e}}_{\mathbf{L}} \quad (6)$$

describes a polarization ellipse with azimuth α and ellipticity ε , which lies on the point with longitude and latitude angles $(2\alpha, 2\varepsilon)$ of the Poincaré sphere.

In this work we encode *HG* and *LG* modes on the $J_x(x, y)$ and $J_y(x, y)$ patterns. *HG* modes are exact solutions of the scalar paraxial wave equations in Cartesian coordinates. We consider an output beam at the waist plane $z = 0$, the complex amplitude can thus be written as:

$$HG_{mn}(x, y, \omega_0) = \frac{1}{\omega_0} \sqrt{\frac{2^{-(m+n-1)}}{\pi m! n!}} H_m\left(\frac{\sqrt{2}}{\omega_0} x\right) H_n\left(\frac{\sqrt{2}}{\omega_0} y\right) e^{-((x^2+y^2)/\omega_0^2)}, \quad (7)$$

where H_m is the m -th order Hermite polynomial, ω_0 is the beam waist, and x and y are the Cartesian coordinates. On the other hand, *LG* modes are expressed at the waist as

$$LG_p^\ell(r, \theta, \omega_0) = \frac{1}{\omega_0} \sqrt{\frac{p! 2^{|\ell|+1}}{\pi (|\ell|+p)!}} \left(\frac{r}{\omega_0}\right)^{|\ell|} L_p^{|\ell|}\left(\frac{2}{\omega_0^2} r^2\right) e^{-(r/\omega_0)^2} e^{i\ell\theta} = A_{p\ell}(r) e^{i\ell\theta}, \quad (8)$$

where $L_p^{|\ell|}$ are the $p\ell$ -th order Laguerre polynomials, and r and θ are polar coordinates. The term $A_{p\ell}(r)$ in this equation accounts for the radial part of the function and does not depend on the sign of ℓ , only on its magnitude. The mode order is $N = m + n$ for an *HG* mode and $N = 2p + |\ell|$ for a *LG* mode, respectively [37].

For simplicity, we will restrict to the first-order modes ($N = 1$), for which the following relations exist [37]:

$$HG_{D/A} = \frac{1}{\sqrt{2}} (HG_{01} \pm HG_{10}), \quad (9a)$$

$$LG_0^{\pm 1} = \frac{1}{\sqrt{2}} (HG_{10} \pm iHG_{01}), \quad (9b)$$

where $HG_{D/A}$ denote the diagonal/antidiagonal *HG* modes. Alternatively, the *HG* beams can be composed of *LG* modes as

$$HG_{10} = \frac{1}{\sqrt{2}} (LG_0^1 + LG_0^{-1}), \quad (10a)$$

$$HG_{01} = \frac{-i}{\sqrt{2}}(LG_0^1 - LG_0^{-1}), \quad (10b)$$

$$HG_D = \frac{e^{-i\pi/4}}{\sqrt{2}}(LG_0^1 + iLG_0^{-1}), \quad (10c)$$

$$HG_A = \frac{e^{-i3\pi/4}}{\sqrt{2}}(LG_0^1 - iLG_0^{-1}). \quad (10d)$$

These relations, equivalent to those found when superposing polarization states, can be used to define the orbital angular momentum (OAM) Poincaré sphere [38]. This Poincaré sphere represents the superpositions of scalar first order HG and LG modes (Fig. 2b), where the equator contains the HG_{10} mode and their in-plane rotated versions, and the poles correspond to the LG_0^1 and LG_0^{-1} modes. Every point in the OAM Poincaré sphere, with longitude 2α and latitude 2ε , is obtained as the superposition of the LG_0^1 and LG_0^{-1} modes as

$$f(x, y) = \sin\left(\varepsilon + \frac{\pi}{4}\right) e^{-i\alpha} LG_0^1 + \cos\left(\varepsilon + \frac{\pi}{4}\right) e^{i\alpha} LG_0^{-1}. \quad (11)$$

Note that this expression is analogous to an elliptic state in Eq. (6).

Finally, Fig. 2(c) shows the higher-order Poincaré sphere of order one [39], which represents the first-order cylindrically polarized VBs. There is a one-to-one mapping between every point on the standard Poincaré sphere and the states in the first-order Poincaré sphere [40]. Each homogeneous polarization state generates one first-order vector beam when it traverses a q -plate device [12,41].

We note that different realizations of the higher-order Poincaré sphere can be obtained, depending on the orthogonal polarization states that are selected to encode the scalar modes. The Poincaré sphere in Fig. 2(c) [39] corresponds to the VBs generated when LG modes are encoded onto the circular polarization components, i.e., vector beams generated as:

$$\vec{V}(x, y) = \sin\left(\varepsilon + \frac{\pi}{4}\right) e^{-i\alpha} LG_0^{-1} \hat{\mathbf{e}}_{\mathbf{R}} + \cos\left(\varepsilon + \frac{\pi}{4}\right) e^{i\alpha} LG_0^1 \hat{\mathbf{e}}_{\mathbf{L}}. \quad (12)$$

The transversal section of these vector beams consists in elliptical states with constant ellipticity, but azimuth that rotates following the polar coordinate. Similarly, the superposition of LG modes encoded onto the vertical and horizontal linear polarizations results in the generation of VBs where the transversal section shows polarization states with constant orientation, but where the ellipticity changes following the polar coordinate [42].

We make use of the above relations to generate different VBs by means of the experimental system described in Section 2 (Fig. 1).

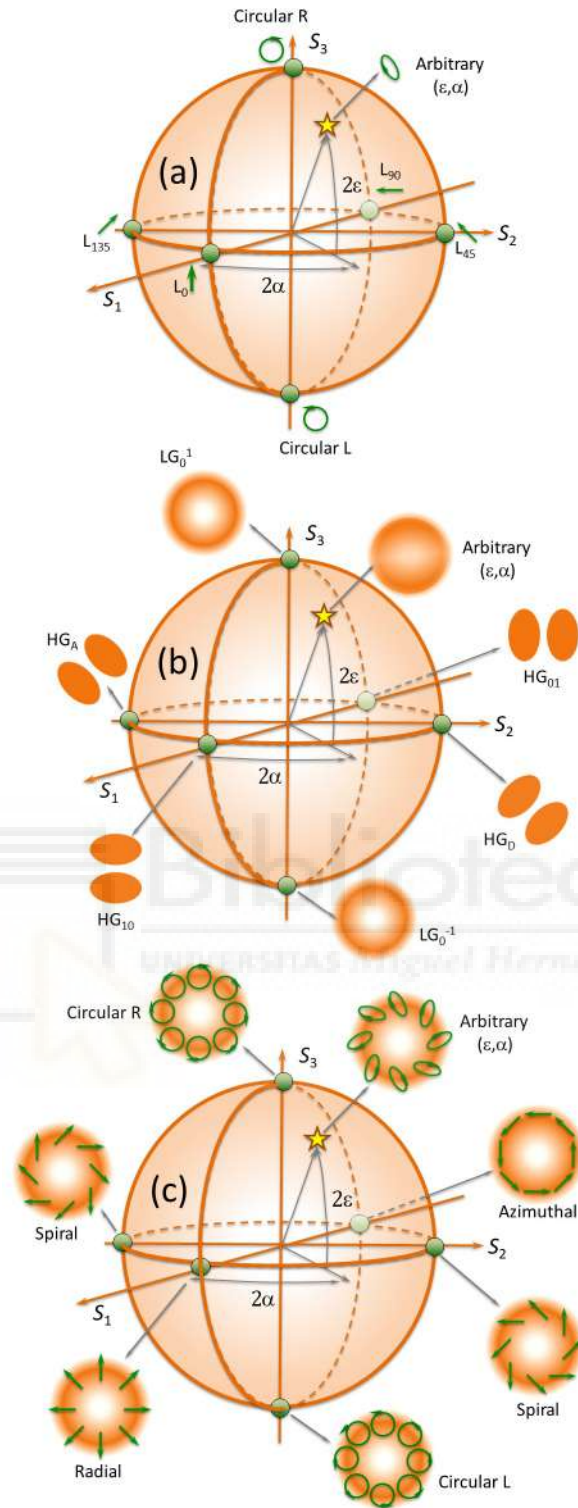


Fig. 2. (a) Standard Poincaré sphere for a homogeneous polarized state. (b) Orbital angular momentum (OAM) generalized Poincaré sphere. (c) Higher-order Poincaré sphere for first-order vector beams.

5. EXPERIMENTAL RESULTS

5.1 Superposition of orthogonally polarized HG modes

Let us start with the classical experiment that combines the HG_{10} and HG_{01} modes to generate a first-order vector beam [5]. The results are displayed in Fig. 3. In this case, we encode the mode HG_{10} on the vertical polarization, while the mode HG_{01} is encoded on the horizontal

polarization (note that the vertical direction is selected as the x axis). The output Jones vector is therefore given by

$$\vec{J}_1(x, y) = \frac{1}{\sqrt{2}} \begin{pmatrix} HG_{10}(x, y) \\ HG_{01}(x, y) \end{pmatrix}. \quad (13)$$

Figures 3(a) and 3(b) show a detail of the center of the phase-only hologram, codified using the technique presented in [35]. These masks show in the center the characteristic phase step of the HG beams (with a horizontal border for Fig 3(a), and a vertical border for Fig.3(b)) but accompanied by the high-frequency circular grating characteristic of the diffractive axicon.

Figure 3(c) shows the expected intensity and polarization pattern obtained from the Jones vector in Eq. (13), which corresponds to the radial polarization [5]. The inset shows the experimental CCD capture without analyzer, that exhibits the characteristic doughnut shape. The local state of polarization becomes evident when a linear analyzer is placed in front of the CCD camera. In Figs. 3(d) and 3(e) the analyzer is oriented vertical and horizontal, and only one polarization component is selected. The scalar modes HG_{10} and HG_{01} are then clearly visible. When the analyzer is oriented at $\pm 45^\circ$ the superposition of the two modes is built. The following simple Jones matrix calculus shows that the resulting field is

$$\vec{J}_{1P} = \frac{1}{2} \begin{pmatrix} 1 & \pm 1 \\ \pm 1 & 1 \end{pmatrix} \vec{J}_1(x, y) = \frac{1}{2} (HG_{10} \pm HG_{01}) \frac{1}{\sqrt{2}} \begin{pmatrix} 1 \\ \pm 1 \end{pmatrix} \propto HG_{D/A} \hat{e}_{\pm 45,0}, \quad (14)$$

where Eq. (9a) was applied and $\hat{e}_{\pm 45,0}$ indicates the linear polarization states at $\pm 45^\circ$. These superpositions, shown in Figs. 3(f) and 3(g), result in the diagonal and antidiagonal HG modes with polarized linear states oriented at $\pm 45^\circ$ respectively. Note how the projection of the polarization states in Fig. 3(c) agree with the intensity patterns in all cases. Note also that the rotation of the analyzer projects the generated vector beam onto a scalar mode that lies on the equator of the OAM Poincaré sphere.

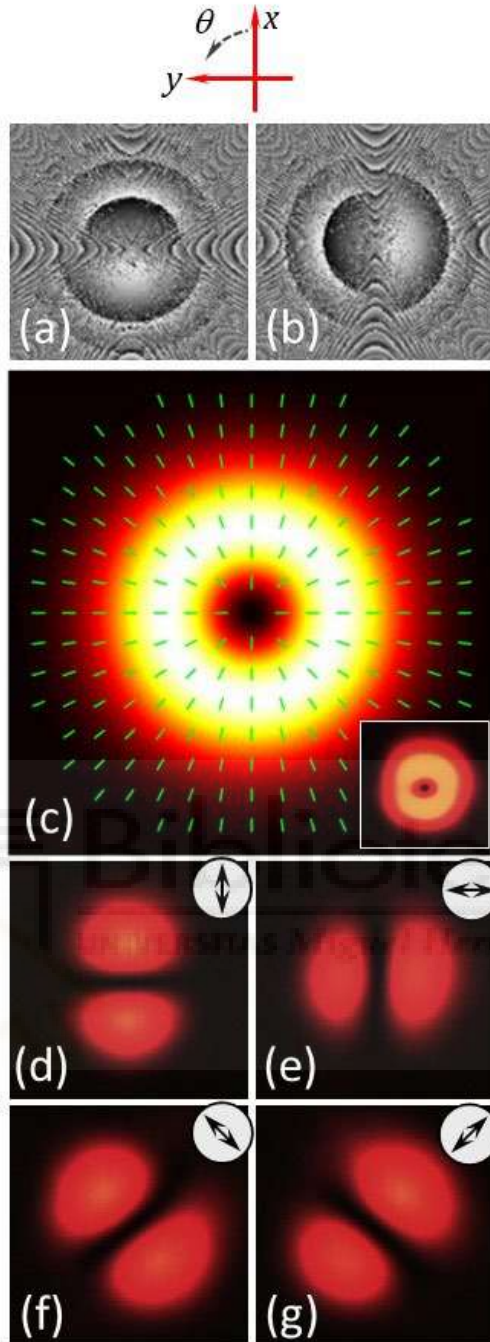


Fig. 3. (a)-(b) Central part of the phase-only holograms displayed on LCoS1 and LCoS2 to generate HG_{10} and HG_{01} modes. (c) Expected polarization pattern (the inset shows the CCD capture without analyzer). Experimental result with a linear analyzer oriented (d) vertical (HG_{10}), (e) horizontal (HG_{01}), (f) at 45° (HG_D) and (g) at -45° (HG_A). The analyzer's orientation is indicated on the top of each picture.

5.2 Phase bias control – Generation of LG modes from superposition of HG modes

Equation (9b) indicates that the LG modes can be obtained from the superposition of HG_{10} and HG_{01} modes with a relative $\pm\pi/2$ phase shift. The phase β in Eq. (4) can be changed simply by adding a constant gray level in one of the two phase holograms displayed on the LCoS-SLMs, in this case LCoS2. Therefore, we build a VB whose output Jones vector is in the form:

$$\vec{J}_2(x, y) = \frac{1}{\sqrt{2}} \begin{pmatrix} HG_{10}(x, y) \\ iHG_{01}(x, y) \end{pmatrix}. \quad (15)$$

Again, Figs. 4(a) and 4(b) show the holograms displayed on LCoS1 and LCoS2 SLMs. The polarization pattern in Fig. 4(c) looks different, since now it is the ellipticity (and not the orientation, as was the case in Fig. 3(c)) the polarization parameter that changes along the polar coordinate. Along the diagonal directions, the polarization becomes circular. This polarization map does not belong directly to the Poincaré sphere in Fig. 2(c), but it is simply the transmission of the radial polarization through a quarter-wave plate (QWP) with axes oriented along the $x - y$ coordinates [43]. Projecting the Jones vector in Eq. (15) onto a linear polarizer oriented at $\pm 45^\circ$ yields

$$\vec{J}_{2P} = \frac{1}{2} \begin{pmatrix} 1 & \pm 1 \\ \pm 1 & 1 \end{pmatrix} \vec{J}_2(x, y) = \frac{1}{2} (HG_{10} \pm iHG_{01}) \frac{1}{\sqrt{2}} \begin{pmatrix} 1 \\ \pm 1 \end{pmatrix} \propto LG_0^{\pm 1} \hat{e}_{\pm 45, 0}, \quad (16)$$

where we used Eq. (9b). The LG beams are obtained at linear states with orientation at $\pm 45^\circ$.

The corresponding experimental results are shown in Fig. 4. In the absence of analyzer (inset in Fig 4(c)), the intensity adopts the same pattern as in Fig 3(c). However, when we place the analyzer, the spatial polarization patterns are revealed. Again, when the analyzer is oriented either vertical or horizontal, the scalar HG modes appear. However, when the analyzer is oriented at $\pm 45^\circ$, the projection given by Eq. (16) results in the scalar modes $LG_0^{\pm 1}$. The polarization pattern in Fig. 4(c) is interesting since it allows transforming a vector beam onto scalar modes HG_{10} , HG_{01} and $LG_0^{\pm 1}$ by simply rotating the analyzer. Polarization ellipses drawn in blue are right states, while those in red denote left states. Linear states are drawn in green.

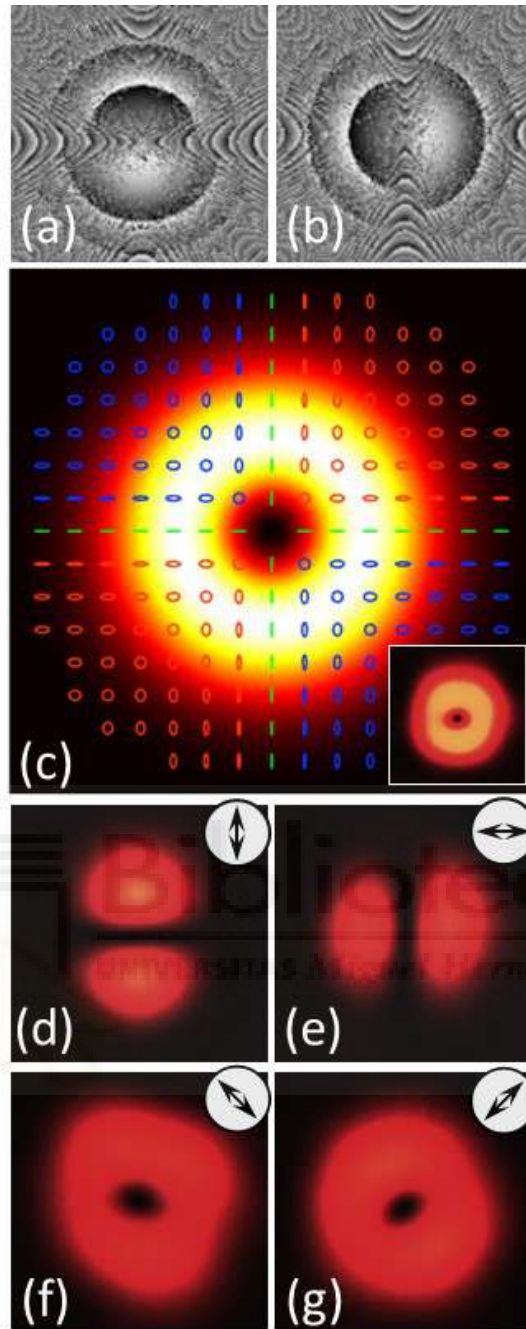


Fig. 4. (a)-(b) Central part of the phase-only holograms displayed on LCoS1 and LCoS2 to generate HG_{10} and HG_{01} modes. (c) Expected polarization pattern (the inset shows the CCD capture without analyzer). Ellipses with left- and right-handed polarization are drawn in red and blue respectively. Experimental result with a linear analyzer oriented (d) vertical (HG_{10}), (f) horizontal (HG_{01}), (g) at 45° (LG_0^1) and (h) at -45° (LG_0^{-1}). The analyzer's orientation is indicated on the top of each picture.

5.3 Stokes polarimetry of generated modes

The experimental images shown in Fig. 3 and Fig. 4 show the correct generation of the expected polarized beams. However, in the most general case the map of polarization states must be experimentally verified. This is typically done using an imaging polarimeter that provides images of the Stokes parameters. In order to complete the Stokes parameters measurement, two

additional images would be required in each case, using a quarter-wave plate (QWP) and a fixed polarizer to create a circular analyzer in front of the CCD camera.

However, alternatively, the QWP can be encoded with the aid of the SLMs, by adding a constant $\pm\pi/2$ phase shift to one of the two holograms. Note that, because we are considering paraxial beams, this is equivalent to the phase bias just mentioned in section 5.2. Adding a constant phase $\pm\pi/2$ to one of the SLMs is equivalent to adding a QWP before the analyzer. Therefore, the set of experimental images in Fig. 3 and Fig. 4 are enough to derive the Stokes parameters in both cases, without requiring a physical QWP. Figures 4(f) and 4(g) represent the right and left circular components of the vector beam in Fig. 3, while Figs. 3(f) and 3(g) represent the left and right circular components of the vector beam in Fig. 4.

Using this technique, we obtained the experimental Stokes parameters images shown in Fig. 5. These images were obtained using standard polarimetric definitions [44]. The case shown in Fig. 5(a), corresponding to the results in Fig. 3, is a radial linear polarized beam. Therefore the ellipticity must be zero, which implies that S_3 is almost zero, whereas S_1 and S_2 varies azimuthally from -1 to $+1$. The case in Fig. 5(b) corresponds to the results in Fig. 4. In this case is the S_2 parameter which remains null over the entire beam, while the S_1 and S_3 parameters show an azimuthal variation. The experimental results agree well with the expected polarization maps.



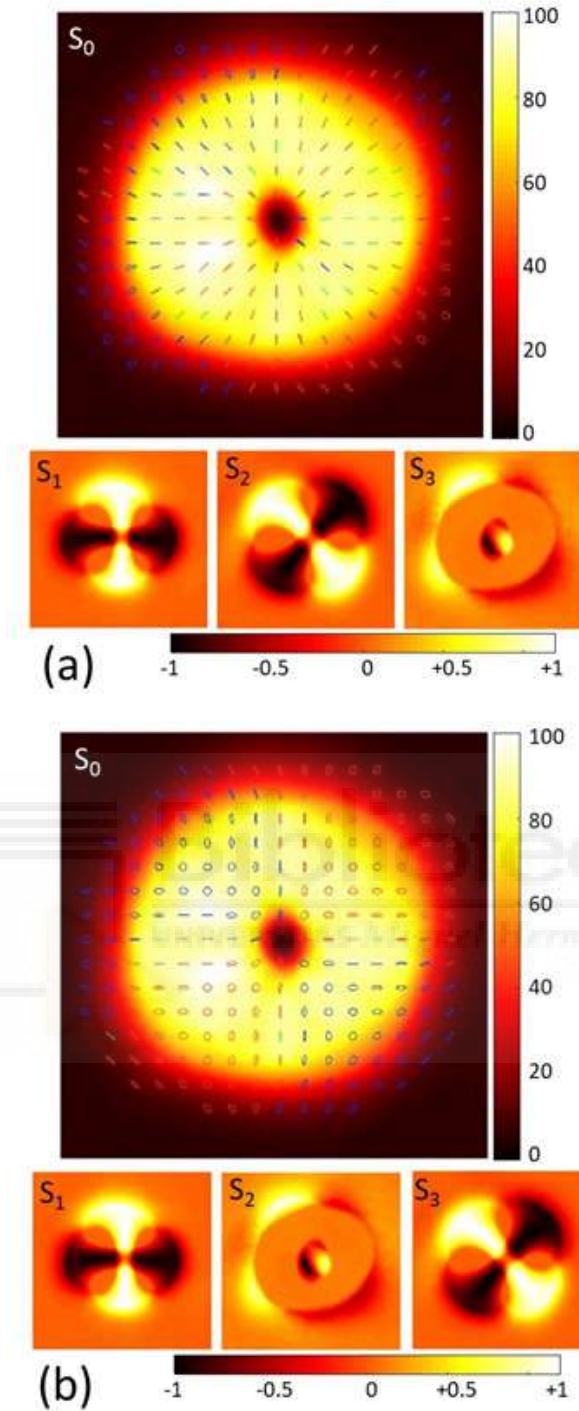


Fig. 5. Images of the experimental Stokes parameters for the vector beams in (a) Figure 3 and (b) Figure 4. S_1 , S_2 and S_3 are normalized Stokes parameters.

5.4 Superposition of LG modes to generate HG modes

In this example, we reverse the previous situation and encode $LG_0^{\pm 1}$ modes on the vertical/horizontal polarization components. The results are shown in Fig. 6. Note how the phase holograms in Figs. 6(a) and 6(b) now adopt the shape of a spiral lens, characteristic of combining the spiral phase of LG beams and the quadratic phase of the lens. Notice the opposite sense of rotation, corresponding to the opposite sign of the spiral phase.

The output Jones vector can thus be described as:

$$\vec{J}_3(r, \theta) = \frac{1}{\sqrt{2}} \begin{pmatrix} LG_0^1(r, \theta) \\ LG_0^{-1}(r, \theta) \end{pmatrix} = \frac{A_{01}(r)}{\sqrt{2}} \begin{pmatrix} e^{i\theta} \\ e^{-i\theta} \end{pmatrix}, \quad (17)$$

where $A_{01}(r)$ is the radial part of the LG function. This again corresponds to a vector beam, whose polarization pattern is drawn in Fig. 6(c). The state of polarization changes azimuthally due to the phase difference between the horizontal and vertical components. It is always an elliptical state aligned at $\pm 45^\circ$, but the ellipticity is changing along the polar coordinate. This again is not a vector beam that belongs to the Poincaré sphere in Fig. 2(c), but it is simply the transmission of the slanted (spiral) polarization state onto a QWP oriented at 45° [43].

When projecting this state onto a linear analyzer oriented at $\pm 45^\circ$ the following superposition is obtained

$$\vec{J}_{3P} = \frac{1}{2} \begin{pmatrix} 1 & \pm 1 \\ \pm 1 & 1 \end{pmatrix} \vec{J}_3(r, \theta) = \frac{1}{\sqrt{2}} (LG_0^1 \pm LG_0^{-1}) \vec{P}_{\pm 45} \propto HG_{10/01} \hat{e}_{\pm 45,0}, \quad (18)$$

which corresponds to the HG modes, according to Eqs. (10).



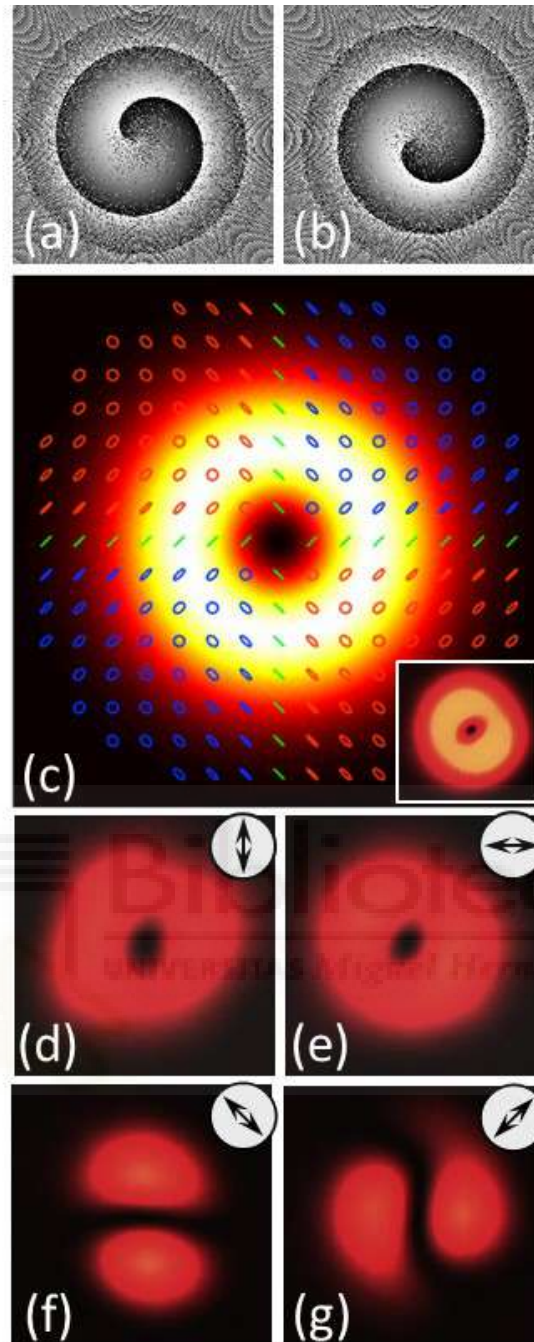


Fig. 6. (a)-(b) Central part of the phase-only holograms displayed on LCoS1 and LCoS2 to generate LG_0^1 and LG_0^{-1} modes. (c) Expected polarization pattern (the inset shows the CCD capture without analyzer). Ellipses with left- and right-handed polarization are drawn in red and blue respectively. Experimental result with a linear analyzer oriented (d) vertical (LG_0^1), (e) horizontal (LG_0^{-1}), (f) at 45° (HG_{10}) and (g) at -45° (HG_{01}). The analyzer's orientation is indicated on the top of each picture.

Figure 6(d) shows the experimental CCD capture of the generated beam without analyzer, which exhibits the characteristic doughnut shape. However, note in Figs. 6(d) to 6(g) the different projections onto a linear analyzer. When the analyzer is oriented either vertical or horizontal, the LG mode encoded on the corresponding LCoS-SLM is generated. But now, when the analyzer is oriented at $\pm 45^\circ$ an HG mode is obtained. Namely, at $+45^\circ$, we get the

superposition $LG_0^1 + LG_0^{-1}$, resulting in the HG_{10} mode, while at -45° , the superposition is $LG_0^1 - LG_0^{-1}$, resulting in the HG_{01} mode.

5.5 Generation of higher-order modes

In this final subsection we generate higher-order vector beams by combining LG modes, LG_0^ℓ and $LG_0^{-\ell}$ with orthogonal polarization states and higher ℓ values. We used again the linear polarization basis (x, y) that comes from the system in Fig. 1. Therefore, the output vector beam can be written as the following Jones vector:

$$\vec{J}_4(r, \theta) = \frac{1}{\sqrt{2}} \begin{pmatrix} LG_0^\ell(r, \theta) \\ LG_0^{-\ell}(r, \theta) \end{pmatrix} = \frac{A_{0\ell}(r)}{\sqrt{2}} \begin{pmatrix} e^{i\ell\theta} \\ e^{-i\ell\theta} \end{pmatrix}, \quad (19)$$

where $A_{0\ell}(r)$ represents the radial amplitude distribution. Figure 7 shows the experimental results obtained from the superposition of the two modes when the analyzer is oriented at $\pm 45^\circ$. The results correspond to the encoding of LG modes with charges $\ell = \pm 2$ (Figs 7(a) and 7(b)) and $\ell = \pm 3$ (Figs 7(c) and 7(d)). They show the characteristic pattern of the so-called petal beams [45], with a total number of four and six lobes respectively.

In Figs. 7(e)-7(h) a more complex superposition is shown. We generate phase-only holograms that encode the modes LG_1^{-3} and LG_0^8 in the vertical and in the horizontal polarization components (Figs. 7(e) and 7(f)). When the analyzer selects one of these two polarizations, the intensity pattern in these two modes arises. However, when the analyzer is oriented at $\pm 45^\circ$ (Figs. 7(g) and 7(h)), the petal interference pattern is observed only in the external ring.

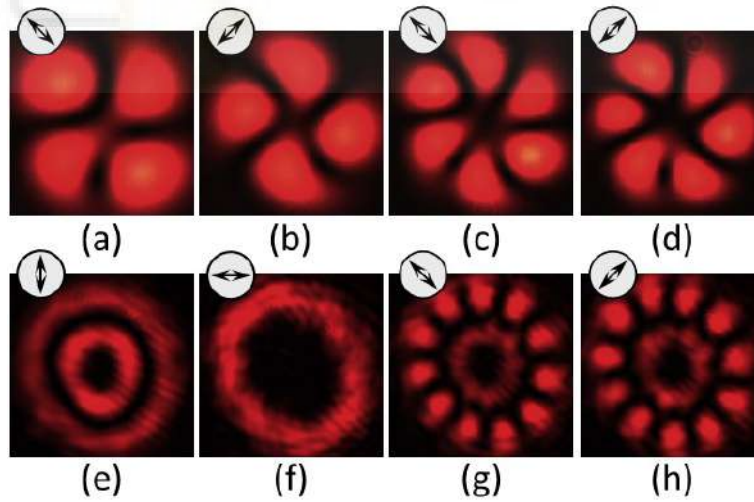


Fig. 7. Experimental CCD captures of the following cases: (a) $LG_0^2 + LG_0^{-2}$, (b) $LG_0^2 - LG_0^{-2}$, (c) $LG_0^3 + LG_0^{-3}$, (d) $LG_0^3 - LG_0^{-3}$, (e) LG_1^{-3} , (f) LG_0^8 , (g) $LG_1^{-3} + LG_0^8$, (h) $LG_1^{-3} - LG_0^8$. The orientation of the analyzer is indicated on the top of each picture.

6. PHASE EVALUATION WITH PROGRAMMED PHASE-SHIFTING

One of the great advantages of using SLMs to generate these modes is the ability to program arbitrary phase holograms. The previous results have demonstrated the accurate generation of the intensity pattern characteristic of different types of modes. However, in order to completely

verify that we are indeed generating the correct vector beam, the phase distribution of the superposition beams should be measured as well. This requires interferometric techniques. In this section we show that our SLM-based optical setup can be employed to perform this phase evaluation through phase-shifting interferometry (PSI) and without requiring any other additional elements.

Phase-shifting interferometry (PSI) [46] uses multiple interferograms with different relative phase shift between the reference and the test beams. We use the four-step algorithm with phase shifts $0, \pi/2, \pi,$ and $3\pi/2$. A similar approach was used in [35] to evaluate the phase of scalar beams generated with a single SLM. Here we extend it to the case of the generated VBs. The interferograms are obtained simply by placing a final analyzer oriented at $\pm 45^\circ$ before the CCD detector. Then, the required relative phase shift is introduced in one of the modulators, with steps of $\pi/2$ phase shift. Four images are captured, $I(x, y; \delta)$, one for each value of the phase shift δ , and the spatial phase distribution $\Delta(x, y)$ is calculated as

$$\Delta(x, y) = \arctan \left[\frac{I(x, y; \frac{3\pi}{2}) - I(x, y; \frac{\pi}{2})}{I(x, y; 0) - I(x, y; \pi)} \right]. \quad (20)$$

Figures 8(a) and 8(b) show the generation of two LG_0^ℓ modes, having $\ell = \pm 5$, respectively. Their superposition is presented in Fig. 8(c) when the analyzer is oriented at 45° , and results in a petal beam with ten lobes. The result of the phase-shift algorithm is shown in Fig. 8(d). We can observe that the experimental superposition $LG_0^5 + LG_0^{-5}$ shows spiral phase pattern with $2\ell = 10$ jumps from 0 to 2π , thus verifying the correct generation of the beam.

A more complex situation is shown in the second row of Fig. 8. In this case, the vertical and horizontal polarization components encode modes LG_0^7 and LG_0^{-2} respectively. The difference in the magnitude of ℓ is noticeable in the different diameter of the two rings. When the analyzer is oriented at 45° to generate their superposition, the intensity pattern shows a null point at the center, but additional nine dark points around it (Fig 8(g)). The measured phase associated to this intensity pattern is displayed in Fig. 8(h) and exhibits nine phase jumps from 0 to 2π along the polar coordinate.

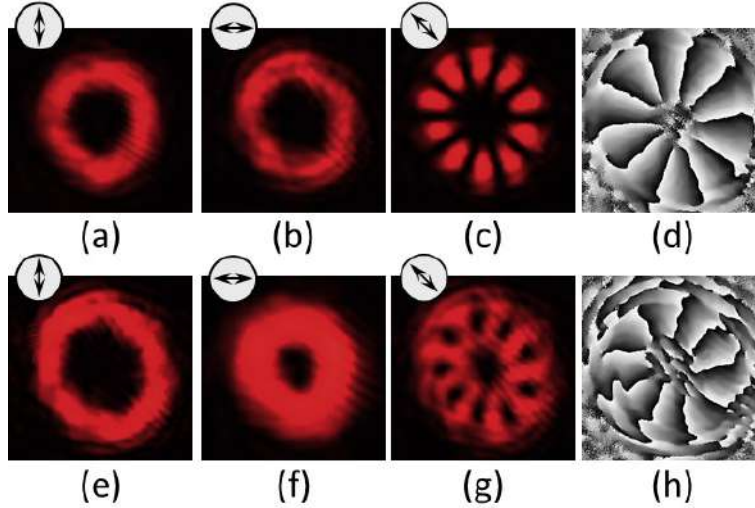


Fig. 8. Experimental CCD captures of: (a) LG_0^5 , (b) LG_0^{-5} , (c) $LG_0^5 + LG_0^{-5}$. (d) Phase of (c) measured using PSI. Experimental CCD captures of: (e) LG_0^7 , (f) LG_0^{-2} , (g) $LG_0^7 + LG_0^{-2}$. (h) Phase of (g) measured using PSI.

7. CONCLUSIONS

In summary, we have presented an optical setup using a Z-configuration which is based on two LCoS panels working in phase-only modulation useful to generate different vector modes that result from the superposition of HG and LG modes encoded on orthogonal **linear** polarizations. A remarkable advantage of this optical arrangement is its high light-efficiency, since no beam splitter is employed. In addition, since the SLMs used in this work do not show flicker, they can be operated in the zero diffraction order (there is no need of a phase carrier). Consequently, the complete space-bandwidth product of the device is employed and we can work on-axis. The optical system energy budget is reduced mainly by the reflectivity ($R \sim 78\%$) and the zero-order diffraction efficiency ($\eta \sim 96\%$) of the LCoS devices. Since two LCoS-SLMs are employed, the total system maximum conversion efficiency is about 56% (additional losses at the lenses and HWP in the system should also be accounted).

We use the LCoS-SLMs to encode spatial patterns that modify the phase but also the magnitude of the vertical and horizontal polarization components. For that purpose, a recently developed technique to encode complex functions in phase-only functions is applied [35], which also reconstructs the desired field on axis. The encoding technique introduces additional losses that depend on the magnitude information that is encoded. Magnitude encoding is accomplished by diffracting light out of axis by means of a diverging axicon whose characteristic Fourier transform ring must be filtered. Nevertheless, the encoding technique generates on-axis hologram reconstruction, thus avoiding any additional phase carrier function. The experimental realization of different vector beams has been demonstrated.

Finally, another interesting result of our proposal relies on the fact that with the same optical setup, the calculation of the phase distribution of the resulting vector beams can be easily retrieved. We use a four-step phase-shifting algorithm to evaluate the phase of the generated beams even for higher orders. As a result, we have developed an efficient facility to generate different types of vector beams, useful for developing complex light beams that could be exploited in any of the many applications of vector beams that are nowadays developed.

Acknowledgements

This work has been financed by Generalitat Valenciana, Conselleria d'Educació, Investigació, Cultura i Esport (PROMETEO-2017-154) and by Ministerio de Ciencia, Innovación y Universidades, Spain (RTI2018-097107-B-C33).

REFERENCES

- [1]. R. Dorn, S. Quabis, and G. Leuchs, "Sharper focus for a radially polarized light beam" *Phys. Rev. Lett.* **91**, 233901 (2003).
- [2]. B. J. Roxworthy and K. C. Toussaint, Jr., "Optical trapping with π -phase cylindrical vector beams," *New J. Phys.* **12**, 073012 (2010).
- [3]. Y. Jin, O. J. Allegre, W. Perrie, K. Abrams, J. Ouyang, E. Fearon, S. P. Edwardson, and G. Dearden, "Dynamic modulation of spatially structured polarization fields for real-time control of ultrafast laser-material," *Opt. Express* **21**, 25333–25343 (2013).
- [4]. P. Török and P. R. T. Munro, "The use of Gauss-Laguerre vector beams in STED microscopy," *Opt. Express* **12**, 3605–3617 (2004).
- [5]. Q. Zhan, "Cylindrical vector beams: from mathematical concepts to applications," *Adv. In Opt. Photon.* **1**, 1-57 (2009).
- [6]. A. Forbes, *Laser Beam Propagation. Generation and Propagation of Customized Light*, (CRC, Pretoria, 2014).
- [7]. C. Rosales-Guzmán, B. Ndagano, and Andrew Forbes, "A review of complex vector light fields and their applications," *J. Opt.* **12**, 123001 (2018).
- [8]. Y. Mushiake, K. Matsumura, and N. Y. Nakajima, "Generation of radially polarized optical beam mode by laser oscillation," *Proc. IEEE* **60**, 1107 (1972).
- [9]. S. C. Tidwell, D. H. Ford, and W. D. Kimura, "Generating radially polarized beams interferometrically", *Appl. Opt.* **29** 2234–9 (1990).
- [10]. Z. Bomzon, G. Biener, V. Kleiner, and E. Hasman, "Radially and azimuthally polarized beams generated by space-variant dielectric subwavelength gratings" *Opt. Lett.* **27** 285–287 (2002).
- [11]. M. Stalder and M. Schadt, "Linearly polarized light with axial symmetry generated by liquid-crystal polarization converters," *Opt. Lett.* **21**, 1948-1950 (1996).
- [12]. L. Marrucci, C. Manzo, and D. Paparo, "Optical spin-to-orbital angular momentum conversion in inhomogeneous anisotropic media," *Phys. Rev. Lett.* **96**, 163905 (2006).
- [13]. F. Cardano, E. Karimi, S. Slussarenko, L. Marrucci, C. de Lisio, and E. Santamato, "Polarization pattern of vector vortex beams generated by q -plates with different topological charges", *Appl. Opt.* **51** (10), C1-C6 (2012).
- [14]. M. Rafayelyan and E. Brasselet, "Laguerre–Gaussian modal q -plates", *Opt. Lett.* **42**, 1966-1969 (2017).
- [15]. C. Maurer, A. Jesacher, S. Fürhapter, S. Bernet, and M. Ritsch-Marte, "Tailoring of arbitrary optical vector beams", *New J. Phys.* **9**, 78 (2007).
- [16]. I. Moreno, M. M. Sánchez-López, K. Badham, J. A. Davis, D. M. Cottrell, "Generation of integer and fractional vector beams with q -plates encoded onto a spatial light modulator," *Opt. Lett.* **41** (6), 1305-1308 (2016).

- [17]. E. J. Galvez, S. Khadka, W. H. Schubert, and S. Nomoto, "Poincaré-beam patterns produced by nonseparable superpositions of Laguerre–Gauss and polarization modes of light," *Appl. Opt.* **51**, 2925-2934 (2012).
- [18]. E. Otte, K. Tekce and C. Denz, "Spatial multiplexing for tailored fully-structured light," *J. Opt.* **20**, 105606 (7pp) (2018).
- [19]. I. Moreno, J. A. Davis, K. Badham, M. M. Sánchez-López, J. E. Holland, and D. M. Cottrell, "Vector beam polarization state spectrum analyzer," *Scientific Rep.* **7**, 2216 (2017).
- [20]. C. Rosales-Guzmán, N. Bhebhe, and A. Forbes, "Simultaneous generation of multiple vector beams on a single SLM," *Opt. Express* **25** (21), 25697-25706 (2017).
- [21]. K. J. Mitchell, N. Radwell, S. Franke-Arnold, M. J. Padgett, and D. B. Phillips, "Polarisation structuring of broadband light", *Opt. Express* **25** (21), 25079-25089 (2017).
- [22]. S. Ngcobo, I. Litvin, L. Burger, and A. Forbes, "A digital laser for on-demand laser modes", *Nat. Communications* **4**, 2289 (2013).
- [23]. D. Naidoo, F. S. Roux, A. Dudley, I. Litvin, B. Piccirillo, L. Marrucci, and A. Forbes, "Controlled generation of higher-order Poincaré sphere beams from a laser", *Nat. Photonics* **10**, 327-333 (2016).
- [24]. M.-Q. Cai, Z.-X. Wang, J. Liang, Y.-K. Wang, X.-Z. Gao, Y. Li, C. Tu, and H.-T. Wang, "High-efficiency and flexible generation of vector vortex optical fields by a reflective phase-only spatial light modulator", *Appl. Opt.* **56** (22), 6175-6180 (2017).
- [25]. S. Liu, S. Qi, Y. Zhang, P. Li, D. Wu, L. Han, and J. Zhao, "Highly efficient generation of arbitrary vector beams with tunable polarization, phase, and amplitude", *Photonics Res.* **6** (4), 228-233 (2018).
- [26]. J. A. Davis, D. M. Cottrell, J. Campos, M. J. Yzuel, and I. Moreno, "Encoding amplitude information onto phase-only filters," *Appl. Opt.* **38**, 5004-5013 (1999).
- [27]. T. W. Clark, R. F. Offer, S. Franke-Arnold, A. S. Arnold, and N. Radwell, "Comparison of beam generation techniques using a phase only spatial light modulator," *Opt. Express* **24**, 6249 (2016).
- [28]. J. B. Bentley, J. A. Davis, M. A. Bandres, and J. C. Gutiérrez-Vega, "Generation of helical Ince-Gaussian beams with a liquid crystal display," *Opt. Lett.* **31** (5), 649-651 (2006).
- [29]. L. Zhu and J. Wang, "Arbitrary manipulation of spatial amplitude and phase using phase-only spatial light modulators" *Scientific Rep.* **4**, 7441 (2014).
- [30]. D. Aguirre-Olivas, G. Mellado-Villaseñor, D. Sanchez-de-la-llave, and V. Arrizón, "Efficient generation of Hermite-Gauss and Ince-Gauss beams through kinoform phase elements," *Appl. Opt.* **54**, 8444-8452 (2015).
- [31]. A. Lizana, I. Moreno, A. Márquez, C. Lemmi, E. Fernández, J. Campos, M. J. Yzuel, "Time fluctuations of the phase modulation in a liquid crystal on silicon display: characterization and effects in diffractive optics," *Opt. Express* **16**, 16711-16722 (2008).
- [32]. B. Khajavi and E. J. Galvez, "High-order disclinations in space-variant polarization," *J. Opt.* **18** (8), 084003 (2016).
- [33]. A. Cofré, A. Vargas, F. A. Torres-Ruiz, J. Campos, A. Lizana, M. M. Sánchez-López, and I. Moreno, "Quantitative performance of a polarization diffraction grating polarimeter encoded onto two liquid-crystal-on-silicon displays", *Opt. Laser Technol.* **96**, 219–226 (2017).
- [34]. A. Cofré, A. Vargas, F. A. Torres-Ruiz, J. Campos, A. Lizana, M. M. Sánchez-López, and I. Moreno, "Dual polarization split lenses", *Opt. Express* **25** (20), 23773-23783 (2017).

- [35].J. L. Martínez-Fuentes and I. Moreno, "Random technique to encode complex valued holograms with on axis reconstruction onto phase-only displays", *Opt. Express* **26** (5), 5875-5893 (2018).
- [36].N. Suchkov, E. J. Fernandez, J. L. Martinez-Fuentes, I. Moreno, and P. Artal "Simultaneous aberration and aperture control using a single spatial light modulator," *Opt. Express* (2019), in press.
- [37].E. J. Galvez, "Vector beams in free space", Chap. 3 in *The Angular Momentum of Light*, D. L. Andrews, M. Babiker Edts., Cambridge University Press (2013).
- [38].M. J. Padgett and J. Courtial, "Poincaré-sphere equivalent for light beams containing orbital angular momentum," *Opt. Lett.* **24** (7), 430-432 (1999).
- [39].G. Milione, H. I. Sztul, D. A. Nolan, and R. R. Alfano, "Higher-order Poincaré sphere, Stokes parameters, and the angular momentum of light," *Phys. Rev. Lett.* **107**, 053601 (2011).
- [40].L. Marrucci, "Liquid crystal "q-plates": classical and quantum photonic applications," *Proc. SPIE* 8475, 84750P (2012).
- [41].J. A. Davis, N. Hashimoto, M. Kurihara, E. Hurtado, M. Pierce, M. M. Sánchez-López, K. Badham, and I. Moreno, "Analysis of a segmented q -plate tunable retarder for the generation of first-order vector beams," *Appl. Opt.* **54** (31), 9583-9580 (2015).
- [42].H. Sroor, I. Litvin, D. Naidoo, A. Forbes, "Amplification of higher-order Poincaré sphere beams through Nd:YLF and Nd:YAG crystals", *Appl. Phys. B* **125**, 49 (2019).
- [43].I. Moreno, J. Albero, J. A. Davis, D. M. Cottrell, J. B. Cushing, "Polarization manipulation of radially polarized beams," *Opt. Eng.* **51** (12), 128003 (2012).
- [44] D.Goldstein, *Polarized Light*, 2nd Edt. (Marcel Dekker, 2003).
- [45].I. A. Litvin, L. Burger, and A. Forbes, "Angular self-reconstruction of petal-like beams," *Opt. Lett.* **38** (17), 3363-3365 (2013).
- [46].H. Schreiber and J. H. Bruning, "Phase shifting interferometry", Ch. 7 in D. Malacara (Edt.) *Optical Shop Testing*, 3rd edtn. (John Wiley & Sons, Hoboken, 2007).

Measuring the spatial deformation of a LCOS spatial light modulator with a self-interference effect

DAVID MARCO,¹ ASTICIO VARGAS,² MARÍA DEL MAR SÁNCHEZ-LÓPEZ,^{1,3} AND IGNACIO MORENO^{1,4,*}

¹Instituto de Bioingeniería, Universidad Miguel Hernández de Elche, 03202 Elche, Spain

²Departamento de Ciencias Físicas, Universidad de La Frontera, Temuco, Chile

³Departamento de Física Aplicada, Universidad Miguel Hernández de Elche, 03202 Elche, Spain

⁴Departamento de Ciencia de Materiales, Óptica y Tecnología Electrónica, Universidad Miguel Hernández de Elche, 03202 Elche, Spain

*Corresponding author: i.moreno@umh.es

Received XX Month XXXX; revised XX Month, XXXX; accepted XX Month XXXX; posted XX Month XXXX (Doc. ID XXXXX); published XX Month XXXX

In this work we show a simple technique to characterize the spatial non-uniformity of a liquid-crystal on silicon (LCOS) spatial light modulator. It is based on illuminating the display with a wavelength out of the operation range so there is a significant reflection at the output surface. As a consequence, a Gires-Tournois interferometer is directly created, without any alignment requirement and insensitive to vibrations. The beam reflected at the output surface is the reference beam while the beam reflected at the LCOS silicon backplane surface can be modulated by adjusting the addressed gray level in order to quantitatively derive its deformation. We provide an experimental demonstration using a LCOS-SLM designed to be operative in the near-infrared (NIR) spectral range, but illuminated with visible light.

© 2020 Optical Society of America

<http://dx.doi.org/10.1364/OL.99.099999>

Spatial light Modulators (SLMs) have become a very common optoelectronic device in many optical laboratories, where they are used to display programmable diffractive elements. Parallel-aligned LCOS devices are nowadays widely employed to display phase-only masks and holograms [1]. They are reflective devices that modulate the phase of an input beam linearly polarized along the direction of the liquid-crystal director.

One of the major issues when operating with LCOS displays is the spatial non-uniformity. This is not so important for display applications, where only the light intensity matters. However, it causes an aberration that must be considered when the SLM is used as a diffractive element. In fact, some companies provide customers with a correcting mask that must be added to the designed phase mask in order to compensate for this backplane aberration. In other

cases, the users must perform their own characterization of the SLM uniformity. For that purpose, several standard interferometric techniques have been applied [2-7]. Other recent techniques have used the LCOS device itself to create the reference and test beams by adding some linear and/or quadratic phase patterns [8,9].

In this paper we propose a different approach based on illuminating the SLM with a wavelength out of the operation range. In this situation, the antireflection (AR) coating does not work properly and it reflects a significant portion of the input beam. Since the output part of the display has good flatness, this reflection can be used as the reference beam. The transmitted part of the beam is then reflected at the LCOS backplane, thus being affected by the non-uniformities in this surface. Multiple reflections are then produced, as analyzed in detail in [10]. Here, instead, we are interested in making the most of this undesired effect as a tool to characterize the backplane non-uniformity.

Because the beam that reached the backplane can be modulated by the liquid-crystal layer, this modulation can be used to obtain different interferograms simply by changing the gray level addressed to the display. The results here presented show how the phase introduced by the LCOS backplane aberration can be quantitatively derived from the position of the fringes of minimum intensity for different interference patterns. Then, this information is employed to design a phase correcting mask that must be added to the desired phase pattern to correct for this aberration.

Figure 1(a) shows the experimental set-up. A Hamamatsu LCOS-SLM model X10468-08 is employed. It consists of 792×600 pixels with pixel spacing of $\Delta=20\ \mu\text{m}$. The nominal wavelength operation of the device is 1000–1500 nm. However, we use light from a He-Ne laser of wavelength 543 nm. This beam is spatially filtered and collimated, and polarized with a linear polarizer (LP) along the direction of the SLM liquid-crystal director which, for this device, is aligned along the horizontal laboratory direction. A non-polarizing beam splitter (NPBS) is used to deviate the reflected beam.

The light reflected by the SLM can be regarded as composed of two beams [10]. Because the device is operated with a wavelength

far outside the designed range, the external AR coating reflects an important fraction of the input beam. This light is therefore not modulated. Another fraction of the input beam enters the SLM and reaches the backplane, where it is reflected. It is this backplane which exhibits a non-negligible spatial deformation which causes an aberration that must be compensated in order to achieve good results. Therefore, an interference pattern is naturally formed by the light reflected on the LCOS-SLM. We emphasize that such an interferogram arises from the SLM itself. Thus, no alignment or any other external interferometer arrangement is required.

The reflected light goes again through the NPBS and enters into a telescopic system composed of two lenses (L1 and L2) that form the image of the SLM screen onto a CCD detector (Basler, model scA1390-17fc with 1392×1040 pixels, of 4.65×4.65 μm pixel size). We use this telescopic system to obtain a perfect image of the LCOS-SLM screen instead of capturing a propagated interferogram in order to avoid the use of back propagation algorithms. The focal lengths are selected to be $f_1=25$ cm and $f_2=10$ cm, in order to create an image with magnification $M=-0.4$, so that the complete image of the LCOS screen fits inside the CCD detector area. With this arrangement, the phase deformation of the SLM screen is directly retrieved.

Figure 1(b) shows different interferograms captured when uniform images with different gray levels ($g=0, 20, 40$ and 60) are addressed to the SLM screen. Two important aspects to consider. First, note that the dark fringes of minimum intensity are very thin compared to the bright areas. This is expected from a Gires-Tournois interferometer, since the beam entering the liquid-crystal layer suffer multiple internal reflections. In such multiple-beam interferometers, dark fringes are located only in a narrow area around the points where the phase difference between the reference and the test beams (light reflected at the first surface and light that enters and reflects inside the LCOS backplane) is an odd multiple of π .

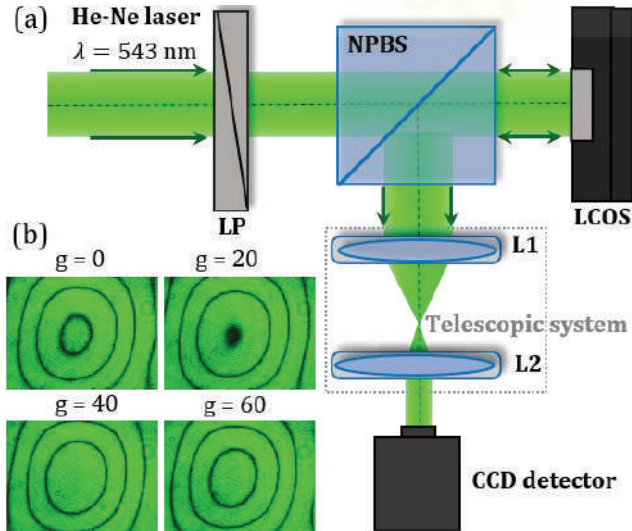


Fig. 1. (a) Scheme of the experimental set-up. LP: linear polarizer, NPBS: non-polarizing beamsplitter, LCOS: Liquid crystal on silicon spatial light modulator, L: Lens. (b) Interference patterns obtained for different gray level g levels addressed to the SLM display.

Secondly, note that the fringes are quite elliptical in shape (thus meaning that the related aberration is mostly spherical). We

observe that when the gray level increases, the dark fringes move towards the center of the screen. This can be seen at the different interferograms in Fig. 1(b). We consider that the phase ϕ_{Total} that the light gains inside the SLM is the sum of the liquid-crystal (LC) layer phase ϕ_{LC} , which is spatially uniform but depends on the gray level g , and the phase caused by the backplane deformation ϕ_{BP} , which only depends on the position x and y on the SLM screen, i.e.:

$$\phi_{Total}(g, x, y) = \phi_{LC}(g) + \phi_{BP}(x, y). \quad (1)$$

The dark fringes move because the phase $\phi_{LC}(g)$ of the liquid-crystal layer decreases as the addressed gray level increases [11]. The new location of the dark fringes is where now the phase ϕ_{Total} attained by the light inside the LCOS-SLM is again an odd multiple of π , compared to the reference beam reflected at the AR coating.

Considering that the phase of the LC layer decreases with the gray level, we deduce that the fringes move towards a region where the phase caused by the spatial deformation increases, in order to compensate the decreasing phase in the LC layer. Because the fringes move towards the center, we conclude that the phase added to the light by the aberration increases towards the center, so the backplane is concave from the point of view of the laser source. Nevertheless, the sign of the phase modulation can be ignored in many cases, as long as we can create a compensating mask, which is the task we introduce next.

Since the interferograms obtained are not simply a two-beam interference patterns (they are instead a multiple-beam interference patterns) they cannot be analyzed with a simple heterodyne technique. Instead, we apply a method based on the identification of the dark fringes, i.e., spatial points where the phase is $m\pi$ with m an odd integer, and their variation with the gray level. Then, this information is used to calculate a polynomial function that best fits the experimental data.

We start from Fig. 1(b), case $g=0$. Each dark fringe corresponds to a phase $m\pi$. Regarding the concave shape of the backplane, we consider that the outer fringe corresponds to a phase of π , the next one is 3π , then 5π and finally the inner fringe is 7π . In order to find the phase values in the rest of the screen, we consider the position of the dark fringes in interferograms obtained for other values of g . We identified that the fringe pattern for $g=0$ is repeated for $g=80$, meaning that the LC phase ϕ_{LC} has diminished in 2π . Since Hamamatsu provides their SLMs with a linear phase response to the addressed gray level, we can assume that it decreases linearly with g as

$$\phi_{LC}(g) = \phi_{LC}(0) - 2\pi \frac{g}{80}, \quad (2)$$

where $\phi_{LC}(0)$ is the maximum LC phase, corresponding to gray level $g=0$. Therefore, there is a phase difference of $\pi/2$ radians between two consecutive interference patterns in Fig 1(b).

We track the movement of each fringe in Fig. 1(b), case $g=0$, while increasing the gray level. The phase at different regions can be identified using the location of the dark fringes transiting in these areas for other values of g . When g is increased, the phase $\phi_{LC}(g)$ is decreased by $2\pi(g/80)$ and the dark fringes move towards the region where the phase ϕ_{BP} induced by the deformation of the backplane is bigger and compensates with the same amount. Therefore, we conclude that the dark fringes for arbitrary value of g are located at points with a phase difference of $2\pi(g/80)$ with

respect to the corresponding fringe in the interference pattern for $g=0$ (fringes with phases $\pi, 3\pi, 5\pi$ or 7π).

In order to precisely localize the dark fringes of the interferograms we followed these steps: First, we remove some noise in the experimental images in Fig. 1(b) by subtracting each interferogram from another interferogram that is phase shifted by π (a gray level difference of 40) and set the negative values to zero. As a consequence, we obtain a gray level image as shown in Fig. 2(a) for the interferogram with $g=0$ in Fig. 1(b). This operation removes a significant fraction of the noise that is common in the two interferograms and results in bright lines at the points where the dark fringes of the interferogram lay. We then apply a median filter to remove the remaining noise. As shown in Fig. 2(b), the filter makes the fringes smoother, thus avoiding discontinuities. Finally, we set all the points over a given threshold to 1 and below it to 0. As a result, we obtain binary images that detect the dark fringes in the interferograms in Fig. 1(b). Figure 2(c) reveals that the lines are thick, so we localize their central part.

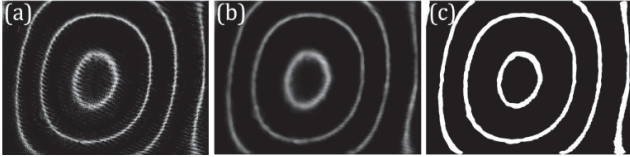


Fig. 2. Image processing procedure to precisely detect the dark fringes of the interference pattern for $g=0$. (a) Gray level image resulting from subtracting the interferogram for $g=0$ to the interferogram for $g=40$. (b) Result after a median filter is applied to the image 2(a). (c) Result after binarization of the image 2(b).

In addition to these four interferograms shown in Fig. 1(b), other interferograms are captured for other gray levels in between. We calculate the position of the dark fringes for the interferograms captured with $g=0, 20, 30, 40, 48$ and 66 . The only fringe that is discarded is the central one for $g=20$ because it is too difficult to determine (Fig 1(b)). As a result, we obtain a set of concentric lines corresponding to well identified phase values. These lines are presented in a scatter plot in Fig. 3(a) and the corresponding fitted phase map is 3D represented in Fig. 3(b), where the color bar indicates the phase value assigned to each edge in units of π .

In order to determine the continuous 2D phase function that the deformation imparts at each point we apply a least-square polynomial fit to the data for each integer value of the polar coordinate (from 0 to 359 degrees). The center of the polar coordinate system is located in the center of the aberration, which was determined as the central point of the inner fringe of the interference pattern where this fringe almost disappears (situation that occurs with $g=26$). Then, a phase value was assigned to this point by adding $2\pi g/80$ to the phase of the central fringe for $g=0$ (7π), so the phase is 7.65π . The data were fitted to a second-order polynomial for two different regions. The first region includes the phase values from 7.64π to 6.00π . We calculate the distance from the center of the aberration to every point of the edges in Fig 3(a). This procedure is calculated along radial lines for each value of the polar coordinate, in steps of one degree. We apply a fit to the phase versus distance data, and we assign the phase value of the rest of the points for a given value of the polar coordinate considering their distance to the center of the aberration and the coefficients of the polynomial fit. Every fit contained the central point with a phase of

7.65π . The same procedure was followed for the data from 6.00π to 0.65π , but this time we used the distance from a point of phase 6.00π to the other points. Combining the phase functions obtained for the two regions we get the phase that the aberration causes at each point of the screen of the SLM. Figure 3(b) shows a 3D plot of this phase and the experimental lines that were used to determine it, also shown in Fig. 3(a).

Finally, following this procedure, the mask that compensates the aberration is obtained. The phase that the deformation generates increases towards the center. So, in order to compensate it, the phase mask must decrease the phase towards the center following the shape of the aberration. Each value of the phase surface shown in Fig. 3(b) is assigned to a gray level by multiplying it by a factor of $80/2\pi$. The phase values are then wrapped so they go from $g=0$ to 80 (from 0 to 2π), and the mask shown in Fig. 3(c) is obtained.

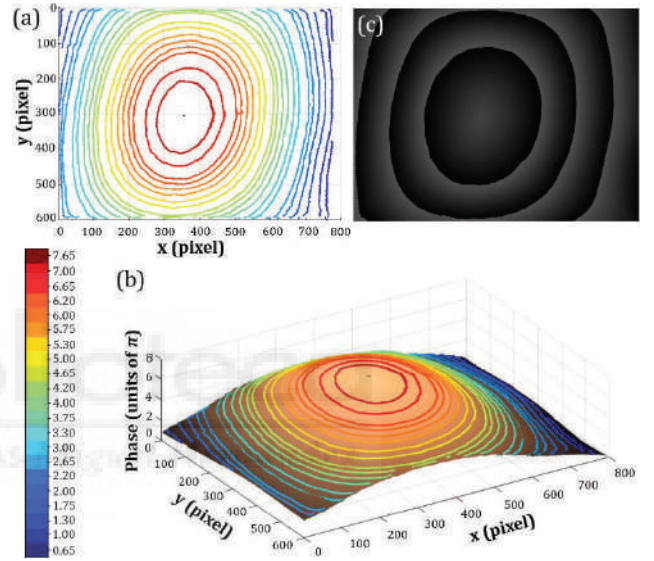


Fig. 3. (a) Scatter plot of the phase levels obtained from the dark fringes in interferograms for different gray levels. (b) Corresponding 3D plot of the phase aberration. The corresponding phase value is indicated in a color bar in units of π . (c) Gray level mask that compensates the spatial deformation.

In order to verify the effectiveness of this correction mask, we performed two kinds of experiments. A first experiment consists simply in adding the correction mask and examine the interference pattern. We call this as the near-field corrected image, since we capture the image of the SLM plane, in the same set-up in Fig. 1. Figure 4(a) shows an image of the interferogram obtained for $g=0$ whereas Fig. 4(b) shows the captured image when the correction mask in Fig. 3(c) is applied. Note how the interference fringes completely disappear when the correction mask is added, thus indicating an effective compensation of the aberration induced by the backplane deformation.

However, the correction shown in Fig. 4(b) is not a complete demonstration of the effectiveness of the technique. As mentioned before, the dark fringes in a Gires-Tournois interferometer are narrower than in a regular two-beam interferometer. Therefore, the elimination of the dark fringes in Fig. 4(b) could occur even if the phase values were not exact, as long as they move from the $m\pi$ (odd m) condition.

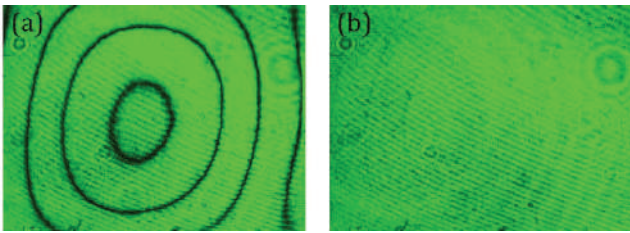


Fig. 4. Near field correction. (a) Image without correction. (b) Image with the correction mask.

Therefore, in order to better verify this correction, we perform an experiment where the far-field pattern generated with a phase diffractive element displayed onto the SLM is analyzed. In this case, the telescopic system in the set-up in Fig. 1(a) is replaced by a converging lens that forms the Fourier transform of the SLM screen onto the CCD detector. We choose a spiral phase pattern as the displayed diffractive element, since it generates a vortex beam. Vortex beams are very sensitive to aberrations and it is easy to identify when they are correct since they produce focus spots in the form of a circular ring of light [12]. However, the non-modulated beam reflected at the SLM external surface focuses on axis, therefore creating a bright spot of light that overlaps the vortex beam. In order to spatially separate the vortex beam from the non-modulated beam, we combine the spiral phase with a linear blazed grating, resulting in the well-known fork diffraction grating.

The results for the far field are presented in Fig. 5. Each subfigure shows the zero-diffraction order (right spot) and the +1 diffraction order (left spot). The vortex beam focuses in the first order, while the zero order gets the non-modulated beam. Images in the left column (Figs. 5(a), 5(c), and 5(e)) were obtained without the correction mask while those in the right column (Figs. 5(b), 5(d), and 5(f)) employ the mask. The first row shows the results when only the linear blazed profile was addressed to the SLM. Note that the zero-diffraction order shows a focalization in the form of a bright rounded light spot, denoting that the beam reflected at the outer surface does not acquire any aberration. On the contrary, the focus on the first diffraction order appears clearly distorted, denoting the aberration this beam acquires when it is reflected by the LCOS backplane. When applying the mask, the deformed spot in the +1 order (Fig. 5(a)) turns almost identical to the spot in the 0 order (Fig. 5(b)), thus verifying the effective compensation of the aberration.

The results in the second and third rows of Fig. 5 confirm this correction. In these cases, we address a fork grating to the SLM, obtained by adding a spiral phase with topological charge one and two, respectively, to the blazed grating. The characteristic ring shape of the vortex beams now appear on the first diffraction order and exhibits larger diameter as the charge increases. However, note how the clear distortion in the vortex beams that is significantly improved when we apply the correction mask, resulting in focus spots with clear circular shapes and a singularity in the center.

Let us mention that in these results we do not illuminate the complete SLM screen since we use a circular diaphragm before the SLM to get a circular input beam. This way it is possible to better identify the circular shape of the focused diffraction orders.

In summary, we have presented a novel and very simple method of determining the spatial deformation of a LCOS-SLM that does not require an external interferometric system. As a consequence, the experimental system is very stable under external conditions.

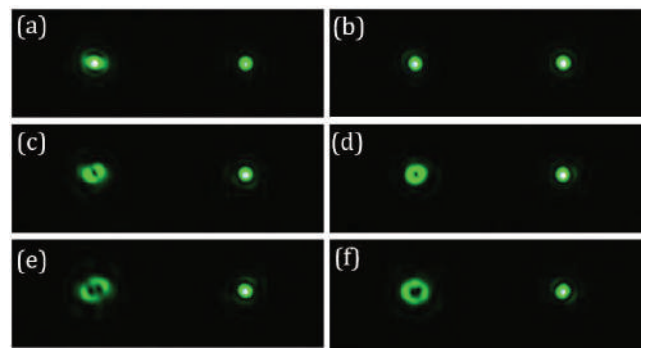


Fig. 5. Far field results for forked blazed diffraction gratings without ((a), (c), (e)) and with the correction mask ((b), (d), (f)). (a)-(b) Charge 0, (c)-(d) charge 1 and (e)-(f) charge 2.

The method is based on illuminating the device with a wavelength out of the operating range. In this situation, the outer AR coating partially reflects the incoming beam, and partially transmits light to the liquid crystal layer which is then reflected at the backplane. Thus, reflected light from the SLM directly generates an interferogram that provides the information to infer the backplane spatial deformation.

Since it is a multiple-beam Gires-Tournois interference, the dark fringes are very narrow at the points where the total phase is an odd multiple of π radians. We showed how the fringes shift by changing the addressed gray level, and this provides the information to derive phase-level maps. From these data it is possible to obtain a continuous 2D phase function that compensates the spatial deformation of the backplane. We have shown the effectiveness of this correction in the near field and in the far field.

Funding. We declare support from Generalitat Valenciana, Conselleria d'Educació, Investigació, Cultura i Esport (PROMETEO-2017-154), Ministerio de Ciencia, Innovación y Universidades, Spain (RTI2018-097107-B-C33) and Fondo Nacional de Desarrollo Científico y Tecnológico ANID/FONDECYT 1191811, Chile.

Disclosures. The authors declare no conflicts of interest.

References

1. Z. Zhang, Z. You, and D. Chu, *Light Sci. Appl.* **3**(10), e213 (2014).
2. X. D. Xun and R. W. Cohn, *Appl. Opt.* **43**(35), 6400 (2004).
3. J. Oton, P. Ambs, M. S. Millán, and E. Pérez-Cabré, *Appl. Opt.* **46**(23), 5667 (2007).
4. D. Engström, M. Persson, J. Bengtsson, and M. Goksör, *Opt. Express* **21**(13), 16086 (2013).
5. T. Haist, C. Lingel, R. Adler, and W. Osten, *Appl. Opt.* **53**(7), 1413 (2014).
6. L. Teng, M. Pivnenko, Br. Robertson, R. Zhang, and D. Chu, *Opt. Express* **22**(21), 26392 (2014).
7. J. Xu, S. Qin, C. Liu, S. Fu, and D. Liu, *Opt. Lett.* **43**(12), 2993 (2018).
8. J. L. Martínez, E. J. Fernández, P. M. Prieto, and P. Artal, *Opt. Express* **24**(13), 14159 (2017).
9. H. Zhang, A. Lizana, C. Iemmi, F. A. Monroy-Ramírez, A. Márquez, I. Moreno, and J. Campos, *Opt. Lasers Eng.* **106**, 147 (2018).
10. J. L. Martínez, I. Moreno, M. M. Sánchez-López, A. Vargas, and P. García-Martínez, *Opt. Express* **22**(21), 25866 (2014).
11. I. Moreno, J. V. Carrión, J. L. Martínez, P. García-Martínez, M. M. Sánchez-López, and J. Campos, *Opt. Lett.* **39**(19), 5483 (2014).
12. A. Jesacher, A. Schwaighofer, S. FÜRhapter, C. Maurer, S. Bernet, and M. Ritsch-Marte, *Opt. Express* **15**(9), 5801 (2007).

References

1. Z. Zhang, Z. You, and D. Chu, "Fundamentals of phase-only liquid crystal on silicon (LCoS) devices", *Light Sci. Appl.* **3**(10), e213 (2014).
2. X. D. Xun and R. W. Cohn, "Phase calibration of spatially nonuniform spatial light modulators," *Appl. Opt.* **43**(35), 6400–6406 (2004).
3. J. Oton, P. Ambs, M. S. Millán, and E. Pérez-Cabré, "Multipoint phase calibration for improved compensation of inherent wavefront distortion in parallel aligned liquid crystal on silicon displays," *Appl. Opt.* **46**(23), 5667–5679 (2007).
4. D. Engström, M. Persson, J. Bengtsson, and M. Goksör, "Calibration of spatial light modulators suffering from spatially varying phase response", *Opt. Express* **21**(13), 16086-16103 (2013).
5. T. Haist, C. Lingel, R. Adler, and W. Osten, "Parallelized genetic optimization of spatial light modulator addressing for diffractive applications", *Appl. Opt.* **53**(7), 1413-1418 (2014).
6. L. Teng, M. Pivnenko, Br. Robertson, R. Zhang, and D. Chu, "A compensation method for the full phase retardance nonuniformity in phase-only liquid crystal on silicon spatial light modulators", *Opt. Express* **22**(21), 26392-26402 (2014).
7. J. Xu, S. Qin, C. Liu, S. Fu, and D. Liu, "Precise calibration of spatial phase response nonuniformity arising in liquid crystal on silicon", *Opt. Lett.* **43**(12), 2993-2996 (2018).
8. J. L. Martínez, E. J. Fernández, P. M. Prieto, and P. Artal, "Interferometric method for phase calibration in liquid crystal spatial light modulator using a self-generated diffraction grating", *Opt. Express* **24**(13), 14159–14171 (2017).
9. H. Zhang, A. Lizana, C. Lemmi, F. A. Monroy-Ramírez, A. Márquez, I. Moreno, and J. Campos, "LCoS display phase self-calibration method based on diffractive lens schemes", *Opt. Lasers Eng.* **106**, 147–154 (2018).
10. J. L. Martínez, I. Moreno, M. M. Sánchez-López, A. Vargas, and P. García-Martínez, "Analysis of multiple internal reflections in a parallel aligned liquid crystal on silicon SLM", *Opt. Express* **22**(21), 25866-25879 (2014).
11. I. Moreno, J. V. Carrión, J. L. Martínez, P. García-Martínez, M. M. Sánchez-López, and J. Campos, "Optical retarder system with programmable spectral retardance," *Opt. Lett.* **39**(19), 5483-5786 (2014).
12. A. Jesacher, A. Schwaighofer, S. Fürhapter, C. Maurer, S. Bernet, and M. Ritsch-Marte, "Wavefront correction of spatial light modulators using an optical vortex image", *Opt. Express* **15**(9), 5801 (2007).



OPEN

Customized depolarization spatial patterns with dynamic retardance functions

David Marco¹, Guadalupe López-Morales¹, María del Mar Sánchez-López^{1,2}✉, Ángel Lizana³, Ignacio Moreno^{1,4} & Juan Campos³

In this work we demonstrate customized depolarization spatial patterns by imaging a dynamical time-dependent pixelated retarder. A proof-of-concept of the proposed method is presented, where a liquid-crystal spatial light modulator is used as a spatial retarder that emulates a controlled spatially variant depolarizing sample by addressing a time-dependent phase pattern. We apply an imaging Mueller polarimetric system based on a polarization camera to verify the effective depolarization effect. Experimental validation is provided by temporal integration on the detection system. The effective depolarization results are fully described within a simple graphical approach which agrees with standard Mueller matrix decomposition methods. The potential of the method is discussed by means of three practical cases, which include non-reported depolarization spatial patterns, including exotic structures as a spirally shaped depolarization pattern.

Controlling the polarization of light is an essential aspect in many different optical techniques¹, and its detection is the basis of polarimetry and ellipsometry². In recent years there has been a great research activity in developing optical polarimetric instruments, mostly based on liquid-crystal (LC) modulators, capable of generating and/or detecting different states of polarization (SoP), to build polarimeters without moving elements^{3–5}.

Partially polarized light can be expressed as a superposition of fully polarized light and unpolarized light weighted by its degree of polarization (DoP). The DoP provides very valuable additional information in the polarimetric analysis of samples⁶, which is becoming especially relevant in biomedical samples where depolarization measurements can provide valuable information^{7–9}. The term depolarization refers to the temporal and/or spatial incoherent coupling of polarized light into unpolarized light and is associated with a reduction in the DoP. There are situations where it is convenient to reduce the DoP of fully polarized light. This is typically necessary when a polarization insensitive response is required, as for instance in a laser pump diode¹⁰, in fluorescence resonance energy transfer (FRET) systems¹¹, in laser microfabrication methods¹² or in optical coherence tomography systems¹³.

There are different techniques to reduce the DoP. A classical method is the Lyot depolarizer¹⁴, which consists of two wave plates with a 2:1 thickness ratio and with a 45° relative orientation angle of their optical axes. This device is intended for use with polychromatic light and it has been applied both with bulk optics¹⁴ and with fiber optics¹⁰. Other recent techniques apply different strategies, as for instance, dividing the input beam in two orthogonal SoPs which are then recombined after modification of their properties in a Mach-Zehnder interferometer^{15,16}, or based on an imbalanced dual-frequency dual-polarization light source¹⁷.

LC devices and LC modulators have been employed to build optical depolarizers, where two general strategies can be adopted. The first one considers the realization of a very fast spatial variation of the SoP along the beam transverse plane. If the detector integration area is much greater than the SoP spatial variation, the resulting beam presents an effective depolarization effect. This is the case of the cholesteric LC wedge depolarizer¹⁸ or the LC depolarizers designed with randomly distributed optical axes^{19,20}. The second strategy considers using optical modulators to generate a fast temporal variation of the SoP. In this case, if the detector integration time is much greater than the SoP temporal variation, again the result is an effective depolarization effect. This effect was noticed originally in liquid-crystal on silicon (LCOS) displays^{21,22}, where it was perceived as a negative effect that reduced the image contrast or the diffraction efficiency of patterns displayed onto these devices. However, more

¹Instituto de Bioingeniería, Universidad Miguel Hernández de Elche, Avda. Universidad s/n, 03202 Elche, Spain. ²Departamento de Física Aplicada, Universidad Miguel Hernández de Elche, Avda. Universidad s/n, 03202 Elche, Spain. ³Departamento de Física, Universitat Autònoma de Barcelona, 08193 Bellaterra, Spain. ⁴Departamento de Ciencia de Materiales, Óptica y Tecnología Electrónica, Universidad Miguel Hernández de Elche, Avda. Universidad s/n, 03202 Elche, Spain. ✉email: mar.sanchez@umh.es

recently it has been exploited to create depolarizer instruments based either on ferroelectric LC modulators²³ or acousto-optic modulators¹⁷.

All these LC depolarizers were performed using a non-expanded laser beam and a single-pixel modulator. However spatial light modulators (SLM) are electronically controlled two-dimensional LC arrays consisting nowadays of over 1000×1000 pixels, and with a pixel size in the order of a few microns. Therefore, such LC-SLMs can be exploited to generate customized depolarization effects.

In this work, we use a parallel-aligned LC-SLM to emulate a temporal depolarizer in order to create an effective DoP image. We obtain this new situation by encoding a pixelated retardance pattern that changes with time. Such temporal variation has been proven to be very effective to reduce speckle noise in computer-generated holograms^{24,25}. In those works, however, SLMs were exploited only as scalar phase-only devices since no variation of the SoP was produced. Here, on the contrary, we use the SLM to produce a temporal SoP variation resulting in an effective depolarization effect which, in addition, is made spatially variant.

Since there is an increasing interest in studying the depolarization indices²⁶ as channels of new information, for instance in biological samples²⁷, this capability of emulating the depolarization with controlled precision can help to understand the physical mechanisms that cause depolarization in these samples. In addition, systems that generate structured light often make use of vector beams²⁸, where the SoP varies spatially but where the beam is usually kept totally polarized²⁹. As illustrated in this work with some examples, including the DoP as a new parameter in the vector beams could lead to completely new concept of structured light designs.

The structure of the paper is as follows. After this introduction, the next section introduces the methods we have applied, including the Mueller matrix analysis of a retarder with a temporal variation of its retardance and a graphical description of the time averaged SoP and its expected depolarization characteristics. It also includes the description of the experimental system. “Results and discussion” section shows the experimental results obtained by Mueller matrix image polarimetry, which proves the expected generation of spatially-variant effective depolarizing patterns. Various cases featuring different time and spatially-varying phase patterns are considered. Their complete interpretation is provided based on the SoP variations in the Poincaré sphere. Finally, “Conclusion” section includes the conclusions of the work.

Methods

Time averaged Mueller matrix. A state of polarization can be described by its Stokes parameters¹ (S_0, S_1, S_2, S_3) and they are represented in a column vector $\mathbf{S} = [S_0, S_1, S_2, S_3]^T$. An effective SoP that corresponds to partially polarized light (mixed state) can be described by a Stokes vector resulting from the incoherent addition of two Stokes vectors that describe fully polarized light (pure states). This addition can be experimentally performed by temporally averaging in a time T two Stokes vectors describing fully polarized light (\mathbf{S}_A and \mathbf{S}_B), each weighted by the time t_A and $t_B = (T - t_A)$, respectively, where $t_A \leq T$ ²³. As a result, an effective Stokes vector ($\langle \mathbf{S}_e \rangle$) is obtained:

$$\langle \mathbf{S}_e \rangle = \frac{1}{T} [t_A \mathbf{S}_A + (T - t_A) \mathbf{S}_B]. \quad (1)$$

In this work, we use this principle to make polarization patterns with a controlled spatially-varying DoP. For this purpose, a LC-SLM is illuminated with polarized light and two patterned gray-level designs are sequentially addressed to the SLM and switched during a period T , which is taken to be the integration time of our detector. As a result, two different spatially-varying pure polarization states are generated at the output, which change in time according to Eq. (1). The resulting light pattern can be regarded as having a customized effective partially polarized SoP, provided the integration time in the detector is large enough compared to the switch time in the SLM. Let us note that this procedure can be extended to include more than two polarization states. However, as shown next, with just two states it is possible to achieve any degree of polarization, including a full depolarization.

Therefore, for simplicity, we assume the situation where $t_A = T/2$. Therefore, using Eq. (1), the effective Stokes vector after the SLM plane is given by:

$$\langle \mathbf{S}_e(\mathbf{x}) \rangle = \frac{1}{2} [\mathbf{S}_A(\mathbf{x}) + \mathbf{S}_B(\mathbf{x})], \quad (2)$$

where $\mathbf{S}_A(\mathbf{x})$ and $\mathbf{S}_B(\mathbf{x})$ are the Stokes vectors describing the SoP that is generated by applying pattern A and pattern B to the SLM, and where $\mathbf{x} = (x, y)$ represent the spatial coordinates in the SLM.

The transformation that the SLM performs on an arbitrary input beam with homogeneous SoP (\mathbf{S}_{in}) can be described by a spatially-varying Mueller Matrix. For each of the two displayed patterns we can define its Mueller matrix $\mathbf{M}_A(\mathbf{x})$ and $\mathbf{M}_B(\mathbf{x})$ that apply over the input polarization state \mathbf{S}_{in} , resulting in two different polarization states: $\mathbf{S}_A(\mathbf{x}) = \mathbf{M}_A(\mathbf{x})\mathbf{S}_{in}$ and $\mathbf{S}_B(\mathbf{x}) = \mathbf{M}_B(\mathbf{x})\mathbf{S}_{in}$. Therefore, the effective averaged Mueller matrix during a time T is:

$$\langle \mathbf{M}_e(\mathbf{x}) \rangle = \frac{1}{2} [\mathbf{M}_A(\mathbf{x}) + \mathbf{M}_B(\mathbf{x})]. \quad (3)$$

The SLM used in this work is a parallel-aligned LC-SLM with its principal axis horizontally oriented. Therefore, it can be considered as a pixelated linear retarder where each pixel has the same principal axis orientation but with a variable retardance. This is represented by the Mueller matrix of a linear retarder with retardance ϕ and its slow axis along the horizontal direction¹.

$$\mathbf{M}_R(\phi) = \begin{pmatrix} 1 & 0 & 0 & 0 \\ 0 & 1 & 0 & 0 \\ 0 & 0 & \cos \phi & -\sin \phi \\ 0 & 0 & \sin \phi & \cos \phi \end{pmatrix}. \tag{4}$$

Substituting Eq. (4) in (3) the effective Mueller Matrix $\langle \mathbf{M}_e(\phi_A, \phi_B) \rangle$ that describes the SLM is:

$$\langle \mathbf{M}_e(\phi_A, \phi_B) \rangle = \frac{1}{2} [\mathbf{M}_R(\phi_A) + \mathbf{M}_R(\phi_B)], \tag{5}$$

$$\langle \mathbf{M}_e(\phi_A, \phi_B) \rangle = \begin{pmatrix} 1 & 0 & 0 & 0 \\ 0 & 1 & 0 & 0 \\ 0 & 0 & \frac{1}{2}(\cos \phi_A + \cos \phi_B) & -\frac{1}{2}(\sin \phi_A + \sin \phi_B) \\ 0 & 0 & \frac{1}{2}(\sin \phi_A + \sin \phi_B) & \frac{1}{2}(\cos \phi_A + \cos \phi_B) \end{pmatrix}, \tag{6}$$

where ϕ_A and ϕ_B are the retardance function for pattern A and pattern B encoded in the SLM during one period, and where the \mathbf{x} dependence in these relations was omitted for simplicity.

Mueller–Stokes transformations. The above effective Mueller matrix is analysed using the well-known Lu–Chipman decomposition³⁰, which defines the Mueller matrix as the product of the Mueller matrices of a depolarizer \mathbf{M}_Δ , a retarder \mathbf{M}_R and a diattenuator \mathbf{M}_D . The Mueller matrix \mathbf{M}_Δ of a depolarizing element with its principal axes aligned along the S_1, S_2 and S_3 axes is given by

$$\mathbf{M}_\Delta = \begin{pmatrix} 1 & 0 & 0 & 0 \\ 0 & a_1 & 0 & 0 \\ 0 & 0 & a_2 & 0 \\ 0 & 0 & 0 & a_3 \end{pmatrix}, \tag{7}$$

with $|a_j| = (1 - \Delta_j) \leq 1, j = 1, 2, 3$, being a_j the principal depolarization factors and Δ_j the depolarizance along the S_1, S_2 and S_3 axes³⁰.

The null value of the elements of the first row and column in Eq. (6) reveals the expected result that the system does not present diattenuation nor polarizance. Therefore, the matrix $\langle \mathbf{M}_e(\phi_A, \phi_B) \rangle$ can be decomposed as the product of a pure depolarizer and a linear retarder. It is thus straightforward to show that it can be written as the following product of two matrices:

$$\langle \mathbf{M}_e(\phi_A, \phi_B) \rangle = \begin{pmatrix} 1 & 0 & 0 & 0 \\ 0 & 1 & 0 & 0 \\ 0 & 0 & \cos \bar{\phi} & 0 \\ 0 & 0 & 0 & \cos \bar{\phi} \end{pmatrix} \begin{pmatrix} 1 & 0 & 0 & 0 \\ 0 & 1 & 0 & 0 \\ 0 & 0 & \cos \bar{\phi} & -\sin \bar{\phi} \\ 0 & 0 & \sin \bar{\phi} & \cos \bar{\phi} \end{pmatrix}, \tag{8}$$

where $\bar{\phi}$ is the arithmetic averaged retardance:

$$\bar{\phi} = \frac{\phi_A + \phi_B}{2}, \tag{9}$$

and $\bar{\delta}$ is their semi-difference:

$$\bar{\delta} = \frac{\phi_A - \phi_B}{2}. \tag{10}$$

Thus, Eq. (8) shows that the effective Mueller matrix can be viewed as the combination of a linear retarder aligned along the S_1 axis followed by a depolarizer aligned along S_1, S_2 and S_3 axes.

Figure 1 illustrates on the Poincaré Sphere (PS) the polarization changes induced by such effective Mueller matrix when acting upon an input polarization state $\mathbf{S}_{in} = [S_{in0}, S_{in1}, S_{in2}, S_{in3}]^T$. Since the neutral axes of the effective retarder are along the horizontal and vertical directions (S_1 axis), the matrix $\langle \mathbf{M}_e \rangle$ only modifies the S_{in2} and S_{in3} parameters. Therefore, the output SoP will lie in the plane of the PS defined by the constant value S_{in1} . Figure 1a shows three different planes that contain all the possible SoPs that can be generated for three different input states with diverse values of S_{in1} . As illustrated, the maximum possible number of SoPs are obtained when $S_{in1} = 0$ (orange plane in Fig. 1a), which is the case considered in this work. Note that at the intersection of planes with the PS surface we find fully polarized states, and the center of the PS corresponds to a fully depolarized state. Any other spot in the plane describes a partially polarized state.

To avoid negative values in the depolarization factors a_j in Eq. (7), it is rewritten as $\langle \mathbf{M}_e(\phi_A, \phi_B) \rangle = \mathbf{M}_\Delta(\bar{\delta}) \cdot \mathbf{M}_R(R)$ with

$$\langle \mathbf{M}_e(\phi_A, \phi_B) \rangle = \begin{pmatrix} 1 & 0 & 0 & 0 \\ 0 & 1 & 0 & 0 \\ 0 & 0 & |\cos \bar{\delta}| & 0 \\ 0 & 0 & 0 & |\cos \bar{\delta}| \end{pmatrix} \begin{pmatrix} 1 & 0 & 0 & 0 \\ 0 & 1 & 0 & 0 \\ 0 & 0 & \cos R & -\sin R \\ 0 & 0 & \sin R & \cos R \end{pmatrix}, \tag{11}$$

where the effective retardance R of the retarder matrix $\mathbf{M}_R(R)$ is now given by:

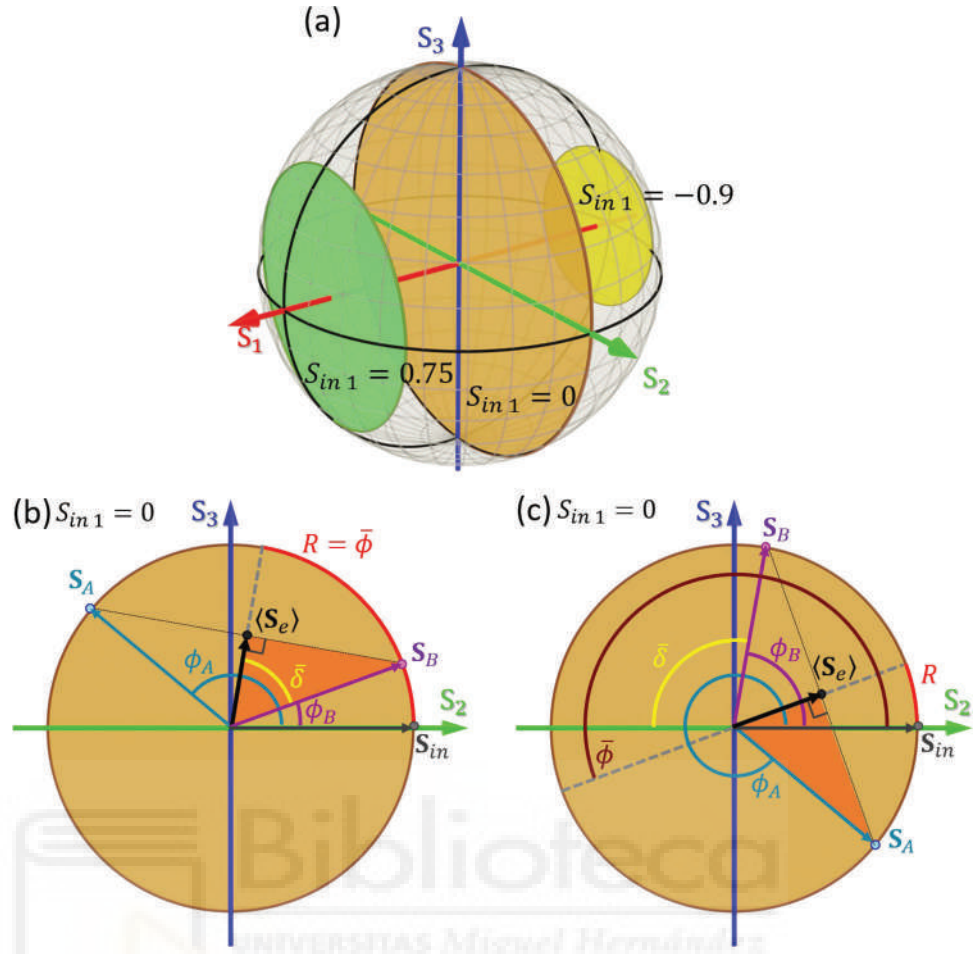


Figure 1. (a) Planes in the Poincaré Sphere defined by a constant value of S_1 . The plane that contains the input state S_{in} defines all the possible SoPs that the effective state $\langle S_e \rangle$ can reach. Note that only the plane $S_1 = 0$ contains all the possible DoP values. (b,c) Composition of the effective output state $\langle S_e \rangle$ as the incoherent addition of states S_A and S_B for an input state with $S_{in1} = 0$ when $\cos \bar{\delta} > 0$ (b) and when $\cos \bar{\delta} < 0$ (c).

$$R = \begin{cases} \bar{\phi} & \text{when } \cos \bar{\delta} > 0 \\ \text{mod } 2\pi (\bar{\phi} + \pi) & \text{when } \cos \bar{\delta} < 0, \\ \text{undefined} & \text{when } \cos \bar{\delta} = 0 \end{cases} \quad (12)$$

where R is defined from 0 to 2π . Note that when $\cos \bar{\delta} = 0$ (situation that occurs when $\phi_A - \phi_B = \pi$) the Mueller matrix $\langle M_e \rangle$ becomes a pure depolarizer (Diag[1, 1, 0, 0]) regardless of the R value. In this situation the retardance is not well defined, since the matrix $M_\Delta(\bar{\delta})$ becomes singular and cannot be inverted, and $M_R(R)$ cannot be determined.

Figure 1b,c illustrate the SoP transformation induced by the effective matrix $\langle M_e \rangle$ on an input state with $S_{in1} = 0$. We consider two situations. In the first case $\cos \bar{\delta} > 0$, i.e., the difference $\phi_A - \phi_B$ modulo 2π between the two phases is lower than π . Figure 1b depicts the plane $S_{in1} = 0$ of the PS and shows how the effective SoP $\langle S_e \rangle$ is obtained from the incoherent addition of the two Stokes vectors (S_A and S_B) that result from the action of matrix $\langle M_e \rangle$ over an input state S_{in} . According to Eq. (2), the effective output Stokes vector $\langle S_e \rangle$ is located at the midpoint on the straight line joining the two points in the PS defined by the vectors S_A and S_B . As depicted in Fig. 1b, the action of the effective retarder matrix $M_R(R)$ can be regarded as a counter-clockwise $R = \bar{\phi}$ rotation of the input vector S_{in} around the S_1 axis of the PS. In turn, the action of the effective depolarizer $M_\Delta(\bar{\delta})$ equally changes the length of the S_{in2} and S_{in3} parameters, and consequently it is related to the DoP of the output vector $\langle S_e \rangle$.

Figure 1c illustrates the SoP transformation when $\cos \bar{\delta} < 0$, a situation that occurs when the difference $\phi_A - \phi_B$ modulo 2π is larger than π . In this case, the global minus sign in $\cos \bar{\delta}$ is equivalent to shifting the effective retardance by π with respect to $\bar{\phi}$, i.e., $R = \text{mod} 2\pi (\bar{\phi} + \pi)$.

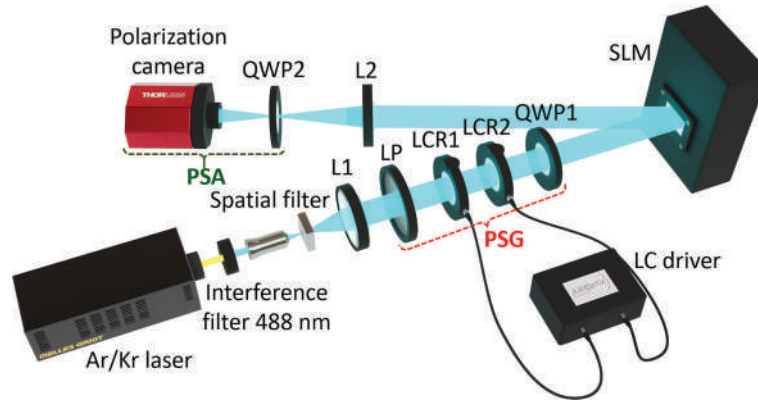


Figure 2. Schematic diagram of the Mueller imaging polarimeter in a reflection configuration (L converging lens, LP linear polarizer, LCR liquid-crystal retarder, QWP quarter wave-plate, SLM reflective spatial light modulator, PSG polarization state generator, PSA polarization state analyzer).

Control of the degree of polarization. The degree of polarization is defined as $DoP = (S_1^2 + S_2^2 + S_3^2)^{1/2}/S_0$, where $0 \leq DoP \leq 1$, and it corresponds to the length of the vector $(S_1, S_2, S_3)/S_0$ in the Poincaré Sphere¹.

While the effective retarder in Eq. (11), defined by the effective retardance R in Eq. (12), describes the rotation in the PS that gives the output polarization state, the corresponding DoP is controlled by the semi-difference $\bar{\delta}$. The matrix $M_{\Delta}(\bar{\delta})$ in Eq. (11) describes a non-homogeneous depolarizer. This is an expected result since we are considering a variable retarder that is always aligned along the horizontal direction. Thus, there is no change of polarization for the horizontal/vertical components. As a consequence, the horizontal/vertical depolarizance in Eq. (7) is $\Delta_1 = 0$, while for the $\pm 45^\circ$ and circular components the depolarizance is given by^{1,30}

$$\Delta_2 = \Delta_3 = 1 - |\cos \bar{\delta}|. \tag{13}$$

The action of the effective Mueller matrix $\langle M_e(\phi_A, \phi_B) \rangle$ on an input polarization state $S_{in} = [S_{in0}, S_{in1}, S_{in2}, S_{in3}]^T$ yields an effective output averaged SoP described by $\langle S_e \rangle = \langle M_e \rangle S_{in}$ with the following effective Stokes parameters:

$$\langle S_e(\phi_A, \phi_B) \rangle = \begin{pmatrix} S_{in0} \\ S_{in1} \\ |\cos \bar{\delta}| (S_{in2} \cos R - S_{in3} \sin R) \\ |\cos \bar{\delta}| (S_{in2} \sin R + S_{in3} \cos R) \end{pmatrix}. \tag{14}$$

Its effective degree of polarization ($DoP_{\langle S_e \rangle}$) is therefore given by:

$$DoP_{\langle S_e \rangle} = \frac{\sqrt{S_{in1}^2 + (S_{in2}^2 + S_{in3}^2) \cos^2 \bar{\delta}}}{S_{in0}}. \tag{15}$$

In this work, we consider input SoPs that are fully polarized, so their degree of polarization is always one: $DoP_{S_{in}} = (S_{in1}^2 + S_{in2}^2 + S_{in3}^2)^{1/2}/S_{in0} = 1$. Applying this condition to Eq. (15) we obtain that the effective DoP for the average output SoP is:

$$DoP_{\langle S_e \rangle} = \sqrt{\left(\frac{S_{in1}}{S_{in0}}\right)^2 \sin^2 \bar{\delta} + \cos^2 \bar{\delta}}. \tag{16}$$

For the case $S_{in1} = 0$ then

$$DoP_{\langle S_e \rangle}(S_{in1} = 0) = |\cos \bar{\delta}|. \tag{17}$$

These relations reveal that a total depolarization ($DoP_{\langle S_e \rangle} = 0$) is attained when $S_{in1} = 0$ and $|\cos \bar{\delta}| = 0$. This happens when the states S_A and S_B lie in antipodal points of the PS (i.e., two orthogonal polarizations are added incoherently) and, consequently, $\langle S_e \rangle$ is right in the center of the sphere. This situation occurs for $\bar{\delta} = \pi/2$.

Experimental setup. The experimental setup used in this work is shown in Fig. 2. It is a Mueller matrix imaging polarimeter³¹ that we have adapted to analyze the polarimetric properties of the reflective LCOS-SLM. It basically consists in two blocks: a tunable polarization state generator (PSG) based on two liquid-crystal retarders and a polarization state analyzer (PSA) based on a polarization camera.

The light source is an Argon/Krypton laser (CVI/Melles Griot, Mod. 35-LTL-835-240) whose 488 nm wavelength is selected using an interference filter. Then, the laser beam is spatially filtered and collimated before entering the liquid-crystal PSG, composed of a vertically-oriented linear polarizer followed by two commercial

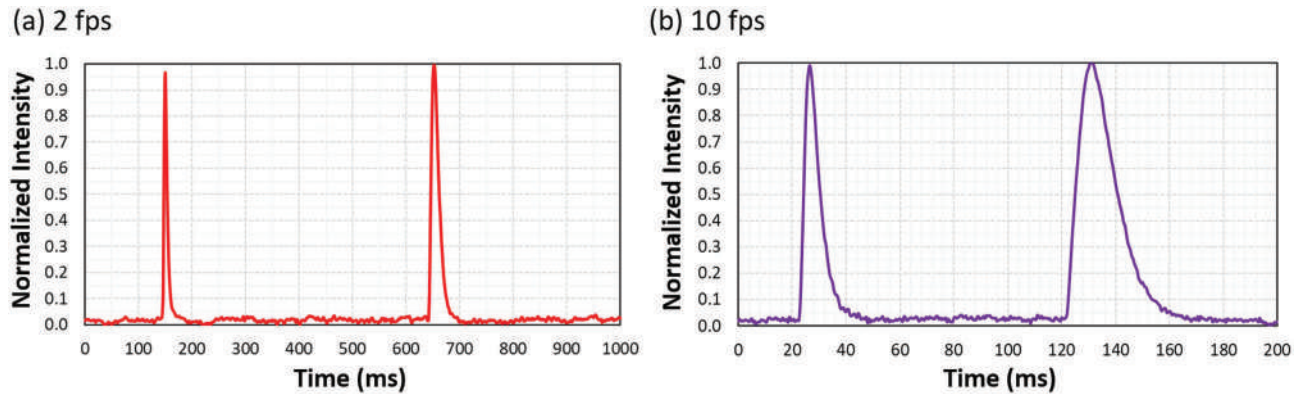


Figure 3. Time-resolved intensity measurements for the SLM between polarizers at 45° . Two gray levels are sequentially addressed to provide a retardance of π and 3π (a) every second and (b) every 0.2 s.

tunable liquid-crystal retarders (LCR) from ArcOptix³² with their fast axis oriented at angles of 45° and 90° , respectively. The final element of the PSG is a quarter wave-plate (QWP1, Thorlabs, AQWP05M600) with its fast axis at -45° . This PSG is a compact version of the one given in³³ consisting of two LCRs and two QWPs. The first LCR in Fig. 2 (LCR1) rotates the input vertical SoP around the S_2 axis in the Poincaré Sphere an angle equal to the selected retardance. The voltage addressed to LCR1 is set to add a $\pi/2$ retardance, resulting in an effective quarter-wave plate placed after LCR1 with its fast axis also oriented at 45° . This effective quarter-wave plate, LCR2 and QWP1 act as a polarization rotator that rotates the SoP around the S_3 axis an angle equals to half the retardance value selected for the second LCR. Therefore, with this PSG, the retardation values of LCR1 and LCR2 provide, respectively, the ellipticity and azimuth angles of the generated SoP. The LCR's retardance were calibrated for the 488 nm wavelength and the generation of the standard SoPs was verified³⁴.

The PSA consists in a second QWP2 with its fast axis vertically oriented and a Kiralux™ Polarization Camera (Thorlabs, CS505MUP). This camera has a monochrome CMOS sensor of 5 megapixels, with integrated four-directional wire grid polarizer array. It has macropixels of $6.9 \mu\text{m}$ consisting in four micropixels of pixel size $3.4 \mu\text{m}$, thus making it possible to detect in a single shot the linear SoPs with orientations at 0° , $\pm 45^\circ$ and 90° . Hence the QWP2 is added before the camera only when the circular polarizations should be detected.

In this work we use as the sample in our imaging polarimeter an LCOS-SLM (Hamamatsu X10468-01), with 800×600 pixels and pixel size $20 \mu\text{m}$. This is a parallel-aligned nematic liquid-crystal on silicon display, thus acting as a reflective linear retarder where the retardance can be tuned through the gray level addressed from a computer. Because it is a reflective device the PSA arm must be placed in a reflection configuration with a reflection angle of $\sim 5^\circ$. The SLM screen plane is imaged on the camera by using a second lens (L2, $f = 200 \text{ mm}$) and by setting the distances to ensure a 1:3 correspondence between the SLM pixels and the camera macropixels. The SLM modulation was calibrated following standard procedures³⁵ in order to obtain the correspondence of the gray scale with the retardation value for the 488 nm wavelength. A retardance variation from 0.65π to more than 4π was found for the standard one-byte gray levels ranging from 0 to 255.

The key aspect of the work is that, instead of addressing the SLM with a standard static gray-level pattern, we make the most of the real-time phase control at each pixel to address a video phase pattern that uses two different images to encode two different retardance values at each pixel. This way, the effective Mueller matrix described in Eqs. (5) and (6) can be experimentally implemented. The first image has a retardance value of $\phi_A(\mathbf{x}) = \phi(\mathbf{x}) + \delta(\mathbf{x})$ and the second has $\phi_B(\mathbf{x}) = \phi(\mathbf{x}) - \delta(\mathbf{x})$, where $\mathbf{x} = (x, y)$ denotes the spatial coordinates at the SLM plane.

The SLM operates at video rate (60 Hz). Figure 3 shows time resolved measurements where we experimentally verified the SoP transitions that occur when frames change. We follow the experimental scheme in²¹, where the light beam reflected from the SLM is measured with a detector (Newport 818-SL) and monitored in an oscilloscope. The SLM is illuminated with linearly polarized light at 45° with respect to the LC director. In addition, a linear polarizer is placed before the detector oriented parallel to the incident polarization. Two gray levels are sequentially addressed to the SLM, selected to provide a retardance of π and 3π . Under this configuration, the phase difference between the gray levels is 2π , so the same polarization state is obtained at the output. The figure shows one period of the sequence when the gray levels are switched at 2 fps (frames-per-second) and at 10 fps. Figure 3a shows how the detected signal remains constant at the expected zero intensity except for the two narrow peaks that correspond to the transitions between the two gray levels. These peaks show a different width depending on whether the gray level is increased or decreased. The sum of their widths in a period is about 60 ms, thus representing a very small fraction of the total interval when operating at 2 fps. On the contrary, when operating at 10 fps (Fig. 3b) these transitions intervals approach the period of the sequence, and therefore cannot be ignored.

Since we want to mimic the situation in Eqs. (5) and (6) with a good fidelity and reduce the impact of these transition intervals, we selected a video film with very low rate of only two frames-per-second. For higher rates, the transition intervals of the LC molecules become much more noticeable and therefore they must be considered in the calculation of the effective Mueller Matrix of the SLM. While the video was displayed on the SLM screen, a total of 36 images were captured by the camera. Each image corresponds to the generation and detection of the six standard SoPs (linear states oriented at 0° , $\pm 45^\circ$ and 90° , and circular states) by the LC-PSG

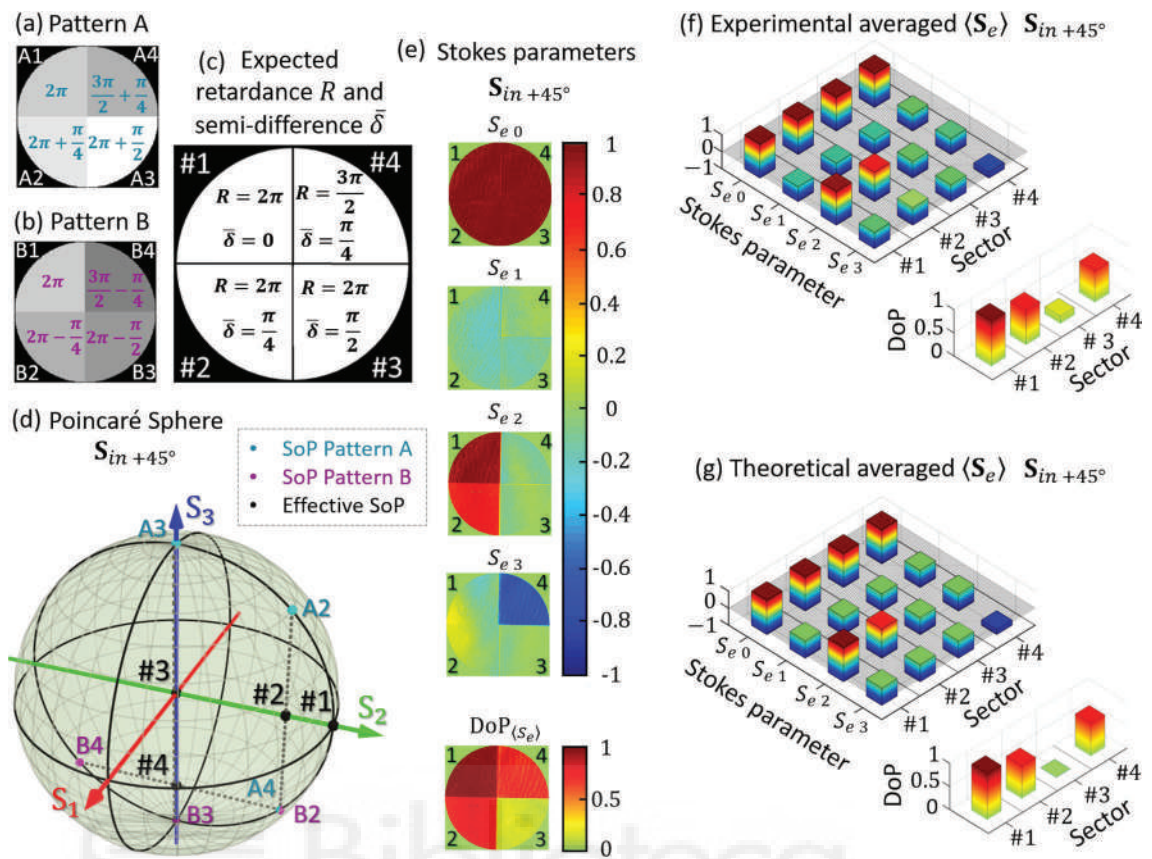


Figure 4. (a,b) Switching phase-pattern images. (c) Expected retardance and semi-difference. (d) Location of the theoretical effective SoP for each j pattern sector where $j = 1, 2, 3, 4$ on the Poincaré sphere for a linear incident SoP at $+45^\circ$. The points A- j and B- j indicate the SoP of the individual phase pattern. (e,f) Experimental output effective Stokes parameters $(S_e) = (S_{e0}, S_{e1}, S_{e2}, S_{e3})$ and their respective effective DoP (S_e) when the incident beam is polarized at $+45^\circ$. (g) Corresponding expected theoretical Stokes parameters and DoP.

and the PSA, respectively. Note that the use of the polarization camera reduces the number of measurements to 12 different PSG-PSA combinations. It can be argued that such a slow rate of two frames per second cannot generate a real depolarization effect. This is the reason why we name this proof-of-concept system an “emulator depolarizer system”. Although, from a theoretical point of view, depolarization is related to polarization changes at electron transitions rates, from a practical point of view, where detectors and CCDs sensors are required to conduct radiometric measurements or images, an effective depolarization would be detected. Therefore, having a detector rate even slower than the LCOS-SLM rate provides equivalent effective polarimetric results. Note that much faster response could be achieved with SLM devices based on ferroelectric liquid crystals, capable to switch at kHz rates³⁶. A faster switching response can be reached with nematic liquid-crystal SLMs by applying a transient effect³⁷.

The coefficients of the experimental Mueller matrix were calculated according to standard methods³⁸ and the polarimeter calibration was made by measuring the air and a quarter wave plate. The use of LCR devices avoid having moving parts in the polarimeter, but when employed with a coherent source, as it is our case, induces interference fringes in the captured images. We applied a digital Notch filter to eliminate this periodic noise in the polarimetric measurements³⁹.

Results and discussion

In this section we provide the experimental results obtained with different phase pattern images that emulate samples featuring different depolarization spatial patterns. Three cases are considered: a four-quadrant pattern, a text and a spiral pattern where the SoP and DoP are spatially varying.

CASE I: four sector patterns. Figure 4a,b illustrate the phase pattern images $\phi_A(x)$ and $\phi_B(x)$, respectively. These are the two gray-level images addressed to the SLM that switch to generate the time varying retarder. In this first example they are divided into four sectors, each with a different retardance value. Sectors #A1 and #B1 lie in the upper left part of the image and the following sectors in a counter-clockwise direction. Sectors #1, #2 and #3 are designed to provide retardances around a mean value $\phi = 2\pi$, so there is no other change than depolarization on the effective SoP compared to the input state. Figure 4c shows the expected effective retardance R and the semi-difference $\bar{\delta}$.

To understand how this effective depolarization generator works, we have illustrated the output SoP for each sector separately, as well as the theoretical effective SoP on the Poincaré sphere for an incident beam with $+45^\circ$ linear polarization ($\mathbf{S}_{in+45^\circ} = [1, 0, 1, 0]^T$). Figure 4d illustrates the expected polarization transformations in the Poincaré sphere. The input state is the black point #1, which also corresponds to the output state for sector #1, thus remaining fully polarized. For the other sectors, the output states for each individual phase pattern (A and B) are indicated in the PS as points A_j and B_j , where $j=2,3,4$ denotes the sector. The time-averaged output SoP is drawn as the black spots #2, #3 and #4. When the retardation difference in both phase images is $2\bar{\delta} = \pi/2$ (sectors #2 and #4), the effective SoPs lie inside the Poincaré sphere on states $\langle \mathbf{S}_{e,2} \rangle = [1, 0, 1/\sqrt{2}, 0]^T$ and $\langle \mathbf{S}_{e,4} \rangle = [1, 0, 0, -1/\sqrt{2}]^T$ (black dots #2 and #4), therefore they have $\text{DoP} = 1/\sqrt{2}$. On the other hand, when the input SoP is reflected by sector #3, the output individual SoP switches between right and left circular polarizations (points A_3 and B_3) and, consequently, the effective SoP lies in the center of the sphere, $\langle \mathbf{S}_{e,3} \rangle = [1, 0, 0, 0]^T$, (black spot number #3). In this case, the generation of two individual orthogonal SoPs results in a fully depolarized averaged SoP.

Images of the experimental output effective Stokes parameters (\mathbf{S}_e) obtained with the imaging polarimeter for an input $+45^\circ$ linear state (\mathbf{S}_{in+45°) are shown in Fig. 4e, together with the corresponding measured DoP. The average parameters at each sector are presented in Fig. 4f and their theoretical values are plotted in Fig. 4g for comparison. Sectors #A1 and #B1 have the same retardance ($R = 2\pi$), therefore the Stokes parameters of the input SoP are not modified and the output effective $\text{DoP}_{(\mathbf{S}_e)}$ approaches to 1. Sectors #2 and #4 modify the polarization of the incident SoP since the output value of S_{e2} and S_{e3} in Fig. 4e are no longer one, resulting in a partially polarized output with effective $\text{DoP}_{(\mathbf{S}_e)}$ close to the expected value of $1/\sqrt{2}$. Finally, the effective output Stokes parameters for sector #3 resembles that of unpolarized light. The experimental non-null parameter S_{e1} makes the $\text{DoP}_{(\mathbf{S}_e)}$ value not exactly zero; this slight discrepancy may be due to the transition intervals between frames in the LCOS-SLM or to experimental errors of the polarimeter system³¹. Nevertheless, these results demonstrate the ability of the procedure to emulate spatial patterns with variable SoP and DoP.

A complete characterization of the SLM as a depolarization emulator requires obtaining its experimental Mueller matrix image. In this case, it is an effective matrix that describes the complete polarimetric response of the SLM when being addressed with time-varying patterns for any incident SoP. For that purpose, we consider the six typical SoPs (H, V, $+45^\circ$, -45° , RCP and LCP) in both the PSG and PSA. Figure 5a shows the experimental effective Mueller matrix (\mathbf{M}_e), normalized by the m_{00} element. Figure 5a shows the images derived for the 16 elements of the Mueller matrix. The four sectors of the encoded phase patterns are only clearly visible in four elements of the lower-right 2×2 submatrix. These Mueller matrix elements are averaged considering all the pixels within each sector and they are plotted in Fig. 5b–e, together with the theoretical values. The corresponding numerical data are provided in Table 1. The result in all cases show a very good agreement. For instance, the effective matrix in sector #1 (Fig. 5b) resembles very well the identity matrix, $\langle \mathbf{M}_{e,1} \rangle \approx \mathbf{I}$, while in sector #2, $\langle \mathbf{M}_{e,2} \rangle$ becomes a diagonal matrix (Fig. 5c) with $m_{00} = m_{11} = 1$ but coefficients m_{22} and m_{33} reduced to $1/\sqrt{2}$. A similar situation occurs in sector #3, where $\langle \mathbf{M}_{e,3} \rangle$ is now the diagonal matrix $\text{Diag}[1, 1, 0, 0]$ (Fig. 5d). Finally, in sector #4 we obtain the Mueller matrix with all elements null except $m_{00} = m_{11} = 1$, $m_{23} = 1/\sqrt{2}$ and $m_{32} = -1/\sqrt{2}$.

Comparison of the theoretical and experimental data in Fig. 5 and in Table 1 show very good agreement, within the limits of the instrumental error provided by our developed imaging polarimeter. This error was estimated in³¹ using polarizers and retarders as samples, and was shown to be in all cases less than 7%. It was attributed to different error sources like the precise retardance of the LCR devices employed in the PSG, the required movable QWP in the PSA, or the speckle noise caused by laser light. In addition, slight deviations of the SLM modulation from the ideal two-phase pattern also contribute to these discrepancies. Nevertheless, these results illustrate how the temporal sequence addressed to the SLM can be used to control its effective Mueller matrix.

The Lu–Chipman decomposition³⁰ was applied to the experimental effective Mueller matrix to calculate the main polarimetric parameters, like diattenuation (D), polarizance (P), retardance (R) and depolarization (Δ), as if there was no a-priori knowledge of the characteristics of the sample³¹. The elements of the first row and column of the normalized \mathbf{M}_e are related to diattenuation and polarizance, respectively. These parameters are not relevant in our analysis since they are almost zero (their maximum values are $D = 0.10$ and $P = 0.18$ in sector #4). This result was expected as LCOS-SLMs are considered non-dichroic elements. Figure 5f–h shows images of the depolarizance parameters Δ_1 , Δ_2 , Δ_3 . Image 4(f) shows how the H/V depolarizance parameter Δ_1 is null for all sectors, while both $\pm 45^\circ$ linear (Δ_2) and circular (Δ_3) depolarizance change in different sectors in Fig. 5g,h, becoming maximum $\Delta_2 \approx \Delta_3 \approx 1$ in sector #3. Finally, the measured effective retardance is shown in Fig. 5i. Sectors #1 and #2 show experimental values close to the expected result $R = 0$, while in sector #4 the average value is $R = 0.48\pi$, very close to the expected result $R = 0.5\pi$. In sector #3, the expected retardance is not well defined, as discussed in the previous section.

CASE II: text pattern encoded in DoP. The SLM allows a full control of the retardance at every pixel. Here, we make the most of this capability in order to encode a text pattern with gradually varying depolarization. For that purpose, two phase patterns were designed, each one encoding the word DESPOLARIZACIÓN (depolarization in Spanish). Figure 6a,b show the pattern gray-level images addressed to the SLM. They encode the phase functions $\phi_A(\mathbf{x})$ and $\phi_B(\mathbf{x})$, where about 30×40 pixels were used for each letter. The phase value in some specific letters and in the background is indicated in the figure. The averaged retardance is always $\bar{\phi} = 3\pi$ and the retardance difference gradually changes from $\bar{\delta} = 3\pi/4$ to $\bar{\delta} = \pi/4$ in steps of $\pi/28$. Again, we illuminate the SLM with a fully polarized state $\mathbf{S}_{in+45^\circ} = [1, 0, 1, 0]^T$. Figure 6c illustrates on the PS, and for each letter, the output states \mathbf{S}_A (blue dots) and \mathbf{S}_B (purple dots) generated by each pattern, and the expected averaged SoP (black dots). Note that states \mathbf{S}_A and \mathbf{S}_B lie on points opposite to each other with respect to the S_2 axis. Therefore,

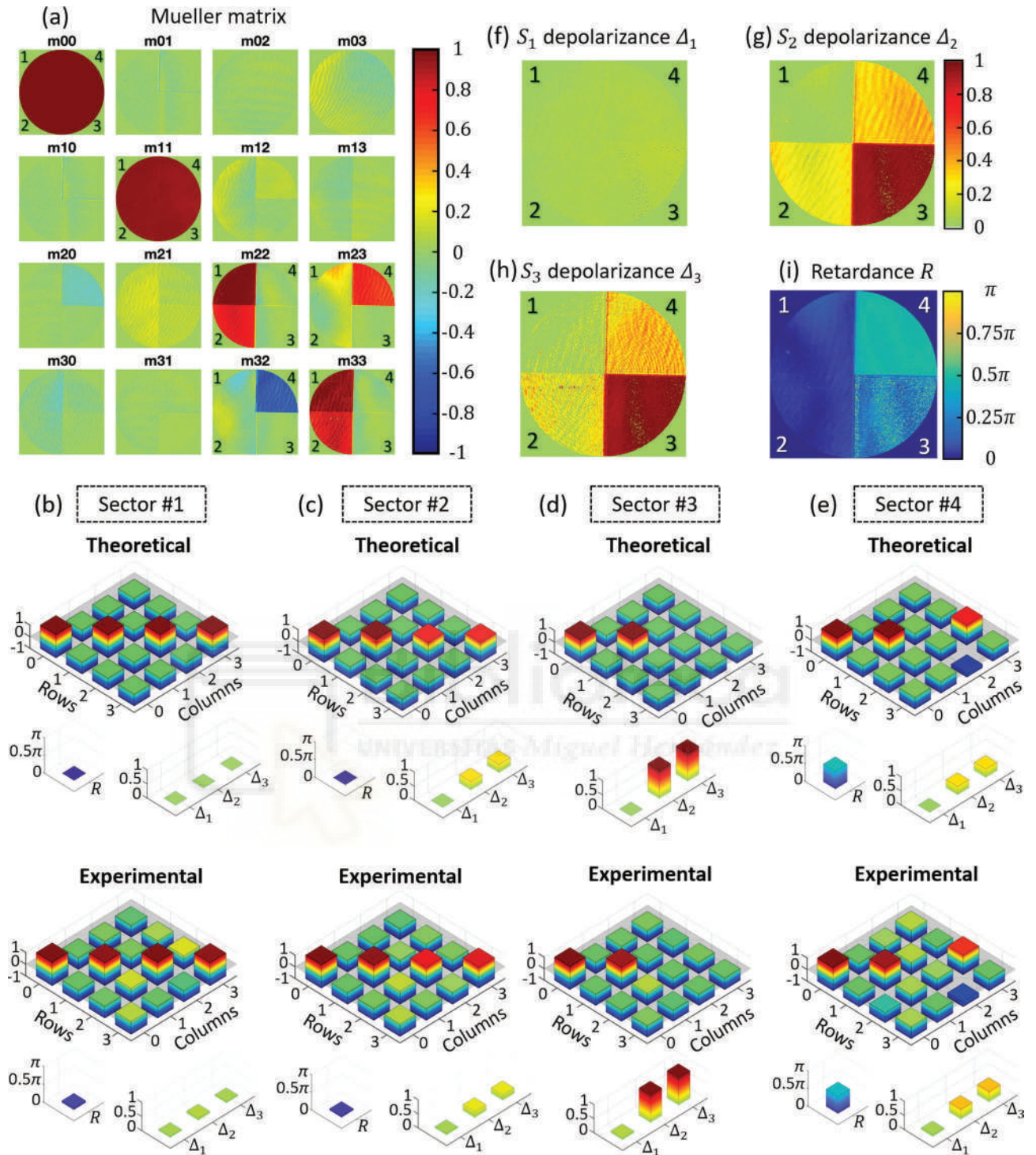


Figure 5. (a) Experimental effective Mueller matrix images for the four-sector pattern. (b–e) Comparison of the theoretical Mueller matrix averaged values. (f–h) Effective depolarization (Δ_1 , Δ_2 , Δ_3) and (i) effective retardance (R).

the averaged states lie all on the S_2 axis with an effective DoP that changes gradually from one letter to the next according to Eq. (17). In the extremes (letters D and N), the semi-difference phase is $\delta = \pi/4$ and $\delta = 3\pi/4$, hence their effective DoP is $\text{DoP}_{(S_e)} = 1/\sqrt{2}$, while in the center (letter R) $\delta = \pi/2$ and the output becomes fully depolarized, $\text{DoP}_{(S_e)} = 0$.

Figure 6d illustrates the measured effective parameter S_2 for input 45° linear polarization, which shows the progressive change as we move along the word. The measured effective $\text{DoP}_{(S_e)}$, plotted in Fig. 6e, displays the

Mueller Matrix, depolarizance and retardance averaged values

| | | Theoretical | | Experimental | | | | | | | | | | | |
|---------------------------|------------|-------------|-------|---------------------------|-------|------|-------|------------|------------|---|-------|------------|-------|------|-------|
| Sector #1 | | | | Sector #4 | | | | | | | | | | | |
| $\langle M_{e,1} \rangle$ | | | | $\langle M_{e,4} \rangle$ | | | | | | | | | | | |
| 1 | 1.00 | 0 | -0.02 | 0 | 0.01 | 0 | 0.04 | 1 | 1.00 | 0 | -0.02 | 0 | 0.03 | 0 | -0.08 |
| 0 | -0.01 | 1 | 0.95 | 0 | 0.00 | 0 | -0.06 | 0 | -0.01 | 1 | 0.93 | 0 | 0.08 | 0 | 0.03 |
| 0 | -0.00 | 0 | 0.14 | 1 | 0.99 | 0 | 0.16 | 0 | -0.17 | 0 | 0.06 | 0 | 0.02 | 0.71 | 0.65 |
| 0 | -0.09 | 0 | 0.01 | 0 | -0.07 | 1 | 0.95 | 0 | -0.05 | 0 | 0.01 | -0.71 | -0.62 | 0 | -0.00 |
| R | | | | Δ_1 | | | | Δ_2 | | | | Δ_3 | | | |
| 0 | 0.05 π | 0 | 0.05 | 0 | 0.08 | 0 | 0.05 | 0.5 π | 0.48 π | 0 | 0.06 | 0.29 | 0.35 | 0.29 | 0.37 |
| Sector #2 | | | | Sector #3 | | | | | | | | | | | |
| $\langle M_{e,2} \rangle$ | | | | $\langle M_{e,3} \rangle$ | | | | | | | | | | | |
| 1 | 1.00 | 0 | -0.02 | 0 | -0.01 | 0 | -0.06 | 1 | 1.00 | 0 | -0.01 | 0 | -0.00 | 0 | -0.01 |
| 0 | -0.02 | 1 | 0.95 | 0 | 0.02 | 0 | -0.01 | 0 | -0.02 | 1 | 0.94 | 0 | -0.01 | 0 | 0.05 |
| 0 | 0.01 | 0 | 0.12 | 0.71 | 0.77 | 0 | 0.01 | 0 | -0.01 | 0 | 0.09 | 0 | -0.00 | 0 | 0.01 |
| 0 | -0.06 | 0 | -0.00 | 0 | 0.02 | 0.71 | 0.79 | 0 | -0.06 | 0 | 0.00 | 0 | -0.01 | 0 | -0.00 |
| R | | | | Δ_1 | | | | Δ_2 | | | | Δ_3 | | | |
| 0 | 0.04 π | 0 | 0.05 | 0.29 | 0.22 | 0.29 | 0.20 | - | - | 0 | 0.07 | 1 | 0.98 | 1 | 0.98 |

Table 1. Experimental and theoretical effective Mueller matrices, depolarizance ($\Delta_1, \Delta_2, \Delta_3$) and retardance (R) averaged values, as presented in Fig. 5.

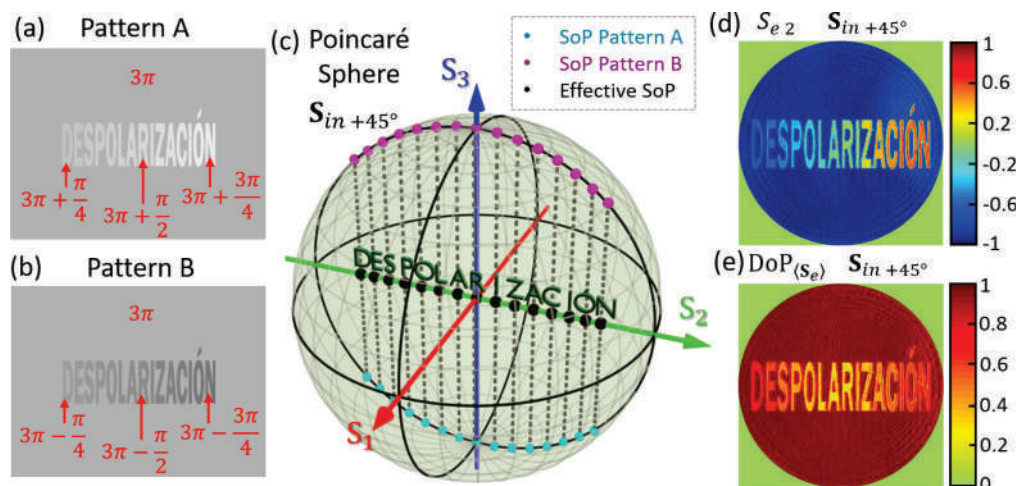


Figure 6. (a,b) Phase pattern images encoding a text, with indication of the phase levels, (c) theoretical S_A, S_B and $\langle S_e \rangle$ Stokes parameters on the Poincaré sphere for each letter and for an input SoP linear at $+45^\circ$, (d) experimental effective Stokes parameter S_{e2} of the output beam, and (e) experimental effective $DoP_{\langle S_e \rangle}$.

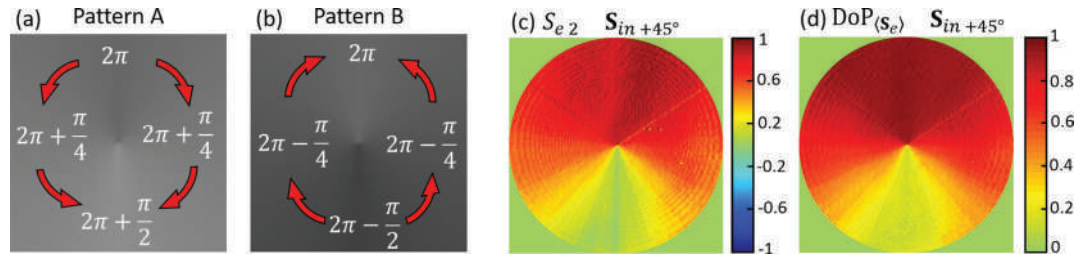


Figure 7. (a,b) Phase pattern images encoding a spiral distribution, with indication of the phase levels. The red arrows denote the sense where the phase increases. (c) Experimental effective Stokes parameter S_{e2} when the incident beam is linearly polarized at $+45^\circ$ and (d) experimental effective DoP(S_{e2}) image.

expected behavior: DoP(S_{e2}) takes the largest value in the letters at the extremes while gradually decreases to the center, reaching the minimum value at the central letter (R).

CASE III: spirally shaped depolarization. As a final example, we generate a DoP spiral pattern. In the same way as spiral phase patterns are basic elements in vortex and vector beam generation, which have become much popular in the last decades, it might be interesting to explore the possibility of using DoP as an additional degree of freedom in the numerous applications of such singular beams⁴⁰.

To probe the effective realization of a DoP spiral pattern, we designed the two phase-patterns $\phi_A(\mathbf{x})$ and $\phi_B(\mathbf{x})$ shown in Fig. 7a,b, where the retardance increases azimuthally from 2π to $5\pi/2$ (starting on the y-axis) and decreases from 2π to $3\pi/2$, respectively. The averaged retardance is $\bar{\phi} = 2\pi$. Considering an input linear state at $+45^\circ$, the effective Stokes parameters are $\langle S_e \rangle = [1, 0, S_{e2}, 0]^T$ where S_{e2} changes azimuthally, as demonstrated experimentally in Fig. 7c. As it is observed, $S_{e2} \approx 1$ at the top of the image and continuously decreases with the azimuth angle, reaching $S_{e2} \approx 0$ at the opposite direction. The experimental effective DoP in this case coincides with the S_{e2} parameter, presenting a depolarization azimuthally variant-pattern, as shown in Fig. 7d. The depolarizing pattern shows a maximum DoP(S_{e2}) ≈ 1 at the top of the image, where δ is zero, and a minimum DoP(S_{e2}) ≈ 0 at the bottom of the image, where $\delta = \pi/2$. Thus, at the center there is a polarization singularity, in this case encoded in the DoP function.

Conclusion

In summary, we have demonstrated a spatially controlled depolarization emulator based on a LCOS-SLM that is addressed with a time-varying gray level pattern, thus encoding a time-varying pixelated linear retarder. This allows us to perform spatial light patterns where both the state of polarization and the degree of polarization can be controlled at will.

As a proof-of-concept, three depolarization spatial patterns are realized. We name the system a “depolarization emulator” because the LCOS-SLM operates at very low rate; hence, large integration times are required in the polarimetric procedure. Nevertheless, the experimental results in this proof-of-concept demonstrate the realization of spatially varying light patterns with controlled DoP, and equivalent results could be obtained with faster SLMs, like ferroelectric liquid-crystal devices.

We describe the polarization transformations for a linear retarder depolarizer consisting in a two-level retardance time-varying pattern. An analysis of the time averaged Mueller matrix and its implications on the Poincaré sphere transformations is provided. We have shown that the output effective polarization state is governed by the averaged retardance $\bar{\phi}$, while the degree of polarization is governed by the retardance semi-difference δ .

Finally, we have shown the generation of different spatial patterns with a controlled variation of the DoP (a four-sector pattern, a text, and a spiral pattern). The polarization properties of the output light beam were verified by imaging the SLM screen onto a polarizing camera and applying a complete Mueller matrix imaging polarimetry procedure. In all cases the measured polarization parameters agree very well with the expected results.

While spatial incoherent coupling depolarization methods are very effective to depolarize a single beam, the proposed technique allows applying a different temporal depolarization effect in different pixels, thus generating different DoP at different points of a given sample. This is a unique characteristic that could not be accomplished with a spatial incoherent depolarizer. It might be interesting for instance in testing imaging polarimeters as well as in applications where a controlled depolarization is needed, especially in situations where a spatial pattern or image is required. The system can also be very relevant in investigating the different origins of depolarization and its relationship with the different depolarization parameters.

Received: 22 February 2021; Accepted: 12 April 2021

References

- Goldstein, D. H. *Polarized Light* (Marcel Dekker, 2010).
- Azzam, R. M. A. & Bashara, N. M. *Ellipsometry and Polarized Light* (Elsevier, 1996).
- Bueno, J. M. Polarimetry using liquid-crystal variable retarders: Theory and calibration. *J. Opt. A Pure Appl. Opt.* **2**, 216–222. <https://doi.org/10.1088/1464-4258/2/3/308> (2000).

4. Uribe-Patarroyo, N. *et al.* IMAx: A polarimeter based on liquid crystal variable retarders for an aerospace mission. *Phys. Stat. Sol. C* **5**, 1041–1045. <https://doi.org/10.1002/pssc.200777771> (2008).
5. Peinado, A., Lizana, A., Vidal, J., Lemmi, C. & Campos, J. Optimization and performance criteria of a Stokes polarimeter based on two variable retarders. *Opt. Exp.* **18**, 9815–9830. <https://doi.org/10.1364/OE.18.009815> (2010).
6. Jaulin, A., Bigué, L. & Ams, P. High-speed degree-of-polarization imaging with a ferroelectric liquid-crystal modulator. *Opt. Eng.* **47**, 033201. <https://doi.org/10.1117/1.2894811> (2008).
7. Van Eeckhout, A. *et al.* Polarimetric imaging of biological tissues based on the indices of polarimetric purity. *J. Biophotonics* **11**, e201700189. <https://doi.org/10.1002/jbio.201700189> (2018).
8. Kupinski, M. *et al.* Polarimetric measurement utility for pre-cancer detection from uterine cervix specimens. *Biomed. Opt. Exp.* **9**, 5691–5702. <https://doi.org/10.1364/BOE.9.005691> (2018).
9. Vizet, J. *et al.* In vivo imaging of uterine cervix with a Mueller polarimetric colposcope. *Sci. Rep.* **7**, 2471. <https://doi.org/10.1038/s41598-017-02645-9> (2017).
10. Wang, J. S., Costelloe, J. R. & Stolen, R. H. Reduction of the degree of polarization of a laser diode with a fiber Lyot depolarizer. *IEEE Phot. Technol. Lett.* **11**, 1449–1451. <https://doi.org/10.1109/68.803075> (1999).
11. Bene, L. *et al.* Depolarized FRET (depolFRET) on the cell surface: FRET control by photoselection. *Biochim. Biophys. Acta* **322–334**, 2016. <https://doi.org/10.1016/j.bbamer.2015.12.003> (1863).
12. Hwang, T. Y., Shin, H., Kang, J., Lee, B. & Guo, C. One-step fabrication of bi- and quad-directional femtosecond laser-induced periodic surface structures on metal with a depolarizer. *Appl. Surf. Sci.* **493**, 231–238. <https://doi.org/10.1016/j.apsusc.2019.07.025> (2019).
13. Sharma, S. *et al.* Input polarization-independent polarization-sensitive optical coherence tomography using a depolarizer. *Rev. Sci. Instrum.* **91**, 043706. <https://doi.org/10.1063/5.0001871> (2020).
14. Burns, W. K. Degree of polarization in the Lyot depolarizer. *J. Light. Technol.* **1**, 475–479. <https://doi.org/10.1364/AO.23.003284> (1983).
15. Lizana, A. *et al.* Arbitrary state of polarization with customized degree of polarization generator. *Opt. Lett.* **40**, 3790–3793. <https://doi.org/10.1364/OL.40.003790> (2015).
16. Kanseri, B. & Gupta, R. Observation of Pancharatnam-Berry phase for unpolarized and partially polarized light fields. *Results Opt.* **2**, 100048. <https://doi.org/10.1016/j.rio.2020.100048> (2021).
17. Ortega-Quijano, N., Fade, J., Parnet, F. & Alouini, M. Generation of a coherent light beam with precise and fast dynamic control of the state and degree of polarization. *Opt. Lett.* **42**, 2898–2901. <https://doi.org/10.1364/OL.42.002898> (2017).
18. Zhang, D. *et al.* Cholesteric liquid crystal depolarizer. *Opt. Eng.* **46**, 070504. <https://doi.org/10.1117/1.2756073> (2007).
19. Wei, B. Y. *et al.* Liquid crystal depolarizer based on photoalignment technology. *Photon. Res.* **4**, 70–73. <https://doi.org/10.1364/PRJ.4.000070> (2016).
20. Maré, P. *et al.* Monochromatic depolarizer based on liquid crystal. *Curr. Comput.-Aided Drug Des.* **9**, 387. <https://doi.org/10.3390/cryst9080387> (2019).
21. Lizana, A. *et al.* Time-resolved Mueller matrix analysis of a liquid crystal on silicon display. *Appl. Opt.* **47**, 4267–4274. <https://doi.org/10.1364/AO.47.004267> (2008).
22. Clemente, P. *et al.* Use of polar decomposition of Mueller matrices for optimizing the phase response of a liquid-crystal-on-silicon display. *Opt. Express* **16**, 1965–1974. <https://doi.org/10.1364/OE.16.001965> (2008).
23. Peinado, A., Lizana, A. & Campos, J. Use of ferroelectric liquid crystal panels to control state and degree of polarization in light beams. *Opt. Lett.* **39**, 659–662. <https://doi.org/10.1364/OL.39.000659> (2014).
24. Amako, J., Miura, H. & Sonehara, T. Speckle-noise reduction on kinoform reconstruction using a phase-only spatial light modulator. *Appl. Opt.* **34**, 3165–3171. <https://doi.org/10.1364/AO.34.003165> (1995).
25. Liu, S.-J., Wang, D., Li, S.-J. & Wang, Q.-H. Speckle noise suppression method in holographic display using time multiplexing. *Opt. Commun.* **436**, 253–257. <https://doi.org/10.1016/j.optcom.2018.12.038> (2019).
26. Chipman, R. A. Depolarization index and the average degree of polarization. *Appl. Opt.* **44**, 2490–2495. <https://doi.org/10.1364/AO.44.002490> (2005).
27. Van Eeckhout, A. *et al.* Synthesis and characterization of depolarizing samples based on the indices of polarimetric purity. *Opt. Lett.* **42**, 4155–4158. <https://doi.org/10.1364/OL.42.004155> (2017).
28. Rosales-Guzmán, C., Ndagano, B. & Forbes, A. A review of complex vector light fields and their applications. *J. Opt.* **20**, 123001. <https://doi.org/10.1088/2040-8986/aaeb7d> (2018).
29. Piquero, G., Martínez-Herrero, R., de Sande, J. C. G. & Santarsiero, M. Synthesis and characterization of non-uniformly totally polarized light beams: Tutorial. *J. Opt. Soc. Am. A* **37**, 591–605. <https://doi.org/10.1364/JOSAA.379439> (2020).
30. Lu, S. Y. & Chipman, R. A. Interpretation of Mueller matrices based on polar decomposition. *J. Opt. Soc. Am. A* **13**, 1106–1113. <https://doi.org/10.1364/JOSAA.13.001106> (1996).
31. López-Morales, G., Sánchez-López, M. M., Lizana, A., Moreno, I. & Campos, J. Mueller matrix polarimetric imaging analysis of optical components for the generation of cylindrical vector beams. *Curr. Comput.-Aided Drug Des.* **10**, 1155. <https://doi.org/10.3390/cryst10121155> (2020).
32. ArcOptix, Variable phase retarder (accessed 2 November 2020); http://www.arcoptix.com/variable_phase_retarder.htm.
33. Davis, J. A. *et al.* Analysis of a segmented q-plate tunable retarder for the generation of first-order vector beams. *Appl. Opt.* **54**, 9583–9590. <https://doi.org/10.1364/AO.54.009583> (2015).
34. López-Morales, G., Sánchez-López, M. M. & Moreno, I. Liquid-crystal polarization state generator. In *Proc. SPIE of the Unconventional Optical Imaging II*, Vol. 11351 113511 (2020). <https://doi.org/10.1117/12.2555697>.
35. Davis, J. A., Tsai, P. S., Cottrell, D. M., Sonehara, T. & Amako, J. Transmission variations in liquid crystal spatial light modulators caused by interference and diffraction effects. *Opt. Eng.* **38**, 1051–1057. <https://doi.org/10.1117/1.602149> (1999).
36. ForthD displays (accessed 3 January 2021); <https://www.forthdd.com/products/spatial-light-modulators/>.
37. Xun, X., Cho, D. J. & Cohn, R. W. Spiking voltages for faster switching of nematic liquid-crystal light modulators. *Appl. Opt.* **45**, 3136–3143. <https://doi.org/10.1364/AO.45.003136> (2006).
38. Espinosa-Luna, R. & Zhan, Q. Polarization and polarizing optical devices. In *Fundamentals and Basic Optical Instruments, Handbook of Optical Engineering* (ed. Hernández, D. M.) (CRC Press, 2017).
39. Moallemi, P. & Behnampourii, M. Adaptive optimum notch filter for periodic noise reduction in digital images. *AUT J. Electr. Eng.* **42**, 1–7. <https://doi.org/10.22060/EEJ.2010.94> (2010).
40. Chen, P. *et al.* Digitalized geometric phases for parallel optical spin and orbital angular momentum encoding. *ACS Photonics* **4**, 1333–1338. <https://doi.org/10.1021/acsp Photonics.7b00263> (2017).

Acknowledgements

This research was funded by Generalitat Valenciana, Conselleria d'Educació, Investigació, Cultura I Esport (Grant PROMETEO-2017-154) and by Ministerio de Ciencia, Innovación y Universidades, Spain (Grants RTI2018-097107-B-C31 and RTI2018-097107-B-C33).

Author contributions

D.M., G.L.M., M.M.S.L. and I.M. conceived the original idea. G.L.M. developed the software and the data analysis. G.L.M. and D.M. carried out the experimental results. D.M., A.L. and J.C. completed the theoretical analysis. All authors analyzed and discussed the experimental results and assisted in writing the manuscript.

Competing interests

The authors declare no competing interests.

Additional information

Correspondence and requests for materials should be addressed to M.M.S.-L.

Reprints and permissions information is available at www.nature.com/reprints.

Publisher's note Springer Nature remains neutral with regard to jurisdictional claims in published maps and institutional affiliations.



Open Access This article is licensed under a Creative Commons Attribution 4.0 International License, which permits use, sharing, adaptation, distribution and reproduction in any medium or format, as long as you give appropriate credit to the original author(s) and the source, provide a link to the Creative Commons licence, and indicate if changes were made. The images or other third party material in this article are included in the article's Creative Commons licence, unless indicated otherwise in a credit line to the material. If material is not included in the article's Creative Commons licence and your intended use is not permitted by statutory regulation or exceeds the permitted use, you will need to obtain permission directly from the copyright holder. To view a copy of this licence, visit <http://creativecommons.org/licenses/by/4.0/>.

© The Author(s) 2021

